Performance of RC Bridge Columns under Cyclic Combined Loading including Torsion

A Dissertation

Presented to

the Faculty of the Department of Civil and Environmental Engineering

University of Houston

In Partial Fulfillment

of the Requirements for the Degree

Doctor of Philosophy

in Civil Engineering

by

Qian Li

December 2012

Performance of RC Bridge Columns under Cyclic Combined Loading including Torsion

Qian Li

Approved:

Chair of the Committee
Dr. Abdeldjelil Belarbi, Professor
Civil and Environmental Engineering

Committee Members

Dr. Yi-Lung Mo, Professor
Civil and Environmental Engineering

Dr. Pradeep Sharma, Professor
Mechanical Engineering

Dr. Gangbing Song, Professor
Mechanical Engineering

Dr. Mina Dawood, Assistant Professor
Civil and Environmental Engineering

Dr. Suresh K. Khator, Associate Dean
Cullen College of Engineering

Dr. Abdeldjelil Belarbi, Professor and Chair
Civil and Environmental Engineering

Acknowledgments

I would like to offer my deeply heartfelt gratitude to my advisor, Dr. Abdeldjelil Belarbi, for his continuous encouragement and guidance, and dedication of his time and energy. Dr. Belarbi inspired me in the field of structural engineering, and took me under his wing so that I might improve myself, more so than just academically. The completion of this dissertation would not have been possible without his support, and I am greatly indebted to all that he has given.

I would also like to share my gratitude with my committee members, Drs. Yi-Lung Mo, Mina Dawood, Pradeep Sharma, and Gangbing Song, for their suggestions and guidance. This research project was funded by NSF-NEESR, the National University Transportation Center, and the Intelligent Systems Center of Missouri S&T. Financial support for this research was also provided by a DSTF fellowship from the University of Houston and by a teaching and research assistantship from the Department of Civil Environmental Engineering, which are both gratefully acknowledged.

Without the help, guidance, and generous time provided by the technicians, helpers, and colleagues who were involved in my research work, I would never have accomplished this massive project or reached this point in my PhD. career. I also extend my heartfelt thanks to Drs. Suriya Prakash Shanmugam, Young-min You, Sang-Wook Bae, Lesley Sneed, Mike Murphy, Carlos Ortega, and Issa Issa for their help and assistance during the research. I would also like to thank Steve Gabel, Gary Abbott, Brian Swift, Jason Cox, Ruili He, Yang Yang, Hishem Belarbi, and Sihem Belarbi who provided their technical expertise and labor to assist me during my construction and testing of columns at the High Bay Laboratory. Special thanks also go to my good friends and fellow graduate students Ray Rodriguez, Lin Fu, Ling Dong, Hui Zhang, Ruiguo Wang, Fei Zhao, Dawei Qin, Jingfeng Wang, Xiaoming Cheng, Guang Yang, Shuang Zhou, Cheng Shi, Shuai Fan, Congpu Yao, Y.Jeannot Ahossin, Yiquan Yan, Sinjaya Tan, Dongmei Pan, Botong Zheng, Flora Kavoura, Kazi A. Hossain, Mossab El-Tahan, and Rachel Howser for their help and friendship, which instilled in my determination and self-confidence.

This short acknowledgment would never be complete without an expression of my sincere gratitude and love to my parents, Fangxin Li and Shumei Wang, and to my sisters, Song Li, Wei Li and Yan Li, for their love, and time, as well as for their emotional and financial support, without reservation. I was always that baby son and little brother to be protected and spoiled by this loving family. From now on, I will be the man to protect and take care of you all for the rest of my life.

Performance of RC Bridge Columns under Cyclic Combined Loading including Torsion

An Abstract

of a

Dissertation

Presented to

the Faculty of the Department of Civil and Environmental Engineering

University of Houston

In Partial Fulfillment

of the Requirements for the Degree

Doctor of Philosophy

in Civil Engineering

by

Qian Li

December 2012

Abstract

Reinforced concrete (RC) bridge columns, specifically in the skewed and horizontally curved bridges, the bridges with unequal spans or column heights, and the bridges with outrigger bents, can be subjected to cyclic combined loading including axial, flexure, shear, and torsion loads during earthquakes. This combined loading condition would affect the performance of RC bridge columns with respect to strength, stiffness, deformation and progression of damage, and cause complex failure modes and in turn influence the overall behavior of the bridge system. This study performed experimental and analytical studies in order to investigate the performance of RC bridge columns under cyclic combined loading including torsion.

The main variables considered here were (i) the ratio of torsion-to-bending moment (T/M), (ii) cross sectional shape, and (iii) transverse reinforcement configurations. The torsional and flexural hysteretic responses, plastic hinge formation, strength and stiffness degradation, rotation and displacement ductility limits, energy dissipation characteristics, and damage progression for these columns are discussed in this dissertation. A unified damage assessment approach was proposed to assess the damage limit states for RC columns under combined loading by unifying the decoupled damage index models for flexure and torsion. Moreover, a semi-empirical model was established to predict the interaction between bending, shear and torsional loads. It was found that the strength and stiffness degradation and progression of damage were amplified by an increase in torsional moment. The damage distribution and failure modes were affected by the combined loading effect. Also the square columns experienced more localized damage due to cross sectional shape and the transverse reinforcement configuration effect.

Table of Contents

List of Figures

List of Tables

Chapter 1 Introduction

1.1. Overview

In three dimensions, a bridge column cross-section can be subjected to a total of six internal forces: three normal (axial force and two bending moments) and three tangential (torsion and two shear forces). During earthquake excitations, reinforced concrete (RC) bridge columns can be subjected to torsional moments in addition to flexure, axial, and shear forces as shown in Fig. 1-1. The currency of torsional moment is more likely in skewed and horizontally curved bridges, the bridges with unequal spans or column heights, the bridges with L-shaped piers, and the bridges with outrigger bents. Moreover, multi-directional earthquake motions including significant vertical motions and structural constraints due to a stiff deck, movement of joints, abutment restraint, soil conditions, and eccentric loads from traffic conditions may also lead to combined loading effects.

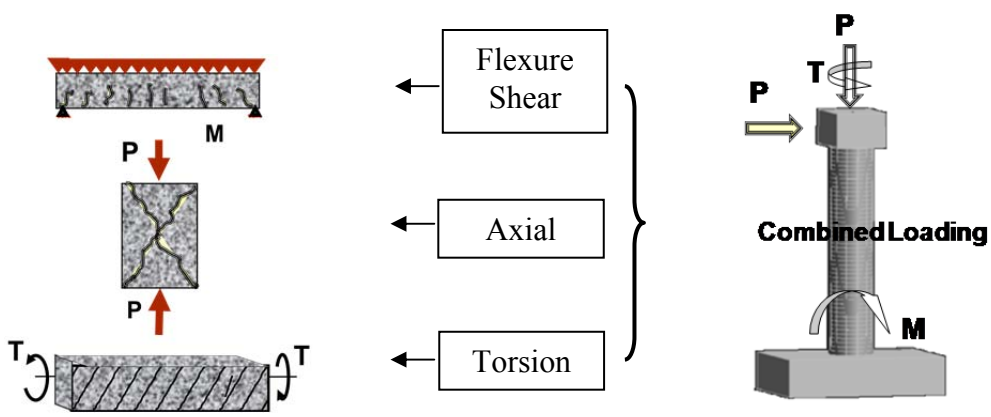

Fig. 1-1 General Combined Loading on Bridge Columns

In the skew bridges, Tirasit and Kawashima (2008) found that the collision bridge deck and abutment can cause in plane rotation of superstructures to induce torsion in the bridge columns as shown in Fig. 1-2. Using the finite element method, this work conducted a time history analysis of a four-span continuous skewed bridge with several parameters such as skewness, pounding, cable restrainer system, and locking of steel

bearing movement after damage. It was found that pounding occurs between a skewed bridge deck and abutments resulting in in-plane deck rotation and increasing the seismic torsion in skewed bridge piers. Also the columns in bents closest to abutments in a skewed bridge are higher than those in a straight bridge. Significant deck rotation due to the seismic torsion response of skewed bridge piers might happen. Moreover, it showed that locking of the bearing movement after failure can significantly amplify seismic torsion in skewed bridge piers.

In addition, the seismic response of curved bridges in longitudinal and transverse directions is coupled which results in multidirectional deformation with torsion in the bridge columns as shown in Fig. 1-3. Also torsion possibly occurs due to eccentricity of inertial force transferred from superstructures in bridges with outrigger bents as shown in Fig. 1-4.

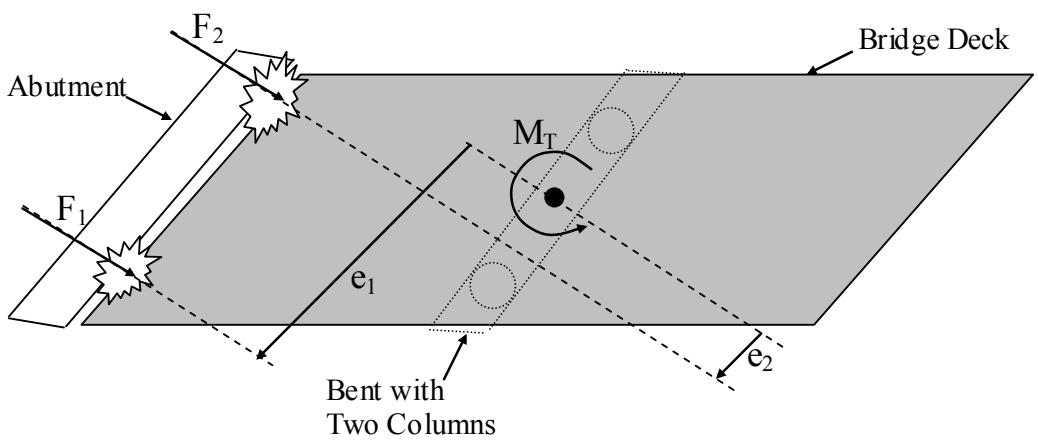

Skewed Bridge – Plan View

Fig. 1-2 Torsional Moment in Columns due to Deck Rotation

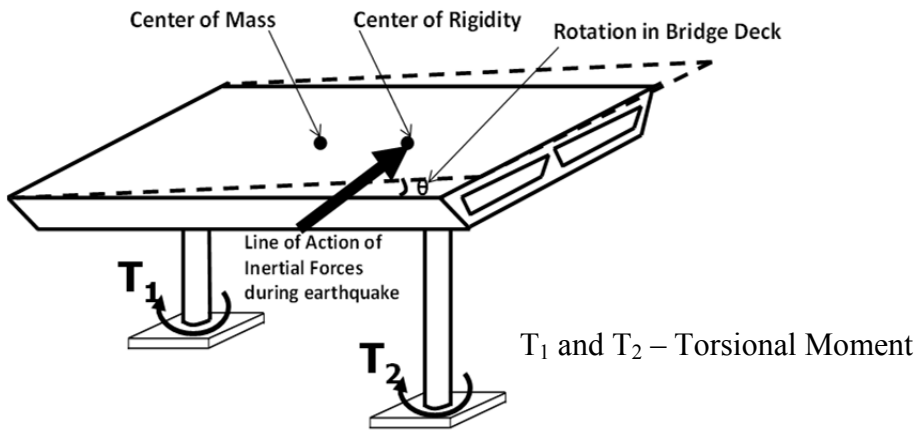

Fig. 1-3 Torsional Moment in Curved Bridge Columns during an Earthquake

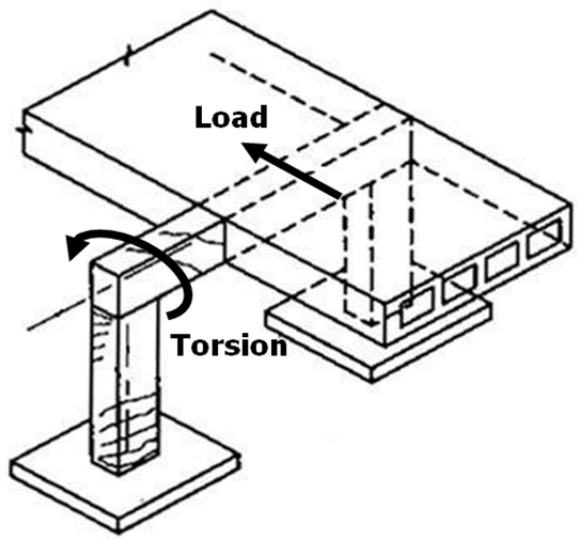

Fig. 1-4 Torsional Moment in Outrigger Bents of Bridges

Belarbi et al. (2008) investigated the presence of torsion in bridge columns by analyzing a bridge structure model as shown in Fig. 1-5. The results of the seismic analyses for various earthquake motions are presented in Fig. 1-6. As this figure indicates, a supporting bent of a bridge under complex deformation is subjected to a combination of axial loads, bending moments, shearing forces, and potentially to torsional rotations as well. Torsion is more evident, however, in columns further from abutments that are under deformation restraints from the abutment keys (e.g., pier line 3 in Fig. 1-4). Torsion effects due to rotation of the superstructure can be significant when

shear keys restrain the bridge superstructure at the abutments, or when there is a significant decrease in torsion stiffness relative to the bending stiffness of the column. The results of seismic analyses clearly show that the bridge columns in the bents closest to the bridge abutments are subject to a T/M of between 0.52 and 0.33, significantly higher than that for the bents closest to the center of the bridge. The other columns are subject to significantly lower T/M ratios of almost 0.08 at maximum response.

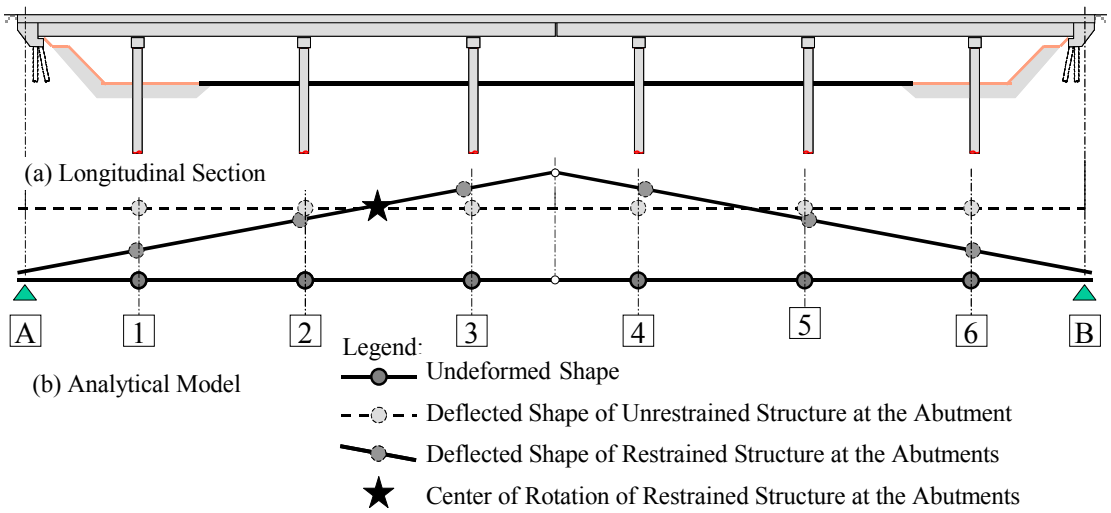

Fig. 1-5 Bridge Transverse Seismic Responses

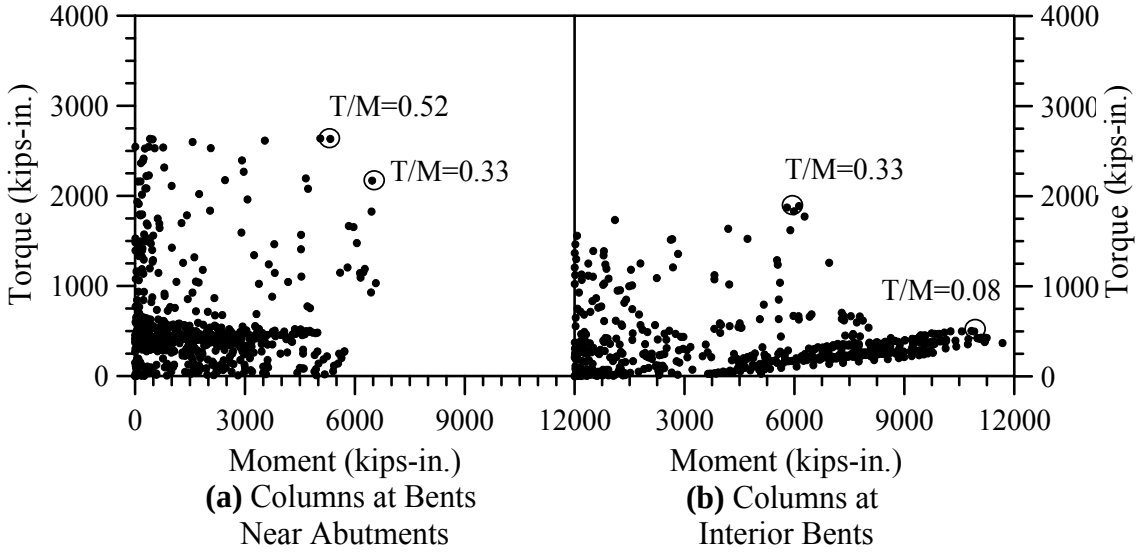

Fig. 1-6 Interaction between Bending and Torsion (1 kip-in. = 0.11299 kN-m)

Design and construction of the bridges with these configurations are often unavoidable due to site constraints such as rivers, railroad tracks, and other obstacles. The combined loading including torsion causes complex failure modes of these bridge columns and in turn influences the overall behavior of the bridge system. There are many challenges to address with regards to this torsional effect on the overall behavior of RC members such as flexural and torsional hysteretic response, the flexural and shear capacities, flexural and torsional ductility capacities, concrete cover spalling, warping effect, localization and distribution of plastic hinges, proper detailing for plastic hinges, energy dissipation, and damage progression, which have not been investigated in depth at either a small-scale or a large-scale level. It shows the urgent challenge and necessity to take torsional effects into consideration in the seismic design of a bridge system.

1.2. Studies on Combined Loading in RC Members

Early experimental studies mainly focused on axial force, flexure, pure shear, pure torsion, and also combined shear and torsion, or combined flexure and torsion considering combined actions and their interactions. First, the compression behavior of the RC member with or without confinement was well investigated based on experimental results (Kent 1969, Park and Paulay 1975, Ahmad and Shah 1982, Mander 1984 and 1988). Second, several experimental studies have investigated the response of RC elements under flexural load under various aspect ratio, confinement of reinforcement, axial load ratio, cover thickness, reinforcement ratio, bar diameter, and loading patterns (Atalay et al. 1975, Davey and Park 1975, Sheikh et al. 1982 and 1994, Ang et al. 1989, Mander et al. 1984, Zahn et al. 1986, Stone et al. 1989, Tanaka and Park 1993, McDaniel et al. 1997, Vu et al. 1998, Kowalsky and Priestley 2000, Ohtaki and

Mizugami 2000, Benzoni et al. 2000, Calderone et al. 2000, Hachem et al. 2003). Third, the shear and torsional behavior of RC members was studied through experimental results and theoretical models (Ritter 1899, Mörsch 1902, Rausch 1929, Birkland 1965, Hamilton 1966, Ersoy and Ferguson 1968, Mirza and McCutcheon 1968, Bishara and Pier 1973, Mitchell and Collins 1974, Badawy 1975, Hsu et al. 1985a, Akhtaruzzaman and Hasnat 1989, Rahal and Collins 1995, Rasmussen and Baker 1995, Koutchoukali and Belarbi 2001, Hindi et al. 2005, Browning et al. 2007). Fourth, the behavior of RC members under combined torsion and bending moment has been studied by researchers since the combined loading causes complex longitudinal reinforcement strain distribution alternating with the longitudinal reinforcement arrangement over the cross section of RC members, which is critical in the design process (Kemp et al. 1961, McMullen and Warwaruk 1967, Hsu 1968, Lim and Mirza 1968, Lampert and Thurliman 1968, Zia 1970, Onsongo and Collins 1978).

In recent decades, researchers conducted experiment focusing on the behavior of RC members under combined bending, shear, and torsion (McMullen and Warwaruk 1970, Onsongo, 1978, Hsu and Wang 2000, Hsu and Liang 2003, Otsuka et al. 2004, Tirasit and Kawashima 2007, Belarbi and Prakash 2008, 2009 and 2010, Belarbi and Li 2010, 2011 and 2012, Arias-Acosta and Sanders 2010). Even for combined actions that have been studied, the effect of cross sectional shape and transverse reinforcement configuration on the cyclic behavior of the RC bridge column under combined loading is not yet clearly understood. In particular, few studies have reported on the behavior of oval sections with interlocking spirals under cyclic combined bending, shear, and torsional loads.

In addition, many analytical models have been proposed to predict the behavior and ultimate strength of RC members subjected to pure torsion and various combinations of shear force, axial compression, torsional and bending moment (Bredt 1896, Rausch 1929, Nylander 1945, Lessig 1959, Yudin 1962, Collins et al. 1968, Lampert and Thürlimann 1968 and 1969, Mitchell and Collins 1974, Elfgren 1974, Onsongo 1978, Vecchio and Collins 1982 and 1986, Mander et al. 1984 and 1988, Hsu and Mo 1985a, Stone and Cheok 1989, Wong et al. 1990 and1993, Rahal and Collins 1995 and 2003, Priestley et al. 1996, Kawano and Watanabe 1997, Galal and Ghobarah 2003, Greene and Belarbi 2006 and 2009, and Zhang and Xu, 2008). These research studies were intended to improve the understanding of the behavior of RC members and provide analytical tools for analyzing their behavior. Based on the literature review, there are limited analytical models including the effect of interaction among flexure, shear, and torsion in the assessment of seismic performance of RC members with axial loads due to the paucity of experimental results on the cyclic and dynamic performance of RC columns under combined loading.

1.3. Objectives and Scope

The torsional behavior of RC columns has not been studied in as much depth as the behavior under flexure and the knowledge of the interaction between the bending and torsional moment in RC bridge columns is also limited. Most research on the behavior of RC under combined loading has relied on small-scale beams. Few researchers have investigated the effect of combined loading on the performance of columns with different cross sectional properties such as a square cross-section with ties and an oval cross-section with interlocking spirals. In addition, a reliable design interaction equation, and

damage or ductility models taking into account the combined loading effects have not been rationally developed due to the paucity of experimental results on the cyclic behavior of RC bridge columns under combined loading. Moreover, an analytical damage estimation model is required to numerically quantify the various damage states under combined loading by a simple damage index based on the performance-based design concept and approach. Therefore, it is necessary to rationally assess the inelastic response of RC columns under combined loading. Thus, the research presented here on RC ridge columns under combined bending, shear, and torsion loading with various cross sectional shapes, transverse reinforcement configurations and torsional-to-bending moment (T/M) ratios will provide essential and previously unavailable experimental and analytical results. The results from the current study will be a useful contribution to support the development of design guidelines and analytical models including damage and ductility models for RC bridge columns under combined loading. They will also provide the basis for further development of interaction surfaces of RC bridge columns subjected to combined loading including torsion.

The objective of this research will be to expand the current state of the art and the understanding of the effect of combined loading including torsion on the behavior of RC bridge columns. The focus of the investigation is to characterize and quantify the cyclic performance of the RC bridge columns under combined loading and also to develop the three dimensional interaction surfaces from combined loading. The research objective is as following: (1) investigate the effect of full-reversal cyclic torsion and combined shear force, bending moment and torsion on the behavior of RC bridge columns; (2) investigate the effects of cross-sectional shapes, transverse reinforcement configurations

and combined loading on torsional and flexural hysteretic responses, reinforcement strain variations, plastic hinge characteristics, strength and stiffness degradation, rotational and displacement ductility limits, energy dissipation, and progression of damage states of the RC bridge column; (3) improve the tools for the design of the RC columns under combined loading at service and ultimate load levels through study on damage-based design approach; (4) establish the interaction diagrams and equations for different failure modes; and (5) establish the decoupled and unified flexural and torsional damage index models for combined loading to identify the implications of combined loading from a performance based seismic design point of view.

1.4. Research Plan and Methodology

This research work is divided into experimental and analytical portions. The experimental portion studied the behavior of square and oval RC bridge columns under constant axial load and full-reversal cyclic torsional, bending, and shear loads. The main variables are cross sectional shapes, transverse reinforcement configurations and T/M ratios. The experimental results were used to determine the effect of combined cyclic loads on the seismic flexural and torsional response, different deformation characteristics and failure modes, the interaction between the torsional and bending moment, the damage progression, the occurrence and severity of concrete cover spalling, and the estimation of plastic hinge lengths.

The analytical work is mainly to study the following aspects: (1) the load-displacement response under pure flexure and the shear-deformation response under pure shear; (2) the development of an analytical softened truss model (STM) under pure torsion to predict torque-rotation relationship; (3) the development of interaction surfaces

using semi-empirical methods to predict the failure of RC members under combined loading; (4) the development of decoupled torsional and flexural damage index models based on decoupled torsional and flexural hysteresis; (5) the development of a unified equivalent damage index model to couple the flexural and torsional actions for combined loading that can be used to predict the damage behavior under combined loading from a performance-based design point of view.

1.5. Organization of the Dissertation

Chapter 1 presents the introduction and overview of this research project with respect to the research objective and scope as well as the research plan and methodology. Chapter 2 presents background information and literature review related to this research by experimental studies, analytical models and code provisions for combined loading. Chapter 3 presents the details of the experimental program, including specimen design and matrix, setup plan, instrumentation layout, material properties, manufacturing progress, and testing procedures. Chapter 4 presents and discusses the experimental results and assesses the performance of test specimens with respect to hysteresis behavior, displacement and twist components, strain plots, strength and ductility characteristics, energy dissipation, damage progression and interaction diagrams. Chapter 5 studies the existing models for flexure and shear and modifies STM for pure torsion to predict the response of the RC bridge column under flexure, shear and torsion, respectively. Also the semi-empirical model for diagrams of interaction between flexural, shear, and torsional loads is developed. Chapter 6 proposes the decoupled torsional and flexural damage index models and validates experimental results for various test parameters. Then a unified equivalent damage index model is developed to couple the

damage index at different limit states under combined loading, which can be correlated to the observed damage states in the experiment for a damage-based design process. Chapter 7 summarizes the conclusions of this study and recommends some directions for future research. The figure below depicts the organization of the dissertation.

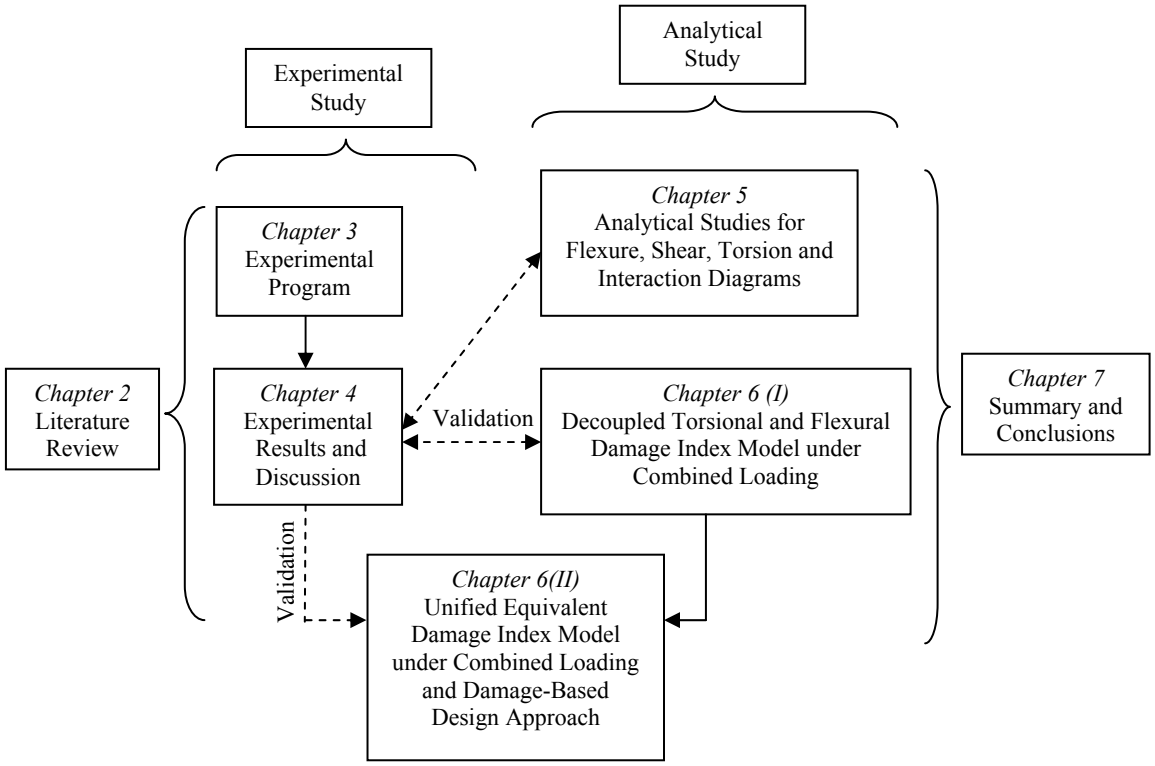

Fig. 1-7 Illustration of the Organization of the Dissertation

Chapter 2 Literature Review on Behavior of the RC Bridge Columns under Combined Loading Including Torsion

2.1. Introduction

A brief review of previous experimental and analytical study on the behavior of RC bridge columns under combined loading including torsion is presented in this section. RC bridge columns are subjected to a combination of axial and shear forces and bending and torsional moments, which can result from spatially complex earthquake ground motions and structural configurations and constraints. The currency of the torsional moment coupled with other internal forces is more likely in skewed and horizontally curved bridges, bridges with unequal spans or column heights, and bridges with outrigger bents. Combined loading would affect the seismic performance of reinforced concrete (RC) bridge columns in terms of strength, stiffness, deformation and progression of damage limit states, and cause complex failure modes of these bridge columns which in turn influence the overall behavior of the bridge system. However, the cyclic behavior of RC columns under combined loading has not been studied in as much depth as the behavior under flexure and shear, which limits the development of rational design provisions. The following summary and discussion reviews previous research on the behavior of RC bridge columns under various loading conditions such as flexure and shear, pure torsion, and combined loading including torsion.

2.2. Experimental Study

Many experimental studies have tested RC members under combinations of torsion, flexure, and shear loads. Previous investigations have focused on the monotonic behavior, the failure modes, the effect of asymmetric longitudinal reinforcement and

transverse reinforcement configurations, reinforcement ratios, and the inclination angle of diagonal cracking. The effect of the ratio of applied torsion-to-bending moments and shear forces has also been studied. However, little research has focused on the cyclic behavior of RC members under cyclic torsion and cyclic combined loading including torsion (Collins and Chockalingam 1979, Otsuka et al. 2004, Tirasit et al. 2005, Greene and Belarbi 2004, Belarbi and Suriya 2008). The following discussion describes existing experimental studies on RC members under various loading conditions.

2.2.1. Behavior under Flexure and Shear and Axial Loads

Several experimental studies have investigated the cyclic response of RC elements under flexural load, with or without axial load. Previous research revealed that most experimental parameters focused on aspect ratio, confinement of reinforcement, axial load ratio, cover thickness, reinforcement ratio, bar diameter, and loading patterns.

The aspect ratio of RC columns, defined by the ratio of effective loading height and cross sectional dimension, determines the level of flexure-shear interaction. RC columns under flexure and axial load might experience flexure-dominated or shear-dominated response, or significant flexure-shear interaction depending on the aspect ratio level. A number of experimental studies have been studied on the effect of aspect ratio (Iwasaki et al. 1985, Davey and Park 1975, Stone et al. 1989, McDaniel et al. 1997, and Vu et al. 1998). Two of the most important conclusions that were drawn according to these studies were (i) displacement ductility capacity decreases with a decrease in aspect ratio and (ii) shear demand increases with a reduction in the aspect ratio.

Several researchers have investigated the reinforcement confinement effect by testing columns under monotonic and cyclic axial loads (Mander 1984, Sheikh 1982, Calderone

et al. 2000). The effect of confinement is mainly determined by the amount and configuration of transverse reinforcement and the axial load level.

Wong et al. (1990) tested columns with various transverse reinforcement ratios to conclude that those with a smaller transverse reinforcement have a smaller curvature demand. In addition, several researchers have examined the effect of the transverse reinforcement ratio on circular columns (Potangaroa et al. 1979, Zhan 1986, and Stone 1989). They stated that an increasing amount of transverse reinforcement confines the concrete core more effectively and increases shear resistance. Tanaka and Park (1993) performed the first test on RC columns with interlocking spirals to evaluate the effectiveness of interlocking spirals as shear and lateral confining reinforcement. They found that the amount of transverse reinforcement required for effective confinement of the core concrete in the plastic hinge of RC column can be reduced significantly by interlocking spirals. Also the spiral reinforcement details required for the columns with interlocking spirals can be designed according to the provisions for the columns with single spirals. Ohtaki and Mizugami (2000) studied the performance of interlocking spirals columns with different volumetric confinement spiral ratios under cyclic lateral loading. The author found that the interlocking spiral columns obtained the same flexural strength and displacement capacity as conventional columns with a 300% higher volumetric reinforcement ratio. In addition, the columns with different volumetric reinforcement ratios showed a different failure mode corresponding to the amount of reinforcement. However, the effect of the transverse reinforcement ratio and configurations on shear-dominated behavior is still limited.

Previous research has shown that an increase in axial compression reduces displacement capacity (Atalay 1975, Saatcioglu1990, and Sheikh 1990). They found that shear strength was increased with the increase in axial compression by enhancing the aggregate interlock and increasing shear transfer across the compression zone. Also, shear strength was reduced when the axial loads are in tension. Benzoni et al. (2000) conducted an experimental study to investigate the behaviors of shear-dominated interlocking spiral columns under different axial load ratios. The shear strength was increased with a higher axial load level. They proposed the formula to predict the shear strength of interlocking spirals columns taking into account the axial load level and effect of neutral axis depth. However, shear strength decays significantly within the plastic regions of columns with increasing displacement ductility demands. Moreover, the vertical ground motions result in varying axial loads during an earthquake, which can cause the failure of the columns as reported in literature (Hachem et al. 2003). However, tests on RC columns under dynamic loading with various vertical ground motions have been limited.

The complex axial-shear-flexure interaction in columns considerably changes the strength and stiffness degradation, cyclic response and pinching behavior of RC columns, which must be evaluated in the presence of very high vertical motions. The flexure-dominated or shear-dominated failure modes of columns are similar to those of conventional beams under flexure and axial load; however, the response of interactive flexure and shear depends on shear transfer mechanisms at the concrete crack's interface, the opening and closing of cracks, local stress variations in concrete and steel from section to section, and the effective depth of the cross section. A number of failures have

been reported due to inadequate shear strength and brittle response under shear. Elwood and Moehle (2003) provided a brief discussion of experimental results based on various shear and axial loading tests for RC columns and/or frames. From the results, it is indicated that a loss of axial load capacity in a an RC column does not always immediately occur after a loss of shear capacity and axial failure occurred when the columns lost all shear capacity for columns with larger aspect ratios. The load transfer mechanisms and failure modes of shear-dominated columns can be categorized into shear tension failure, shear compression failure and shear bond failure (Sasani 2004). A few studies address flexure and shear interaction; however, a full understanding is yet lacking (Ang et al. 1989, Wong et al. 1990 and 1993, Kowalsky and Priestley, 2000, Xu et al. 2010). They found that axial compression increased shear strength and strength degradation was gradual in the columns with small axial compression and significant in the columns with large axial due to the development of the wedge mechanism compression.

2.2.2. Behavior under Pure Torsion

Investigating the behavior of RC members subjected to pure torsion is necessary for generalizing the analysis of a structural member under torsion combined with other actions. However, only a few investigations have focused on it during the last few decades (Mitchell and Collins 1974, Bishara and Pier 1973, Akhtaruzzaman and Hasnat 1989, Rasmussen and Baker 1995, Koutchoukali and Belarbi 1997, Hindi et al. 2005, Browning et al. 2007). Experimental studies and general behavior of RC members under pure torsion is described in this section.

The torsional behavior of an RC column is mainly affected by transverse and longitudinal reinforcement ratios and configurations, the sectional dimensions including clear cover, cross sectional shape, and concrete strength. Mitchell and Collins (1974) investigated the behavior of structural rectangular concrete beams under pure torsion. They stated that the longitudinal and transverse reinforcement were in tension after concrete cracking, and the concrete struts between the diagonal cracks were in compression, as shown in Fig. 2-1. The surfaces of the beam were warped under torsional rotation, causing bending stresses in addition to compressive stresses in the concrete struts. The concrete between inclined cracks is capable of acting in tension and will increase the overall beam torsional stiffness, which is known as "tension stiffening" and demonstrated immediately after the first cracks appeared, and decreased with increasing torsion. For beams with ρ_t larger than ρ_l, the crack angle is greater than 45° relative to the horizontal, and the strain is larger in the longitudinal direction, causing wider cracks. Similarly, in beams with ρ_t less than ρ_l, the angle is less than 45° relative to the horizontal, the transverse strain is larger, and the cracks are also wider than when α is 45°.

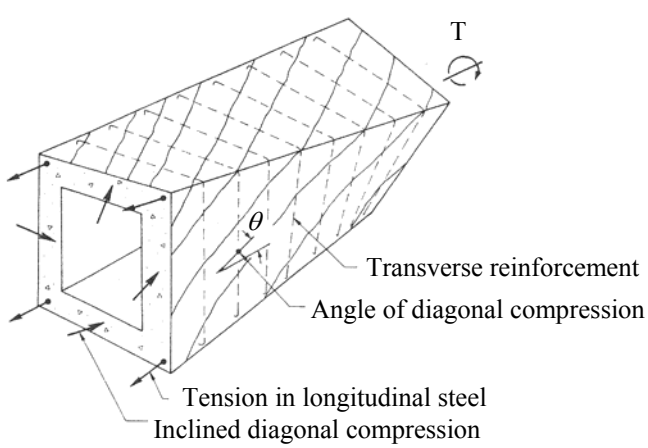

Fig. 2-1 Diagonal Cracks in Members under Pure Torsion (Mitchell and Collins 1974)

Akhtaruzzaman and Hasnat (1989) tested concrete deep beams under torsion and found that the torsional strength was significantly reduced at the presence of the opening for span-to-depth ratios smaller than three, and the torsional strength of beams with or without opening remained constant for span-to-depth ratios greater than three. Torsional strength of the deep beams was proportional to the square root of the concrete strength. For deep beams at very low span-to-depth ratios, torsional resistance was provided by a horizontal bar more effectively than the vertical stirrups.

Rasmussen and Baker (1995) studied the behavior of concrete members with the normal and high concrete strength under torsion. High strength concrete showed a higher cracking load and higher torsional strength. High strength concrete for a given cross section and given torque resulted in higher torsional stiffness, lower crack width and lower reinforcement stresses compared to normal strength concrete.

Koutchoukali and Belarbi (1997) tested nine full size beams with pure torsion to conclude that the torsional capacity of under-reinforced beams is independent of concrete strength, and the amount of longitudinal reinforcement was more effective in controlling the crack width than the stirrups.

Hindi et al. (2005) summarized the variation in torsional strength with respect to the transverse reinforcement ratio based on the specimen under pure torsion in the previous literature. The ultimate torque versus transverse reinforcement ratio curve is plotted in Fig. 2-2. This plot indicates that an increase in the transverse reinforcement ratio increases torsional strength.

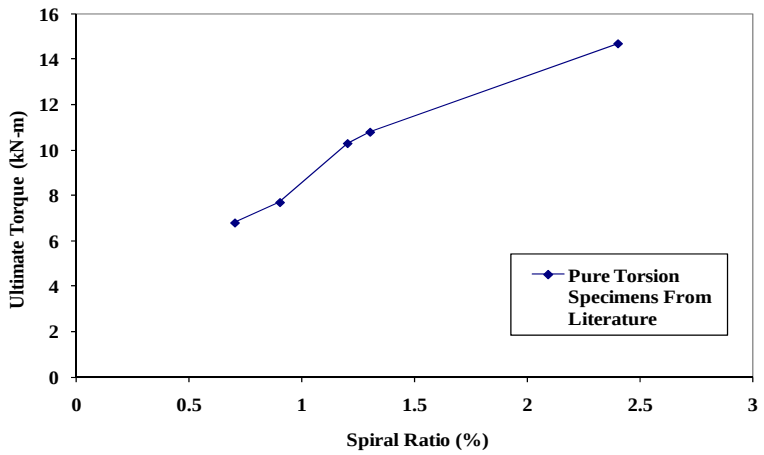

Fig. 2-2 Variation of Torsional Strength with Increase in Spiral Reinforcement Ratio

In addition, seismic design restricts the ductility requirement of RC columns, mainly determined by concrete strength and the transverse reinforcement ratio and configurations. RC bridge columns may have different transverse reinforcement configurations such as hoops, ties, or spirals. The hoops and ties are used in either a rectangular cross section or a circular cross section without a direction bias. The single spiral or interlocking spirals are used in either a circular, or rectangular, or oval cross section with a direction bias. The direction bias could result in an unsymmetrical response of columns. The spirals lock themselves in one loading direction producing more confinement to the concrete core, thereby increasing strength and stiffness; and the spirals unlock themselves in the other direction generating less confinement to concrete core and lower strength and stiffness. Hindi et al. (2005) proposed the use of two cross-spirals in opposite directions to eliminate the locking and unlocking effect of spiral reinforcement under pure torsion and improve the strength and ductility characteristics. Turechek and Hindi (2006) continued to study the columns with two cross-spirals in opposite directions under increasing axial load and combined axial and flexural loads. Browning et al. (2007) tested the RC columns with cross spirals (two spirals crossing

opposite each other at 45º) under torsion. Test results revealed that the elimination of locking and unlocking effect in cross spirals reduced strength deterioration and increased the ductility capacity. In post-peak behavior, the dowel action of longitudinal bars contributed to load resistance significantly at higher ductility levels.

In the design process, the effective cross sectional dimensions must be calculated if the concrete cover spalling starts before peak torque. Therefore, the occurrence of concrete cover spalling is an important timeline from a torsional design point of view. Previous research has investigated concrete cover spalling under several assumptions for RC rectangular and box sections. Mitchell and Collins (1974) tested two beams with a concrete cover of 1.5 mm and 40 mm respectively, PT5 and PT6, to investigate the effects of concrete cover spalling. The results of the tests showed that although the concrete outside the hoop reinforcement had a significant effect on the cracking torque, it had very little effect on the peak torque after significant spalling occurred, as shown in Fig. 2-3.

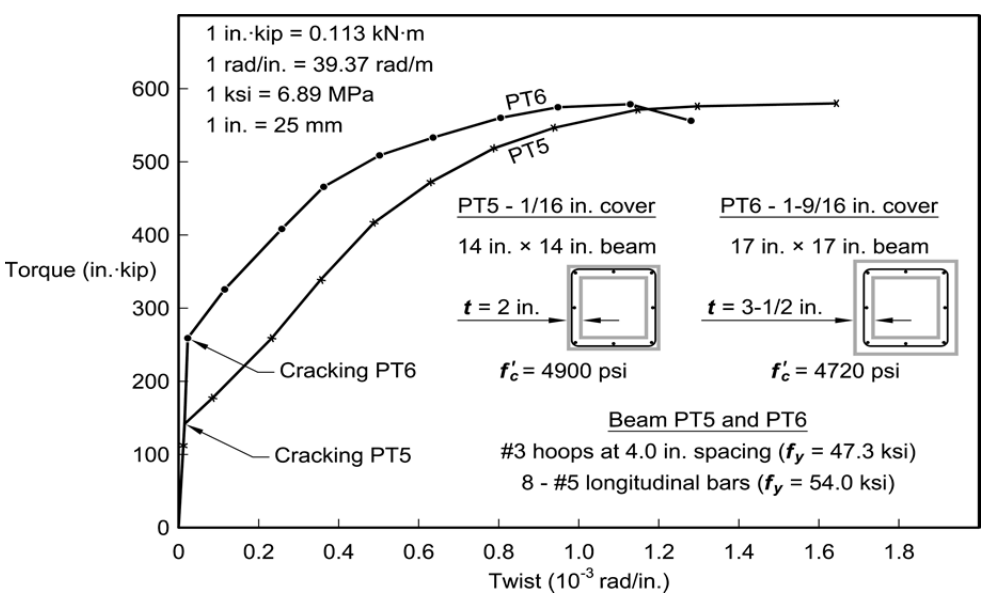

Fig. 2-3 Concrete Cover Spalling Effect on the Torque-Twist Behavior
(Mitchell and Collins 1974, 1 in.-kips = 0.113 kN.m)

For the RC members under torsion, Hsu and Mo (1985a) proposed a simple equation to determine the effective cross sectional dimensions based on concrete cover thickness and shear flow thickness to consider the effect of concrete cover spalling. For the RC members under combined shear and torsion, Rahal and Collins (1995a) proposed that the effect of concrete cover spalling are proportional to the compressive force in the concrete cover, the cover thickness, and the area of the splitting plane occupied by the reinforcement and inversely proportional to the concrete tensile strength and the size of the cross section. Rahal and Collins (1995b) tested the RC beams with two different concrete covers thicknesses to observe that the one with the smaller covers did not experience spalling until after the torsional strength had been reached and the one with larger covers spalled before reaching the torsional strength. Experiments have also shown that spalling occurs if the cover thickness is greater than 30% of the ratio of the area to the perimeter of the cross section. Moreover, concrete cover spalling can be affected by the reinforcement ratio and the cross sectional shape (square/rectangular/circular/oval), which has not been investigated in depth under pure torsion.

2.2.3. Behavior under Torsion and Axial Load

Based on literature review, very few experimental researches have been done on RC columns under torsion combined with axial load. Bishara and Peir (1973) tested few rectangular columns under torsion combined with axial compression. It is concluded that torsional strength is increased linearly with an axial load up to an axial compressive stress level at 65% of the concrete cylinder strength ($0.65f_c'$) as shown in Fig. 2-4. The torsional strength was increased by more than 200% compared to torsion without an axial load when the compressive stress level was about $0.65f_c'$.

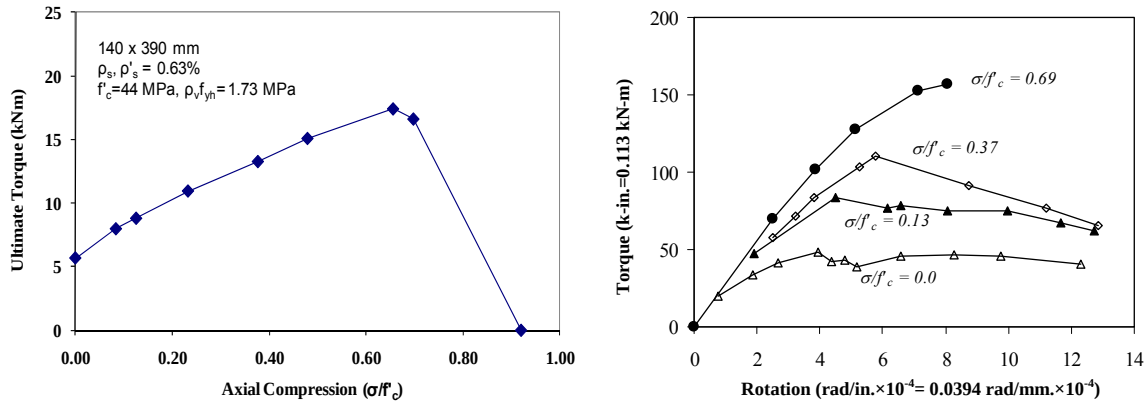

(a) Torsion Moment-Axial Compression Interaction Diagrams

(b) Torque-rotation relationships under various compressive stresses

Fig. 2-4 Behavior of RC member under Torsion and Axial Load (Bishara and Peir, 1973)

Pandit and Mawal (1973) reported tests on four plain concrete and six reinforced columns subjected to axial compression and torsion. An expression for the ultimate torsional strength is proposed and compared with the test results of this investigation providing the best correlation with the test results. Jakobsen et al. (1984) tested RC box members to investigate the cyclic torsion effect on the torsional stiffness degradation and energy dissipation. They concluded that the torsional stiffness degraded significantly at post-cracking stage and the axial compression load increased the torsional energy dissipation capacity. Moreover, the columns under an axial compression load with a smaller transverse reinforcement ratio obtained a larger torsional energy dissipation capacity. Otsuka et al. (2004) tested two rectangular columns with different transverse reinforcement ratios under torsion and a constant axial load level. They concluded that the pitch of lateral ties significantly affected the torsional hysteresis curves and the torsional energy dissipation increased with less hoop spacing. Tirasit et al. (2007) conducted an experimental study on cyclic behavior of RC bridge columns under combined loading. Two of the columns were tested under torsion with and without axial load, respectively. The test results showed that the torsional strength of the column under

with axial load was greater and occurred earlier than that of the column without the axial load due to the axial force effect. They found that the axial force effect on the torsional hysteresis was gradually less significant as the applied rotation increased at post-peak torque state. Recently, Prakash and Belarbi (2008) performed an experimental study on a circular RC bridge column with spirals loaded under cyclic pure torsion with a constant axial load level and also stated locking and unlocking effect, and dowel action of longitudinal bars. Under the pure torsional moment, the rigid boundary conditions of foundation and top loading block and uniform torsion distribution along the column result in damage progression as following: (i) the inclined torsional cracks near mid-height of the column first occur, (ii) these cracks spread continuously at an inclined angle with increasing levels of rotation, (iii) the torsional stiffness degrades significantly soon after concrete cracking, which can be reflected from the nonlinear torsional moment-rotation curves, (iv) transverse reinforcement yields and concrete cover spalls at the same stage, (v) a plastic zone forms near the mid-height of the column at post-yield stage along with longitudinal reinforcement yielding, (vi) core concrete crushing occurs at the final failure stage.

However, there is no experimental data reported for the combination of torsion and axial tension since interaction between torsion and axial tension is not a common load combination. Rahal (1995a and 2003a) proposed a diagonal compression field theory (DCFT) for RC members to calculate torsion-axial tension interaction for an under-reinforced section as shown in Fig 2-5. It showed that axial tension reduced the torsional strength most significantly after tensile forces reach 85% of the pure tensile strength of the section.

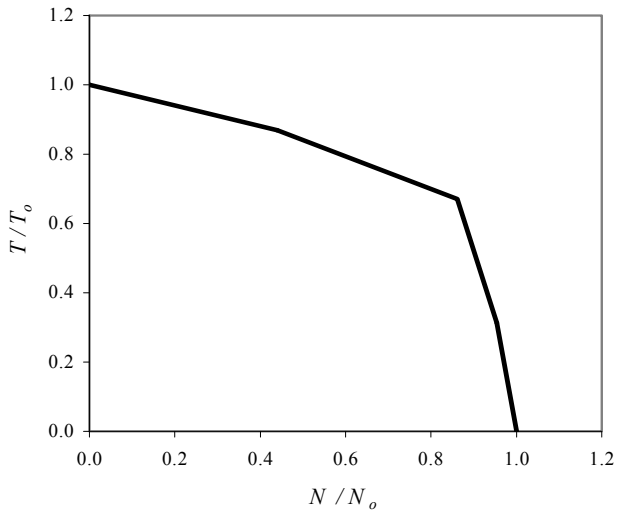

Fig. 2-5 Normalized Torque-Axial Tension Interaction Curves
Calculated using DCFT (Rahal and Collins 1995a)

2.2.4. Behavior under Torsional Moment and Shear Forces

Nylander (1945) reported that the test results on concrete members containing only longitudinal reinforcement indicated considerable scatter feature and most tests falling between a linear and a circular interaction curve. Other tests by Birkland (1965), Hamilton (1966), and Ersoy and Ferguson (1968) have shown that a circular interaction is more accurate. Mirza and McCutcheon (1968) tested quarter-scale RC members and found the longitudinal reinforcement has a significant effect on the interaction curve. The result's scatter was considerable and a lower bound linear interaction was recommended. Collins et al. (1972) and Hsu et al. (1985a) provided test results to conclude that torsional resistance of RC member was provided by outer parts of the cross section more effectively defined as shear flow zone for torsion. They also found that core concrete of the RC member had little contribution to the torsional resistance, which can be disregarded after the concrete cover completely spalled. Mitchell et al. 1974 and Belarbi et al. 2001 have also reported an experimental and analytical study to investigate the characteristics of the shear flow zone for members under pure torsion. However, the

research regarding the shear flow zone characteristics and shear stresses distribution under combined shear and torsion is limited since the shear force in a prismatic member is always generated by inducing flexure except at the point of contra-flexure. Shear force and torsional moment both cause shear stresses across the cross section, which are additive in values with conventions for the shear flow zone as shown in Fig. 2-6. The applied torsional moment generates shear stress, q_T, circulating around the shear flow zone as shown in Fig. 2-6 (a); the applied shear force also induces shear stresses in the shear flow zone as shown in Fig. 2-6 (b). Fig. 2-6 (c) describes the combined shear flows distribution in the RC member under combined shear and torsion. The side of the section with larger stress, where concrete cover spalling more likely happens first, is critical from a design point of view.

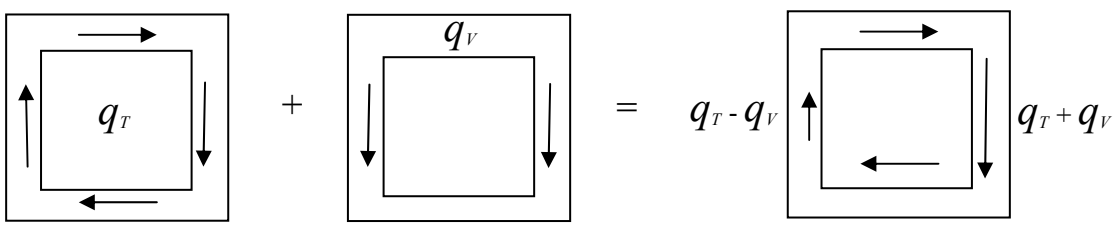

(a) Applied Torsion (b) Applied Shear Force (c) Combined Torsion and Shear

Fig. 2-6 Shear Stresses in RC Members under Combined Shear Force and Torsional Moment for Shear Flow Zone

According to previous experimental studies, all the tests investigating combined torsional moment and shear force were conducted along with some amount of flexure, which can be disregarded. Klus (1968) proposed a bilinear shear-torsion interaction curve for RC members under combined shear and torsion with a relatively low bending moment. The author also suggested that an increase in transverse reinforcement ratio will increase the curvature of the T-V interaction diagram. McMullen and Woodhead (1973) tested eccentrically prestressed beams under various combinations of torsion and flexure to propose a reliable equation to agree with the test results. Ewida and McMullen (1981)

conducted an experimental and theoretical study to find out that an increase in the amount of reinforcement increases the curvature of the interaction diagram and a small shear force can increase the torsional strength for an over-reinforced cross section due to "shear relief" effect, which means that the compressive stresses are decreased and the shear strength is thus enhanced. Moreover, three different equations for the interaction of fully over-reinforced, partially under-reinforced, and under-reinforced sections were proposed as given by

$$\frac{T}{T_o}+\left(\frac{V}{V_o}\right)^n = 1, \tag{2-1}$$

where T is the applied torsional moment at the section, T_0 is pure torsional capacity of the section, V is the applied shear force at the section, V_0 is pure shear capacity of the section, n is taken as 1.2 for under-reinforced sections in which both longitudinal and transverse reinforcement yields when the section reaches ultimate strength, n is taken as 1.75 for partially under-reinforced sections in which only the transverse reinforcement yields or only the longitudinal reinforcement yields when the section reaches ultimate strength, n is taken as 3.0 for completely over-reinforced sections in which concrete crushes before yielding in any of the reinforcement.

Rahal (1995a and 1995b) tested seven large reinforced concrete beams with two different thicknesses of concrete cover at different shear-to-torque ratios, and a relatively low bending moment. Test results showed that the thickness of the concrete cover can substantially contribute to the strength of sections subjected to pure shear, or combined shear and torsion, but that it results in an undesirable increase in crack spacing. They also proposed a three-dimensional behavioral truss model based on a MCFT approach to predict the shear-torsion interaction curve, which consisted of a convex curve resulting

from a straight addition of torsional shear stress and “shearing” shear stress and some “redistribution” of shearing stresses or “plasticization” in the section. In addition, the test results on beams under different shear forces and torsional moments from Pritchard (1970) and Badawy (1977) were bounded to be the linear and circular interaction by Rahal (1995). Fig. 2-7 plots the experimental results of some researchers indicating that the test data fell between linear and circular interaction curves, which provided the lower and higher boundary for shear and torsion interaction. The presence of the torsional moment reduces shear strength, especially if the torque is more than 25% of the pure torsional strength. The amount of transverse reinforcement is considered the main factor affecting the shape of the curve. The proposed interaction curves by Klus (1968) and Ewida and McMullen (1973) are compared to linear and circular interaction curves as shown in Fig. 2-8. For under-reinforced sections, the curve is almost linear, whereas for completely over-reinforced sections, the interaction is closer to a circular curve. Klus’s bilinear interaction curve lies in between the linear and circular curves.

2.2.5. Behavior under Torsional and Bending Moment

The behavior of RC members under combined torsion and shear with a small bending moment has been discussed as above. The combined torsional and bending moment results in complex longitudinal reinforcement strain distribution altering with the longitudinal reinforcement arrangement over the cross section of RC members, which is critical in the design process. In the absence of shearing forces, a four-point loading condition can easily be modified to apply a constant torsional moment along with the bending moment in the central portion of the members. Fig. 2-9 shows that the central loads in the four-point load test setup can be applied at an eccentricity, *e*, to subject the

test region of the specimen to a uniform combination of torsion and flexure. The torsional moment to the bending moment ratio is controlled by distances *e* and *a*. The most significant factors affecting the behavior of members subjected to combined torsion and flexure are transverse reinforcement ratios, the ratio of torsional and bending moment (T/M), longitudinal reinforcement ratio and distribution, and the cross section shape and the concrete strength (Zia 1970).

Torsional moment causes uniformly tensile strain in all the longitudinal reinforcement over the cross section; and flexure produces linear strain variation over the cross section with tensile strains at the bottom and compressive strains at the top. The symmetrical and asymmetrical features of the reinforcement arrangement affect the longitudinal strain distribution and cross sectional curvature as shown in Fig. 2-10.

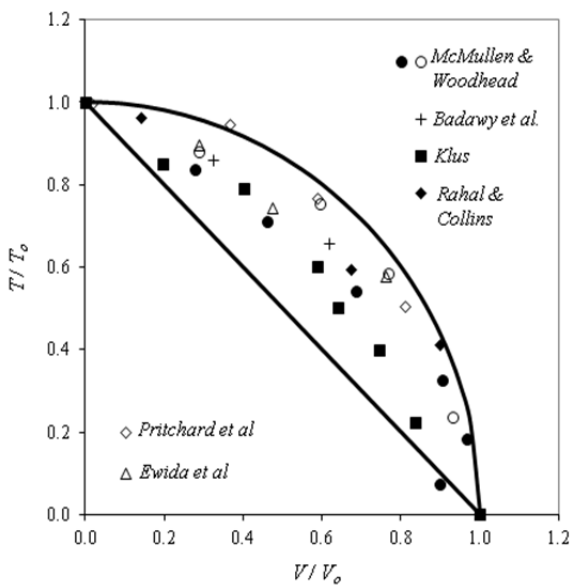

Fig. 2-7 Normalized Linear and Circular Shear-Torsion Interaction Curves

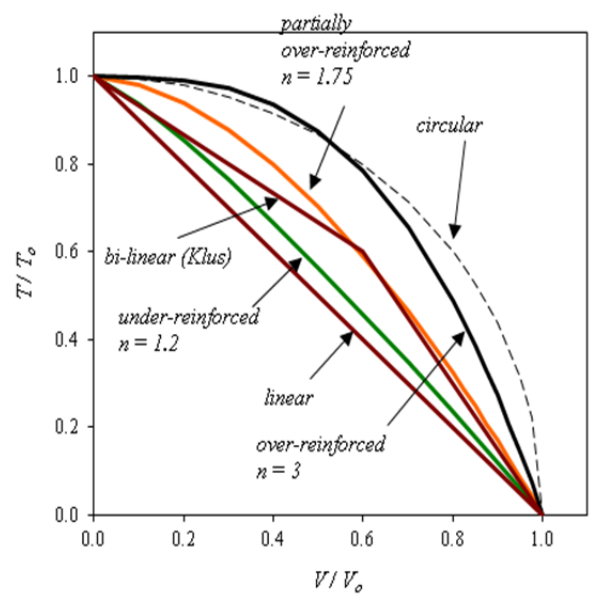

Fig. 2-8 Various Normalized Shear- Torsion Interaction Curves in the Literature

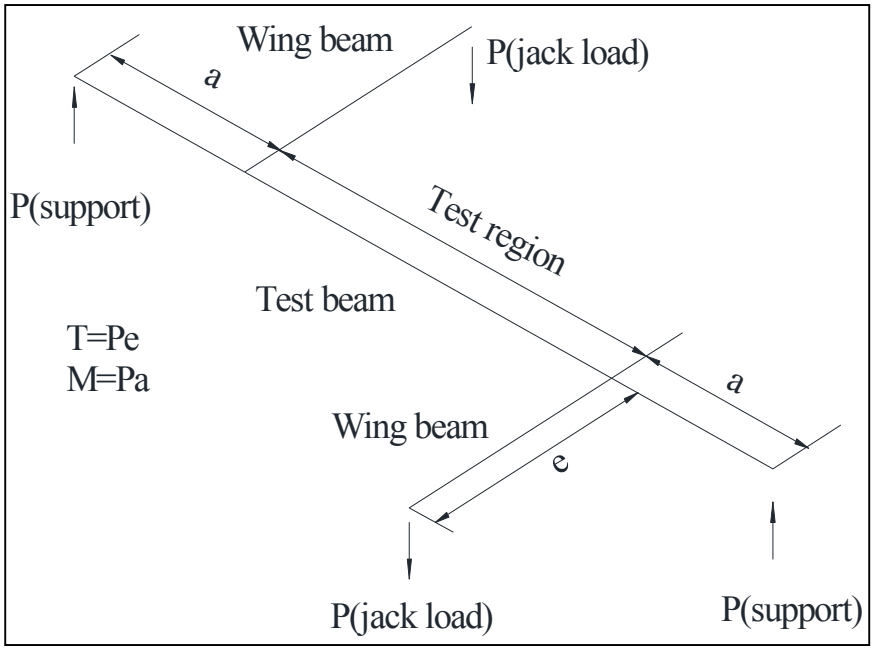

Fig. 2-9 Test Set-up for Combined Torsion and Flexure

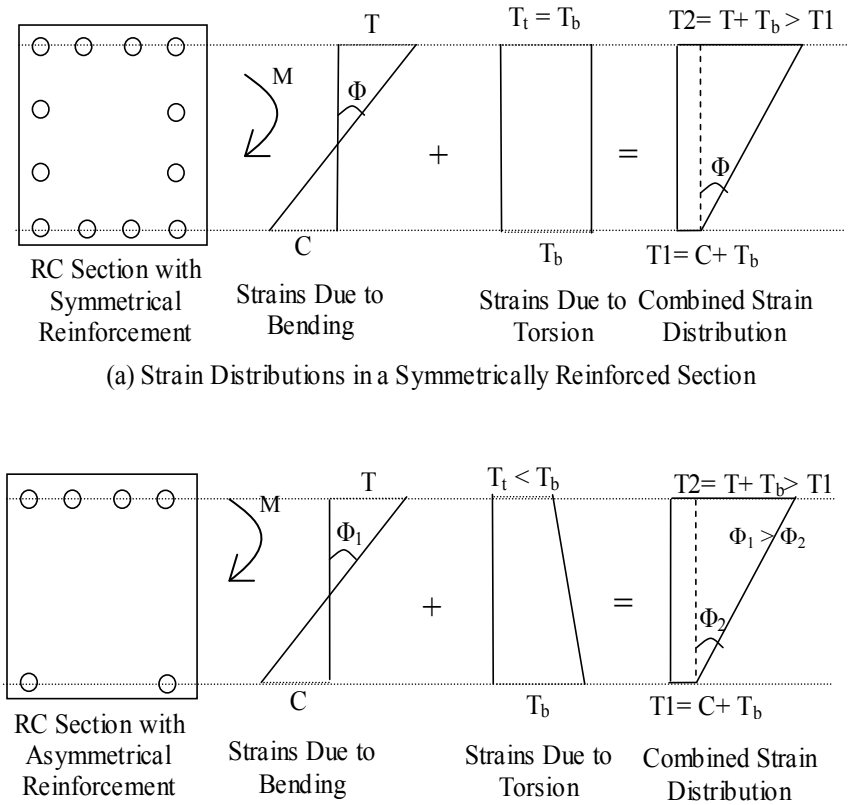

Fig. 2-10 Strain Distributions in RC Section under Bending and Torsional Moment

In an RC member with asymmetrical reinforcement under pure torsion, the side with less longitudinal reinforcement yields first due to larger tensile strain and controls the member's capacity. In an RC member with symmetrical or asymmetrical reinforcement under combined torsion and flexure, the side with additive tensile strain of torsion and flexure yields first and controls the member's capacity. The asymmetrical reinforcement arrangement may cause extra curvature from torsion to increase the curvature and deflection under combined loading, and the additional strain in the weak face may cause a difference in curvature profile and deflection.

According to literature review, previous research on the torsional and bending moment (T-M) interaction in concrete members reinforced with only longitudinal reinforcement is mainly experimental. Kemp et al. (1961) and Hsu (1968a) independently proposed the tri-linear T-M interaction for square and rectangular sections. Victor and Ferguson (1968) recommended a similar tri-linear interaction for L sections, and a square interaction for T-section beams. Lim and Mirza (1968) also proposed a square interaction curve for T-section beams. Based on the evaluation of previous experimental results, Zia (1970) observed that torsion strength was significantly reduced when M/M_o occurred between 0.5 and 1.0 and a circular interaction curve could be taken as a lower boundary for the larger portion of the experimental results. In addition, a linear T-M interaction was suggested based on some experimental results (McMullen and Woodhead 1973). Fig. 2-11 shows examples of the interaction curves recommended by various researchers.

Test results showed that concrete members reinforced with both longitudinal and transverse reinforcement achieves larger post-cracking strength and ductility compared to members reinforced in the longitudinal direction only. The behavior of these members is

also significantly affected by the distribution and amount of longitudinal reinforcement. McMullen and Warwaruk (1967) tested small scale under-reinforced RC specimens with symmetrical longitudinal reinforcement under variable T/M ratios. Fig. 2-12 (a) shows the torque-rotation relationship which concludes that the addition of the bending moment significantly reduced the torsional strength and ductility and magnified torsional post-cracking strength and stiffness degradation. Fig. 2-12 (b) plots the experimentally observed normalized T-M interaction, which shows that a flexural moment equal to 60% of the ultimate flexural strength caused only about a 15%-20% reduction in the torsional capacity; and a torsional moment equal to 40% of the ultimate pure torsion capacity caused about 20% reduction in the flexural strength.

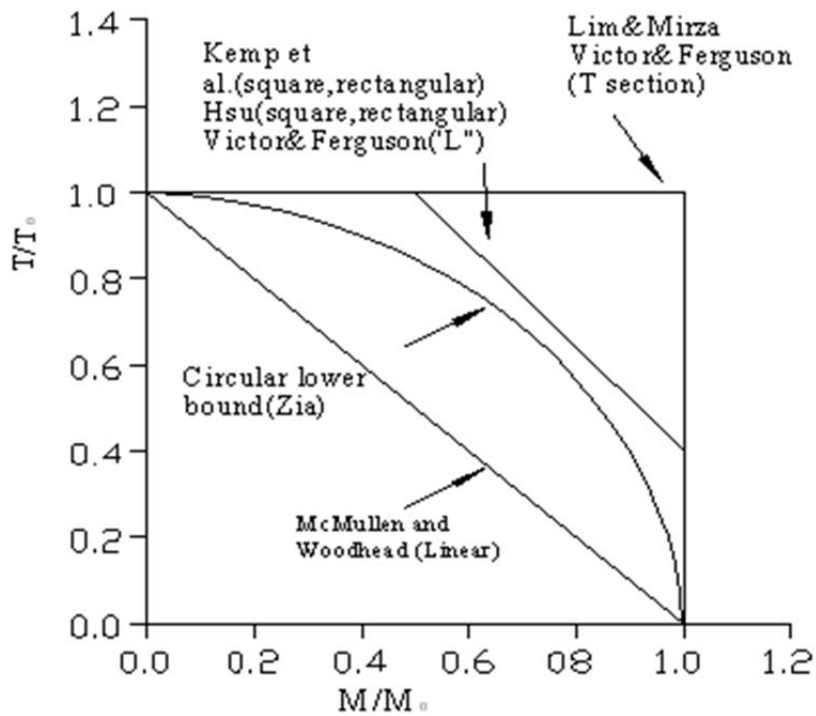

Fig. 2-11 Normalized T-M Interaction Curves for Members without Transverse Reinforcement

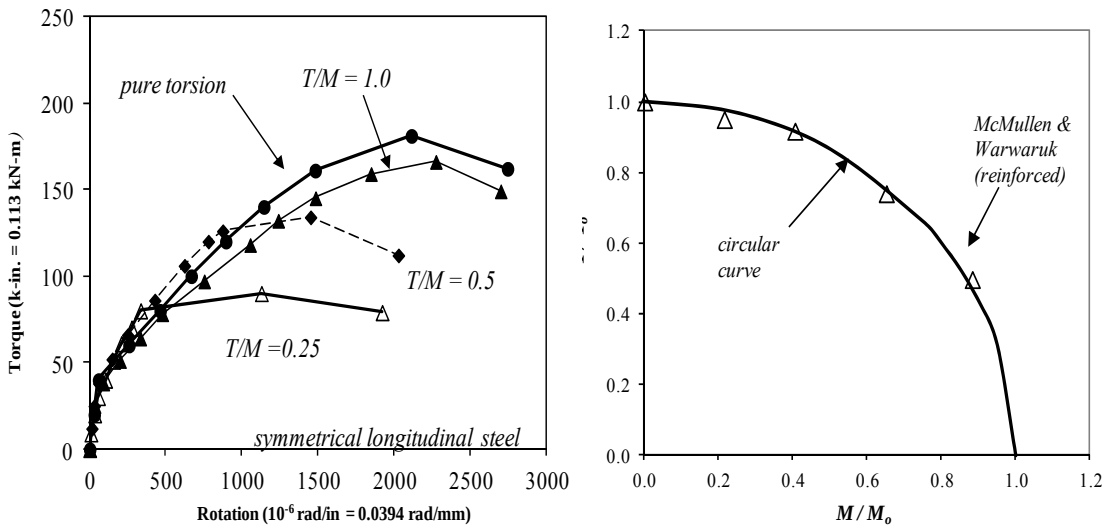

(a) Torque-twist Relationships at Various T/M Ratios

(b) Normalized T-M interaction curves

Fig. 2-12 Test Results of RC members with Symmetrical Longitudinal Reinforcement (McMullen and Warwaruk 1967)

However, asymmetrical reinforcement distribution in RC members significantly alters behavior compared to the one with symmetric reinforcement distribution. Onsongo and Collins (1978) tested three under-reinforced hollow RC beams with asymmetrical longitudinal reinforcement at variable T/M ratios from 0.63 to 4.27. The torque-rotation relationship is plotted in Fig. 2-13. Fig. 2-14 shows experimental results under T-M interaction from four series of asymmetrically reinforced beams (McMullen and Warwaruk 1967, Onsongo and Collins 1978, Lampert and Thurliman 1968). The ratio of yield force in compression and tension longitudinal reinforcement r ($A'_s f_y / A_s f_y$) ranged from 0.1 to 0.27. It shows that the addition of a small flexural moment can significantly increase the torsional capacity and the post-cracking stiffness of asymmetrically reinforced beams. The addition of a flexural moment introduces compression in the weaker top reinforcement and increases its resistance to the torsional shear stresses.

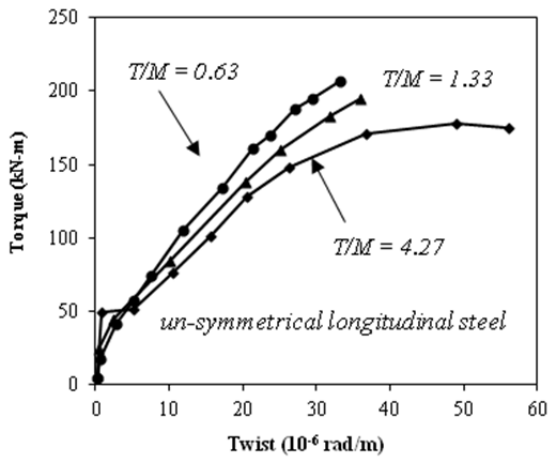

Fig. 2-13 Torque-twist Relationships at Various T/M Ratios for Members with Asymmetrical Reinforcement (Onsongo 1978)

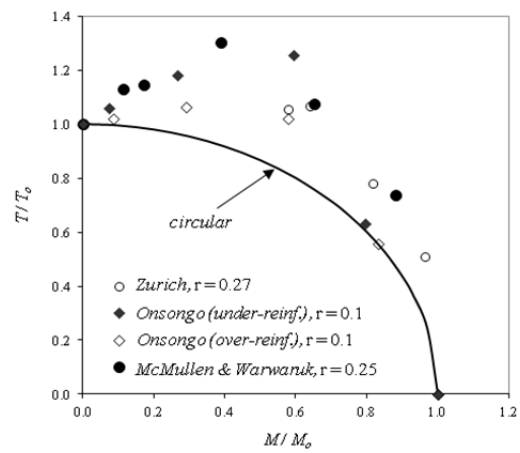

Fig. 2-14 Normalized T-M interaction Curves for Members with Asymmetrical Reinforcement

The T-M interaction is dependent on the ratio *r* and on whether the beam is under-reinforced or over-reinforced in the transverse direction. Test results for members with asymmetrical reinforcement by McMullen and Warwaruk (1967) indicated that an increase of up to 30% in torsional capacity was observed with the addition of a flexural moment equal to 40% of the pure flexural strength in the under-reinforced case. Onsongo (1978) observed a 25% and 6% increase in torsional capacity with an additional flexural moment for under-reinforced and over-reinforced beams, respectively. According to the test results comparison, the presence of flexural moment reduces the torsional ductility of a member for both symmetrical and unsymmetrical cases. In theoretical study, the interaction curves from Lampert and Collins (1972) have been simplified in under-reinforced sections. Two simple equations, Eq. (2-2) and Eq. (2-3), are derived for two different cases that the bottom longitudinal reinforcement yields along with the transverse reinforcement and the weaker top longitudinal reinforcement yields along with the transverse reinforcement, respectively. Fig. 2-15 shows the interaction curves for members with *r* values of 0.3, 0.5, and 1. The increase in torsional

strength calculated using the equations for lower r case is a little larger than the experimentally observed results in Fig. 2-14. Lampert and Collins (1972) recommended two equations providing acceptable results, when the pure torsion capacity T_0 is taken as the conservatively calculated value as given by

$$r\left(\frac{T}{T_o}\right)^2 + \frac{M}{M_o} = 1, \tag{2-2}$$

$$\left(\frac{T}{T_o}\right)^2 - \frac{1}{r}\frac{M}{M_o} = 1. \tag{2-3}$$

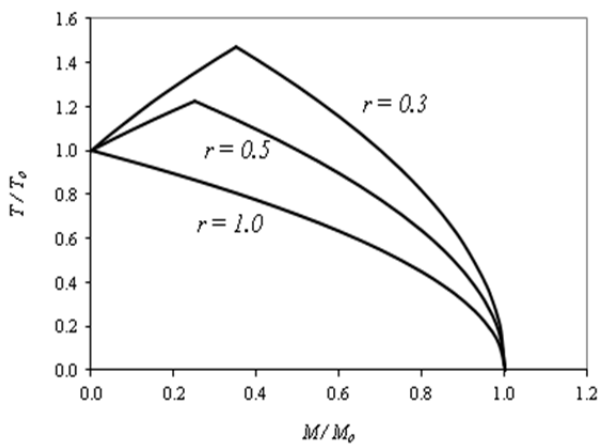

Fig. 2-15 Normalized T-M Interaction Curves for Members with Asymmetrical Longitudinal Reinforcement (Lampert and Collins 1972)

2.2.6. Behavior under Axial and Shear Forces and Torsional and Bending Moment

In most cases of practical importance, torsion acts in combination with shear and flexure. Nylander (1945) first tested concrete beams reinforced only with longitudinal reinforcement under combined flexure, shear, and torsion and found that the bending and torsional moment strength were significantly influenced by the combined loading effect. Lessig (1959) performed an experimental study on combined loading to propose two possible failure modes and derived equations for the torsional strength of beams under the bending moment effect, which indicated that the addition of the bending moment could reduce the torsional strength of a beam. The experimental studies have focused on

the failure modes and derived equations to define three-dimensional interaction surfaces under combined loading (Lessig 1961, Yudin 1962, Gesund and Boston 1964, Hsu 1968a, Johnston 1971 and 1975, McGee 1973, Elfgren et al. 1974a). McMullen and Warwaruk (1970) tested 18 rectangular RC beams subjected to combined flexure, torsion and shear with principal variables as the ratio of the torsional and bending moment, the transverse shear force, and the reinforcement configuration. Test results revealed that the torsional moment needed to cause failure decreased with the decreasing ratio of torsion and bending moment in a member with symmetrically arranged reinforcement, and the addition of the bending moment has a minimal effect on post-cracking stiffness. Three failure modes were observed and characterized by the different features of the formatting plastic hinge. Also idealized failure surfaces were defined and expressions for the strength of these beams were derived using an equilibrium approach. Other researchers also found that the addition of a small bending moment with torsion reduced the net tensile stress on the critical side with less reinforcement and enhanced the member's torsional capacity (Lampert and Thürlimann, 1969; Onsongo, 1978). These failure modes and interaction surfaces have typically been described by the skew bending theory in which torsion combined with other loads skew the failure surface with the compression zone inclined at an angle to the member's longitudinal axis. The analytical study on the failure modes and interaction surfaces under combined loading will be discussed in the next analytical section.

However, the very little experimental work has been reported on the behavior of rectangular and oval RC columns with interlocking spirals under combined loading. Suda et al. (1997) conducted cyclic loading tests under the combination of flexure, shear, and

torsion using a 6-degree of freedom loading machine to study the effect of torsional loading on the seismic performance of high strength RC hollow section piers, which were designed to fail by bending-torsion not by shear-torsion. From the test results they found that the member failed by compression before tensile failure of the main reinforcement occurred.

Hsu et al. (2000 and 2003) conducted an experiment to investigate the performance of composite columns with H-steel sections under combined loading including torsion. They reported that the flexural strength and ductility capacity decreases when constant torsion was simultaneously applied.

Otsuka et al. (2004) tested nine rectangular columns under pure torsion, flexure and shear, and combined shear, flexure and torsion at various T/M ratios. They concluded that the transverse reinforcement ratios significantly affected the torsional hysteresis and the energy dissipation under combined loading increases.

Tirasit and Kawashima (2007) have reported tests on RC columns under cyclic flexure and shear, pure torsion, and combined cyclic flexure, shear and torsional loads. The rotation-drift ratio was defined to represent the level of combined cyclic flexure and torsion, which was not necessarily the same to T/M ratio after concrete cracking. The authors stated that the flexural strength and displacement capacity decreased and the damage shift upward above the flexural plastic-hinge region as the rotation-drift ratio increased. In addition, the peaks of torsional and bending moments may not occur simultaneously. The experimental interactions of normalized ultimate bending and torsional moments for different transverse reinforcement ratio from Otsuka (2004) and Tirasit (2007) are presented in the Fig. 2-16.

Belarbi and Prakash (2008 and 2009) reported experimental study on behavior of circular RC columns under combined loading including torsion. They found that the effect of concrete strength degradation in the presence of shear and torsional loads and confinement of core concrete due to transverse reinforcement significantly affected the ultimate strength of concrete sections under combined loading. A combination of flexural and torsional moments reduces the torsional moments required to cause yielding of the transverse reinforcement and the peak torsional strength. Similarly, a combination of flexural and torsional moment reduces the bending moment required to cause yielding of the longitudinal reinforcement and the peak flexural strength. The effect of spiral ratio and shear span ratio are also reported in the literature. An increase in the spiral reinforcement ratio provides more confinement and thus reduces the degradation of flexural and torsional strength under combined flexural and torsional moments. The ultimate displacement and rotation decreases significantly with a reduction in aspect ratio.

Arias-Acosta and Sanders (2010) conducted dynamic testings of bridge columns on shake table with the axial, shear, bending and torsional load combinations. The results showed significant combined load reduced the capacity of reinforced concrete bridge columns under seismic loads. Based on above research review, three failure modes are possible under combined bending and torsional moment, and shear forces for RC member reinforced with longitudinal and transverse reinforcement: completely under-reinforced (when both longitudinal and transverse steel yield), partially over-reinforced (when longitudinal steel or transverse reinforcement yields only), and completely over-reinforced (when concrete crushing begins before steel yields).

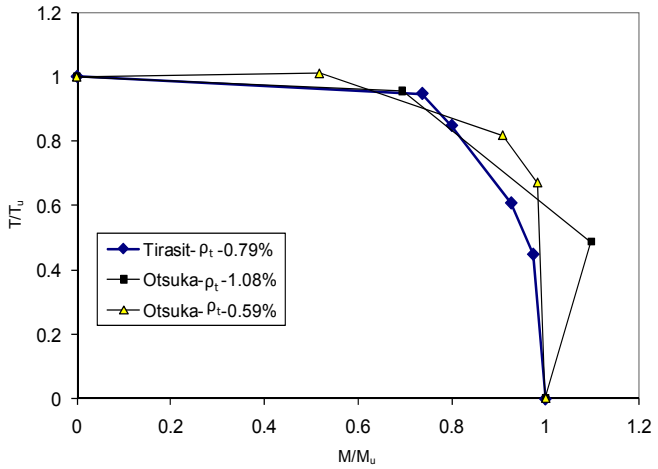

Fig. 2-16 Interactions between Normalized Torsional and Bending Moments

2.3. Analytical Study

Several theories have been proposed for reinforced concrete members subjected to pure torsion, flexure and shear, and combined shear, flexure and torsion. Notably the skew bending theory and space truss models are well known theories for combined loading. The skew bending theory is based upon equilibrium which calculates the resisting loads at failure, while truss models are based upon equilibrium and compatibility which allows predicting the load deformation response of the member. They are briefly discussed in the following sections.

2.3.1. Analytical Study for Members under Torsion

Many theories have been proposed to predict the cracking and peak torsional strength of RC members. Bredt (1896) derived the thin-tube theory with simple equations for describing torsional behavior. According to Bredt's theory, the constant shear stress can be converted to a shear flow by multiplying it by the tube's thickness. In 1929, Rausch developed an analytical model to predict the torsional capacity of RC members using space truss concepts. Theories for the torsion of plain concrete started from the elastic theory (Saint-Venant, 1856) and the plastic theory (Nylander, 1945). Early theories were

based on the assumption that an RC member would behave as a homogeneous member of plain concrete before cracking. The truss model theory has developed with four major breakthroughs by different researchers.

First, Lampert and Thürlimann (1968 and 1969) introduced variable crack angles into the space truss model and discovered the bending phenomenon in diagonal concrete struts. Second, Collins (1973) derived compatibility equations to determine the angle of diagonal concrete struts. Also Mitchell and Collins (1974) developed a compression field theory (CFT) based on a space truss concept including the concrete cover spalling concept, which can be used to determine the shear flow zone thickness. Third, Vecchio and Collins (1982) introduced a soften coefficient in concrete stress-strain relationship to quantify the softening concept in the diagonal concrete struts under biaxial loading, which was proposed by Robinson and Demorieux (1972). Fourth, Hsu and Mo (1985a) developed a Softened Truss Model (STM) theory to determine the shear and torsional behavior of RC members throughout the post-crack loading history up to the peak capacity by combining the equilibrium, compatibility, and softened stress-strain relationships. The STM theory can calculate shear flow zone thickness t_d accurately to determine the torsional strength of RC members.

The test data for solid and hollow beams indicated that the contribution to torsional strength of the cross section from the core ignored once the concrete cracking occurred (Hsu 1968b, Lampert and Thurlimann 1968, Leonhardt and Schelling 1974). Thus the beams can be considered to be equivalent tubular members, which are the basis of torsion design procedures introduced in ACI 318-95 (MacGregor and Ghoneim 1995). In addition, several theories were proposed to estimate the ultimate strength of RC members

under torsion based on skew bending theory (Lessig 1959, Yudin 1962, Collins et al. 1968, Hsu 1968c, Elfgren 1974).

2.3.1.1 Space Truss Model using Struts and Ties

Rausch developed a theory for torsion of RC members by extending the 2-D plane truss model to a 3-D space truss model as shown in Fig. 2-17. The truss model is composed of 45 degree diagonal concrete struts, longitudinal reinforcement, and transverse reinforcement connected at the joints by hinges. Torsional moment is carried by the concrete struts in axial compression (dotted lines), and by the straight reinforcing bars in axial tension (solid lines) in the longitudinal (horizontal) and lateral (hoop) directions. Equilibrium of the joints requires that the forces *X* in the longitudinal bars, Q in the hoop bars, and *D* in the diagonal struts in the longitudinal, lateral, and radial directions must be evenly distributed among all cells and joints. To satisfy equilibrium, these forces must satisfy the relationship of $X = Q = D/\sqrt{2}$. The series of hoop forces Q at the joints generate a shear flow $q = Q/s$ as shown in Fig. 2-17.

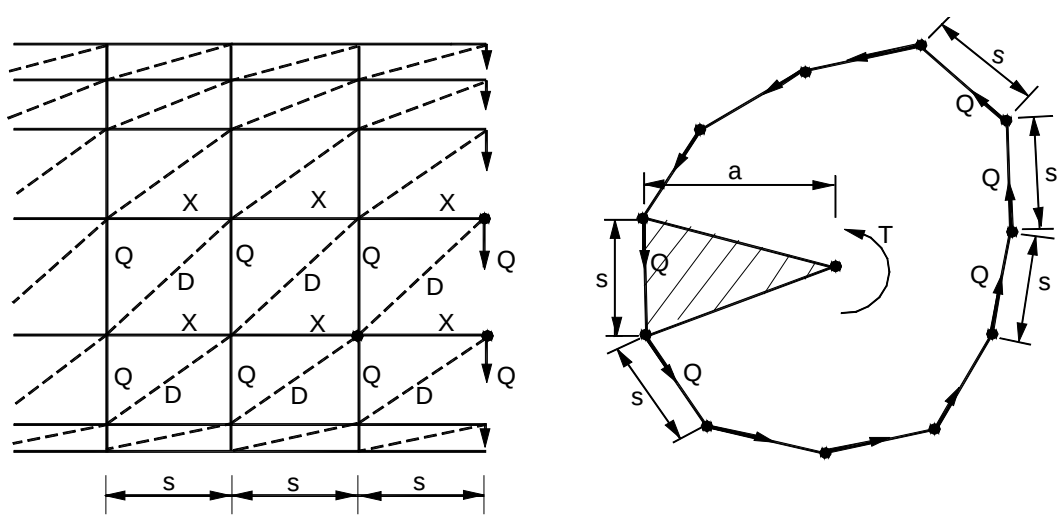

(a) Member under torsion
struts = dashed lines, ties = solid lines

(b) Section

Fig. 2-17 Rausch's Space Truss Model with Struts and Ties (Rausch 1929)

Based on Bredt's lever arm area concept, the torque T can be calculated by the concept of shear flow and enclosed area by a series of straight lines connecting the joints of the cross section as expressed in Eq. (2-4). The theory assumed that the forces in the transverse reinforcement reached the yield stress at the ultimate torque level, therefore the shear flow q and ultimate torque T_n can be expressed as

$$q = \frac{T}{2A_o}, \tag{2-4}$$

$$q = Q / s = A_t f_{ty} / s_t, \tag{2-5}$$

$$T_n = 2A_{oh} \frac{A_t f_{ty}}{s_t}. \tag{2-6}$$

However, Rausch's equation was unconservative by more than 30% for under-reinforced beams (Hsu 1968a, b). This is mainly because Rausch's model over evaluated the lever arm area A0 in members with a high percentage of reinforcement when the softening of concrete is taken into account.

2.3.1.2 Skew Bending Theory

The skew bending theory assumes that cracks form around the member in a helical pattern and create a skew failure surface with the compression strut inclined at an angle to the member's longitudinal axis. Thus three possible failure modes were proposed as shown in Fig. 2-18 (Elfgren 1974). In these failure modes, the crack angle along a face of the member was either assumed to be 45° or was calculated based on the relative yielding force that could be developed in the longitudinal and transverse reinforcement.

The torsional resistance is calculated from the equilibrium equations by summing the torsional moment in different failure surfaces about the assumed failure mode. In addition, this theory made some assumptions:

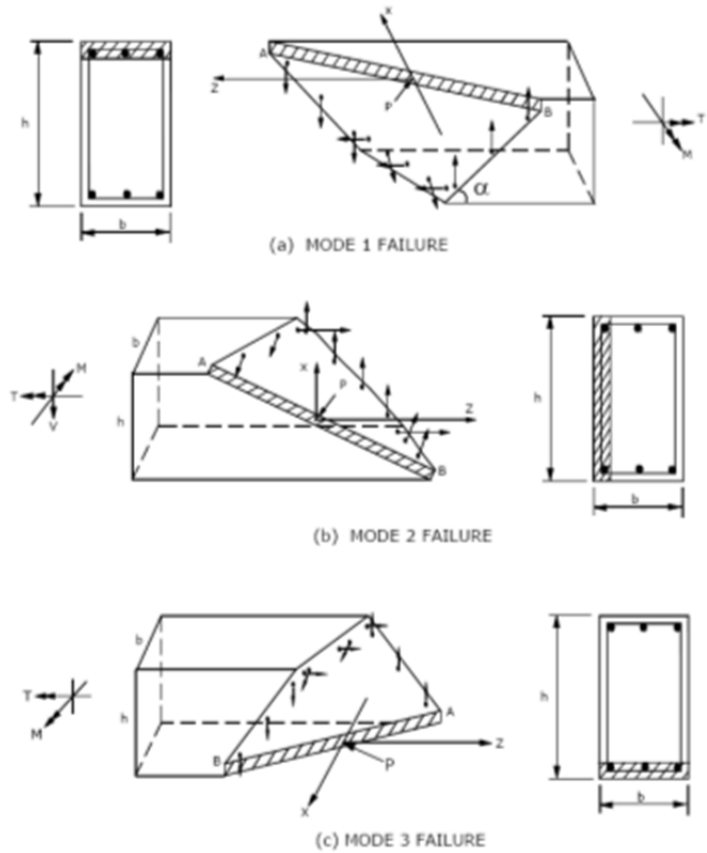

Fig. 2-18 Skew Bending Failure Modes (Elfren, 1974)

(1) shear stress in the compression zone does not affect concrete strength; (2) both the longitudinal and transverse reinforcement crossing the failure surface are yielding; (3) there are no applied loads or changes in transverse reinforcement spacing in the failure zone; (4) neglect of tension stiffening and dowel action in the reinforcement.

The RC beams without transverse reinforcement under torsion failed quickly and abruptly at cracking level, which is similar to the behavior of plain concrete beams predicted by St. Venant's theory. However, the experimental results were found to be greater than the theoretical strength (St. Venant). To find a reason for this discrepancy, Hsu (1968a) used high-speed photography to record failure process and observed that plain concrete members failed abruptly in a skew-bending mode. Based on the skew-bending failure, the torsional strength was expressed as

$$T_n = (1/3)\, x^2 y (0.85 f_r)\,, \tag{2-7}$$

where x is the shorter overall dimension of the rectangular part of the cross section, y is the longer overall dimension of the rectangular part of the cross section, f_r is the rupture modulus of concrete. The constant *1/3* is an approximation of St. Venant's coefficient when the ratio of *x/y* becomes large. This coefficient was used as the calibration for the torsional strength of beams without reinforcement, and for the "concrete contribution" of the torsional strength of beams with web reinforcement (Hsu 1968b, c).

2.3.1.3 Variable-Angle Truss Models

For pure torsion, variable-angle truss models combined strain compatibility and force equilibrium to predict a member's load-deformation behavior as well as its capacity. The angle of the compression strut is calculated based on the compatibility of strains, rather than by assuming an angle or using a function of force in the reinforcement at yielding. Several theories based on the truss model adopted different constitutive relationships for concrete under uniaxial compression, and for the softened concrete. In addition, the geometry idealization of the member and the consideration for the warping effects due to torsion vary considerably from different models. Compression field theories (CFT) and softened truss model (STM) are both based on this model with the concept of average or smeared stress and strain. Both theories adopted force equilibrium and strain compatibility obtained from a shear panel, in an idealized wall of a member's cross section. Additional equilibrium and compatibility equations are derived to assemble the membrane elements (shear panel) to a closed noncircular torsional member from Bredt's thin tube theory, which include specific equations that relate twist to shear strain and twist to the curvature in the concrete strut. Out-of-plane warping in the walls of

noncircular sections causes curvature in the concrete struts to introduce flexure in the concrete strut. The angle of the diagonal cracks to the member's longitudinal centerline is variable in both CFT and STM as shown in Fig. 2-19. The use of variable-angle truss models allows a unified treatment of shear and torsion. Further, it allows the interaction of torsion, shear, bending, and axial load to be treated rationally as discussed in the next section.

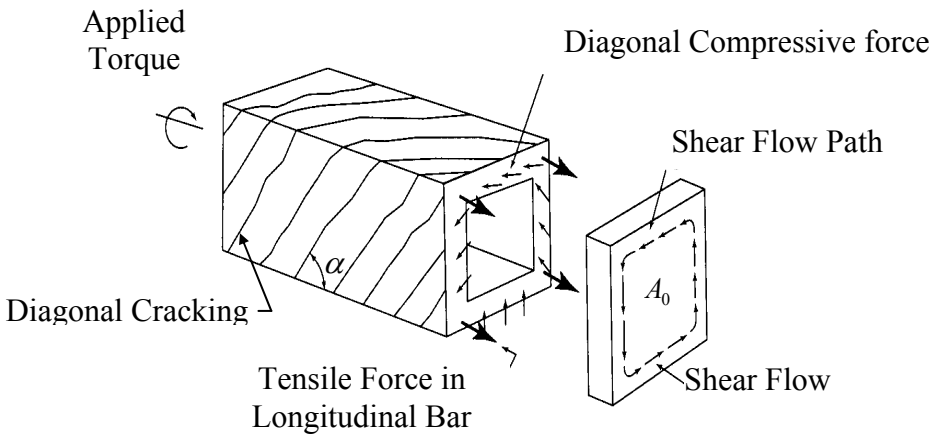

Fig. 2-19 Truss Model for RC Section under Pure Torsion

2.3.1.4 Compression Field Theory (CFT)

In a major development of the truss model for torsion, Mitchell and Collins (1974 and 1978) established the CFT to calculate the complete torque-twist response of RC members under torsion, irrespective of sectional shape or amount of reinforcement. Before the truss analogy equilibrium equations can be used to design a member for torsion, the diagonal struts inclination must be determined from the compatibility equations. The new model is made up of membrane elements treated as trusses made up of struts and ties after cracking as shown in Fig. 2-20. The four equilibrium equations (Nielsen 1967 and Lampert and Thürlimann 1968) and three compatibility equations (Baumann 1972 and Mitchell and Collins 1974) for the elements under torsion were combined in CFT theory through Eq. (2-4) and Eq. (2-8) through Eq. (2-15) as given by

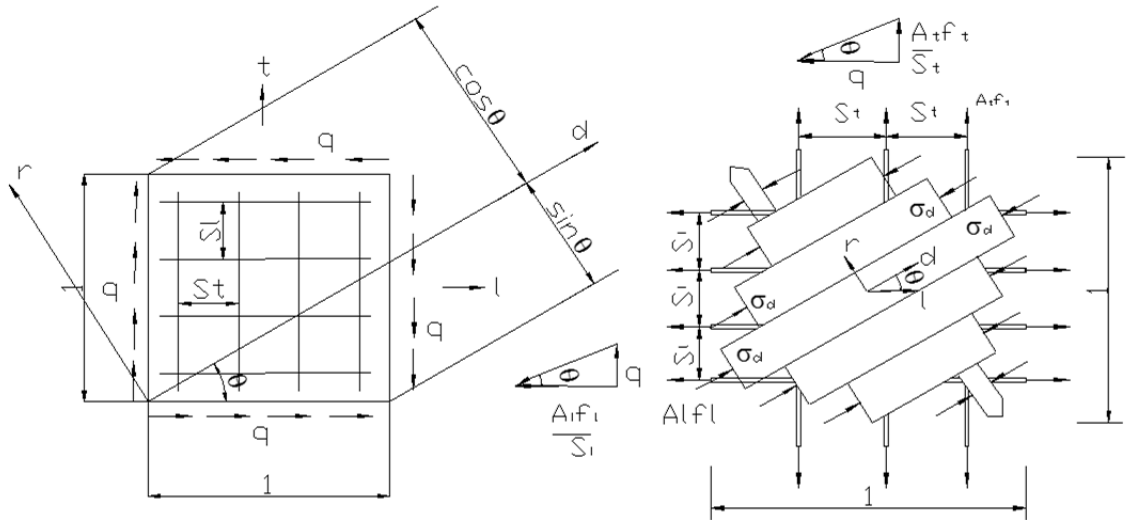

(a) Shear Element under Torsion (b) Truss Model

Fig. 2-20 Membrane Element in Shear (Hsu 1993)

$$\sigma_l = \sigma_d cos^2\theta + \sigma_r sin^2\theta + \rho_l f_l, \tag{2-8}$$

$$\sigma_t = \sigma_d sin^2\theta + \sigma_r cos^2\theta + \rho_t f_t, \tag{2-9}$$

$$\tau_{lt} = (-\sigma_d + \sigma_r) sin\theta cos\theta, \tag{2-10}$$

$$\varepsilon_l = \varepsilon_d cos^2\theta + \varepsilon_r sin^2\theta, \tag{2-11}$$

$$\varepsilon_t = \varepsilon_d sin^2\theta + \varepsilon_r cos^2\theta, \tag{2-12}$$

$$\frac{\gamma_{lt}}{2} = (-\varepsilon_d + \varepsilon_r) sin\theta cos\theta, \tag{2-13}$$

where σ_l is the normal stress in longitudinal direction for reinforced concrete, σ_t is the normal stress in the transverse direction of reinforced concrete, τ_{lt} is the applied shear stress in *l-t* coordinate for reinforced concrete, σ_d is the principal stress in *d* direction for concrete struts, σ_r is the principal stress in *r* direction for concrete struts, θ is the angle between axis of strut, compression diagonal, or the angle between *l-t* direction axis and *d-r* direction axis, ρ_l is the reinforcement ratio in *l* direction, ρ_t is the reinforcement ratio in t direction, f_l is the reinforcement stress in the *l* direction, f_t is reinforcement stress in the *l* direction, ε_l is the normal strain in longitudinal direction for reinforced concrete, ε_t is the normal strain in the transverse direction of reinforced concrete, γ_{lt} is the applied shear

strain in *l-t* coordinate for reinforced concrete, ε_d is the principal stain in *d* direction for concrete struts, and ε_r is the principal strain in *r* direction for concrete struts.

In addition, the relationship between the shear strain γ_{lt} in the tube wall and the member angle of twist Φ can be derived from the compatibility condition of warping deformation when a tube is subjected to torsion (Bredt 1896). The equation was derived and expressed as

$$\Phi = \frac{p_o}{2A_o}\gamma_{lt}, \tag{2-14}$$

where p_0 is the perimeter of the area enclosed by shear flow path, A_0 is the enclosed area by shear flow path, and Φ is the angle of twist in torsional beam.

In a torsional member, the angle of twist Φ also produces warping in member walls, which means that the concrete struts are not only subjected to compression due to the circulatory shear stress, but also subjected to bending due to the warping of the walls. The illustration of the bending curvature of the concrete strut in the wall of a box section subjected to torsion is described in Fig. 2-21 (Mitchell and Collins 1974; Hsu and Mo 1985a). Fig. 2-21 (a) shows a box member with four walls of thickness *t* subjected to a torsional moment *T,* in which each wall generates a shear flow zone with a thickness of t_d. The perimeter of the centerline of shear flow *q* is identified by a width of l_p along the top wall, and the length of the member in the longitudinal direction is calculated by $l_p cos\theta$ since the diagonal line, in the center plane of shear flow in the top wall '*OABC',* has an angle of inclination θ with respect to the longitudinal axis. When this member is subjected to an angle of twist Φ, the center plane '*OABC'* becomes a hyperbolic paraboloid surface *OADC* as shown in Fig. 2-21 (b). The plane edge '*CB'* rotates to the position '*CD'* through an angle of $\Phi l_p cos\theta$. Finally, the curved line '*OD'* represents a

bending curvature of the concrete strut, Ψ, which can be calculated according to Fig. 2-21 (c) and expressed as

$$\psi = \Phi \cdot sin2\theta, \tag{2-15}$$

where Ψ is the bending curvature of the concrete strut. Although the imposed curvature is illustrated by a rectangular box section, this equation is applicable for any arbitrary, bulky section with multiple walls. The inclination θ of the diagonal compression represents the principal strain direction, which can be derived by combining the two compatibility equations (2-11) and Eq. (2-12) as given by

$$\tan^2\theta = \frac{\varepsilon_l - \varepsilon_d}{\varepsilon_t - \varepsilon_d} \ . \tag{2-16}$$

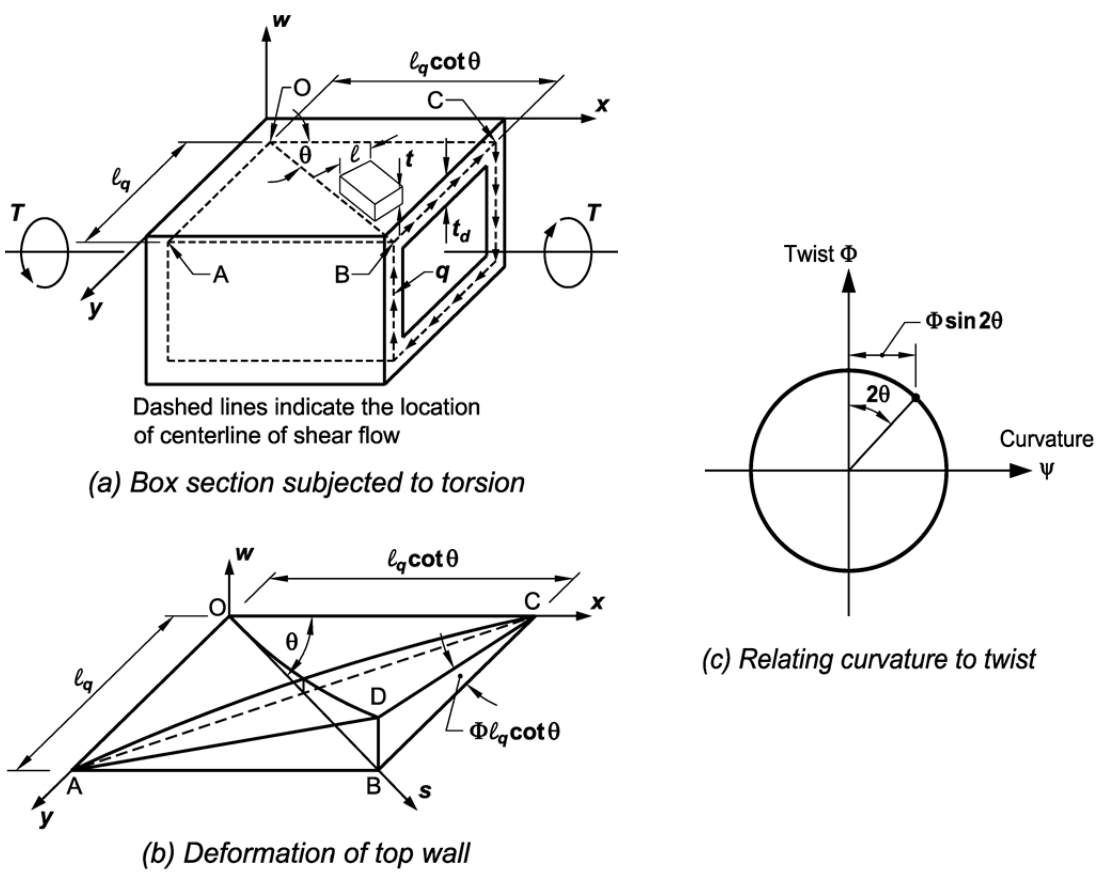

Fig. 2-21 Bending of Concrete Strut in the Wall of A Box Section Subjected to Torsion (Mitchell and Collins 1974; Hsu and Mo 1985a)

They proposed that not all of the concrete is effective in providing diagonal compressive stresses in resisting torsional load. Estimating the equilibrium of a corner element for a beam in torsion reveals that the compression in the concrete tends to push off the corner while the tension in the hoops holds it in place as shown in Fig. 2-22. Since concrete is weak in tension, the concrete outside of the hoops spalls off at higher torsions and the effective outer surface of the concrete is assumed to coincide with the hoop centerline. Because the concrete cover is assumed to have spalled before the section reaches the maximum strength, this theory is also known as the "spalling model."

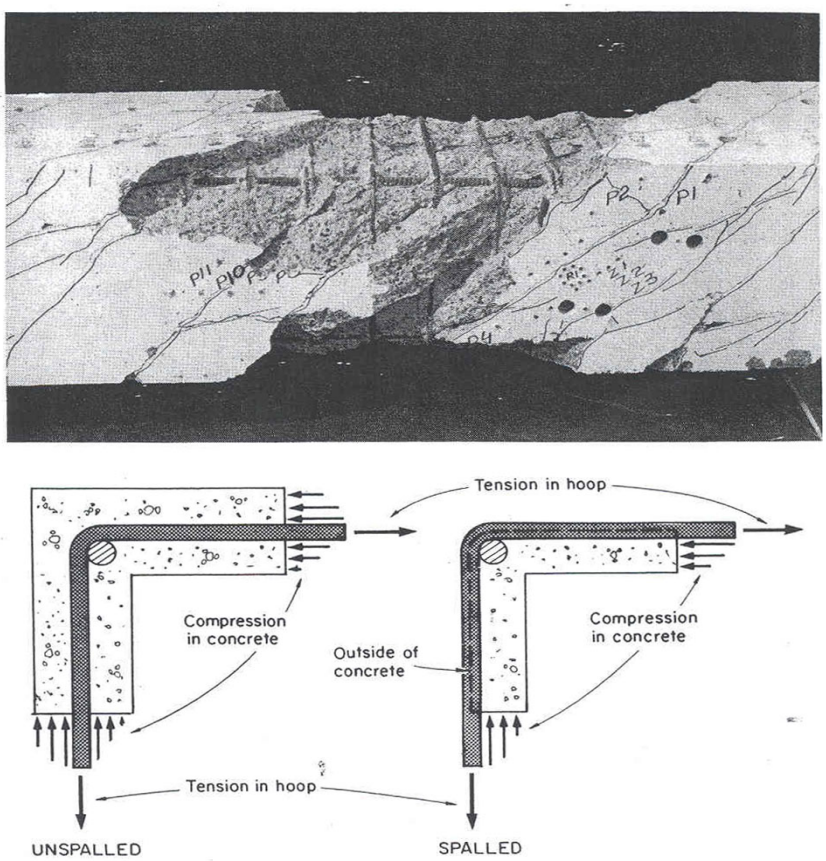

Fig. 2-22 Spalling of the concrete cover due to torsion (Mitchell and Collins 1974)

The constitutive relationship of the concrete strut unit width is shown in Fig. 2-23. The tension area in the cross section inner portion is disregarded. The area in the outer portion, which is in compression, is considered effective in resisting the shear flow. The

compression zone depth from the neutral axis to the extreme compression fiber is defined as the shear flow zone thickness t_d. The assumption that the diagonal compressive strains are reduced linearly with depth below the surface was experimentally verified. As shown in Fig. 2-23, the diagonal concrete stresses vary in magnitude from zero at the inside to a stress value f_{ds} corresponding to the strain ε_{ds} at the effective outer surface over the thickness of the effective concrete tube. Analogy to the case in flexure, the actual stress distribution can be equivalently replaced by a stress block with a uniform stress of $f_d=\alpha_1 f'_c$ acting over a depth of $a_0=\beta_1 t_d$, where the stress block factors α_1 and β_1 depend on the shape of the concrete stress-strain curve and the value of the surface compression strain ε_{ds}. The centerline of the equivalent uniformly stressed concrete tube, with a thickness of a_0, is assumed to coincide with the shear flow path. Thus the shear flow lies on the centerline of the tube at $a_0/2$ height as shown in Fig. 2-23.

Given the shear flow path as above, the terms A_0 (the area enclosed by the shear flow) and p_0 (the perimeter of the shear flow path) can be calculated using Eq. (2-17) and (2-18) as given by

$$A_o = A_{oh} - \frac{a_o}{2} p_h, \tag{2-17}$$

$$p_o = p_h - 4a_o. \tag{2-18}$$

The shear flow, q, in a box section can be expressed in terms of the longitudinal reinforcement force, ΔN, and the transverse reinforcement force, $A_t f_t$ based on the equilibrium of an element in the shear flow zone. The longitudinal reinforcement force, ΔN, is assumed to be distributed uniformly along the shear flow path p_o. Thus equilibrium in Eq. (2-8) and (2-9) can be simplified by considering $\sigma_\ell = \sigma_t = 0$ for pure torsion and neglecting the concrete tensile stress by $\sigma_r = 0$. In the CFT, several

approximate algorithms have been developed to plot the torque-twist curve using the above equilibrium and compatibility relationships.

The following solution algorithm is the approach used by Rahal et al. (2000a, b). As shown in Fig. 2-24, two equations related to longitudinal reinforcement force can be derived from the equilibrium of an element in the shear flow zone as expressed by

$$q = \sqrt{\frac{\Delta N}{p_o}\frac{A_t f_t}{s}}\,, \tag{2-19}$$

$$tan\theta = \sqrt{\frac{A_t f_t}{s}\frac{p_o}{\Delta N}}\,. \tag{2-20}$$

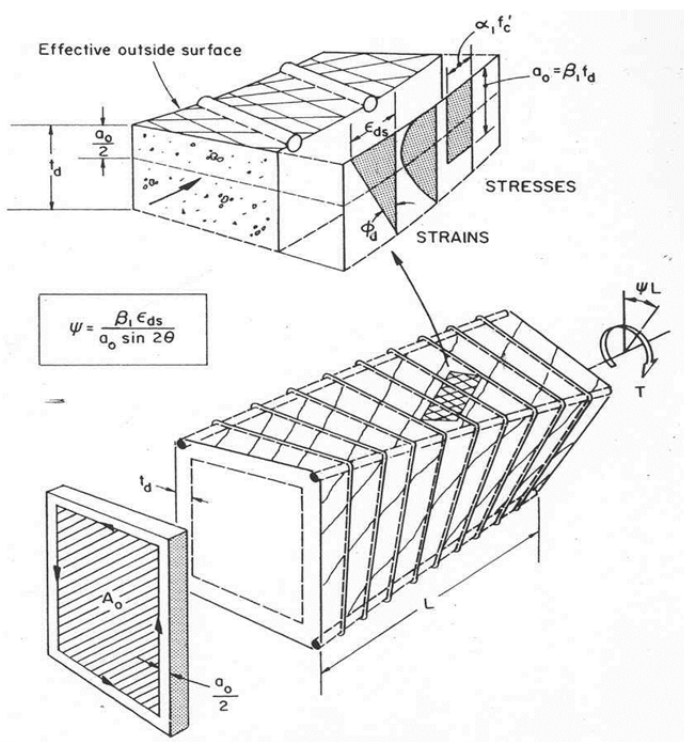

Fig. 2-23 Effective Wall Thickness of A Twisted Beam (Collins and Mitchell 1980)

The torsional moment T can be related to the longitudinal and transverse reinforcement forces ΔN and $A_t f_t$ by substituting Eq. (2-19) into Eq. (2-4) as given by

$$T = 2A_o\sqrt{\frac{\Delta \mathrm{N}}{p_o}\frac{A_t f_t}{s}}\,, \tag{2-21}$$

where s is the spacing of transverse reinforcement. In addition, the compression zone depth is a function of longitudinal and transverse reinforcement forces, and is derived from equilibrium conditions by eliminating θ from Eq. (2-8) through (2-10) as expressed by

$$a_o = \frac{\Delta N}{\alpha_l f_c^{'} p_o} + \frac{A_t f_t}{\alpha l_1 f_c^{'} s} . \tag{2-22}$$

Once the compression block depth a_o is known, the terms A_o and p_o can be calculated according to Eq. (2-17) and (2-18).

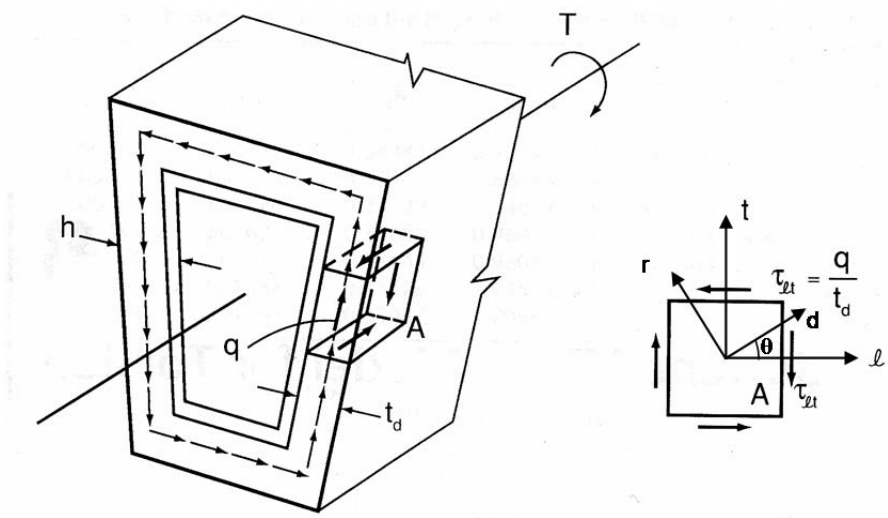

(a) Element in shear flow zone (b) Shear stress on element A

Fig. 2-24 Element in the Shear Flow Zone Subjected to Torsion

The basis compatibility Eq. (4-11) through Eq. (4-15) were manipulated to develop two expressions to determine the longitudinal and transverse beam strains, ε_l and ε_t, which correspond to the chosen value of ε_{ds}, as given by

$$\varepsilon_t = \left[\frac{\alpha_1 \beta_1 f_c^{'} A_{oh} s}{2 p_h A_t f_t} - 1 \right] \varepsilon_{ds} , \tag{2-23}$$

$$\varepsilon_1 = \left[\frac{\alpha_1 \beta_1 f_c' A_{oh} p_o}{2 p_h \Delta N} - 1 \right] \varepsilon_{ds} , \tag{2-24}$$

where A_{oh} is the area enclosed by the centerline of the outermost closed transverse torsional reinforcement, and p_h is the perimeter of the area enclosed by the centerline of the outermost closed transverse torsional reinforcement. When the tensile strength of the concrete is neglected, the stress-strain relationship of mild reinforcement is taken as the elastic perfectly plastic relationship, expressed as following:

$$f_l = E_s \varepsilon_l \qquad (\varepsilon_l < \varepsilon_{ly}), \tag{2-25a}$$

$$f_l = f_{ly} \qquad (\varepsilon_l \geq \varepsilon_{ly}), \tag{2-25b}$$

$$f_t = E_s \varepsilon_t \qquad (\varepsilon_t < \varepsilon_{ty}), \tag{2-26a}$$

$$f_t = f_{ty} \qquad (\varepsilon_t \geq \varepsilon_{ty}), \tag{2-26b}$$

where f_l is the reinforcement stress in the l direction, f_t is the reinforcement stress in the t direction, f_{ly} is the reinforcement yield stress in the l direction, f_{ty} is the reinforcement yield stress in the t direction, E_s is the elastic modulus of reinforcement, ε_{ly} is the reinforcement yield strain in the l direction, and ε_{ty} is the reinforcement yield strain in the t direction.

After the derivation of all the equations above, a trial and error process can be used to solve the eight variables (θ, a_0, ε_t, ε_l, A_0, p_0, ΔN, and $A_l f_t$) using Eq. (2-16) through Eq. (2-18), Eq. (2-20), Eq. (2-22) through Eq. (2-26). The solution algorithm is shown in following chart Fig. 2-25.

2.3.1.5 Softened Truss Model (STM)

Hwang and Hsu (1983) have developed a bi-linear model to evaluate the post-cracking torsional behavior including the warping effect. Hsu and Mo (1985a) first presented a softened truss model (STM) for reinforced concrete subjected to pure torsion, which

introduced softened stress strain curve suggested by Vecchio and Collins (1981). Based on previous analytical study, Hsu (1993) derived an algorithm with a Softened Truss Model (STM) and conducted the nonlinear analysis of reinforced concrete members under pure torsion. Although many aspects of CFT and STM are similar such as equilibrium equations and compatibility equations for the elements, their treatment of the shear flow zone and the stress-strain relationship for concrete in compression differ significantly as discussed in the following section.

The STM incorporates the softening effect and several new assumptions about the shear flow zone determination. Fig. 2-26 (a) shows a concrete strut unit width in a hollow section with a wall thickness of t. The tension area in the cross section inner portion is disregarded. The area in the outer portion, which is in compression, is considered effective in resisting the shear flow. The shear flow zone thickness t_d is also defined as the compression zone depth from the neutral axis to the extreme compression fiber, within which the strain distribution is assumed to be linear as shown in Fig. 2-26 (b) and (d) based on Bernoulli's plane section hypothesis used in the bending theory. The thickness t_d can also be related to the curvature Ψ and the maximum surface strain ε_{ds} by the simple relationship as expressed by

$$t_d = -\frac{\varepsilon_{ds}}{\psi}. \tag{2-27}$$

The peak stress $\zeta f_c'$ and average compressive stress σ_d in the concrete strut including the proportional stress and strain softening of concrete by the soften coefficient ζ are shown in Fig. 2-26 (c).

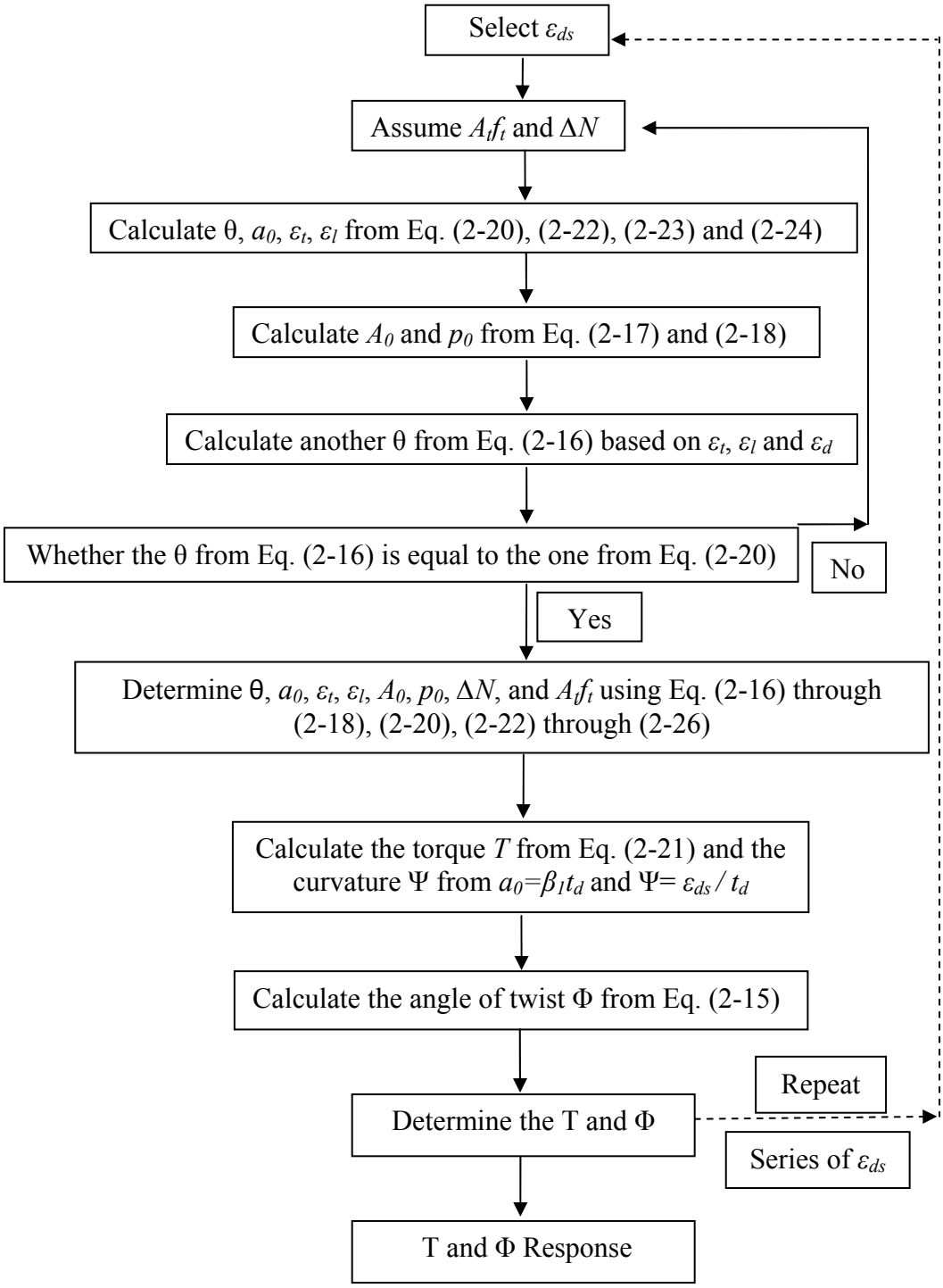

Fig. 2-25 Solution Algorithm of Compression Field Theory (CFT)

The stress-strain relationship of concrete in compression can be analytically expressed by two branches of parabolic curves (Hsu and Mo 1985a) as given by

Ascending branch: $$\sigma_d = \zeta f_c^{'}\left[2\left(\frac{\varepsilon_d}{\zeta\varepsilon_0}\right)-\left(\frac{\varepsilon_d}{\zeta\varepsilon_0}\right)^2\right] \qquad \frac{\varepsilon_d}{\zeta\varepsilon_0}\le 1, \tag{2-28 a}$$

Descending branch: $$\sigma_d = \zeta f_c^{'}\left[1-\left(\frac{\varepsilon_d/\zeta\varepsilon_0-1}{2/\zeta-1}\right)^2\right] \qquad \frac{\varepsilon_d}{\zeta\varepsilon_0}> 1, \tag{2-28b}$$

where $f_c^{'}$ is the concrete cylinder compressive strength, ζ is the softening coefficient. The stress-strain relationship of concrete in tension is irrelevant, if the concrete tensile stress σ_r is assumed to be zero in the equilibrium Eq. (2-8) through (2-10).

In a simple way, the average stress σ_d of the concrete stress block in Fig. 2-26 (c) can be expressed by

$$\sigma_d = k_1\zeta f_c^{'}, \tag{2-29}$$

where the coefficient k_1 is the ratio of the average stress to the peak stress. The coefficient k_1 can be derived by integrating the stress-strain curve in Eq. (2-28 a) and (2-28 b) as given by

$$k_1 = \frac{\varepsilon_{ds}}{\zeta\varepsilon_0}\left(1-\frac{1}{3}\frac{\varepsilon_{ds}}{\zeta\varepsilon_0}\right), \qquad \frac{\varepsilon_d}{\zeta\varepsilon_0}\le 1 \tag{2-30 a}$$

$$\mathrm{k}_1 = \left[1-\frac{\zeta^2}{(2-\zeta)^2}\right]\left(1-\frac{1}{3}\frac{\varepsilon_{ds}}{\zeta\varepsilon_0}\right)+\frac{\zeta^2}{(2-\zeta)^2}\frac{\varepsilon_{ds}}{\zeta\varepsilon_0}\left(1-\frac{1}{3}\frac{\varepsilon_{ds}}{\zeta\varepsilon_0}\right). \qquad \frac{\varepsilon_d}{\zeta\varepsilon_0}> 1 \tag{2-30 a}$$

For normal strength concrete up to 42 MPa, the softening coefficient ζ can be expressed as proposed by Belarbi and Hsu (1995) in Eq. (2-31), which is a function of tensile strain ε_r as expressed by

$$\zeta = \frac{0.9}{\sqrt{1+400\varepsilon_r}}. \tag{2-31}$$

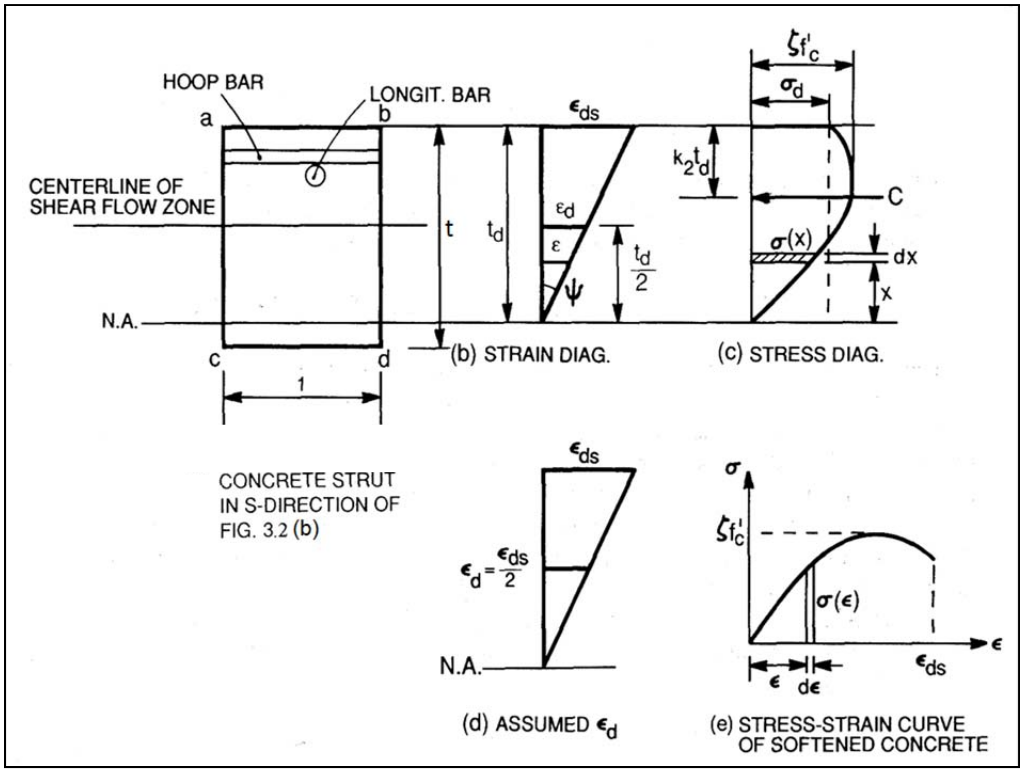

Fig. 2-26 Strains and Stresses in Concrete Struts (Hsu and Mo 1985a)

For high strength concrete up to 100 MPa, Zhang and Hsu (1997) proposed that the softening coefficient should be a function of both concrete strength f_c' and tensile strain ε_r, which was expressed as

$$\zeta = \frac{5.8}{\sqrt{f_c'(MPa)}} \frac{1}{\sqrt{1+400\varepsilon_r}} \quad \text{and} \quad \frac{5.8}{\sqrt{f_c'(MPa)}} \le 0.9 . \tag{2-32}$$

In addition, the location of resultant force from the compression stress block *C* can be determined at a distance $k_2 t_d$ from the surface as shown in Fig. 2-26 (c), where the coefficient k_2 defines the location of the resultant force *C*. The coefficient k_2 is found to depend on concrete strength within the range of 0.40 to 0.45 by integrating the concrete stress-strain curve given in Eq. (2-28 a) and (2-28 b). Unlike the CFT, therefore, the average compressive strain in the STM was assumed to occur at the mid-depth of the shear flow zone and the centerline of the shear flow is assumed to coincide with ε_d as

shown in Fig. 2-26(b), which also results in a compatible agreement between theory and tests. The average compressive strain can be expressed as

$$\varepsilon_d = \frac{\varepsilon_{ds}}{2}. \tag{2-33}$$

Therefore, the A_0 and p_0 should include the full section dimensions instead of the spalled dimensions, which are also assumed to be valid in any arbitrary bulky cross-section. Hence, the formula for calculating A_0 must include the square of shear flow thickness $t_d^{\,2}$, which is different from the thin tube formula used in the CFT neglecting the term $a_o^{\,2}$. Thus the cross sectional dimension parameters are given by

$$A_0 = A_{cp} - 0.5 p_c t_d + t_d^2, \tag{2-34}$$

$$p_0 = p_c - 4t_d. \tag{2-35}$$

where, p_c is the perimeter of the cross section, and A_{cp} is the area of bounded by p_c. The thickness of the shear flow zone t_d can be expressed in terms of strain by the substitutions and manipulations of five compatibility equations, Eq. (2-11) through Eq. (2-15), Eq. (2-27), and Eq. (2-33), which can be expressed as

$$t_d = \frac{A_o}{p_o}\left[\frac{(-\varepsilon_d)(\varepsilon_r - \varepsilon_d)}{(\varepsilon_l - \varepsilon_d)(\varepsilon_t - \varepsilon_d)}\right]. \tag{2-36}$$

The variable t_d is related to the strains in all *d, r, l,* and *t* directions (ε_d, ε_r, ε_l, ε_t). The variable t_d is also involved in equilibrium equations through the terms of A_o, p_o, ρ_l, and ρ_t. Hence, the variable t_d must first be assumed and then checked by Eq. (2-36). The compressive strain is defined as negative and tensile is positive.

In the Eq. (2-36), the strain ε_l should be related to the reinforcement stresses, f_l, by eliminating the angle θ from the equilibrium in Eq. (2-8) using compatibility equations in Eq. (2-13) through (2-15), Eq. (2-27), and Eq. (2-33) as expressed by

$$\varepsilon_l = \varepsilon_d + \frac{A_0(-\varepsilon_d)(-\sigma_d)}{A_l f_l}. \tag{2-37}$$

Therefore, the unknown variables ε_l and f_l can be solved using Eq. (2-37) and the stress-strain relationships in Eq. (2-25 a) and Eq. (2-25 b) for longitudinal reinforcement. Similarly, the strain ε_t can be related to the reinforcement stresses f_t by eliminating the angle θ from equilibrium Eq. (2-9) using the compatibility conditions in Eq. (2-13) through Eq. (2-15), Eq. (2-27), and Eq. (2-33). The expression of transverse reinforcement strain ε_t is expressed as

$$\varepsilon_t = \varepsilon_d + \frac{A_o s\left(-\varepsilon_d\right)\left(-\sigma_d\right)}{p_o\left(A_t f_t + A_{tp} f_{tp}\right)}. \tag{2-38}$$

The unknown variables ε_t and f_t can be solved using Eq. (2-38) and the stress-strain relationships in Eq. (2-26 a) and Eq. (2-26 b) for transverse reinforcement.

In order to facilitate the reasonable solution procedures, two more compatibility equations are required by combining computability conditions in Eq. (2-11) and Eq. (2-12). One of the equations is as expressed in Eq. (2-16) and another one is aiming to connect the two variables ε_r and θ directly to the strains ε_l, ε_t, and ε_d as expressed by

$$\varepsilon_r = \varepsilon_l + \varepsilon_t - \varepsilon_d. \tag{2-39}$$

The solution procedure is illustrated by a flow chart shown in Fig. 2-27 as given by a hand-calculation illustration procedure from Hsu (1993). The STM theory was used by Hsu and Mo (1983, 1985a) to calculate the strength and behavior of 108 torsional beams

for calibration of the model. As a result, the experiment-to-calculated torsional strengths had a mean value of 1.014 and a standard deviation of 0.051 for the 61 under-reinforced beams with stirrup spacings within the ACI Code limits. The efficiency of this solution procedure arises from the elimination of the angle θ in the calculations of Eq. (2-36) through (2-38) to avoid involvement in the iteration process of shear flow thickness. Moreover, McMullen and El-Degwy (1985) used torsion tests to compare the STM (softened theory) and the CFT (spalling theory), concluding that the STM model gives a better prediction of maximum torque for the beams tested in this investigation. McMullen and El-Degwy also observed that concrete cover spalled only after the peak torque.

2.3.1.6 Tension Stiffening-Softened Truss Model (TS-STM)

The original STM for torsion neglects the tensile strength of concrete and excludes the tension stiffening effect of concrete, which contributes to torsional resistance. Greene and Belarbi (2006a, b) expanded STM to include the tension stiffening of concrete and proposed a tension stiffening-softened truss model for torsion. The incorporation of tension stiffening of concrete is important for a more accurate prediction of the service-level torsional deformation. The TS-STM assumes that a member was uniformly reinforced in the longitudinal and transverse directions by constant spacing. It also uses average stress-strain relationships to model the constitutive material laws for concrete and reinforcement to be the same as STM. The model accounts for the concrete in tension with a stress-strain relationship and modifies the shear flow zone to account for the transition between an uncracked and fully cracked member. For concrete under tension, the material stress-strain relationships treat cracked concrete as a continuum based on smeared concept. The angle of crack rotates to remain normal to the principal

tensile stress and the contribution of concrete and longitudinal reinforcement in shear is neglected, which means that it disregards the dowel action. In addition, a perfect bond between the concrete and reinforcement is assumed. The model has been validated by comparing the predicted and experimental behavior of members loaded under pure torsion and having a symmetric distribution of longitudinal reinforcement and normal strength concrete.

2.3.2. Analytical Study for Members under Combined Flexure, Shear and Torsion

During earthquake excitations, torsion acts in combination with axial and shear forces and bending moment. Previous study on behaviors of RC members under pure torsion, torsion and flexure, and torsion and shear was performed to understand the behavior of members under the combination of the three stress-resultants forces T, M, and V. There are two main types of theories for predicting the combined loading effect on RC members: skew bending and truss models.

Early research (Lessig 1959, Yudin 1962, Hsu 1968a, Johnston 1971, McGee 1973, Elfgren et al. 1974) investigated the ultimate strength under combined loading to establish three-dimensional interaction surfaces based on the skew bending theory using equilibrium conditions. Further analytical study was based on truss models considering both equilibrium and strain compatibility to obtain the full response of reinforced concrete beams subjected to various load combinations (Rabbat and Collins 1978, Onsongo and Collins 1978, Rahal and Collins 1995a, 2003a, Greene and Belarbi 2009a, b).

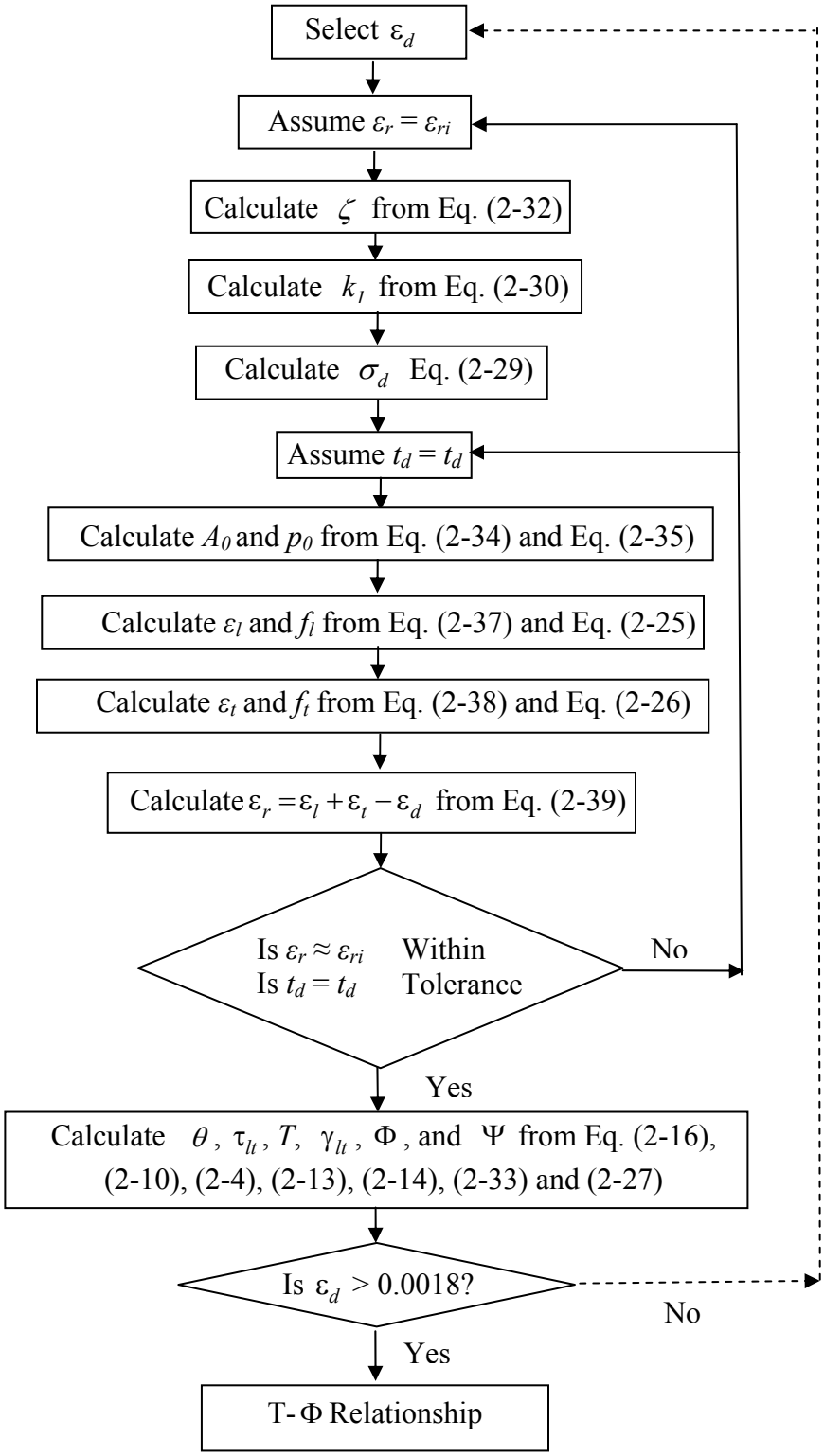

Fig. 2-27 Solution Algorithm of Softened Truss Model (STM)

2.3.2.1 Skew Bending Theory

In the skew bending theory, internal resistance is calculated by summing internal forces along an assumed failure surface through equilibrium equations. There are some assumptions of this theory as discussed above. The skew bending theory is limited to only predict a member's strength, not corresponding deformation since it only considers the equilibrium of forces without strain compatibility. Elfgren et al. (1974) developed a three-dimensional interaction surface for members under combined torsion, flexure, and shear, based on three failure modes as shown in Fig. 2-18. In the first mode failure, the top longitudinal reinforcement and the transverse reinforcement yield on the side where the shear and torsional stresses are additive. The second failure mode occurs when the longitudinal and transverse reinforcement on the additive side yield. In the third mode failure, the bottom longitudinal reinforcement and the transverse reinforcement both yield on the additive side. The Elfgren idealized a rectangular member as a box with reinforcement lumped into the four corners as "stringers" to resist axial force induced by superposing the applied torsional moment, *T*, bending moment, *M*, and shear force, *V*. This model considers that the failure of the concrete occurs before the longitudinal reinforcement yields, so over-reinforced or partially over-reinforced sections could not be evaluated with this theory. In addition, the warping effect in the cross section due to torsion was disregarded. Non-dimensional interaction relationships for *M*, *V*, and *T* for the three failure modes are given by Eq. (2-40) through Eq. (2-42) as follows:

Mode 1: $$-\frac{1}{r}\left(\frac{M}{M_o}\right)+\left(\frac{V}{V_o}\right)^2+\left(\frac{T}{T_o}\right)^2=1 \quad \text{Eq. (2-40 a)}$$

Mode 2: $$\left(\frac{V}{V_o}\right)^2+\left(\frac{T}{T_o}\right)^2+2\left(\frac{VT}{V_oT_o}\right)\sqrt{\frac{2d_v}{p_o}}=\frac{1+r}{2r} \quad \text{Eq. (2-40 b)}$$

Mode 3: $$\frac{M}{M_o} + r\left(\frac{V}{V_o}\right)^2 + r\left(\frac{T}{T_o}\right)^2 = 1 \quad \text{Eq. (2-40 c)}$$

where T_0, M_0, V_0 is the capacity of a member under the pure torsional moment, bending moment, or shear force respectively, d_v is the centerline distance between the top and bottom stringers, p_0 is the perimeter around the member measured along the centerline of the stringers, r is the ratio of the force in the top stringers at yielding to the force in the bottom stringers at yielding ($A'_s f_y / A_s f_y$) accounting for an asymmetrical reinforcement configuration in a member. In this model, the term r has the effect of shifting the interaction surface along the M/M_0 axis and allows the model to predict an increase in torsional capacity for members with a small bending moment and asymmetrical reinforcement. The interaction surface described by the Elfgren equations is shown in Fig. 2-8 for r =1/3 as presented by Hsu (1993).

Later on, Elfgren (1979) loaded rectangular RC beams at mid-span with an eccentric point load acting downwards. The beam had dimensions in 100 × 200 × 3300 mm (width × height × length). It was found that the relationship among the T, V, and M in the failure section was M: T: V = 0.1:0.5:0.2. The crack pattern and failure mechanism for the beam are shown in Fig. 2-29.

Based on his test results and other studies reported by Lüchinger (1977), Müller (1976 and 1978), and Thürlimann (1978), Elfgren proposed a kinematics model as illustrated in Fig. 2-30. This kinematics model can also be described by the same equations Eq. (5-6) through (5-8) as earlier equilibrium methods. As shown in Fig. 2-29, two failure cracks ABC and FED, as well as a rotation hinge AD can be identified to the kinematics failure model.

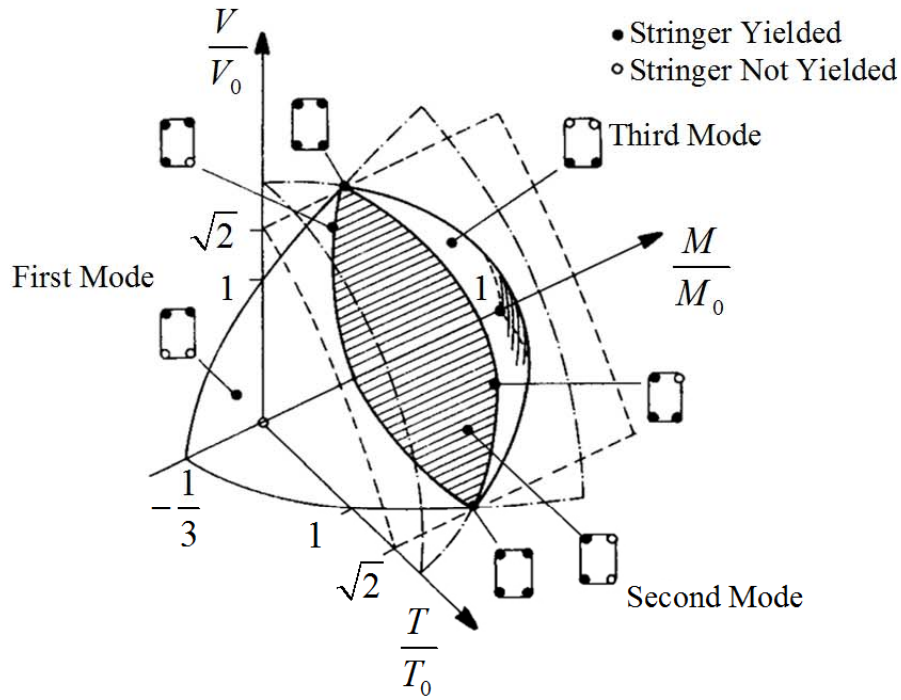

Fig. 2-28 Interaction Surface for Torsion, Bending, and Shear
(Adapted from Hsu, 1993)

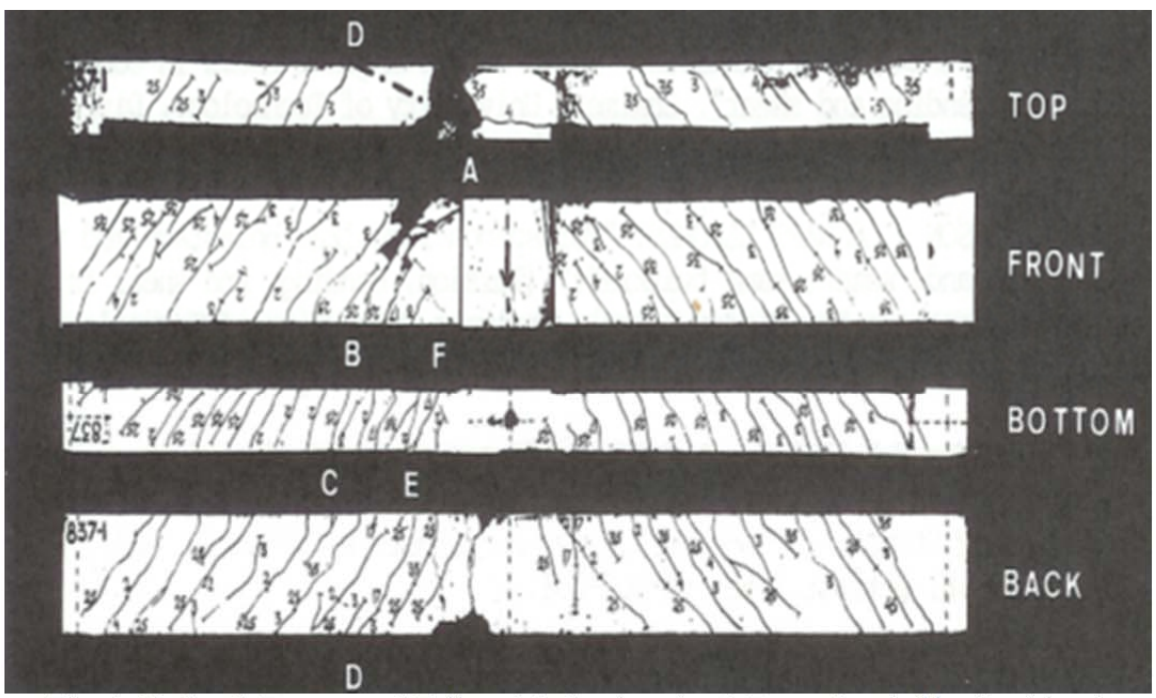

Fig. 2-29 Crack Pattern and Failure Mechanism for A Beam Loaded in Combined Torsion, Shear, and Flexure (Elfgren 1979)

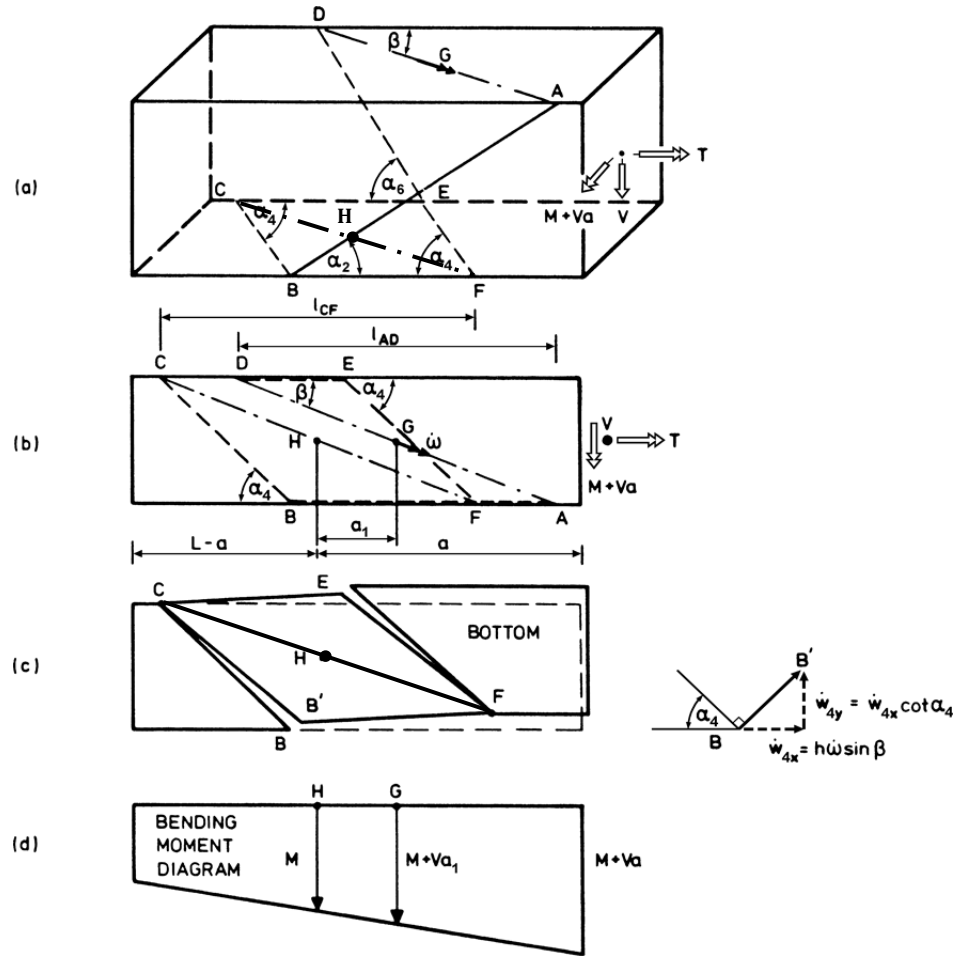

Fig. 2-30 Kinematics Failure Model: (a) General View; (b) Model Seen from Above; (c) Deformations in Bottom; (d) Bending Moment Diagram (Elfgren 1979)

2.3.2.2 Variable-Angle Space Truss Model

Rabbat (1977) developed the variable-angle space truss (VAST) model to account for combined loading by idealizing an RC member into four chords, representing longitudinal reinforcement, and four wall panels, representing RC concrete. The chords were encased in concrete blocks for developing uniform tension or compression to resist the applied bending moments and axial force. Also the idealized chords were assumed to resist the axial force from warping effect in the member due to an applied torque. Both the concrete and reinforcement resist compressive stress in the chord, and only the reinforcement alone resists tension stresses since tension stiffening is disregarded. The

applied torsional moments and shear forces caused a uniform shear stress along the wall panels, which has a consistent thickness and are assumed to remain plane under combined loading. The strain compatibility was introduced into this model by determining the angle of the diagonal compressive strut on each face by strain compatibility conditions, which is the advantage of VAST over the skew bending models. Also the angle of the diagonal compressive strut was affected by the applied load and the amount of reinforcement. This model uses an elastic, perfectly plastic stress-strain relationship for the reinforcement and the uniaxial stress-strain relationship of a concrete cylinder for concrete compression.

2.3.2.3 Compression Field Theory (CFT)

The CFT theory for the RC member under pure torsion was first reported by Mitchell and Collins in 1974, which neglected the tensile stress in the cracked concrete. Later on, this theory was developed by Onsongo (1978) to predict the behavior of beams under combined torsion, bending moment and axial load. The CFT for combined loading models an RC member as a series of wall panels, and incorporates all the equations for equilibrium, compatibility, and stress-strain relationships of materials to be satisfied at each longitudinal reinforcing bar. Concrete strut curvature can also be accounted for by introducing the longitudinal and transverse curvature in the wall panel in term of strains. The strain compatibility equations were developed to maintain the compatibility of strain in the longitudinal reinforcement. Compressive stresses are assumed to be resisted only by the concrete and tensile stresses only by the longitudinal reinforcement. In addition, the shear strain calculated at each longitudinal reinforcing bar affects twist in the member to account for contribution from longitudinal reinforcement. In the model, the uniaxial

stress-strain relationship of a concrete cylinder is assumed for concrete in compression, and the concrete cover is disregarded since the concrete cover is assumed to spall down to the plane of hoop centerlines at yielding stage.

2.3.2.4 Modified Compression Field Theory (MCFT)

The CFT theory for combined loading (Onsongo 1978) was modified by Vecchio and Collins (1986 and 1989) for panels subjected to in-plane shearing and axial stresses, and then for beams subjected to shearing forces, bending moment, and axial load. The modified compression field theory (MCFT) quantified and introduced the effects of concrete softening and tension stiffening under uniaxial stress. Rahal and Collins (1995a and 2003a) incorporated the softening behavior of concrete under biaxial stress into models to extend MCFT to the case of combined shear, flexure and torsion actions. For the cross section of a beam reinforced in the transverse and longitudinal directions as shown in Fig. 2-31 (a), the six stress resultants ($N, T, V_z, M_z, V_y,$ *and* M_y) can produce complex three-dimensional shearing and normal stresses distributed on the small elements within the section. In this model, the section was idealized into two systems to consider one- and two-dimensional stress patterns on the elements, respectively, as shown in Fig. 2-31 (b) and (c). The one-dimensional system consisted of a cross section with only longitudinal reinforcement, which not only resisted the longitudinal stress from stress resultants such as the axial force and the bending moments, but also by the shearing stresses from the shear forces and torsional moment. Plane sections assumption was used in one-dimensional system in the case of flexure, and the longitudinal strains are assumed to vary linearly over the section, which are related to the longitudinal strains by the usual uniaxial stress-strain relationships for the materials. Therefore, the longitudinal

deformation can be expressed by the longitudinal strain at the centroid of the section, ε_{cen}, and the curvatures Φy and Φz about the y and z axes, respectively, as described in Fig. 2-31 (b). The two-dimensional system was composed of four shear walls locating near the periphery of the cross section as shown in Fig. 2-31 (c), which were reinforced by the transverse stirrups to resist in-plane shearing stresses from shear forces and the torsional moment. The shear stresses act simultaneously with specified longitudinal strains computed from the one-dimensional system. For each wall, the strain at the center of the wall was used as the average constant strain, which meant the assumed uniform strain distribution on the walls. In addition, the thickness of the walls can be calculated from the curvature of the walls in the diagonal direction, which can be calculated from the curvature in the longitudinal and transverse directions of the walls. It adopted the strain compatibility equations developed by CFT and the equations for longitudinal strain compatibility and curvature of the concrete struts. In addition, this model included an empirical coefficient to predict concrete cover spalling. Once the model captured the initiation of spalling, the concrete cover would be disregarded on the faces due to high shearing stress. The shear due to torsion was assumed to flow around the member. Bredt's expression for torsion in a thin tube was used in this model.

The model also assumed that the tension at a crack was transmitted across the crack through local shear stresses after the reinforcement yielded. Thus this assumption of a shear stress at the cracks violated the defined crack direction, normal to the principal tensile direction. As compared to experimental results, however, this model can accurately calculate the full response of members subjected to combined axial and shear forces, and bending and torsional moment.

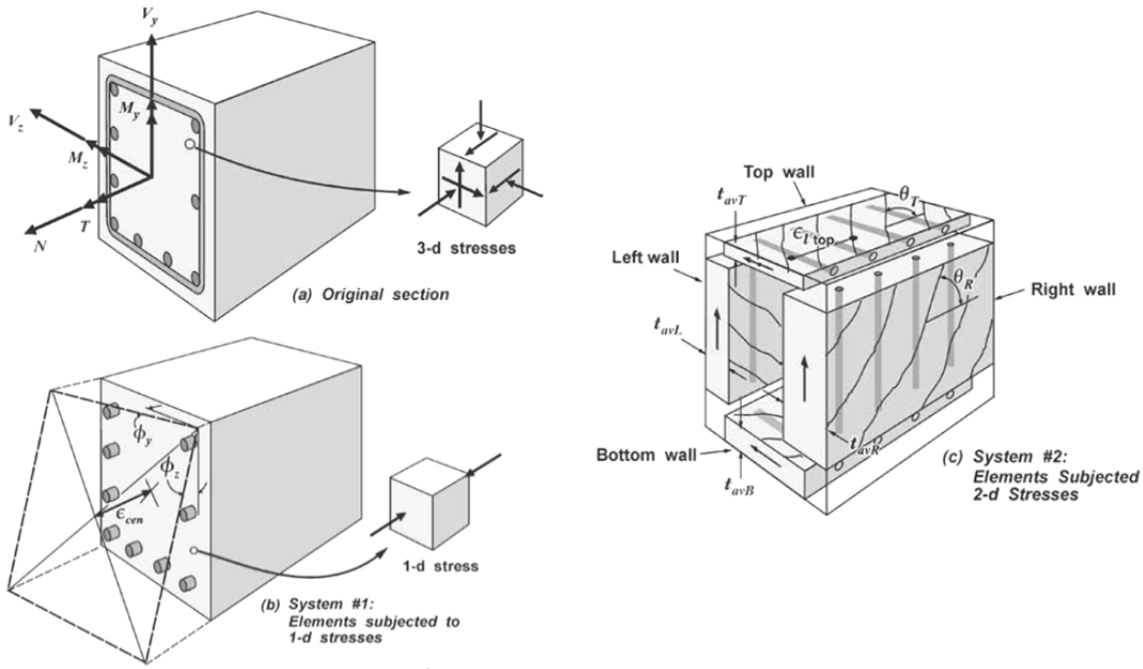

Fig. 2-31 Modified Compression Field Theory (MCFT) Model for Combined Axial and Shear, Bending and Torsional Load (Rahal and Collins1995a and 2003a)

2.3.2.5 Combined-Action STM

Greene and Belarbi (2006) expended STM to predict the load-deformation response of a member under torsion, T_x, combined with bending moment, M_z, and shear, V_y, which was named as Combined-Action Softening Truss Model (CA-STM). The CA-STM assumed that any hollow or solid members under combined loading including torsion can be considered as a thin tube, and the concrete core of a solid member is in tension not contributing to the torsional resistance. The thickness of the thin tube in which the shear stresses act is also known as the shear flow zone t_d. After cracking, the wall panels will act as a "truss" consisting of diagonal concrete struts under compression and an orthogonal tie of reinforcement under axial tension or compression.

Idealized Model of Cross Section - The CA-STM modeled the walls of an RC member as shear panels as shown in Fig. 2-32, and the thickness of each shear panel is the depth of the shear flow zone t_d in that shear panel. The idealized width of shear panels can be

identified by b_0 and h_0 based on the actual cross sectional dimension, b and h, and the thickness of shear flow zone, t_d. The cross sectional area of each shear panel, A, can be calculated by the product of its modeled width and thickness. The small overlap effect between two shear panels at the corner can be neglected because curvature in the shear panels resulted in reduced thickness of shear panel compared to the actual cross section. The total area of reinforcement was distributed equally into each wall panel for the case of symmetrical longitudinal reinforcement configurations.

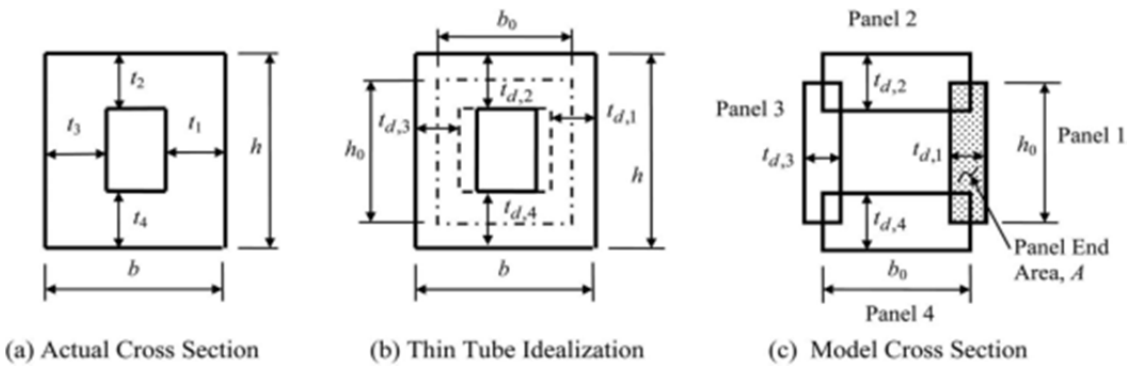

Fig. 2-32 Actual and Model Cross Section of a Hollow Member

Distribution of Applied Torsional Moment and Shear Force - The shear flow distribution along the shear panels can be determined by the combined shear and torsion load. The shear stress due to torsion, T_x, was taken as a constant over the thickness of the shear panels and the shear stress from shear force, V_y, distributed along the centerline of the shear flow zone. Based on the shear distribution characteristics, the CA-STM also assumed that an applied shear resulted in a uniform shear flow in the shear panels parallel to the applied shear, and neglected any shear flow in the wall panels acting in a direction perpendicular to the applied shear. Therefore, the superposition of shear stress from torsion and shear load can be described in Fig. 2-33, obtaining the smallest shear stress in one of the shear panels and the largest shear stress in another one of the shear panels, as well as two equal medium shear stresses in two other ones.

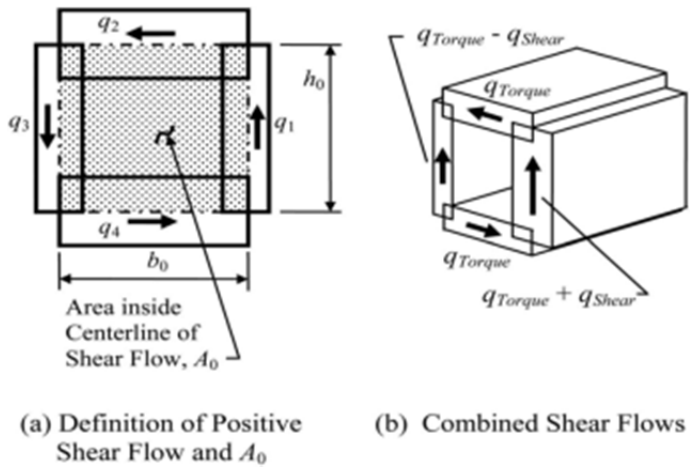

Fig. 2-33 Shear Stress Distribution under Shear Force and Torsion

Distribution of Applied Bending Moment and Axial Force - The applied bending moments and axial force need to be resisted by the uniformly distributed normal stress σ_L from both concrete and longitudinal reinforcement. The resultant force of the normal stress at each shear panel was determined by the product of normal stress and shear panel area, $\sigma_L A$, which generated a moment, M, about the centerline of the member and axial load, N, along the longitudinal direction by summation as shown in Fig. 2-34.

Equilibrium and strain compatibility - The proposed CA-STM adopted the equilibrium and compatibility equations used in the STM for torsion (Hsu 1993). The model included three equilibrium equations and three strain compatibility equations for an RC wall panel under in-plane membrane stresses. The equilibrium is maintained in each panel, and strain compatibility in the longitudinal direction is maintained at the center of each panel. In addition, the shear panels are connected by several compatibility conditions such as: (1) the longitudinal strain in each wall panel is related to the longitudinal strain at the centerline of the member as shown in Fig. 2-35; (2) the curvature in the shear panel under combined loading is not only caused by both the member's twist and the longitudinal and transverse curvature in the shear panel; and (3)

the unit twist of the member is related to the cumulative shear strain in the four wall panels.

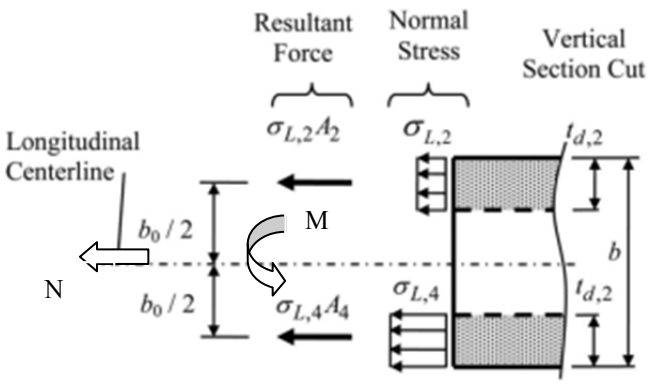

Fig. 2-34 Normal Stress Distribution under Axial Force and Bending Moment

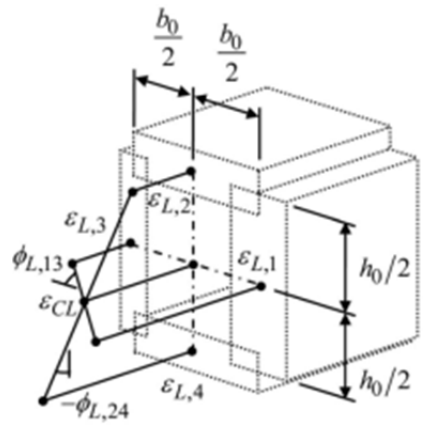

Fig. 2-35 Strain Compatibility in Longitudinal Direction

Stress-Strain Relationships of Materials – Reinforced concrete under uniaxial compression will have a stress-strain response similar to that of a plain concrete cylinder. However, the response will significantly alter when the compression is accompanied with tensile strain in the transverse direction. The biaxial behavior indicates that either the compressive stress is reduced in scale or the stress and strain are both proportionally scaled down. The magnitude of the scaling factor is referred to as the softening coefficient in STM. The CA-STM adopted a softened stress-strain relationship for concrete acting in compression based on the one proposed by Belarbi and Hsu (1991 and 1994). Tensile stress of the concrete had a significant affect on a member's load-deformation response at service load level due to tension stiffening, which was accounted for in CA-STM by the stress-strain response of the concrete acting in tension. The CA-STM adopted the tensile stress-strain relationships for concrete previously validated for RC members with normal strength up to 40 MPa under pure torsion (Greene and Belarbi 2006). For the STM model, the stress-strain relationships for reinforcement had been

developed by Belarbi and Hsu (1994) and Pang and Hsu (1995 and 1996) to describe the average stress and average strain of reinforcement embedded in concrete shear panels, in which an apparent yield stress for the embedded reinforcement was proposed which was less than the yield stress of bare reinforcement. Belarbi and Hsu (1994) also reported that yielding stress of reinforcement and the load carried by the member at a given deformation level will both be overestimated if the stress-strain relationship for bare reinforcement is used in the STM. However, CA-STM adopted the elastic-perfectly-plastic relationship of bare reinforcement to account for the average stress and average strain of reinforcement embedded in concrete for the following reasons: (i) the average tensile stress is relatively small compared to tensile force in reinforcement at the yielding state during the load-deformation response, so it will not significantly affect the prediction; (ii) the empirical relationship for embedded reinforcement was developed using shear panel tests not for the three dimensional case under combined loading; (iii) the elastic-perfectly-plastic expression is simpler to use; (iv) the apparent yield stress relationship for embedded reinforcement has not been validated for rectangular members or members twisted due to applied torsional moment.

Finally, the solution method was developed for the CA-STM predicting load-deformation response under specific ratios of torsional moment to bending moment, shear and axial load. Six unknown variables in the equations for CASTMT were found exceeding the total number of the equations. So six variables were selected first and then the remaining variables could be solved using the equations by iterations. This model had been validated by comparing the predicted load-deformation response to the experimental results of 28 specimens under torsion combined with different ratios of bending and

shear. The behavior predicted by the model is limited to the torque which causes spalling or ultimate, whichever occurs first. The CA-STM can also be used to create interaction surfaces to predict the failure of a member under different ratios of applied torsion, flexure, and shear. The CA-STM can be used to create interaction surfaces to predict the failure of a member under different ratios of applied torsion, flexure, and shear in a good agreement with the ultimate torques from experimental results. Also the interaction surfaces created by the CA-STM can be identified in different load stages other than ultimate, unlike the expressions based on the skew-bending theory.

2.4. Code Provisions for Pure Torsion and Combined Loading

In the United States, most code provisions are based on the pure shear, pure torsion, and pure flexure cases, and bending moments and shear forces are considered primary effects, whereas torsion is regarded as secondary. There is no unified approach to the design of the section subject to combined shear, torsion, and bending moment. This section discusses the development of ACI and AASHTO code provisions and their limitations for pure torsion and combined loading.

2.4.1. ACI Code

Most shear and torsion provisions of the ACI code are developed according to the modified 45°-truss model. Shear resistance is provided by both the concrete contribution (V_c) and the reinforcement contribution (V_s). Torsion design provisions were first introduced into the ACI building code in 1971, assuming that torsional resistance was also provided by concrete and reinforcement. However, the concrete contribution to torsional resistance was removed, and the influence of torsion on shear strength of concrete was disregarded in 1995.

2.4.1.1 Pure Torsion

The design philosophy for torsion in the ACI318-08 building code is based on a thin-walled tube and space truss analogy in which compression diagonal concrete wraps around the tube with closed stirrups and longitudinal bars in the corners, and the tensile contribution of concrete is neglected. The inclined angle of cracks is permitted to be taken as 45˚ for nonprestressed members or lightly prestressed members and 37.5˚ for prestressed members. Both solid and hollow members are considered as tubes in accordance with St. Venant's circulatory shear flow pattern both before and after cracking; the torsional resistance is assumed to be provided by the outer part of the cross-section centered along the stirrups with the contribution of the core concrete cross-section being neglected. Once a reinforced concrete beam has cracked in torsion, the torsional resistance is provided primarily by closed stirrups and longitudinal bars located near the surface of the members as well as the diagonal compression struts. In accordance with the above, ACI318-08 makes the following specific assumptions in torsion design: concrete tensile strength in torsion is neglected; torsion has no effect on the shear strength of concrete; torsion stress determination is based on the closed thin-walled tube with uniform stress distribution and specific thickness, which is known as shear flow; the combined torsional, flexural, and shear strength can be accounted for by adding together longitudinal reinforcement calculated for torsion and flexure and the longitudinal reinforcement calculated for torsion and shear.

Ultimate Torsional Strength - According to St. Venant's circulatory shear flow pattern, the most efficient cross section to resist torsion is tube-shaped which is a 3-D problem involving the shear in an RC 2-D wall element of a hollow tube and the out-of-

wall bending of the concrete struts. In the ACI Code (ACI318-08), the concrete strut bending is neglected and the shear stress required in the tube can be determined from Bredt's (1896) equilibrium equation of a cross section as expressed by

$$q_y = T_u / 2A_0 , \tag{2-41}$$

where q_y is the shear flow stress at yield, T_u is the torsional moment, and A_0 is the lever arm area enclosed by the centerline of the shear flow. The transverse and longitudinal reinforcement are assumed to yield at the ultimate strength. To design the steel reinforcement in a 2-D shear element, combining the three equilibrium equations will give a very simple equation for yield shear flow (Hsu, 1993) as given by

$$q_y = \sqrt{(A_t f_y / s_t)(A_l f_y / s_l)} , \tag{2-42}$$

where f_y is yield stress of transverse and longitudinal reinforcement, A_t and A_l are the area of transverse and longitudinal reinforcement, respectively, and s_t and s_l are the spacing of transverse and longitudinal reinforcement, respectively. The ultimate torsional strength is calculated by substituting the shear flow q_y into Bredt's equation as given by

$$T_u = 2A_0 \sqrt{(A_t f_y / s_t)(A_l f_y / s_l)} , \tag{2-43}$$

which is the essence of the ACI Code provision.

The lever arm area A_0 is formed by sweeping the lever arm of the shear flow one full circle around the axis of twist. The centerline of shear flow was taken by Rausch (1929) to be the centerline of the hoop steel bar, and the corresponding lever arm area is denoted as A_{0h}. However, this definition of area A_{0h} was found to under estimate the torsional strength of lightly reinforced small members by up to 40% and over estimate the torsional strength of heavily reinforced large members by up to 20% (Hsu and Mo 2010). As a

result, the ACI Code provides a simple, albeit approximate, formula for calculating the lever arm area as given by

$$A_0 = 0.85 A_{oh}. \tag{2-44}$$

To provide a more accurate formula for the ultimate torsional strength, it is necessary to take into account the softening of concrete struts in the RC 2-D wall elements of a tube. Under a biaxial tension-compression stress condition, the compressive stress-strain curve of the 2-D elements should be multiplied by a softening coefficient. This softening coefficient is a function of the principal tensile strain (Zhang and Hsu, 1998) and varies from about 0.25 to 0.50. Applying this "softened stress-strain curve" of concrete to the study of reinforced concrete tubes under torsion (Hsu 1990, 1993), the thickness t_d of the shear flow zone and the lever arm area can be determined as

$$t_d = 4T_u / A_{cp} f_c^{'}, \tag{2-45}$$

$$A_0 = A_{cp} - (2T_u p_{cp} / A_{cp} f_c^{'}), \tag{2-46}$$

where A_{cp} is the area enclosed by the outer boundary of the cross section, and p_{cp} is the periphery of the outer boundary. These formulas are stated in the ACI Code Commentary, and the background was stated in a paper by Hsu (1997).

Cracking Torque - The cracking torsional moment is given by

$$T_{cr} = \frac{1}{3}\sqrt{f_c^{'}(MPa)}\left(\frac{A_{cp}}{P_{cp}}\right), \tag{2-47}$$

where P_{cp} is the perimeter of the concrete section and A_{cp} is the area enclosed by this perimeter. The tensile strength of concrete in biaxial tension-compression is taken as $\frac{1}{3}\sqrt{f_c^{'}}$ MPa. Torsional moments can be disregarded in the design and also in the torsion

effect on the flexural and shear strength if the design torsional moment is less than the one quarter of T_{cr}.

Torsion Transverse Reinforcement - Based on the hollow tube analogy, the steel contribution T_s to the torsional resistance is given by

$$T_s = 2A_0 \frac{A_t f_{yt}}{s} \cot\theta, \tag{2-48}$$

where A_t represents the area of one leg of closed torsion reinforcement within a spacing s , f_{yt} is the yielding stress of transverse reinforcement which is limited up to 415 MPa for the concrete crack control, and θ is the angle of cracks which may be taken between 30º and 60º. Thus the required cross sectional area of one stirrup leg for torsion is calculated by

$$A_t = \frac{T_u s}{2\phi A_0 f_{yt} \cot\theta}. \tag{2-49}$$

Minimum Torsional Transverse Reinforcement - The provisions of minimum torsional reinforcement are mainly based on the tests by Hsu, reporting that beams with the same transverse and longitudinal yield strengths should have a minimum volumetric ratio of reinforcement in the order of 0.9 to 1 percent. Hence, for torsional design, the provisions of minimum reinforcement should be around 1 percent.

Torsional Longitudinal Reinforcement - The torsional longitudinal reinforcement can be designed based on the assumption of yielding of the steel as given by

$$A_l = \frac{A_t}{s} p_h \left(\frac{f_{yt}}{f_{yl}}\right) \cot^2\theta, \tag{2-50}$$

where A_l is the total area of torsional longitudinal reinforcement in the cross section, p_h is the perimeter of the center line of the outermost transverse reinforcement, and f_{yl} is the yielding stress of longitudinal reinforcement.

Minimum Torsional Longitudinal Reinforcement - To avoid the brittle failure, a minimum amount of torsional longitudinal reinforcement is required in a member subjected to torsion. The basic criterion for deriving this equation is by equating the ultimate strength T_u to the cracking strength T_{cr}, which results in the following equation

$$A_{l,\min} = \frac{0.42\sqrt{f_c^{'}}A_{cp}}{f_y} - (\frac{A_t}{s})p_h(\frac{f_{yt}}{f_{yl}}), \tag{2-51}$$

where $A_{l.min}$ is the total area of minimum longitudinal steel. To limit the value of $A_{l.min}$, the transverse steel area per unit length, A_t / s, needs not be taken less than $0.17(MPa)b_w / f_{yt}$ and b_w is the width of the cross section. The longitudinal torsional reinforcement required by these two equations should be distributed uniformly along the periphery of the cross section. They should meet the spacing requirement of $s_l \leq 305$ mm and the minimum bar diameter of $d_b \geq s/16$ or 9.5 mm.

2.4.1.2 Pure Shear

Shear Transverse Reinforcement - In the ACI code, the nominal shear V_n is assumed to include the contribution of steel V_s and contributed by concrete V_c. The simplified expression of V_c is given by

$$V_c = 0.166\sqrt{f_c^{'}(MPa)}b_w d, \tag{2-52}$$

where $0.166\sqrt{f_c^{'}(MPa)}b_w d \leq V_c \leq 0.42\sqrt{f_c^{'}(MPa)}b_w d$. The shear force resisted by reinforcement (V_s) is derived from the applied shear (V_u) subtracting the concrete shear contribution (V_c) as expressed by

$$V_s = V_n - V_c. \tag{2-53}$$

When the shear reinforcement perpendicular to the axis of members is used, the shear web reinforcement required is calculated by

$$\frac{A_t}{s} = \frac{V_s}{df_{yt}} = \frac{V_n - V_c}{df_{yt}} \ , \tag{2-54}$$

where d is the distance from extreme compression fiber to centroid of longitudinal tension reinforcement. The spacing s is limited to d / 2 when $V_s \leq 0.33\, f_c^{'}\, (MPa) b_w d$, and d / 4 when $V_s > 0.33\, f_c^{'}\, (MPa) b_w d$.

Longitudinal Shear Reinforcement – Shear force also induces stresses in the longitudinal direction which needs to design longitudinal shear reinforcement. In the ACI Code, this requirement is fulfilled by shifting the bending moment diagram towards the support by a distance of effective depth d so that consideration for the longitudinal shear reinforcement is provided by extending the bending longitudinal reinforcement by a length d.

2.4.1.3 Combined Shear and Torsion

For large hollow box sections, the vertical stress due to shear force and circulative stress due to torsion are additive on one side of the wall, which governs the design under combined shear and torsion as given by

$$\frac{V_u}{b_w d} + \frac{T_u p_h}{1.7 A_{oh}^2} \leq \phi(\frac{V_c}{b_w d} 0.667\sqrt{f_c^{'}(MPa)} \ . \tag{2-55}$$

For solid sections, the ACI Code assumes that the core of the cross section resist the shear stress due to shear force and the outer shear flow zone area resists the shear stress due to torsion. The design equation under combined shear and torsion is provided by

$$\sqrt{(\frac{V_u}{b_w d})^2 + (\frac{T_u p_h}{1.7 A_{oh}^2})^2} \leq \phi(\frac{V_c}{b_w d} 0.667\sqrt{f_c^{'}(MPa)} \ . \tag{2-56}$$

Under combined shear and torsion, the reinforcement provided for torsion must be added with the required shear reinforcement in both longitudinal and transverse directions. The code specifies that transverse stirrups used for torsional reinforcement should be of a

closed form to provide the required tensile capacity across the diagonal cracks of all the faces. Also the code requires the transverse reinforcement to be anchored within the concrete core since the concrete cover tends to spall off under torsional loading. Based on a typical two-leg stirrup, this may be expressed as

$$\frac{A_{V+T}}{s} = \frac{A_{Vt}}{s} + 2\frac{A_{Tt}}{s}, \tag{2-57}$$

where A_{V+T} is the transverse reinforcement under combined shear and torsion, A_{Vt} is the transverse reinforcement required by shear, and A_{Tt} is the transverse reinforcement required by torsion.

2.4.1.4 Combined Torsion and Bending Moment

The axial force, N, resulting from torsion should be resisted by longitudinal reinforcement, which is placed around the perimeter of the section to control concrete crack. In addition, the corresponding longitudinal torsion reinforcement must be added to the flexural reinforcement under the combined torsion and bending moment. In a flexural compression zone, the tensile force produced by torsion is counteracted by the compressive force resulting from the bending moment. This combined effect results in a reduced area of longitudinal torsional reinforcement in the compression zone corresponding to the flexural compressive force. In a flexural tension zone, the tensile force from torsion is additive with the tensile force resulting from the bending moment, which governs the area of longitudinal reinforcement in the compression zone corresponding to the combined torsion and bending moment. The spacing of the longitudinal bars should not exceed 300 mm. In addition, the code permits reinforcement required for torsion to be combined with other forces as long as the area furnished is

equal to the sum of the individually required areas and the most restrictive requirements of spacing and placement are met.

2.4.2. AASHTO LRFD

The AASHTO provisions for shear and torsion are mainly based on the modified compression field theory. Similar to the ACI provisions, the general method in the AASHTO Code allows a concrete and reinforcement contribution to the shear resistance and only a steel contribution to the torsional resistance. Variable concrete contribution stress can be provided depending on concrete strength, prestressing, axial force, bending moment, and the amount of longitudinal reinforcement.

2.4.2.1 Pure Shear

The shear resistance of an RC section is provided by the contribution from concrete, reinforcement, and prestressing tendons and is expressed as

$$V_n = V_c + V_s, \tag{2-58}$$

where V_c is the concrete contribution provided by the concrete, and V_s is the shear contribution provided by the stirrups The concrete contribution to the shear resistance V_c is given by

$$V_c = 0.083\beta\sqrt{f_c^{'}(MPa)}b_v d_v, \tag{2-59}$$

where β is a factor that depends on the ability of concrete to transmit the tensile stress, $f_c^{'}$ is the specified compressive strength of concrete at 28 days, b_v is the effective web width, d_v is the effective shear depth taken as $0.9d$, and d is the distance from extreme compression fiber to the center of tension reinforcement. The contribution of vertical stirrups is given by

$$V_s = \frac{A_v f_{yt} d_v}{s} \cot\theta, \tag{2-60}$$

where A_v is the area of the stirrups within a spacing s, s is the spacing of the stirrup measured along the longitudinal direction, f_{yt} is the yield strength of the stirrups, and θ is the angle of the principal compressive stresses and strains to the longitudinal axis of the members, which also presents the orienting angle of diagonal cracks.

2.4.2.2 Pure torsion

The AASHTO provisions for torsion are based on the hollow tube analogy and disregard the concrete contribution to torsional resistance. Thus the reinforcement contribution T_s to the torsional resistance is given by

$$T_s = 2A_0 \frac{A_t f_{yt}}{s} \cot\theta, \tag{2-61}$$

where A_t is the area of one leg of the closed torsion reinforcement within a spacing s, A_0 is the area enclosed by the shear flow path (taken as 0.85 A_{oh}), and A_{oh} is the area enclosed by the centerline of the outermost closed transverse reinforcement.

2.4.2.3 Combined Shear and Torsion

Shear and torsion causes diagonal cracks in members resulting in brittle failure, which was explained by Rahal and Collins (2003, 2005) in the AASTHO LRFD provisions for this case. The concrete and reinforcement contribution for torsion and shear can be calculated from the factors of β and θ, which depend on the level of strain in the section ε_x and applied shear stress $v / f_c^{'}$ as presented in the following sections.

The level of the longitudinal strain indicator at mid-depth of the section can be taken as 0.001 or conservatively calculated at the level of the centroid of the flexural tension reinforcement as given by

$$\varepsilon_x = \frac{0.5N + 0.5\cot\theta\sqrt{V^2 + \left(\frac{0.9 p_h T^2}{2A_0}\right)} + \frac{M}{d_v} - A_{ps} f_{p0}}{E_s A_s + E_p A_{ps}}, \tag{2-62}$$

where A_s is the area of the nonprestressed reinforcement in the section's flexural tension zone, A_{ps} is the area of prestressed tendons in the section's flexural tension zone, E_s is the modulus of elasticity of nonprestressed reinforcement, E_p is the modulus of elasticity of prestressed tendons, N represents the applied axial load, M is the applied bending moment, and F_{po} is average stress in prestressing tendons when stress in the surrounding concrete is 0.0, and this later term can be conservatively taken as the effective prestress. In addition, the strain indicator must be multiplied by a factor F_e that accounts for the area and modulus of elasticity of concrete in compression when the calculated value is negative (i.e., the section is in compression). This factor is calculated by

$$F_\varepsilon = \frac{E_s A_s + E_p A_{ps}}{E_s A_s + E_p A_{ps} + E_c A_c}, \tag{2-63}$$

where E_c is the modulus of elasticity of the concrete.

The nominal shear stress v for the solid section and the hollow section under combined shear and torsion are calculated by

$$v = \sqrt{\left(\frac{V_n}{b_v d_v}\right)^2 + \left(\frac{T_n p_h}{A_{oh}^2}\right)^2}, \tag{2-64}$$

$$v = \left(\frac{V_n}{b_v d_v}\right) + \left(\frac{T_n p_h}{A_{oh}^2}\right). \tag{2-65}$$

To avoid the over-reinforcement of a section, which results in brittle failure, and to ensure yielding of the transverse reinforcement, this normalized shear stress by the square root of concrete strength ($v/\sqrt{f_c'}$) is limited to less than 0.25.

The angle of diagonal compression strut θ and factor β are calculated by

$$\theta = 29 + 7000\varepsilon_x , \tag{2-66}$$

$$\beta = \frac{0.40}{1+1500\varepsilon_x} \cdot \frac{1300}{1000+s} \ . \tag{2-67}$$

AASHTO provisions suggest that the tensile capacity of the longitudinal reinforcement on the flexural tensile side of the member should satisfy some criteria to avoid premature failure of longitudinal steel with consideration of partial development of the reinforcement. Thus the adequacy of the longitudinal reinforcement for the resisting stresses are given by

$$A_s f_{yl} + A_{ps} f_{ps} \geq \frac{M_n}{d_v} + 0.5N_n + \cot\theta \sqrt{(V_n - 0.5V_s - V_p)^2 + (\frac{0.45 p_h T_u}{2A_0})^2} \ , \tag{2-68}$$

where f_{ps} is the stress level in prestressing tendons, and V_p is the shear force provided by prestressing tendons.

2.4.3. Comparison of Code Provisions

For torsional design, the ACI and AASHTO code provisions disregard the concrete contribution and only consider the longitudinal and transverse reinforcement contribution, which is necessary to be added to the reinforcement required for shear and bending moment. The AASHTO provisions are similar to ACI provisions in most cases. The angle of the compression diagonal is assumed to be 45° for nonprestressed members and as low as 37.5° for the prestressed concrete members in the ACI code. However, in the AASHTO provisions the θ is determined based on the longitudinal strain conditions of the section. In addition, the AASHTO provisions are based on the variable angle truss model, which allows variable concrete contribution sources based on the amount of prestressing, and the longitudinal reinforcement as well as the axial load and bending

moment. The AASHTO provisions are conservative for rectangular sections and their applicability to circular sections of bridge columns is uncertain. The equations for cracking torque and minimum torque that must be considered in design, and the minimum reinforcement requirement and crack width limitation have not been adequately verified by experimental results. The design provisions are based on the sections with under-reinforced or balanced conditions and lacking some inconsistency for pure torsion and combined torsion and shear. Under pure torsion, the ACI code underestimates the cracking torque by as much as 30% for rectangular sections (Koutchkali and Belarbi, 2001; Ghoneim and MacGregor, 2003). The effect of parameters such as size, reinforcement ratios, and delimits for combined loading have not yet been established in design process. Also, no analytical models are yet available to predict concrete spalling behavior under combined torsion, flexure and shear. The behavior of RC columns with different sectional shapes under combined loading should be investigated to validate current design provisions.

2.5. Summary of Review

In this chapter, the background information on experimental and analytical studies of the behavior of RC columns under different loading conditions is presented. First, the literature review is conducted on an experimental program for pure flexure and shear, pure torsion, and various combinations of axial and shear, and torsional bending moment. More experimental results are needed to improve the knowledge of hysteresis response and damage characteristics of RC columns under combined loading. The lack of experimental results imposes difficulties for conducting the nonlinear time history analyses and validating analytical models. Further, no dynamic or pseudo-dynamic test

data are currently available to clarify dynamic behavior of RC columns under combined loading. Second, the analytical models available to predict the behavior under flexure and shear, pure torsion, and a combination of flexure, shear, and torsion are reviewed and summarized, which address the limitations of various models and discuss possibilities for further improvement. The concrete softening due to combined loading and the effectiveness and spalling mechanisms of the concrete cover need be further investigated. Also simplified models must be developed incorporating the interaction of combined loading and confinement of concrete due to transverse reinforcement. Third, ACI and AASHTO provisions were compared in the case of pure flexure, pure shear, pure torsion, and combined loading including torsion.

Chapter 3 Experimental Program

3.1. Introduction

The inelastic cyclic performance of an RC bridge column can be determined by several design parameters such as reinforcement ratio, column shear demand, axial load ratio, column aspect ratio, concrete strength, and cross-sectional shape. Most code provisions restrict these design parameters independently based on the pure shear, pure torsion, and pure flexure cases and there is no unified approach or simplified design guidelines to design the cross section subject to combined shear, torsion, and flexure. In addition, few experimental studies have been performed to investigate the ranges and limitations for these parameters or their effect on the cyclic performance of RC columns under combined loading including torsion. The lack of experimental data also limits the analytical models for seismic performance of RC bridge columns and interactive action relationship under combined loading including torsion.

This chapter provides the details of the experimental program intended to investigate the combined loading effect on the cyclic behavior of RC bridge columns with different cross-sectional shapes. Typically, RC bridge columns vary in diameter from 1.0 m to 2.4 m in the state of California. The columns were designed with a cross-sectional dimension between 500 mm and 1200 mm to obtain a reduced scale of 1/2. All of them were heavily instrumented in order to measure their local and global deformations and internal strain distribution. Among eleven columns, five were designed with a square cross section and six ones were designed with an oval cross section. They were tested under various loading conditions: pure torsion, flexure and shear, and combined flexure, shear, and torsion. The test setup applied cyclic lateral loads on the loading block of each column to

simulate the combined loading including the torsional moment. The columns were heavily instrumented to measure their local and global behavior and their internal strain distribution. This chapter states the experimental objective, column details, and process of fabrication, test setup, instrumentation layout, and loading protocol.

3.2. Objectives

The objective of this experimental study was to investigate the complex behavior of RC bridge columns under combined loading. The main variables being considered are the ratio of torsion to bending moment (T/M), and cross-sectional shape and transverse reinforcement configurations. The experimental data would be used to study the behavior of columns under combined loading with regard to (i) the effects of cross-sectional shapes, transverse reinforcement configurations and combined loading on the torsional and flexural hysteretic responses, (ii) reinforcement strain variations, (iii) plastic hinge characteristics, (iv) strength and stiffness degradation, (v) rotational and displacement ductility, (vi) energy dissipation, and (vii) progression of damage states.

3.3. Test Setup

The test setup was designed to apply various amounts of bending and torsional moments cyclically and constant axial load. A vertical hydraulic jack and two horizontal actuators were used to create the loads. The axial load was applied by hydraulic jack on top of the columns to obtain the specific axial load ratio. Cyclic pure torsion, flexure, and combined flexure, shear and torsion were generated by controlling the two horizontal servo-controlled hydraulic actuators connected to the loading frame and strong wall. The load footing of the column was anchored to a strong floor by means of prestressed Dywidag bars. The test setup drawing is shown in Fig. 3-1.

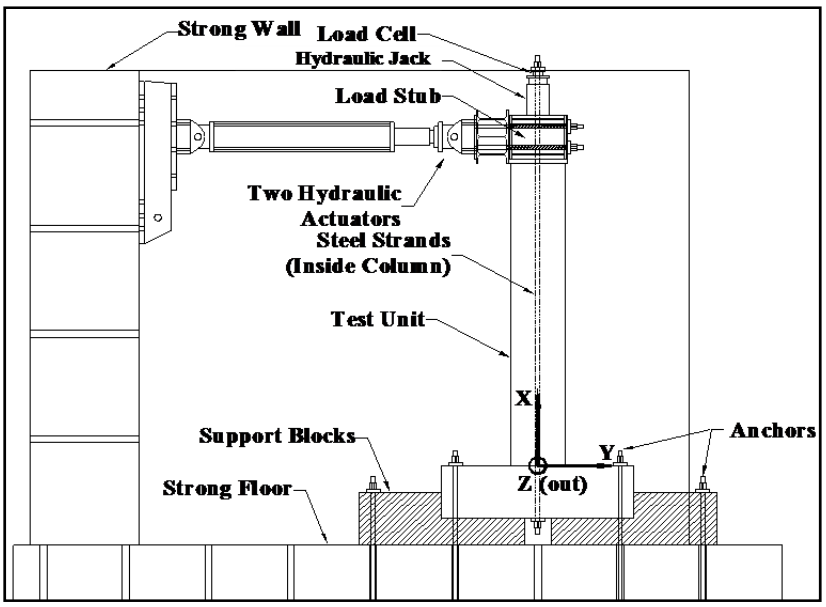

(a) Side Elevation

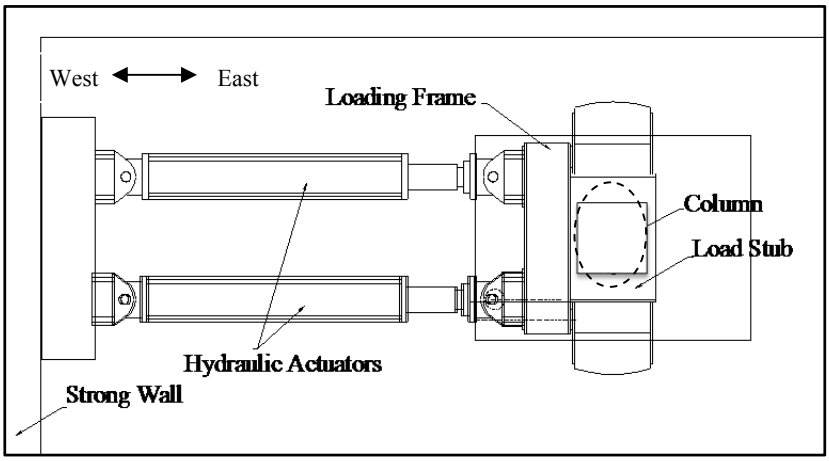

(b) Plan

Fig. 3-1 Test Setup Sketch

3.3.1. Axial Load Application

The hydraulic jack, on the top of the loading block, transferred the load to the column via seven unbonded high-strength prestressing tendons running through a duct in the center of the column and anchored to a plate underneath the column. Typically, the axial load from the superstructure dead weight to bridge columns varies between 5% and 10% of the axial concrete capacity of the column's cross section. A target 7% of the axial

concrete capacity ($0.07f'_cA_g$) was applied to simulate the dead load on the column in a bridge situation (Caltrans, 2004). The unbonded external prestressing in this structural system can be treated as a self-balanced system due to the fact that a relatively broader and thicker high-strength steel plate was used to uniformly distribute loads from the jack to the loading block, and similarly, a thicker and broader high-strength steel plate was used to uniformly distribute the load beneath the load footing. In addition, the tendons ran through the PVC duct that was closer to the neutral axis under flexure and the prestressing strands do not influence torsional behaviors since the outer portion of the concrete column is more effective for torsional resistance. In terms of overall behavior, therefore, the structural differences between unbonded prestressing strands and a hydraulic jack are not significant and also the P-Δ effect can be eliminated to simplifying the analysis since the axial load was always applied along the longitudinal axis through the undonded external prestressing strands.

3.3.2. Shear Force and Flexural Moment Application

Shear force and flexural moments were applied to the columns using two servo-controlled hydraulic actuators. Both actuators were manufactured by the MTS Corporation in the 243.45T series and in the 243.7T series. The 243.45T series actuator had a total stroke capacity of 508 mm, compression capacity of 650 kN, and tension capacity of 445 kN at a maximum oil pressure of 20.7 MPa. The 243.7T series actuator had a total stroke of 712 mm and was capable of 1460 kN in compression and 961 kN in tension at a maximum oil pressure of 20.7 MPa. The actuators were controlled by a FlexTest GT digital controller programmed by the MTS Corporation. The controller is capable of real-time closed-loop control and load protocol function generation. Shear

force and bending moment was generated through horizontally equal forces in the same direction with the two actuators. The actuators used to apply the lateral load had been built with load cells to measure the axial forces produced by the actuator and linear variable displacement transformers (LVDTs) to measure the piston displacements at the loading level.

3.3.3. Torsional Moment Application

Torsional moment was generated through horizontally equal forces in the opposite direction with the two actuators. However, the twist calculated from the displacements measured by the building in LVDTs of the actuators could not be used as an accurate calculation of the rotation in the columns for several reasons: (i) the rotation calculated from the actuator displacement will not be the same as that applied at the center of the column due to connections with the loading frame, and (ii) the stiffness of the actuators was different and resulted in different piston movements. Therefore, we had installed plenty of displacement transducers to the columns at various height levels which were connected to the reference loading frame.

3.3.4. Shear Force and Flexural and Torsional Moment Application

One end of each actuator was connected to the steel loading frame, which was clamped to the column, and the other end of each actuator was connected to a large steel plate post-tensioned to the strong wall as shown in Fig. 3-2. Cyclic combined flexure, shear, and torsion were generated through applying different forces with each actuator determined by the various T/M ratios. In the force control mode, the ratio of T/M was controlled by maintaining the ratio of the forces in the two actuators until the first yielding of the transverse or longitudinal reinforcement. In the displacement control

mode, the displacements of the actuators were adjusted to maintain the desired T/M ratio and ductility level. The actuator forces measured from the load cell were directly used to calculate torsional and bending moments, which are given by

$$T = (P_1 - P_2) \times \frac{d}{2} \ , \tag{3-1}$$

$$M = (P_1 + P_2) \times H \ , \tag{3-2}$$

where T is the applied torsional moment, M is the applied bending moment, P1 and P2 represent the forces in the two actuators, respectively, d is the distance between the centerlines of two actuators (914 mm), and H is the height of the column (3.35 m). The applied load caused internal axial and shear forces as well as torsional and bending moments in the columns. The axial and shear forces and torsional moment all uniformly distribute along with the height of the columns, and the bending moment is linear with the height of the columns as shown in Fig. 3-3.

(a) Square Cross Section (b) Oval Cross Section

Fig. 3-2 Test Setup for Different Cross Sections

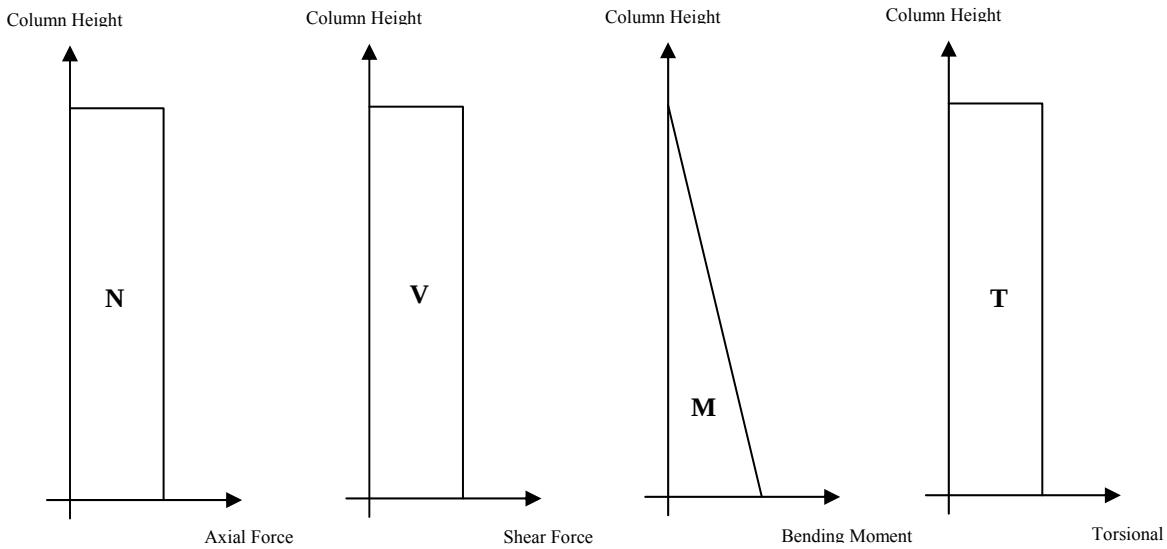

(a) Axial Force (b) Shear Force (c) Flexure (d) Torsion

Fig. 3-3 Internal Axial and Shear Forces, Torsional and Bending Moments Profile

3.4. Test Matrix

3.4.1. Geometry and Reinforcement Configuration

The experimental program was designed to investigate the cyclic behavior of RC bridge columns under combined loading and establish the interaction diagrams between shear forces, flexural, and torsional moments for different cross sectional shapes and transverse reinforcement configurations with specific reinforcement ratios. Eleven columns were tested in two series, one with a square cross section and ties, and another with an oval cross section and interlocking spirals. The geometry and reinforcement configuration details for square and oval columns are shown in Fig. 3-4 and Fig. 3-4 respectively. The square column had a width of 550 mm and a clear concrete cover of 38 mm. The oval column was designed with the cross sectional dimension of 610 mm×915 mm and the clear concrete cover of 25.4 mm. The square and oval columns were designed with an effective height (from the top of the footing to the centerline of the applied forces) of 3.35 m. The aspect ratio was defined as the ratio of effective loading

height and cross section dimension, which was designed as 6 and 5.5 for square and oval columns respectively. Four No.9 bars (28 mm in diameter) and eight No.8 bars (25 mm in diameter) were employed as the longitudinal reinforcement to obtain the longitudinal reinforcement ratio of 2.1%. To achieve a better confinement of the core concrete, rectangular and octagonal No. 3 (9 mm in diameter) rebar was used for transverse reinforcement with spacing of 83 mm and the transverse reinforcement ratio was kept constant at 1.32%. No. 8 bars (25 mm in diameter) were used to provide a longitudinal reinforcement ratio of 2.13%. The two sets of spirals were interlocked by No. 4 bars (12.5 mm in diameter) with a pitch of 70 mm to obtain transverse reinforcement ratios of 1.32%. All the columns and joint details are shown in Fig. 3-3. The nominal strength of concrete for all the columns was 34.5 MPa; however, the concrete strength varied by approximately 5 MPa on the day of testing for some specimens. Table 3-1 provides the parameter details of effective height, reinforcement ratios, aspect ratios, T/M ratios, axial load, and loading directions for all the columns.

3.4.2. Design Requirements

Inelastic response is expected in RC bridge systems subjected to seismic loading according to the seismic design of bridge columns, which requires the formation of plastic hinges at the specific location of the columns. All the columns and joint regions were designed based on the Caltrans Bridge Design Specification (Caltrans, 2004). Brittle failure and inelastic response in the joint should be repressed to limit the inelastic response and force the formation of a plastic hinge in the columns. The longitudinal bars were embedded with the length of approximately 52 times the diameters into the joint,

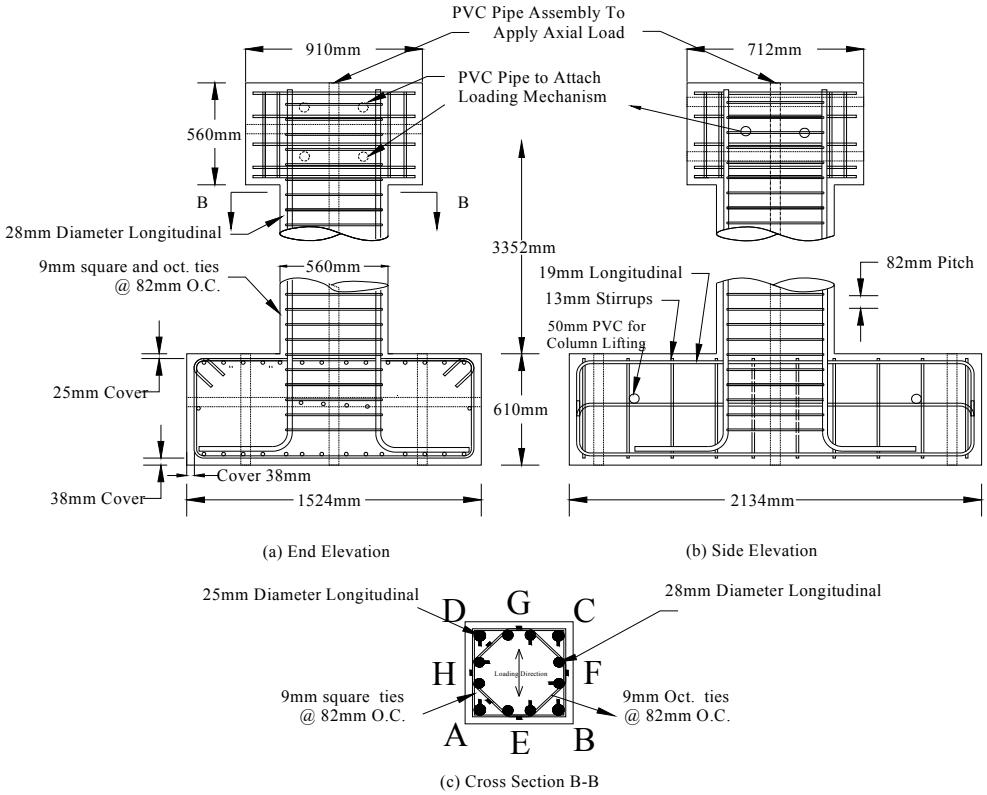

Fig. 3-4 Geometry and Reinforcement Configuration Details for Square Columns

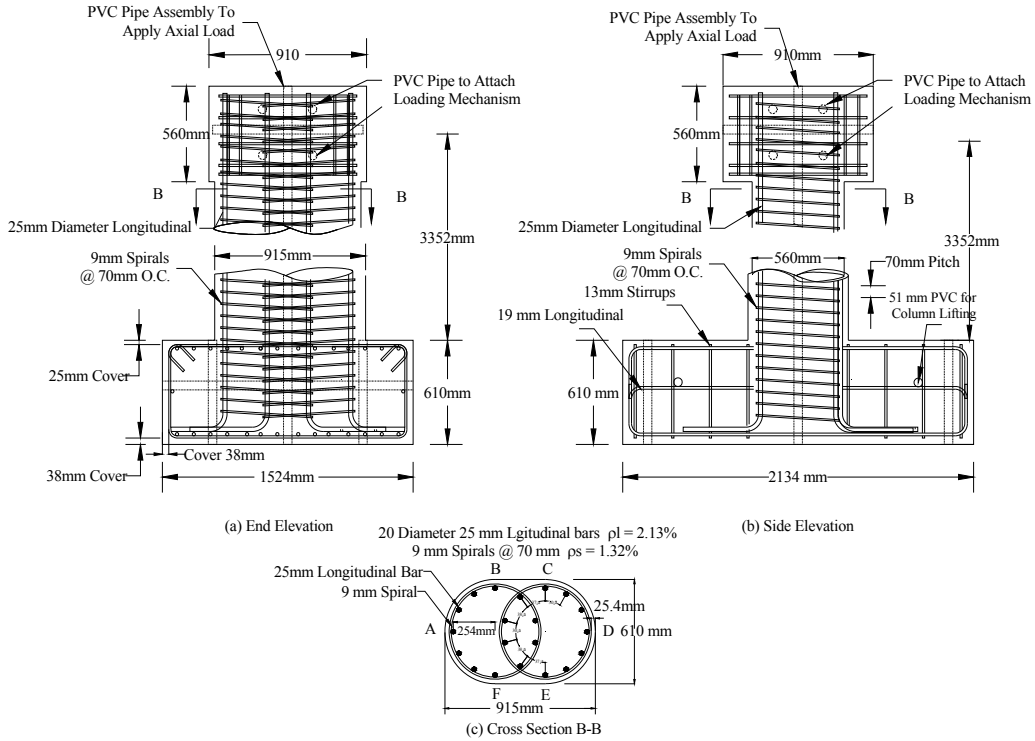

Fig. 3-5 Geometry and Reinforcement Configuration Details for Oval Columns

Table 3-1 Parameter Details of All Columns

Column Name		ρ_l (%)	ρ_t (%)	Ht. (m)	H/D	Axial (kN)	T/M Ratio	Loading Direction
Square	S-H/B(6)-T/M(0)	1.32	2.1	3.35	6	668	0	Uniaxial
	S-H/B(6)-T/M(0.2)	1.32	2.1	3.35	6	668	0.2	Uniaxial
	S-H/B(6)-T/M(0.4)	1.32	2.1	3.35	6	668	0.4	Uniaxial
	S-H/B(6)-T/M(0.6)	1.32	2.1	3.35	6	668	0.6	Uniaxial
	S-H/B(6)-T/M(∞)	1.32	2.1	3.35	6	668	∞	Uniaxial
Oval	O-H/B(5.5)-T/M(0.2)-U	1.32	2.1	3.35	5.5	980	0.2	Uniaxial
	O-H/B(5.5)-T/M(0.6)-U	1.32	2.1	3.35	5.5	980	0.6	Uniaxial
	O-H/B(5.5)-T/M(∞)-U	1.32	2.1	3.35	5.5	980	∞	Uniaxial
	O-H/B(5.5)-T/M(0)-B	1.32	2.1	3.35	5.5	980	0	Biaxial
	O-H/B(5.5)-T/M(0.2)-B	1.32	2.1	3.35	5.5	980	0.2	Biaxial
	O-H/B(5.5)-T/M(0.4)-B	1.32	2.1	3.35	5.5	980	0.4	Biaxial

which was approximately 25% greater than by Caltrans specifications. The footings in the test columns did not follow any standard design since the response of it was not expected to correspond to any actual footing in the field. But they were intended to remain elastic under the full inelastic action of columns. The maximum allowable tensile strains in the main longitudinal reinforcement of the footing were limited to 75% of the yield strain. All the longitudinal and reinforcement in the joint region were using No. 6 bars (19 mm. in diameter) with expected tensile strength of 450 MPa.

The volumetric reinforcement ratios of longitudinal and transverse reinforcement are calculated according to Caltrans Bridge Design Specification (Caltrans, 2004) as shown

in Eq. (3-3) and Eq. (3-4). In addition, the volumetric transverse reinforcement ratio was chosen to satisfy the confinement criteria of CALTRANS (2004) according to Eq. (3-5). This requirement also satisfies the minimum required spiral reinforcement ratio according to AASHTO (1998) and ACI (2008). The volumetric reinforcement ratio can be calculated by

$$\rho_l = \frac{100A_l}{A_g}, \tag{3-3}$$

$$\rho_l = \frac{100A_t \times P_c}{s \times A_c}, \tag{3-4}$$

$$\rho_{l,\min} = 0.45(\frac{A_g}{A_c} - 1)\frac{f_c^{'}}{f_{ty}}(0.5 + \frac{1.25N}{f_c^{'}A_g}), \tag{3-5}$$

where ρ_l is the longitudinal reinforcement ratio, ρ_t is the transverse reinforcement ratio, $\rho_{l,\min}$ is the minimum required transverse reinforcement ratio, N is the applied axial load, f_{ty} is the specified yield strength of transverse reinforcement, $f_c^{'}$ is the specified compressive strength of concrete, A_l is the total area of longitudinal bars for the cross section, A_t is the total cross sectional area of transverse bars, A_c is the confined area enclosed by the centerline of the transverse reinforcement, P_c is the perimeter of confined concrete core section measured with respect to the centerline of transverse reinforcement, and s is the spacing of the transverse reinforcement.

3.4.3. Materials Properties

3.4.3.1 Concrete

The material properties specifications satisfied the requirements for ASTM designations A 615, Grade 60, or A 706. The concrete mix was designed to achieve a full-scale mix to obtain the specified compressive strength, fracture energy, and modulus

of elasticity. All the concrete was supplied by Rolla Ready Mix, a local ready-mix plant. It requires a compressive strength of 34.5 MPa design mix with a maximum aggregate size of 25 mm. Table 3-1 summarized the batch weights provided for each column. The high-range water reducer (super-plasticizer) agitated according to the manufacture's requirements was added to the mix and placed on the forms. The water was added only when required to improve the workability of the concrete. The concrete cylinder specimens were made according to Specification ASTM C 31 (2003) to obtain the compressive strength of concrete. The cylinders were capped according to ASTM C 617 (1998) and tested according to ASTM C 39 (2005). The concrete cylinders that were 152 mm in diameter and 305 mm in height were cast and cured with columns at the same time. They were capped with Rediron 9000 sulfur mortar capping compound manufactured by Global Gilson and tested to failure using a concrete cylinder testing machine with a 2700 kN capacity manufactured by Forney. All the concrete cylinders were tested on the seventh day, the 28th day and the day of testing. Table 3-3 provides concrete material properties for all the columns.

3.4.3.2 Reinforcement

The reinforcement for columns was supplied by Ambassador Steel Corporation, Kansas City, Missouri. The steel coupons of the reinforcement were tested under uniaxial tension using a Tinius-Olsen universal testing machine. The stress-strain curves of the longitudinal and transverse reinforcement are shown in Fig. 3-6 based on three coupons for each cross sectional dimension. The yield stress was measured using the 0.20% offset method, and the modulus of elasticity and peak stress were determined as described in ASTM A370 (2005). The modulus of elasticity, yielding stress and peak strength can be

captured by the test machine. Table 3-4 provides the average measured material properties such as Modulus of Elasticity, Yield Stress (0.20% Offset Method), and Peak Stress.

Table 3-2 Concrete Material Quantities

Material	Quantity
Cement	1366 kg
Fine Aggregate	3415 kg
Coarse Aggregate	4412 kg
Water	550 L
Air entrainment	0.6 L
High-Range Water Reducer	4.3 L

Table 3-3 Concrete Material Quantities

Concrete Material Properties		Compressive Strength f'_c, MPa	Modulus of Rupture f_{cr}, MPa
Square Column	S-H/B(6)-T/M(0)	36.3	3.73
	S-H/B(6)-T/M(0.2)	40.5	3.68
	S-H/B(6)-T/M(0.4)	40.4	3.64
	S-H/B(6)-T/M(0.6)	40.5	3.65
	S-H/B(6)-T/M(∞)	34.6	3.57
Oval Column	O-H/B(5.5)-T/M(0.2)-U	37.2	3.65
	O-H/B(5.5)-T/M(0.6)-U	36.2	3.55
	O-H/B(5.5)-T/M(∞)-U	35.3	3.42
	O-H/B(5.5)-T/M(0)-B	40.4	3.78
	O-H/B(5.5)-T/M(0.2)-B	40.3	3.71
	O-H/B(5.5)-T/M(0.4)-B	34.3	3.43

Table 3-4 Reinforcement Material Properties

Measured Property	Nominal Reinforcement Size			
	#3 (Ties)	#4 (Spirals)	#8 (Longitudinal Reinforcement)	#9 (Longitudinal Reinforcement)
Modulus of Elasticity (GPa)	211	229	205	216
Yield Stress (0.20% Offset Method) (MPa)	454	455	512	515
Peak Stress (MPa)	720	715	718	752

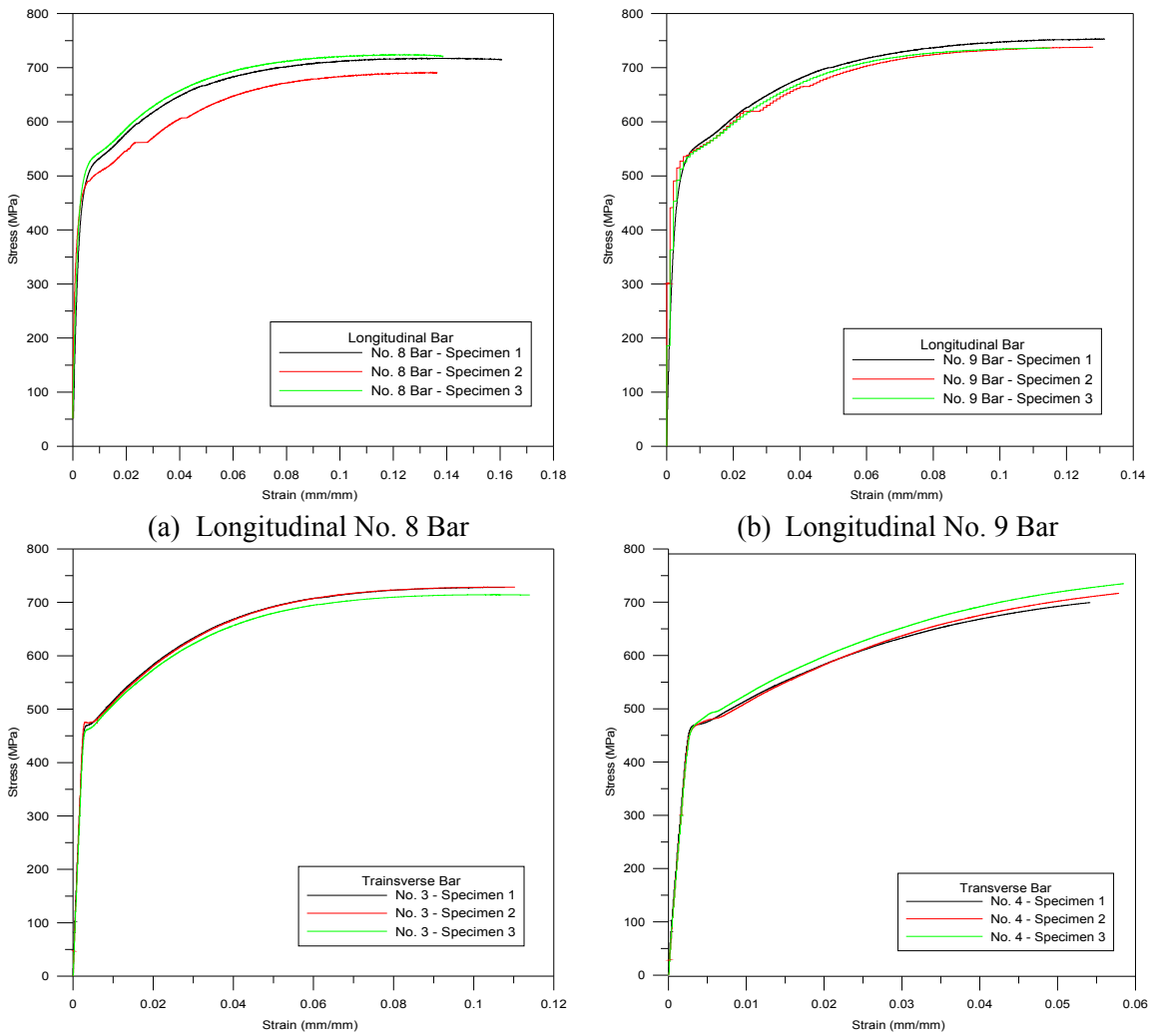

(a) Longitudinal No. 8 Bar (b) Longitudinal No. 9 Bar

(c) Transverse No. 3 Bar (d) Transverse No. 4 Bar

Fig. 3-6 Stress Strain Curves for Steel Reinforcement

3.5. Instrumentation

3.5.1. String Transducers System

All the columns were heavily instrumented to measure their global and local response, and their internal strain distribution. A system of string transducers was used to measure horizontal displacement at multiple locations along the height of the columns. The instrument pairs were located at six different levels along the height of the column to obtain the lateral displacement and rotation as shown in Fig. 3-7. Lateral displacement was calculated by averaging the horizontal displacements measured by the string

transducer pairs; rotation was calculated by taking the difference between the string transducer pairs divided by the distance between the transducer pairs as shown in Eq. (3-7). In addition, a system of LVDT rosettes was installed at the bottom of column as shown in Fig. 3-8, where the plastic hinge was expected to occur under combined loading, to obtain deformation components for calculating the curvature, shear, and principal strains. The lateral displacement and rotation can be expressed as

$$\Delta_{avg} = \left[\frac{(\Delta_1 + \Delta_2)}{2} \right], \tag{3-6}$$

$$\theta_{twist} = \arctan\left[\frac{(\Delta_1 - \Delta_2)}{d} \right], \tag{3-7}$$

where Δ_{avg} is the average horizontal displacement, θ_{twist} is the rotation due to torsion, Δ_1 and Δ_2 are the displacements measured by the string transducer pairs. For the pure torsion case, they would be nearly equal in values with opposite signs. For the flexure and shear case, they would be nearly equal in values with the same sign. For the combined loading case, their values and signs would vary depending on T/M ratios.

3.5.2. Average Strain Measurement

A system of LVDT rosettes was used to obtain the average displacement across the cracks in the expected plastic hinge region. The LVDT rosettes were comprised of several instruments with maximum displacement up to +/- 25.4 mm to measure and calculate the distributed strain in the horizontal, vertical, and diagonal directions. The LVDT instruments were fitted to an aluminum tubing system, which was connected to two threaded bars precast into each column. The gauge length of the vertical and horizontal instruments is 355.6 mm and the gauge length of the diagonal instrument is 502.8 mm. Six LVDTs were connected to each other to form a square LVDT rosette; and

three rosette systems were installed on the western face at different levels. Fig. 3-8 shows the system of LVDT rosettes. Six distance readings can be taken for each square LVDT

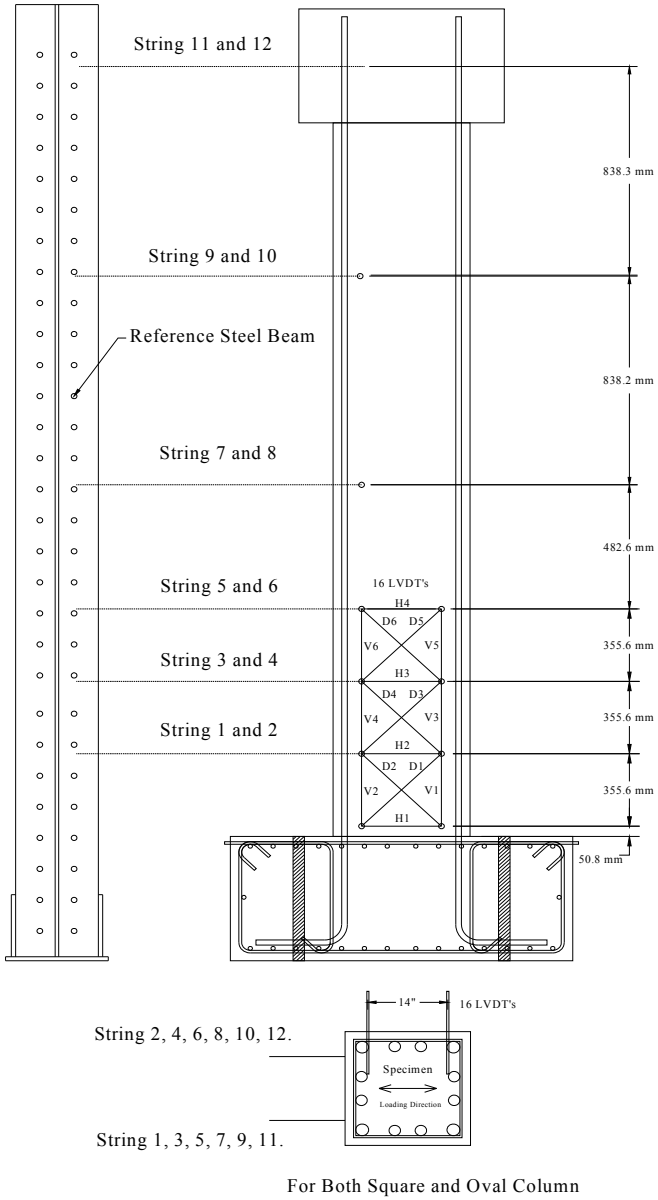

Fig. 3-7 Layout of String Transducers

rosette. For each square LVDT rosette layer, two transverse strains are calculated by the average of the distance readings 1 and 2; two longitudinal strains are calculated by the average of distance readings 3 and 4. And two-diagonal distance readings 5 and 6 can be used to complete the Mohr's circle of strains. So the strains ε_x (along the x-axis), ε_y (along

the y-axis), ε_{45} (at axis inclined 45° to x directions) can be recorded by LVDTs rosettes. The engineering shear strain, ε_{xy}, and the principal strains, ε_1 and ε_2, were calculated from the recorded strains. The calculated strains, the distance reading divided by the original gauge length, should be taken as the average strain in the concrete and reinforcement since the distance reading stretched across several cracks. In addition, the strain values cannot be considered as accurate, and they are considered as approximate value due to the sensitivity of distance reading to the crack development occurring over the gauge length.

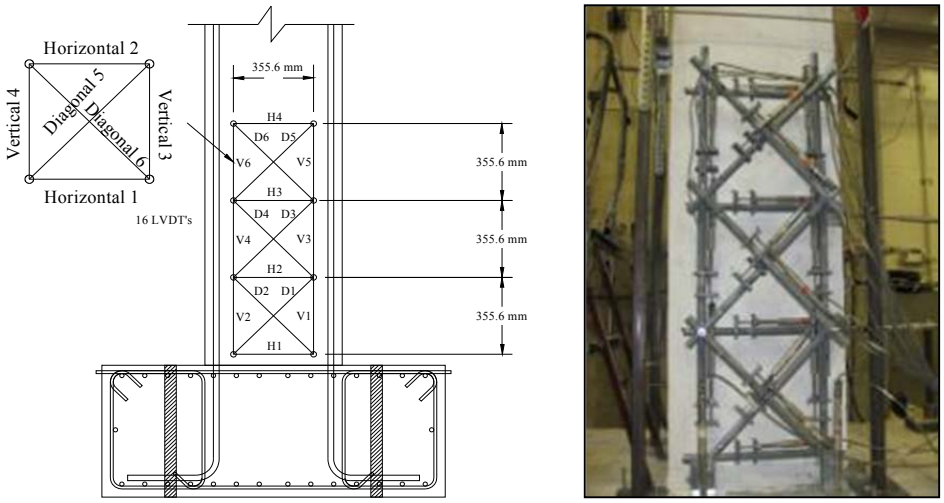

Fig. 3-8 System of LVDT Rosettes

3.5.3. Reinforcement Strain

Electric resistance foil strain gauges, made of Constantan foil with 120 ohm resistance and 6.4 mm gauge length, were used to measure the strains in the transverse and longitudinal reinforcement. About 70 gauges were installed at various locations along all the columns. The strain gauges were applied on the longitudinal reinforcement after the surfaces of reinforcement were polished and cleaned with a specific process as shown in Fig. 3-9. The typical layouts of strains gauges on the longitudinal and transverse reinforcement are shown in Fig. 3-10 and 3-11 respectively for square and oval columns.

More strain gauges were applied on the portion of columns where the plastic hinge and damage zone were expected to occur along the column.

(a) Application of Strain Gauges after Reinforcement Surface Punishment and Clean

(b) Strain Gauges Cover and Wire Connection

(c) Strain Gauges on Reinforcement

Fig. 3-9 Strain Gauges Application on Reinforcement

Gauge No.	Gauge Profile							
11	A			D				
10	A	B	C	D				
9	A			D				
8	A	B	C	D				
7	A	B	C	D	E		G	
6	A	B	C	D	E		G	
5	A	B	C	D	E		G	
4	A	B	C	D	E	F	G	H
3	A	B	C	D	E	F	G	H

46 Longitudinal Gauges

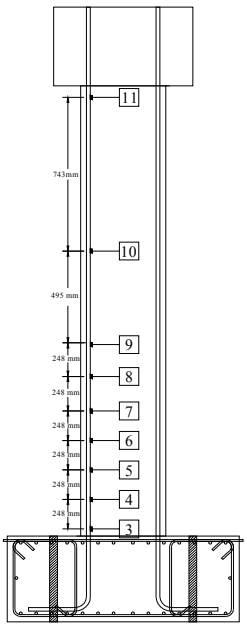

Gauge No.	Gauge Profile					
10		F		H		
9		F		H		
8		F		H		
7		F		H		
6		F		H	1	2
5		F		H	1	2
4	E	F	G	H	1	2
3	E	F	G	H	1	2

28 Transverse Gauges

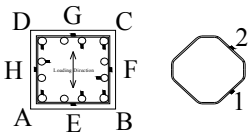

(a) Flexure and Shear

Gauge No.	Gauge Profile							
11	A	B	C	D				
10	A	B	C	D				
9	A	B	C	D	E	F	G	H
8	A	B	C	D				
7	A	B	C	D	E	F	G	H
6	A	B	C	D				
3	A	B	C	D	E	F	G	H

32 Longitudinal Gauges

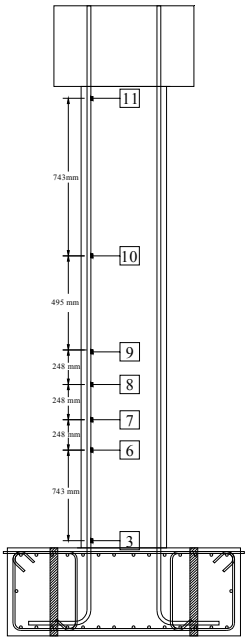

Gauge No.	Gauge Profile					
11		F		H		
10	E	F	G	H		
9	E	F	G	H	1	2
8	E	F	G	H		
7	E	F	G	H	1	2
6	E	F	G	H		
3	E	F	G	H	1	2

32 Transverse Gauges

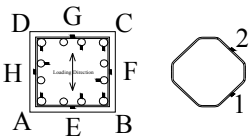

(b) Torsion

Gauge No.	Gauge Profile							
11	A			D				
10	A	B	C	D				
9	A			D				
8	A	B	C	D				
7	A	B	C	D	E	E	G	E
6	A	B	C	D				
5	A	B	C	D	E	F	G	H
4	A	B	C	D				
3	A	B	C	D	E	F	G	H

42 Longitudinal Gauges

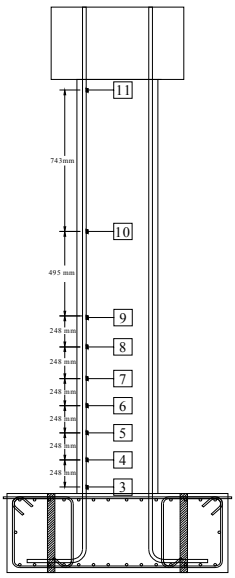

Gauge No.	Gauge Profile					
11		F		H		
10	E	F	G	H		
9		F		H		
8	E	F	G	H	1	2
7						
6	E	F	G	H	1	2
5						
4		F		H	1	2
3	E	F	G	H	1	2

30 Transverse Gauges

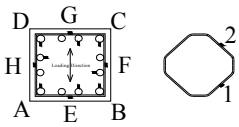

(c) Combined Loading

Fig. 3-10 Typical Strain Gauge Locations of Square Columns

Gauge No.	Gauge Profile			
10	A			
9	A			
8	A	C	E	
7	A	C	E	
6	A	C	E	
5	A	C	E	
4	A	C	E	
3	A	C	E	
2				
1				
	A D	B C	E F	

34 Longitudinal Gauges

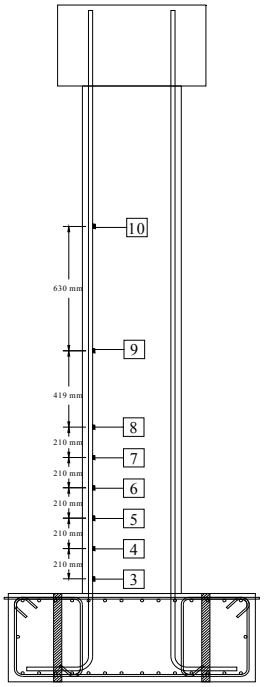

Gauge No.	Gauge Profile			
10	A			
9	A			
8	A	C	1	
7	A			
6	A	C	1	
5	A	C	1	
4	A	C	1	
3	A	C	1	
	A D	B C	1 2	

38 Transverse Gauges

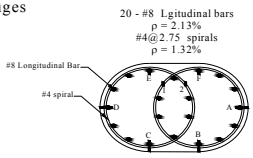

(a) Flexure and Shear

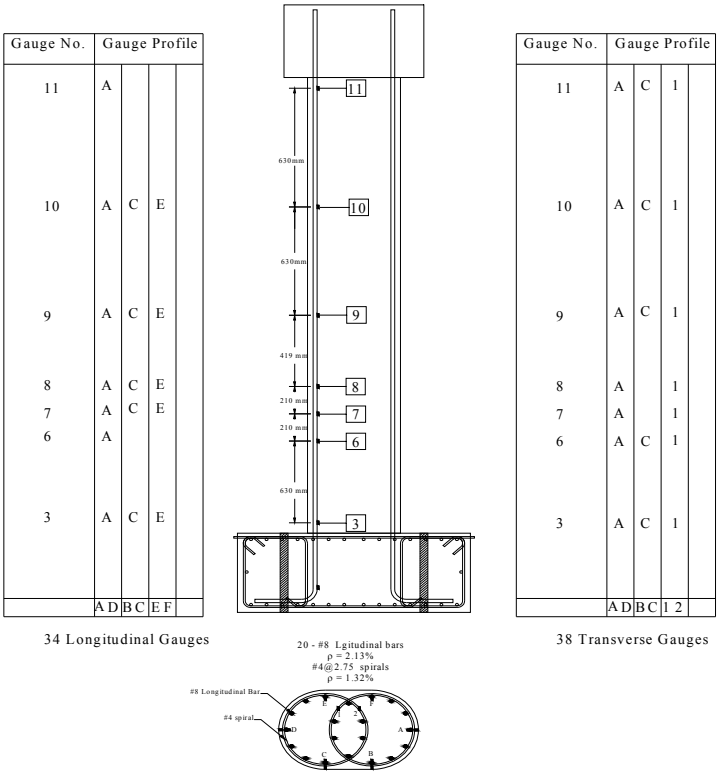

(b) Torsion

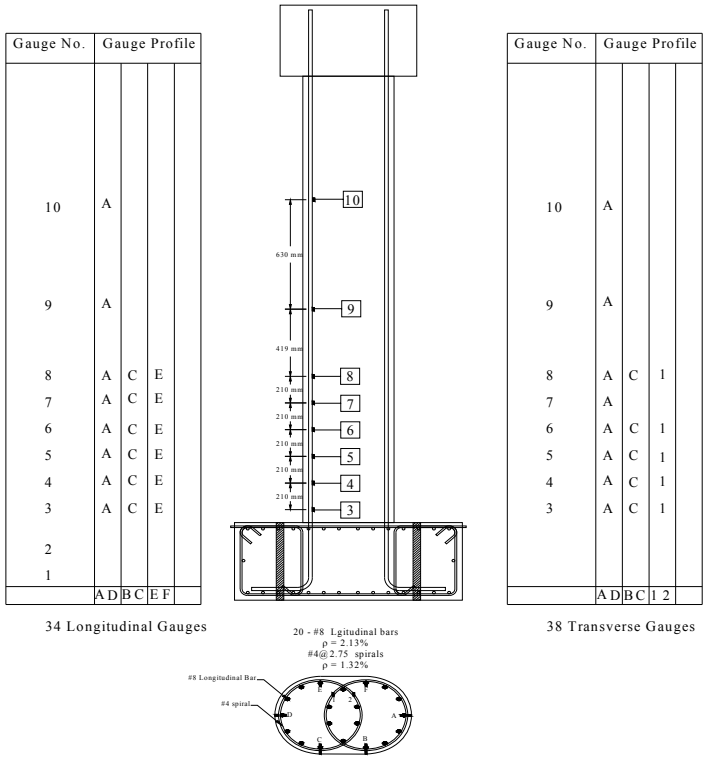

(c) Combined Loading

Fig. 3-11 Typical Strain Gauge Locations of Oval Columns

3.5.4. Load Cell

The axial load was measured by placing a tension load cell between the jack and the top chucks with the capacity of 890 kN. The load cell was connected to a data acquisition system to collect and record the axial load.

3.5.5. Data Acquisition (DAQ)

Two conditioner cabinets A and B were adopted as the data acquisition (DAQ) system to collect the electronic instruments' data. There are a total of 128 channels in total used to condition and amplify the voltage signals, which were then sent to DAQ, converted to a digital signal, then scaled and recorded by a personal computer. The data recording cabinet contained analog-to-digital boards to convert the voltage into a digital signal. Once converted, the digital signal was sent to a Dell precision 340 personal computer with 2.20 GHz and 120 GB hard disk capacity. Measurement and Automation Explorer (MAX) and LABVIEW version 7.1 were used as programs to convert, scale and record data. In MAX, the data signal was assigned to a scale file to convert the signal from voltage measurements into load, displacement, and strain data for the respective instruments and strain gauges. The LABVIEW was used to scan and record the data. The scale files in MAX were created by calibrating the instruments and strain gauges. The load cells were calibrated with a micrometer fitted on an LVDT calibration block, and the strain gauges were calibrated with a strain gauge calibration box. The 128 channels on the conditioner cabinets A and B were divided into different channel groups for recording the signal from load cells, strain gauges, LVDTs, and string transducers as shown in Fig. 3-12.

(a) Two conditioner cabinets A and B

(b) Channel Connection

Fig. 3-12 Data Acquisition (DAQ) System

3.6. Column Manufacturing Process

All the columns were fabricated at the High Bay Structures laboratory at Missouri S&T. Fig. 3-13 presents the typical assembly of reinforcement cages. The slotted wooden spacer was assembled on the base supporting frame at the correct height to locate the longitudinal reinforcement. The longitudinal and transverse reinforcement were assembled on the slotted wooden spacer and supporter with the pre-manufactured tie wires. The locations of strain gauges were marked and ground on the reinforcement before the reinforcement cages were assembled. Then the bottom foundation mat was placed on the strong floor and the foundation bottom reinforcement cages were fabricated on top of the mat as shown in Fig. 3-14. The assembled column reinforcement cage was anchored into the center of the foundation bottom reinforcement cage, then the top foundation reinforcement and shear legs were installed as shown in Fig. 3-15. The reinforcement cages for the top loading block was assembled with proper shear legs connecting the stirrups and extended longitudinal reinforcement of columns as shown in Fig. 3-16. The PVC tubes were installed inside the cages to generate holes for connecting the loading frame to the column and transverse guide frames for lateral prestressing. The formwork of foundations included a top cover to resist the upward pressure created by the

column concrete pouring and steel frame around the side formwork to strengthen it as shown in Fig. 3-17. All the columns were poured at once from the top working platform. The formwork was removed after three days of concrete pouring. The processes of concrete pouring and formwork removing were presented in Fig. 3-18. Auxiliary specimens for concrete compression tests, splitting tension tests and modulus of rupture tests were fabricated during the concrete pour as shown in Fig. 3-19.

(a) Side Elevation (b) Plan View

Fig. 3-13 Fabrication of Reinforcement Cage

(a) Foundation Mat (b) Foundation Reinforcement Cages

Fig. 3-14 Fabrication of Foundation Reinforcement Cage

Fig. 3-15 Completed Foundation Reinforcement Cage

Fig. 3-16 Formwork and PVC Layout of Top Loading Block

(a) Side Formwork for Foundation

(b) Completed Formwork for Foundation

Fig. 3-17 Fabrication of Foundation Reinforcement Cage

(a) Foundation Concrete Pour and Vibrating

(b) Placed Foundation Cover with Clamps

(c) Lifting Concrete Bucket to Top Platform

(d) Dump Concrete and Vibrating

(e) Completed Concrete Pour

(f) Removing Formwork

Fig. 3-18 Concrete Pour for Foundation and Column and Formwork Removing

Fig. 3-19 Auxiliary Specimens for Concrete Material Testing

3.7. Loading Protocol

All the tests were conducted in combination with load and displacement control modes. Tests under flexure and shear were conducted in load control mode until the first yielding of the longitudinal bars. During the load control mode, the load was applied at intervals of each 10% of the yielding load with respect to the first yielding of the longitudinal bar defined as F_y. The displacement corresponding to the yielding load was taken as yielding displacement Δ_y. Displacement ductility, μ_Δ, is calculated from the ratio of displacement at any instant cycle during loading to the yielding displacement. Hence, the horizontal ductility corresponding to yielding of the first longitudinal reinforcement is defined as displacement ductility of one (μ_Δ=1). Ductility control was conducted after ductility one. The average pushing force of two actuators was defined as positive load to cause a positive bending moment, and the average pulling force of two actuators was defined as negative load to cause a negative bending moment.

Under pure torsion, the column was also tested at intervals of each 10% of the yielding of the first transverse reinforcement defined as yielding torque T_y. The rotation corresponding to the yielding torque was taken as yielding rotation θ_y. Rotation ductility, μ_θ, is calculated from the ratio of rotation at any instant cycle during loading to the yielding rotation. The rotation ductility corresponding to the yielding rotation was defined as rotation ductility one (μ_θ=1). After the yielding torque, the tests were performed switching to displacement control mode until the failure of the columns at high ductility levels. The clockwise torque was taken as positive; and the counterclockwise was taken as negative.

Under combined loading, the load control was conducted at intervals of each 10% of the yielding load with respect to the first yielding of reinforcement. The T/M ratios were controlled to be constant by adjusting the forces of two actuators before the yielding load. After the load control mode, the results were analyzed to compute the yield displacement and rotation for the next ductility control. In the displacement control mode after the yielding torque, three cycles were applied for each ductility level until the failure of the column to assess the degradation of column strength and stiffness. The T/M ratio for each cycle was maintained to be constant according to the calculated piston movements during the testing. There were some difficulties in maintaining the desired T/M ratios during loading and unloading cycles, and there was some difference in the stiffness of the actuator systems. However, the ratios were within the acceptable range before the peak bending moment or the peak torque was reached. It is impossible to maintain the constant T/M ratios after any of the peak bending moments and peak torque was attained due to the different strength degradation intensity of them. The loading protocol and control flow chart are shown in Fig. 3-20 and Fig. 3-21.

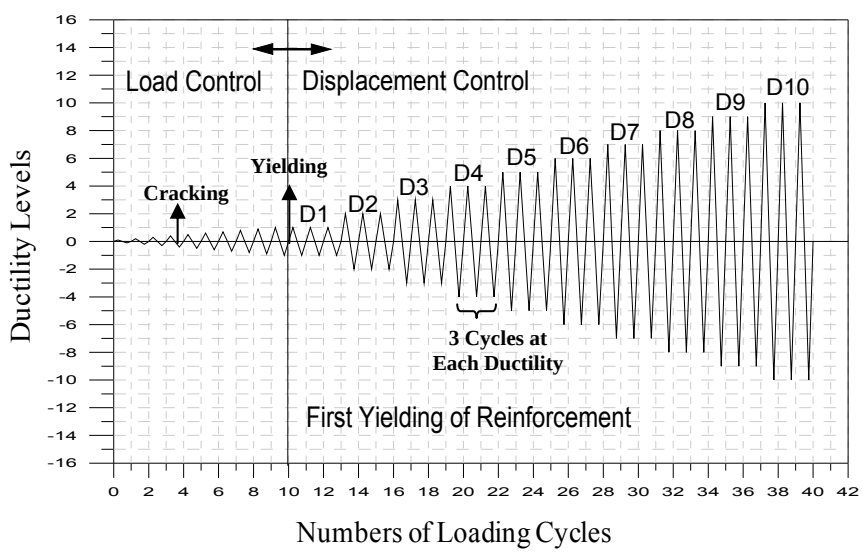

Fig. 3-20 Loading Protocol for Columns

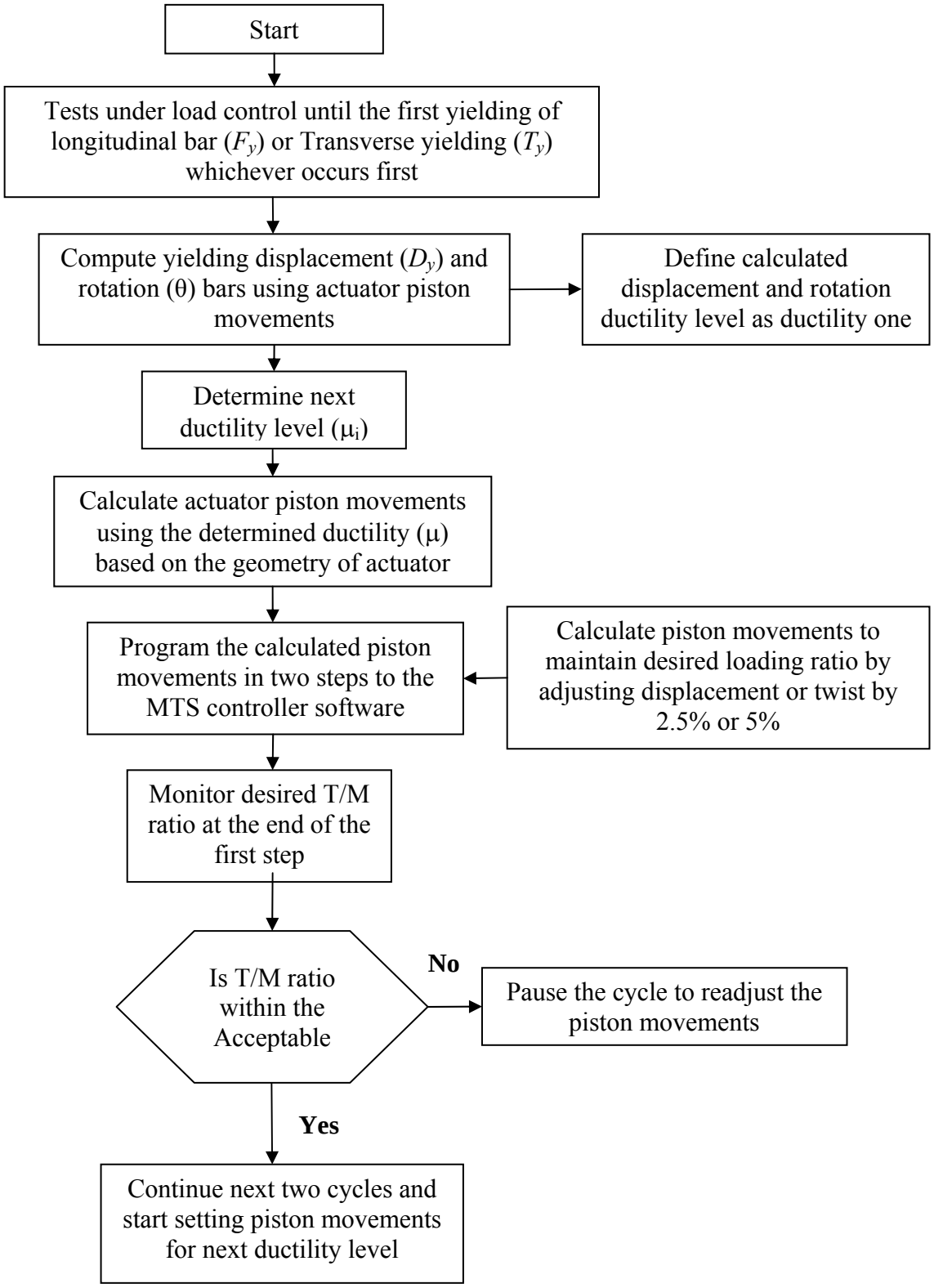

Fig. 3-21 Loading Control Flow Chart for Specimens

Five square columns were loaded under combined loading at various T/M ratios of 0, 0.2, 0.4, 0.6, and ∞, respectively. The lateral combined loading was applied along the west-east direction as shown in Fig. 3-22 (a). However the lateral combined loading for oval columns could be about a weak axis, strong axis or any axis between them with an angle of θ' as shown in Fig. 3-22 (b) and (c). One of the oval columns was loaded under pure torsion, which was not related to the strong or weak axis; two of the oval columns were tested about weak axis at T/M ratios of 0.2 and 0.6; and three of oval columns were tested about the axis, between the strong and weak axis, at T/M ratios of 0, 0.2, and 0.4 to consider the biaxial combined loading. The angle of θ' was chosen as 35° to expect the longitudinal reinforcement along the "BC' or 'EF' side and 'A' or 'D' side to yield simultaneously under this biaxial combined loading, which was recommended by the experimental results of the oval columns from the shaking table test (Saiidi et al. 2007).

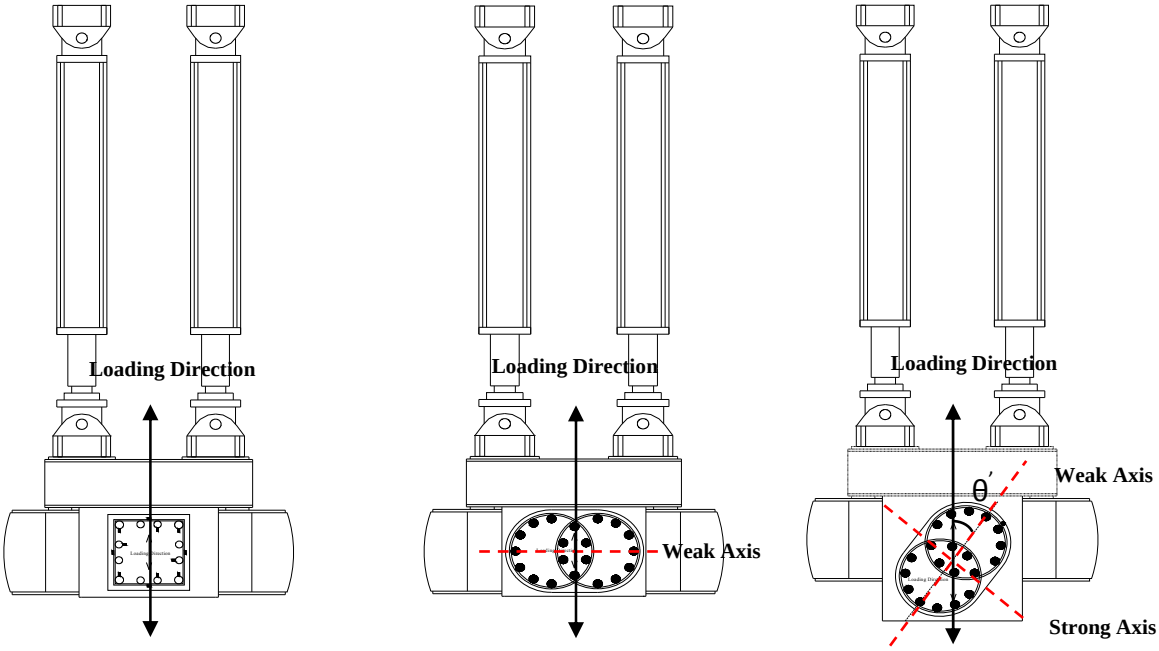

(a) Square Columns Under Combined Loading

(b) Oval Columns Under Uniaxial Combined Loading about Weak Axis

(c) Oval Columns Under Biaxial Combined Loading about 35° Axis

Fig. 3-22 Loading Direction of Square and Oval Columns under Combined Loading

3.8. Concluding Remarks

Column testing was intended to explore the hysteretic response under strength and stiffness degradation, plastic hinge zone, energy dissipation, damage progression; and interaction diagram under combined shear force, flexural and torsional moments at constant axial compression. Two servo-controlled hydraulic actuators were used to apply the cyclic flexural and torsional moments; one jack was placed on the top of column to apply for the axial load. The columns were heavily instrumented to capture the local and global behavior and strain distribution. A complete description of column fabrication, test setup, and loading protocol was provided. Test results for all columns are explained in the next chapter.

Chapter 4 Experimental Results and Discussion

4.1. Introduction

This chapter provides the experimental data analysis results and observed behavior of RC bridge columns under flexure, shear, and torsional loads. The experiment data discussion covers lateral load-displacement and torsional moment-twist hysteresis curves, plastic hinge location, concrete cover spalling, and damage progression under combined loading. The effects of cross sectional shape, transverse configurations, and T/M ratios on the strength and stiffness degradation, locking and unlocking efficiency, failure modes and energy dissipation characteristics under combined loading will be highlighted. It also addresses the deformation distribution along the columns, the variation in longitudinal and transverse strains, as well as interaction diagrams between torsional and bending moments.

4.2. Experimental Results and Damage Observations

In this section, the overall lateral-displacement and torque-twist hysteresis curves are presented according to different cross sectional shapes and loading conditions. Also it provides a general description of damage progression by describing each category of damage. The observed damage characteristics can be categorized as follows:

1. *Flexure cracking* - Horizontal flexural cracks occurred prior to inclined torsional or shear cracking on columns under flexure and shear, and combined flexure, shear, and torsional loads. The flexural cracking extended with an inclined angle on the side faces at a higher ductility level. Also the spacing of the newly formed cracks decreased at higher displacements and stabilized after the yielding of the longitudinal bar, leading to localized concrete cover spalling.

2. *Inclined cracking* - Inclined cracks can be caused by both torsion and shear, which formed prior to flexural cracking under pure torsion and after flexural cracking under combined flexure and torsion. The spacing of inclined cracks decreased with increasing displacement/twist demands under combined flexure, shear, and torsion. And it will develop spirally around all faces of the column with a specific angle depending on various loading conditions.
3. *Longitudinal reinforcement yielding* - Longitudinal reinforcement strain was detected using the strain gauge readings. Yielding of the longitudinal reinforcement was observed in the lateral displacement or torsional rotation response under flexure and shear, pure torsion, and under combined flexure, shear, and torsion. The timeline of longitudinal reinforcement yielding was mainly affected by various T/M ratios.
4. *Transverse reinforcement yielding* - Transverse reinforcement strain was detected by closely monitoring the strain gauges on the transverse reinforcement during testing. Yielding of the transverse reinforcement was noticeable in the torsional rotation or lateral displacement response under pure torsion, flexure and shear, and combined flexure, shear, and torsion. The transverse reinforcement yielding could occur prior to or after longitudinal reinforcement yielding, which was also mainly determined by various T/M ratios.
5. *Concrete cover spalling* - The onset of spalling of the cover concrete depends on a number of factors such as the cover-to-lateral dimension ratio, transverse reinforcement ratio, the axial load ratio, the aspect ratio, sectional shape, and stress distribution. For the flexure-dominated failure mode, concrete cover spalling started at the bottom of the column due to the maximum bending moment. For columns under

pure torsion, concrete cover spalling started at the middle of the column and developed towards the top and bottom with the increasing torsional moment. Under combined loading, the spalling zone increased from the bottom portion of the column with an increase in the T/M ratio.

6. *Complete concrete cover spalling and exposure of reinforcement* - The reinforcement would be exposed after complete loss of the concrete cover, which introduced significant transverse strain and facilitated the easy buckling of longitudinal reinforcement.
7. *Concrete core crushing* - After concrete cover spalling and transverse reinforcement yielding, the increasing applied load could be resisted by the diagonal concrete compression struts as a compressive element and by reinforcements as a tension element similar to a truss mechanism. The concrete compression strut started crushing once the compressive stress exceeded the compressive strength of the core concrete. The crushing of the diagonal strut occurred at the ultimate damage limit state representing the excessive damage of the RC member.
8. *Reinforcement buckling and rupture* - After severe spalling of concrete cover and significant degradation of the concrete core, the longitudinal reinforcement was exposed without any confinement and protection from concrete. The longitudinal bars then began to buckle due to the cyclic compressive or tensional force from combined loading, which was observed in the plastic-hinge zone. Excessive transverse strain caused transverse reinforcement rupturing within the buckled length of the longitudinal reinforcement. The lateral stiffness from the transverse reinforcement decreased after it was ruptured, which permitted the other longitudinal reinforcement

to buckle over a longer length. Rupturing of the longitudinal reinforcement occurred after significant buckling, which resulted in significant strength and stiffness degradation, and overall column failure.

4.2.1. Square Columns

Based on the literature review in Chapter 2, the large scale experimental data are limited on the cyclic behavior of rectangular or square bridge columns under combined loading including torsion. Therefore five square columns were tested under a cyclic combined loading with various T/M ratios to study the cyclic performance of RC square columns. The interactive effects of combined loading with torsion and flexure on the flexural and torsional hysteretic load-deformation response, strength and stiffness degradation, and progression of damage zone are discussed in the following sections.

4.2.1.1 Cyclic Torsion

Investigating the behavior of members subjected to pure torsion is necessary for generalizing the analysis of a structural member under combined loading. However, only very few studies have been reported on the behavior of RC sections under pure torsion due to the fact that torsion usually occurs in combination with other actions in structural members. The torsional strength of RC members depends mainly on transverse and longitudinal reinforcement ratios, the sectional dimensions, transverse reinforcement configurations, and the concrete strength. This column was tested under pure torsion without a lateral load. Square and octagonal ties were both used to obtain adequate confinement to the core concrete and enhance the strength and ductility characteristics. The torsional moment-twist hysteresis response is plotted in Fig. 4-1. Under pure torsion, inclined torsional cracks ˚ started to develop near mid-height of the column, when loaded

to 60% of the yielding torsional moment as shown in Fig. 4-2 (a). The torsional moment-twist curve is approximately linear before cracking and thereafter becomes nonlinear with a decrease in the torsional stiffness. The post cracking stiffness decreased proportionally with an increase in the cycles of loading due to the inclined torsional cracks development. The transverse reinforcement near mid-height of the column first reached the yield strain at the torsional moment of 260 kN-m and twist angle of 1.72˚ as shown in Fig. 4-2 (b), which was defined as rotation ductility one. Meanwhile the first concrete cover spalling occurred around mid-height of column at ductility one and extended along the column. The peak torsional moment of 332 kN-m was achieved in the ductility three with concrete cover spalling extending to the half height of the column as shown in Fig. 4-2 (c). The longitudinal bars on sides A and C remained elastic until they reached a ductility level of 4.5 with significant contribution to the load resistance from the dowel action. At higher cycles of loading, a torsional plastic hinge formed near the mid-height of the column due to significant concrete cover spalling and concrete core crushing. The complete concrete cover spalling, severe concrete core crushing, longitudinal reinforcement buckling, and transverse reinforcement rupturing in the plastic hinge zone led to the overall failure of the column at ductility eight as shown Fig. 4-2 (d). The rotational capacity at ductility eight was achieved at the twist angle of 17.8˚. Typical damage progression of the column under pure torsion was demonstrated in Fig. 4-2. It indicated that torsion failure mode was significantly different from the flexure failure mode, which was concentrated near the middle of the column height instead of at the typical flexural plastic hinge zone at the base of column.

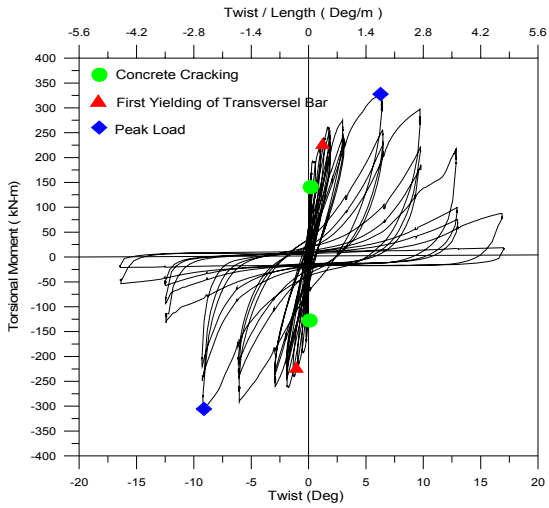

Fig. 4-1 Torsional Hysteresis Curves under Pure Torsion

(a) Cracking (b) Yielding (c) Peak (d) Final failure

Fig. 4-2 Damage Progression and Failure Modes under Pure Torsion

4.2.1.2 Cyclic Flexure and Shear

The column was tested under flexure and shear from lateral loading. The lateral load-displacement hysteresis of the square column tested under flexure is plotted in Fig. 4-3. The column first exhibited horizontal flexural cracking near the bottom around 400 mm from the base on side 'AB' and 'CD' when cyclical load reached 50% of the lateral yielding load F_y as shown in Fig. 4-3 (a). These the flexural cracks extended to form new inclined cracks on the two sides of the column at a higher location. The flexural stiffness degraded at post-cracking stage, which was milder than torsional stiffness degradation.

The longitudinal reinforcement on side 'AB' and 'CD' yielded first around 200 mm above the base at the bending moment of 558.4 kN-m and the displacement of 21.5 mm, which was defined as displacement ductility one. The spacing of the new cracks decreased at higher displacements and stabilized after the yielding of the longitudinal reinforcement as shown in Fig. 4-3 (b). The concrete cracking led to localized concrete cover debonding. Subsequently, the concrete cover started to spall at about 2% drift due to interfacial failure on the plane between the concrete cover and the concrete core, when it was loaded to displacement ductility three. The peak lateral load of 277.2 kN was achieved in displacement ductility 4.5 and the height of concrete cover spalling also increased with the increasing displacement ductility level as shown in Fig. 4-3 (c). After the concrete cover spalled at the bottom of the column, the square and octagonal transverse reinforcement strain increased and remained elastic until a ductility level of eight, which provided more confinement to concrete core. The failure of the column began with the formation of a flexural plastic hinge around a height of 360 mm from the base of the column, followed by core concrete degradation due to crushing. The column finally failed by the buckling and rupturing of the longitudinal reinforcement on the compression side during the last cycle of ductility 12 with a drift of about 8%, as shown in Fig. 4-3 (d). The typical progressive damage of the square column is shown in Fig. 4-3.

4.2.1.3 Cyclic Combined Flexure, Shear and Torsion

The above test results of columns under pure flexure and pure torsion can be used as benchmarks to analyze the behavior of columns under combined flexure, shear, and torsion. To investigate the combined loading effect and flexure-torsion interaction feature, three square columns were tested under combined flexure, shear and torsion by

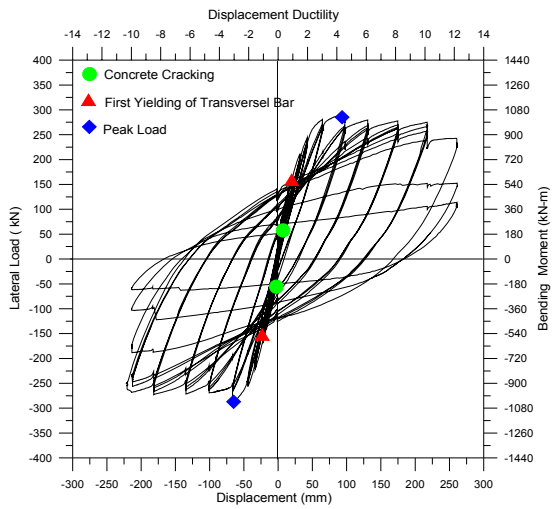

Fig. 4-3 Flexural Hysteresis Curves under Flexure and Shear

(a) Cracking (b) Yielding (c) Peak (d) Final failure

Fig. 4-4 Damage Progression and Failure Modes under Flexure and Shear

maintaining T/M ratios of 0.2, 0.4, and 0.6, respectively. One column was tested at a T/M ratio of 0.4 to establish a point in the interaction diagram by yielding the longitudinal and transverse reinforcement simultaneously. During the above two tests, the yielding bending moment under flexure and shear was achieved at M_y = 558.4 kN-m; and the yielding torsional moment under pure torsion was achieved at T_y = 220 kN-m. Thus the ratio of M_y/T_y was calculated to be 0.39, which was taken as about 0.4 to investigate the sequence of longitudinal and transverse reinforcement yielding. The other two columns were tested at a lower T/M ratio of 0.2 and a higher T/M ratio of 0.6 respectively to

determine the strength and stiffness degradation and failure modes at different torsion effect levels.

The flexural and torsional hysteresis behaviors of the columns under the T/M ratio of 0.2 are shown in Fig. 4-5 and Fig. 4-6. For column under T/M ratio of 0.2, inclined cracks with 26˚ to 28˚ first occurred near the bottom of the column at a smaller loading level 40% of the yielding load. The cracks developed upwards along the column with more loading cycles as shown in Fig. 4-7 (a). Torsional and flexural stiffness degradation was observed with an increased loading level after concrete cracking. Longitudinal reinforcement on side 'AB' and 'CD' yielded first, around 280 mm above the base, at the lateral load of 184.6 kN and the torsional moment of 123.3 kN-m corresponding to the displacement of 29.0 mm and twist of 0.55˚, which was taken as ductility level one. The concrete cracking was distributed along the whole height of the column at the yielding stage as shown in Fig. 4-7 (b). The concrete cover started spalling at peak load level with a lateral load of 240.7 kN and torsional moment of 190.5 kN-m as shown in Fig. 4-7 (c). The displacement and twist corresponding to peak load level were 60.6 mm and 1.5˚, which was at achieved at ductility level two. The transverse reinforcement strain increased gradually after the concrete cover spalled at the bottom of the column, and remained elastic until it reached a ductility level of 4.5 with a drift of 5.6%. The column failed by longitudinal reinforcement buckling and rupturing on side 'AB' and 'CD' and significant concrete core degradation, where the plastic hinge was formatted as shown in Fig. 4-7 (d). The typical damage progression is shown in Fig. 4-7.

The flexural and torsional hysteresis behaviors of the columns under a T/M ratio of 0.4 are shown in Fig. 4-8 and Fig. 4-9. For the column under the T/M ratio of 0.4, inclined

cracks with 32˚ to 36˚, which was more inclined compared to the one under the T/M ratio of 0.2, first occurred at the low portion of the column when loaded to 40% of the yielding load. The cracks developed spirally along the column due to a larger torsional moment being applied as shown in Fig. 4-10 (a). Flexural stiffness experienced more degradation compared to the column under smaller a T/M ratio of 0.2, which was caused by the twist of the column from the torsion effect. Longitudinal reinforcement on side 'AB' and 'CD' and transverse reinforcement on side 'BC' yielded simultaneously around 450 mm above

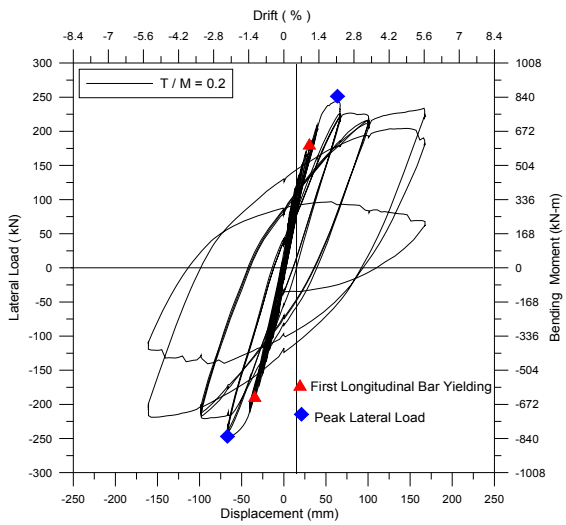

Fig. 4-5 Flexural Hysteresis Curves under T/M Ratio of 0.2

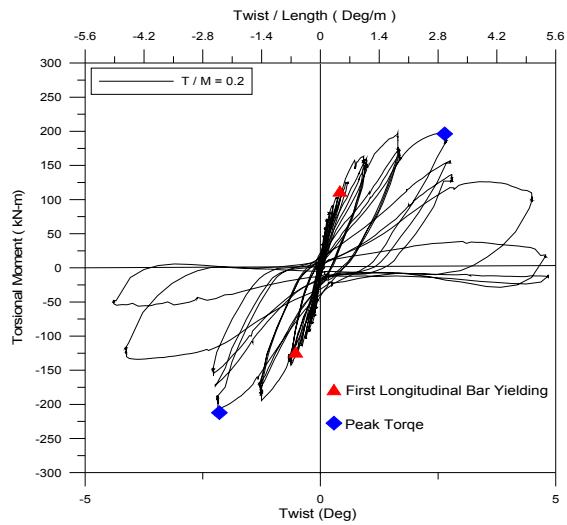

Fig. 4-6 Torsional Hysteresis Curves under T/M Ratio of 0.2

(a) Cracking (b) Yielding (c) Peak (d) Final failure

Fig. 4-7 Damage Progression and Failure Modes under T/M Ratio of 0.2

the base. The transverse strain on side 'BC' was always larger than other sides due to the larger additive shear stress from torsion and shear. In addition, the T/M ratio of 0.4 was defined as the balanced T/M ratio since this combined ratio caused the reinforcement to yield at the same load level in the longitudinal and transverse direction, which was an important parameter to discern flexural and torsional failure mode. At ductility level one, the yielding lateral load was at 143 kN corresponding to the displacement of 29.7, and the yielding torsional moment was at 205.3 kN-m corresponding to the twist of 0.93˚. The column experienced severe flexural and torsional concrete cracking along the whole height of the column at the yielding stage as shown in Fig. 4-10 (b). The concrete cover started spalling right after the reinforcement yielding and developed from the bottom to the higher portion with more loading cycles, which indicated significant torsional stiffness degradation. The concrete cover spalled up to one-third the height of the column at peak load level with a lateral load of 220.2 kN and a torsional moment of 253.6 kN-m as shown in Fig. 4-10 (c), which was at observed at ductility level two. At the same time, the longitudinal reinforcement was exposed and the concrete core started crushing. The displacement and twist corresponding to the peak load level were 62.9 mm and 2.1˚, which were both larger compared to the one under the T/M ratio of 0.2. The plastic hinge was formatted with reinforcement buckling and rupturing and concrete core crushing as shown in Fig. 4-10 (d). The typical damage progression is presented in Fig. 4-10.

The flexural and torsional hysteresis behaviors of the columns under a T/M ratio of 0.6 are shown in Fig. 4-11 and Fig. 4-12. For column under T/M ratio of 0.6, inclined cracks of 38˚ to 42˚ first occurred near the mid-height of column when loaded to 40% of the yielding load. The inclined angle of crack was almost close to 45˚ compared to the one

under pure torsion due to the higher T/M ratio. The inclined torsional crack well developed spirally along the column as shown in Fig. 4-13 (a).

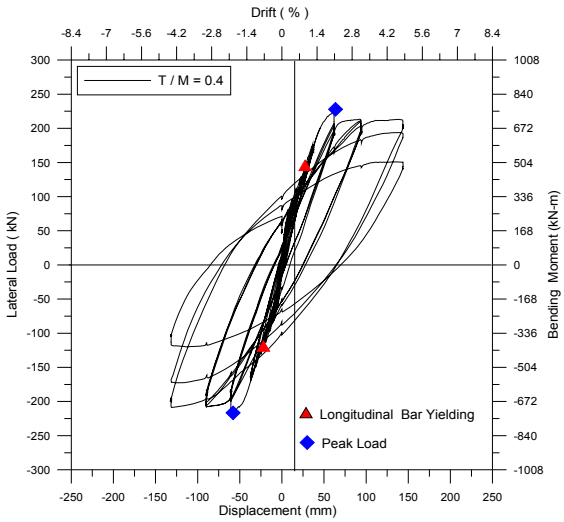

Fig. 4-8 Flexural Hysteresis Curves under T/M Ratio of 0.4

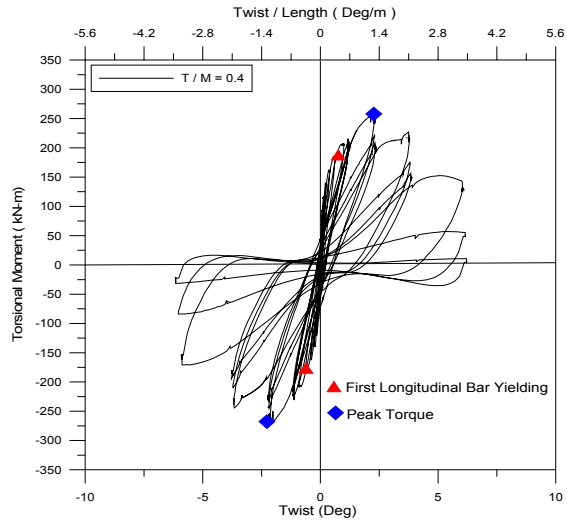

Fig. 4-9 Torsional Hysteresis Curves under T/M Ratio of 0.4

(a) Cracking (b) Yielding (c) Peak (d) Final failure

Fig. 4-10 Damage Progression and Failure Modes under T/M Ratio of 0.4

Flexural stiffness significantly degraded after this torsional cracking due to a high level of torsion. Transverse reinforcement on side 'BC' yielded first at the height of 900 mm above the base of the column, which was considered as ductility one with the yielding lateral load of 106 kN corresponding to the displacement of 24.9 mm, and the yielding torsional moment was at 238.8 kN-m corresponding to the twist of 2.1˚. At this load

level, two sets of diagonal concrete cracking were formed in a perpendicular direction around all the faces of the column, which generated amounts of small diamond-shaped concrete pieces between the cracks similar to the pure torsion case as shown in Fig. 4-13 (b). The concrete cover also started debonding at the yielding stage along with significant torsional stiffness degradation. The concrete cover spalled up to half the height of the column at peak load level as shown in Fig. 4-13 (c). However, the peak torsional moment of 312.8 kN-m was obtained in ductility two and the peak lateral load of 210.1 kN was lagged to ductility three. The displacement and twist corresponding to the peak load level were 81.4 mm and 4.38˚. At same time, longitudinal reinforcement buckling and concrete core crushing were also observed. The plastic hinge formatted at around 1000 mm above the base of the column with significant concrete cover spalling up to two-thirds the height of the column, reinforcement buckling, and concrete core totally crushing at final failure as shown in Fig. 4-13 (d). The typical damage progression is presented in Fig. 4-13.

Compared to test results for the pure flexure and torsion, it can be observed that the ultimate lateral load and displacement capacity of the columns significantly decreased

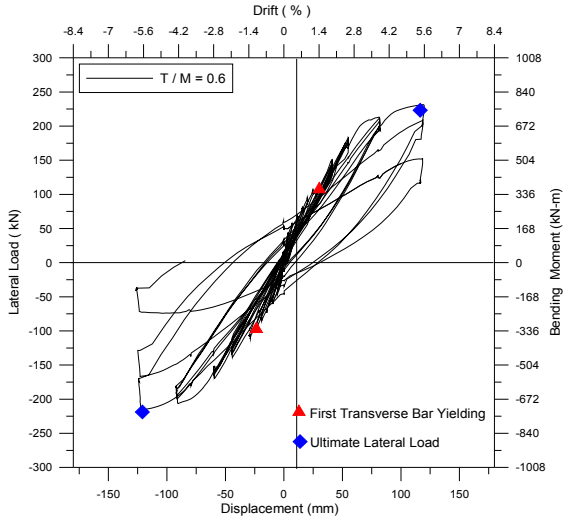

Fig. 4-11 Flexural Hysteresis Curves under T/M Ratio of 0.6

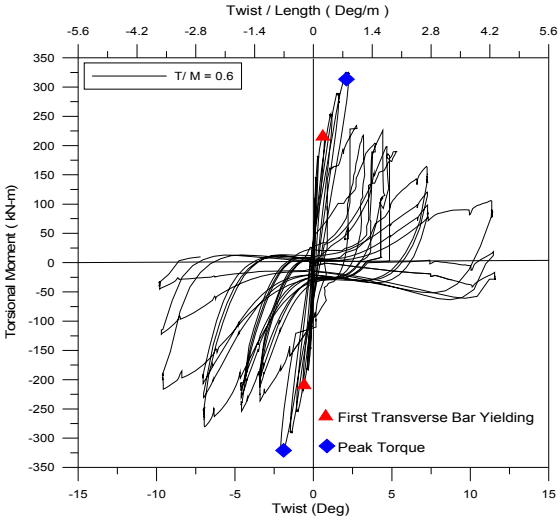

Fig. 4-12 Torsional Hysteresis Curves under T/M Ratio of 0.6

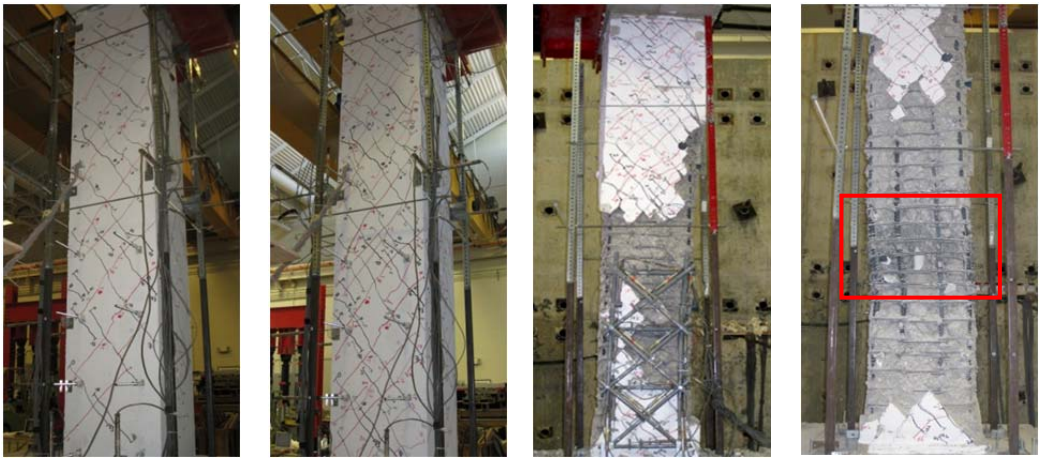

(a) Cracking (b) Yielding (c) Peak (d) Final failure

Fig. 4-13 Damage Progression and Failure Modes under T/M Ratio of 0.6

with more levels of torsion or increasing T/M ratio; and the increase of the bending moment led to the deterioration of the torsional capacity and the ultimate twist. So then the flexural and torsional capacities in both strength and deformation can be considerably affected by combined loading including torsion. Additionally the strength and stiffness degradation were observed with increasing load cycles at each ductility level.

The concrete cover spalling distribution was identical to various T/M ratios. The spalled region of the column under a T/M ratio of 0.6 first happened at around the mid-height portion, and then developed upward and downward going through almost the entire column, which is similar to the column under pure torsion. The spalled region of the column under a T/M ratio of 0.4 distributed approximately up to half the height of the column from the footing, while it was about one-third the height for the column under the T/M ratio of 0.2. The longitudinal reinforcement yielded before the transverse bar for the column under the T/M ratio of 0.2; while the longitudinal and transverse bars of column under the T/M ratio of 0.4 yielded at the same loading level, which is the balanced condition from a design point of view. For the columns under combined loading at T/M ratios of 0.2 and 0.4, flexural dominant failure formatted from severe combinations of

inclined cracks under combined actions and were followed by reinforcement yielding, concrete cover spalling, concrete core crushing, and failed with buckling and rupturing of the longitudinal reinforcement as shown in Fig. 4-7 and Fig. 4-10. However, the column under a combined loading at T/M ratios of 0.6 failed in the torsional dominant mode as the torsional plastic hinge formed near the lower mid-height of the column due to significant concrete spalling and severe core degradation and finally the longitudinal bars buckled and were extremely distorted as shown in Fig. 4-13.

4.2.2. Oval Columns

Seismic performance of the RC bridge column is largely controlled by the level of confinement provided by transverse reinforcement. Interlocking spirals are commonly used in non-circular RC bridge columns due to the fact that doubly interlocking spirals can provide more effective confinement than rectilinear hoops or ties and also simplify the column fabrication. The California Department of Transportation (Caltrans) "Bridge Design Specifications (BDS)" and "Seismic Design Criteria Version (SDC)," and the American Association of State Highway and Transportation Officials (AASHTO) "Recommended LRFD Guidelines for the Seismic Design of Highway Bridges" are the only codes in the United States that state provisions for the design of columns with interlocking spirals. However, the provisions are addressed mainly by a combination of single spirals and constructability detailing consideration.

Previous experimental and analytical studies were conducted to investigate the effect of main design parameters on flexural and shear behavior such as transverse reinforcement ratios, horizontal distance between the centers of interlocking spirals,

configuration of longitudinal reinforcement, and cross section shape and variation of axial load ratios.

Tanaka and Park (1993) first tested three columns with interlocking spirals under cyclic horizontal loading, and one column with rectangular hoops and cross ties for comparison. The test results indicated that the transverse reinforcement ratio value adequately effective for the confinement of core concrete could be reduced significantly by using interlocking spirals other than rectangular hoops and cross ties. The authors concluded that the limiting distance between the centers of interlocking spirals and extra crossties connecting the spirals would result in sufficient interlocking confinement to core concrete and adequate shear transfer between the spirals. Buckingham and McLean (1994) performed an experimental study on eight columns under constant axial load and cyclic lateral displacement. The author found that the increased spiral overlap percentage did contribute to dissipating energy and prevented significant flexural stiffness degradation and the interlocking spirals performed better a lot better than the ties despite a 50% less amount of transverse reinforcement. Tsitotas and Tegos (1996) conducted a test on 21 members under monotonic and cyclic loading with single spiral, interlocking spirals or multiple spirals apart from each other. The test results indicated that the strength of the complex section was found to be approximately equal to the sum total of the strength of the two single cyclical overlapped sections and also the structural elements of a rectangular section with interlocking spirals had given an excellent performance from a mechanical behavior point of view. In the past decades, just a few experimental studies (Benzoni et al. 2000, Mizugami 2000, Wehbe and Saiidi 2000, and Kawashima et al. 2008, Belarbi and Li 2010) have been performed to investigate the

monotonic and cyclic elastic behavior of the RC columns with interlocking spirals under flexure with and without axial compression. In addition, the research efforts for interaction between flexure, shear and torsion for RC bridge columns was limited on the circular and square RC bridge columns (Hsu, H.L. and Wang 2000, Otsuka et al. 2004, Tirasit and Kawashima 2005, Belarbi et al. 2008, Suriya Prakash et al. 2008, Qian Li and Belarbi 2010).

A careful review of related literature for RC bridge columns under various loading conditions indicated that there have been few experimental studies reported on the seismic behavior of oval RC columns with interlocking spirals under pure torsion, combined flexure, shear and torsion. Accordingly, the knowledge of the interaction effect between bending and torsional moments and biaxial flexure effect on the behavior of the RC bridge columns with interlocking spirals is also limited. Therefore six oval columns with interlocking spirals were tested under pure cyclic torsion, uniaxial and biaxial pure flexure as well as combined cyclic flexure and shear and torsion with various T/M ratios. The effects of combined loading on hysteretic torsional and flexural response, damage distribution and progression, ductility characteristics, stiffness degradation, and energy dissipation with respect to various T/M ratios will be discussed in the following sections. Also the uniaxial and biaxial loading effects under combined loading are highlighted. Finally, interaction diagrams were established based on the experimental results.

4.2.2.1 Cyclic Torsion

There is no experimental study on the cyclic behavior of RC oval sectional bridge columns with interlocking spirals under pure torsion according to the previous research review. The torsional hysteresis curve of the specimen under pure torsion in this study is

presented in Fig. 4-14. The torsional moment-twist hysteretic curve was approximately linear before the concrete cracking at the level of 70% yielding torsional moment, which was defined as a cracking torsional moment of 408.8 kN-m; thereafter it became nonlinear with a decrease in the torsional stiffness since the outer concrete played an important role in torsional resistance. The inclined torsional cracks occurred first at the mid-height of the column and continued to develop along the inclination of the spiral reinforcement with 44˚ to 45˚ as the more loading cycles were applied as shown in Fig. 4-15 (a). The transverse reinforcement near the upper mid-height of the column first reached the yielding strain when the torsional moment of 525.0 kN-m was achieved with a corresponding twist of 1.76˚, which was defined as rotation ductility one. Meanwhile, two perpendicular sets of severe diagonal shear cracks resulted in the first concrete spalling at mid-height of the column with a big torsional crack as shown in Fig. 4-15 (b). The concrete cover spalling continued to develop upward and downward to the whole column with an increased loading level as shown in Fig. 4-15 (c).

At post-yielding stage, the transverse reinforcement provided effective confinement to the concrete core; and also the two spirals were locked together during the negative cycles of twisting, which enhanced the confinement of the spirals to the concrete core contributing to the strength of it. The two interlocking spirals were unlocked in the positive cycles of twisting, which resulted in a reduction of the confinement effect on the concrete core. As a result, the torsional moment on the negative cycles was much higher than the positive cycles of loading, especially at higher ductility levels due to the extra confinement effect from the locking actions of interlocking spirals. This locking and unlocking effect can be reflected in the asymmetric nature of the torsional hysteresis

curve for positive and negative cycles as observed in Fig. 4-14. At ductility level three, the peak torques in positive and negative loading cycles were achieved at 756.7 kN-m and 809.9 kN-m, respectively. The twisting angles corresponding to peak torque in positive and negative cycles were at 7.53˚ and 6.49˚, which indicated that the locking effect of the spirals increased torsional stiffness with less rotation deformation. After peak torque, the significant concrete cover spalling caused the formation of the torsional plastic hinge at the upper mid-height of the column which is different from the typical flexural plastic hinge distribution. Dowel action of longitudinal bars did contribute to the torsional loading resistance at high ductility levels, which led to the yielding of the longitudinal reinforcement after rotation ductility level 4.5. In addition, the longitudinal reinforcement located within the interlocking region transferred the shear stress from spiral to spiral by dowel action considerably contributing to the resisting torsional load at high ductility levels. The concrete core started crushing at rotation ductility level six with all the longitudinal reinforcement exposed, which resulted in longitudinal reinforcement buckling during cyclic torsion as shown in Fig. 4-15 (d).

Finally, the column failed at rotation ductility level 10 with the average rotation deformation capacity of 23.0˚. The damage characteristics and failure sequence in this column were in the order of inclined torsional cracking, spiral yielding and concrete cover spalling, peak torque with complete concrete cover spalling, longitudinal reinforcement yielding and then overall failure by significant core concrete degradation and longitudinal reinforcement buckling. The typical damage progression of the oval column with interlocking spirals is presented in Fig. 4-15.

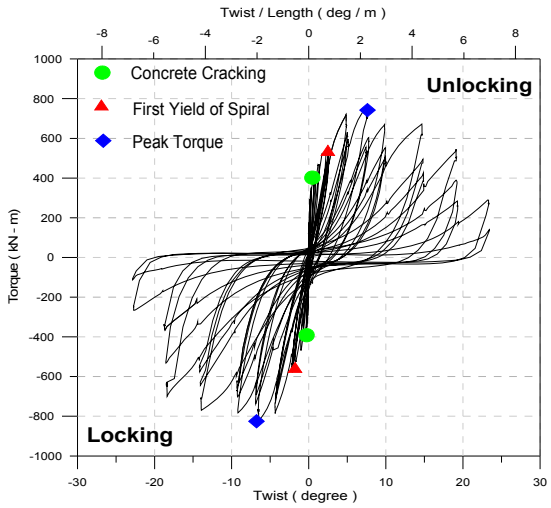

Fig. 4-14 Torsional Hysteresis Curves under Pure Torsion

(a) Cracking (b) Yielding (c) Peak (d) Final failure

Fig. 4-15 Damage Progression and Failure Modes under Pure Torsion

4.2.2.2 Cyclic Flexure and Shear under Biaxial Loading

Current seismic design is based on two lateral components about weak and strong axes independently for oval columns, which overestimates the strength and ductility capacity due to neglecting the biaxial loading effect. In this study, the column was tested under cyclic flexure and shear in the biaxial direction with 35˚ to the cross-sectional weak axis, and the lateral load-displacement hysteresis curve is shown in Fig. 4-16. The horizontal flexural crack first appeared on side ‘AF’ and ‘CD’ at the bottom of the column around 500 mm from the base when loaded up to 50% of yielding load. Thereafter the flexural

cracks extended and wound all around the column, and more new cracks developed at higher portion with the increasing load level as shown in Fig. 4-17 (a). The horizontally flexural cracks were distributed around all the side faces of column due to the bending moments in the bilateral directions, which was different from the uniaxial directional loading. The flexural stiffness degraded at post-cracking stage resulting in nonlinear load-deformation response. All the longitudinal reinforcement about the strong and weak axis simultaneously reached the yielding strain at the lateral load of 386.7 kN and displacement of 28.8 mm, which was taken as ductility one. Simultaneous yielding of the longitudinal reinforcement about two axes confirmed that the 35˚ is the balanced diagonal angle to yield the column about strong and weak axis. More cracks occurred at a higher position on the column at ductility level one as shown in Fig. 4-17 (b). When it was loaded to the higher ductility level of three, and the concrete cover at the bottom level began to spall off, which was caused by tensile failure on the surface between the concrete cover and the concrete core. The concrete cover spalling also developed upwards with the increasing displacement ductility level after cumulative cycles of loading.

At the peak lateral loading level, the concrete cover about the strong axis experienced more spalling off than the one about the week axis as shown in Fig. 4-17 (c) due to the larger bending moment component about strong axis. The peak lateral load was captured at the value of 596.6 kN corresponding to the displacement of 118.5 mm at ductility level four. In addition, the longitudinal strain penetrated into the base at peak load stage showing cracks on the top of the base. Then the concrete cover spalling extended to the sides about the week axis with the increased ductility level. At post-peak stage, the strain

of interlocking spirals at the bottom of the column increased significantly and provided sufficient confinement to the core concrete after concrete cover spalling off. The flexural strength degraded mildly compared to the torsional strength degradation. The failure of the column began with the formation of a flexural plastic hinge at a height of 560 mm from the base of the column, followed by concrete core crushing and buckling of the longitudinal reinforcement over the cross section at ductility level 10. The progressive damage of this oval column is also shown in Fig. 4-17.

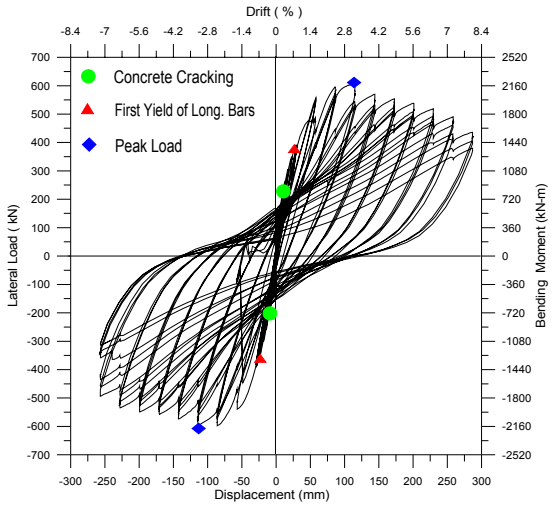

Fig. 4-16 Flexural Hysteresis Curves under Biaxial Flexure and Shear

(a) Cracking (b) Yielding (c) Peak (d) Final failure

Fig. 4-17 Damage Progression and Failure Modes under Biaxial Flexure and Shear

4.2.2.3 Cyclic Combined Flexure, Shear and Torsion under Uniaxial Loading

Two oval columns were tested about the weak axis under combined flexure, shear and torsion by maintaining T/M ratios of 0.2 and 0.6, respectively. One column was tested at a *T/M* ratio of 0.6 to establish a point in the interaction diagram by yielding the longitudinal and transverse reinforcement simultaneously. The yielding torsional moment for pure torsion tests was achieved at T_y = 525 kN-m; and the yielding bending moment under flexure and shear was predicted by Response 2000 to be M_y = 864.7 kN-m. Thus the ratio of M_y/T_y was calculated to be 0.607, which was taken as about 0.6 in order to investigate the sequence of longitudinal and transverse reinforcement yielding. Another column was tested at a lower T/M ratio of 0.2 to determine the strength and stiffness degradation and failure modes at different torsion effect levels.

The flexural and torsional hysteresis behaviors of the one under the T/M ratio of 0.2 were plotted in Fig. 4-18 and Fig. 4-19. The inclined flexural cracks first appeared in the interlocking region near the bottom of the column at 50% of the yielding load. The cracking load level is lower than that applied for the column under pure torsion due to the combined loading including the flexure effect. As the lateral and torsional loading increased, the flexural cracks extended in an inclined angle of 32˚ - 34˚ to the side faces of the column and new shear cracks occurred at increasing heights due to torsion effect as shown in Fig. 4-20 (a). The angle of inclined cracks mainly depended on the amount of the T/M ratios. The column reached the longitudinal reinforcement yielding first on side 'BC' and 'EF' at a lateral load of 224 kN and torsional moment of 149 kN-m corresponding to a lateral displacement of 24.2 mm and twist of 0.22˚, which was defined as ductility level one. The flexural and torsional inclined cracks spread over the whole

column as shown in Fig. 4-20 (b). After longitudinal reinforcement yielding, the concrete cover started spalling at the bottom of the columns and developed upwards with the increased loading level. The spirals on side 'D' at the low portion of the column remained elastic until ductility three along with more concrete cover spalling. When the column was loaded to the ductility level of 4.5, the peak lateral load of 390 kN and torsional moment of 280 kN-m were obtained corresponding to a lateral displacement of 114.7 mm and twist of 1.45˚. The asymmetric nature of torsional behavior under combined flexure and torsion as shown in Fig. 4-19 is due to the locking and unlocking actions of spirals and also the fact that one side of the cross section is always subjected to higher additive shear stress from combined flexure and torsion, leading to more damage and less load resistance. At the same reason, the positive cycle always reached the peak loading force first and the negative cycle could still obtain a higher peak loading at the next ductility level. The concrete cover spalling extended to around 250 mm above the base as shown in Fig. 4-20 (c). At post-peak stage, the concrete cover continued to spall upwards and all the reinforcements were exposed resulting in excessive reinforcement strain. The concrete core started crushing which was an important indication of significant strength degradation. Finally, the columns failed with the plastic hinge forming at the height of 300mm above the base with respect to severe concrete core crushing and longitudinal reinforcement buckling and rupturing as shown in Fig. 4-20 (d). The typical damage progression of the column under a T/M ratio of 0.2 is shown in Fig. 4-20.

For a column under the T/M ratio of 0.6, the flexural and torsional hysteresis curves were plotted in Fig. 4-21 and Fig. 4-22. The inclined torsional cracks first appeared in the interlocking region near the mid-height of the columns at 40% of the yielding load. The

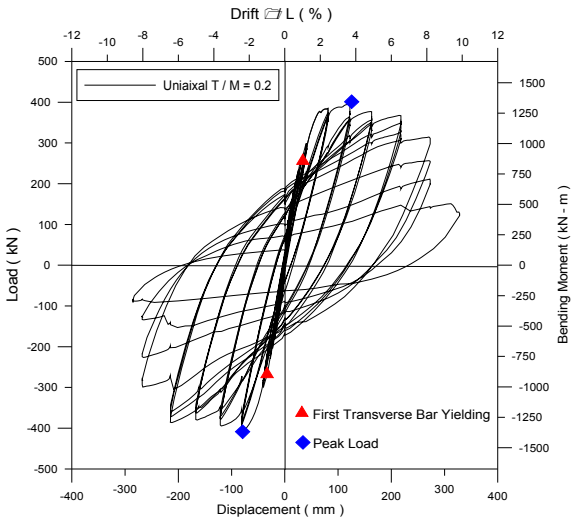

Fig. 4-18 Flexural Hysteresis Curves under Uniaxial T/M Ratio of 0.2

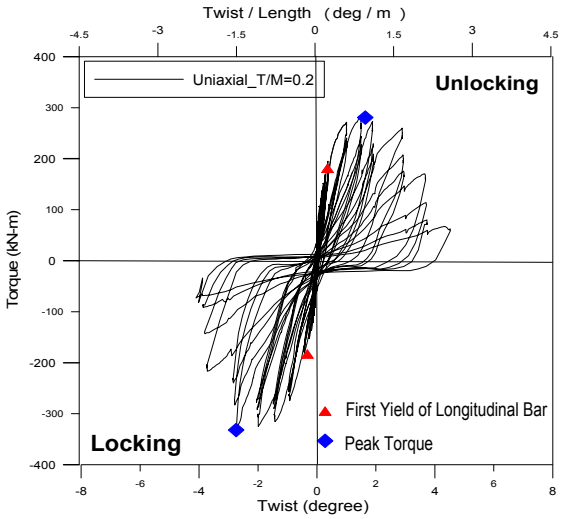

Fig. 4-19 Torsional Hysteresis Curves under Uniaxial T/M Ratio of 0.2

(a) Cracking (b) Yielding (c) Peak (d) Final failure

Fig. 4-20 Damage Progression and Failure Modes under Uniaxial T/M Ratio of 0.2

cracking load level is lower than the column under a T/M ratio of 0.2 due to more torsion effect. The inclined cracks developed spirally around the whole column in an inclined angle of 40˚-42˚ as shown in Fig. 4-23 (a). Flexural stiffness experienced more degradation compared to the column under the smaller T/M ratio of 0.2, which was caused by the twist of the column from the torsion effect. Longitudinal reinforcement on side 'BC' and 'EF' and transverse reinforcement on side 'D' yielded simultaneously around 550 mm above the base at a lateral load of 195 kN and torsional moment of 484

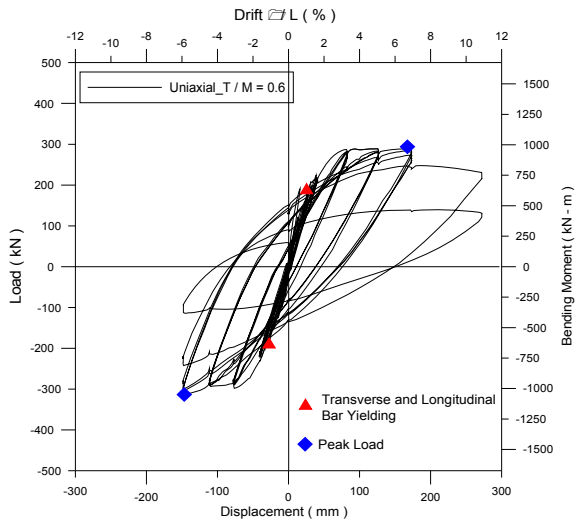

Fig. 4-21 Flexural Hysteresis Curves under Uniaxial T/M Ratio of 0.6

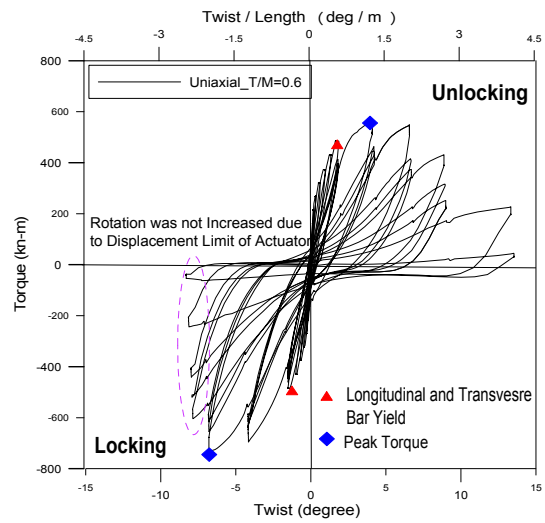

Fig. 4-22 Torsional Hysteresis Curves under Uniaxial T/M Ratio of 0.6

kN-m corresponding to a lateral displacement of 38.5 mm and twist of 1.63˚, which was defined as ductility level one. The flexural and torsional inclined cracks spread over the whole column and severe inclined concrete cracking resulted in concrete cover debonding as shown in Fig. 4-23 (b). Thus the T/M ratio of 0.6 was defined as the balanced T/M ratio for this oval cross section under uniaxial loading, which was larger compared to the square cross section due to the dimension size of the cross section. After reinforcement yielding, the concrete cover spalled at the low portion of the column around 600 mm above the column and developed upwards and downwards as the loading level increased. When the column was loaded to ductility level two, the peak torsional moment of 562 kN was obtained corresponding to a twist of 3.97˚. However, the peak lateral load of 286 kN was reached at next ductility level of three with a lateral displacement of 113 mm. Thus torsional strength was reached first because of the large additive stress distribution from combined shear and torsion and the corresponding additional damage of the concrete. Also more locking and unlocking effects were observed from the asymmetric nature of torsional behavior as shown in Fig. 4-22

compared to the column under the lower T/M ratio of 0.2, which is due to a larger torsion effect. The concrete cover spalling distributed along the two-thirds height of the column as shown in Fig. 4-23 (c). At post-peak stage, the concrete cover continued to spall upwards and the concrete core started crushing with excessive transverse strain. The torsional and flexural strength significantly degraded. Finally, the columns failed with the plastic hinge forming at the height of 500mm above the base due to severe concrete core crushing and longitudinal reinforcement buckling and rupturing as shown in Fig. 4-23 (d). The typical damage progression of this column is presented in Fig. 4-23.

(a) Cracking (b) Yielding (c) Peak (d) Final failure

Fig. 4-23 Damage Progression and Failure Modes under Uniaxial T/M Ratio of 0.6

As observed in testing, more inclined shear cracks were observed at a higher location of the column under the T/M ratio of 0.6 compared to the one under the T/M ratio of 0.2 due to more torsion effect. For the specimen loaded at the T/M ratio of 0.6, longitudinal bars and spirals yielded at the same load level, which was called balanced condition from a design point of view; while the specimen loaded at T/M ratio of 0.2 reached the longitudinal bar yielding first at ductility one and then the spiral yielded at ductility three. According to the test hysteresis curve comparison, the torsional and flexural strength and post-crack stiffness considerably decreased due to the combined loading effect. Also, the

deterioration of column strength and stiffness is obvious in the first loading cycle and becomes less significant with more loading repetitions. The torsional stiffness was found to degrade faster than that observed under pure torsion due to flexure effect. The column loaded at the high T/M ratio of 0.6 was observed with torsion dominated failure, which started from the severe inclined cracks leading to progressive spalling of the concrete cover along most portions of the column and failed with total core concrete crushing and longitudinal reinforcement extremely twisting as shown in Fig. 4-20. While the column loaded at the low T/M ratio of 0.2 behaved in flexure failure mode finalized by less concrete spalling, total concrete core crushing and longitudinal reinforcement buckling as shown in Fig. 4-23. Core degradation distributions for these two columns were observed to be lower than that under pure torsion, which concluded that the plastic hinge location moved upwards along with increasing T/M ratios.

4.2.2.4 Cyclic Combined Flexure, Shear and Torsion under Biaxial Loading

For biaxial combined loading, two specimens were tested about the axis at 35˚to the week axis at T/M ratios of 0.2 and 0.4, respectively. One column was tested at a *T/M* ratio of 0.4 to establish a point in the interaction diagram by yielding the longitudinal and transverse reinforcement simultaneously. The yielding torsional moment for pure torsion tests was achieved at T_y = 525 kN-m, and the yielding bending moment under flexure and shear test was captured at M_y = 1296.5 kN-m. Thus the ratio of M_y/T_y was calculated to be 0.405, which was taken as about 0.4 to investigate the sequence of longitudinal and transverse reinforcement yielding. Another column was tested at the lower T/M ratio of 0.2 to determine the strength and stiffness degradation and failure modes at different torsion effect level.

For column under a T/M ratio of 0.2, the flexural and torsional hysteresis behaviors are shown in Fig. 4-24 and Fig. 4-25. The flexural cracks first appeared in the interlocking region near the bottom of the column at 50% of the yielding load, which was lower than pure torsion due to the combined loading. The flexural cracks developed in an inclined angle of 30˚-33˚, and new inclined cracks occurred at increasing heights due to the torsion effect as shown in Fig. 4-26 (a). Longitudinal reinforcement yielded first on side 'AB' and 'ED' at a lateral load of 348 kN and torsional moment of 263 kN-m corresponding to a lateral displacement of 31.4 mm and twist of 0.42˚, which was defined as ductility level one. The yielding load and deformation were larger compared to the column under the uniaxial T/M ratio of 0.2 due to the biaxial loading about the axis between the strong and weak axis. The flexural and torsional inclined cracks spread around all the faces of the column along the whole height of column as shown in Fig. 4-26 (b). At post-yielding stage, concrete cover spalling occurred at the bottom of the columns and developed upwards with increasing loading level. Meanwhile, the longitudinal strain penetrated into the base of the column due to the biaxial loading about the 35˚ axis deviating from the weak axis, which caused concrete cracking on the top surface of the base.

A peak lateral load of 540 kN and torsional moment of 378 kN-m were captured at ductility level three corresponding to a lateral displacement of 98.4 mm and twist of 1.85˚. The spirals on side 'CD' at the low portion of column remained elastic until the peak load stage along with more concrete cover spalling. The lateral displacement at peak load stage was smaller compared to the one under the uniaxial loading; and rotation deformation was larger than the one under uniaxial loading, which was caused by the

biaxial loading. Locking and unlocking actions of spirals could be reflected from the asymmetric nature of torsional behavior under combined flexure and torsion as shown in Fig. 4-25. Also the locking and unlocking effect was magnified by biaxial loading compared to uniaxial loading. The concrete cover spalling extended to around 280 mm above the base as shown in Fig. 4-26 (c). Thereafter the concrete cover continued to spall upwards and spread spirally around all the faces of the column and all the reinforcement were exposed resulting in excessive reinforcement strain in the longitudinal and transverse direction. Also the plastic hinge occurred at the height of 320mm above the base and all the longitudinal reinforcement over the cross section yielded at this loading level. Finally, the columns failed with severe concrete core crushing and longitudinal reinforcement buckling and rupturing as shown in Fig. 4-26 (d). The typical damage progression of the column under a T/M ratio of 0.2 is shown in Fig. 4-26.

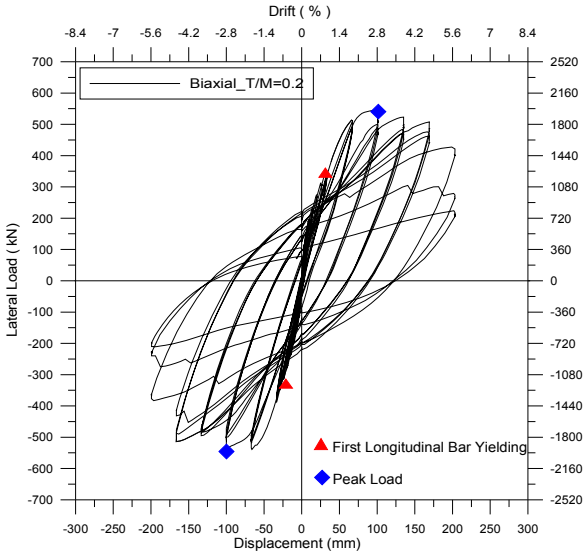

Fig. 4-24 Flexural Hysteresis Curves under Biaxial T/M Ratio of 0.2

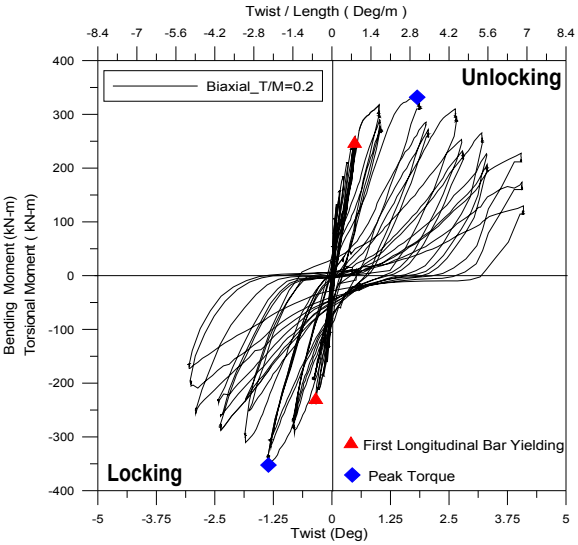

Fig. 4-25 Torsional Hysteresis Curves under Biaxial T/M Ratio of 0.2

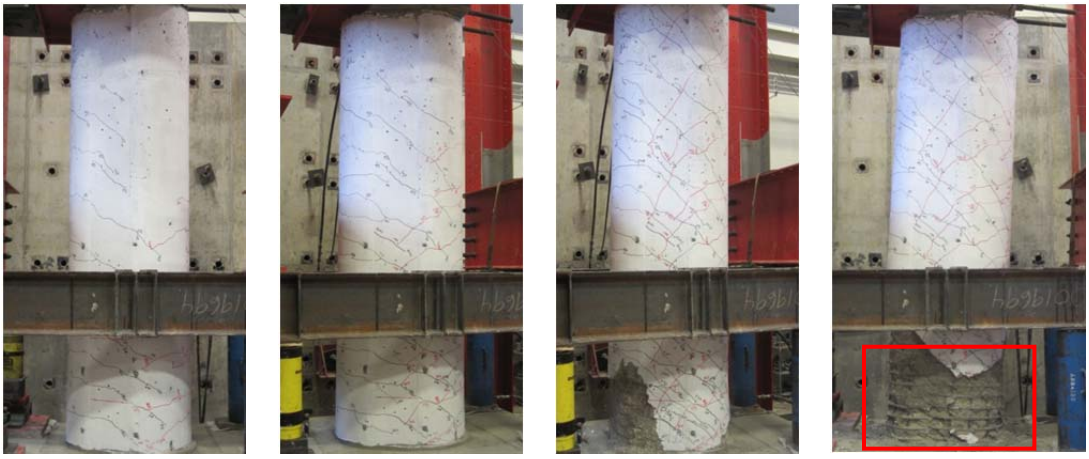

(a) Cracking (b) Yielding (c) Peak (d) Final failure

Fig. 4-26 Damage Progression and Failure Modes under Biaxial T/M Ratio of 0.2

For the column under a T/M ratio of 0.4, the flexural and torsional hysteresis curves were plotted in Fig. 4-27 and Fig. 4-28. The inclined torsional cracks with around 40˚ first appeared in the interlocking region near the mid-height of the columns at 40% of the yielding load due to torsion effect. Fig. 4-29 (a) showed the inclined cracks wound around the whole column. Torsional and flexural stiffness both degraded after concrete cracking. But the torsional stiffness degraded more than flexural stiffness because the concrete cover contributed to a large portion of torsional resistance. When the column was loaded with a lateral load of 263 kN and torsional moment of 418 kN-m, longitudinal reinforcement on side 'AB' and 'ED' and transverse reinforcement on side 'D' yielded simultaneously around 500 mm above the base with a lateral displacement of 38.5 mm and a twist of 1.63˚, which was defined as ductility level one. The inclined cracks spread over the whole column and severe inclined concrete cracking resulted in the concrete cover debonding at the mid-height of the column as shown in Fig. 4-29 (b). The T/M ratio of 0.4 was defined as the balanced T/M ratio for this oval cross section under biaxial loading, which was smaller compared to uniaxial loading because the biaxial flexural strength about the axis deviating from the weak axis was larger than the uniaxial flexural

strength about the weak axis. At post yielding stage, concrete cover spalling started at the 550 mm height of the column and developed upwards and downwards with increasing applied displacement and rotation. A peak torsional moment of 509 kN was obtained at ductility level two corresponding to a twist of 2.38˚; and the peak lateral load of 463 kN was reached at next ductility level of three with a lateral displacement of 86.5 mm. Compared to the column under the lower T/M ratio of 0.2, more locking and unlocking effects were observed from the asymmetric nature of torsional behavior as shown in Fig. 4-28. Also the biaxial loading under the T/M ratio of 0.4 magnified this locking and unlocking effect when compared to the uniaxial loading under the T/M ratio of 0.6. The concrete cover spalling developed along the two-thirds height of the column as shown in Fig. 4-29 (c). At post-peak stage, the concrete cover continued to spall upwards and the concrete core started crushing resulting in significant torsional and flexural strength/stiffness degradation. The failure of the column was finalized at ductility level six with severe concrete core crushing and longitudinal reinforcement buckling as shown in Fig. 4-29 (d). The typical damage progression of this column is presented in Fig. 4-29.

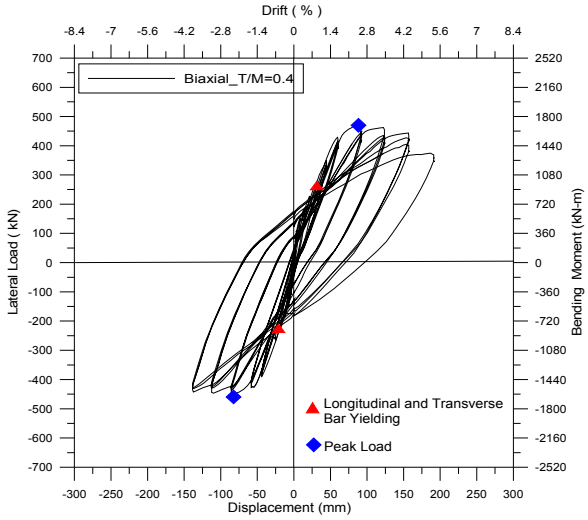

Fig. 4-27 Flexural Hysteresis Curves under Biaxial T/M Ratio of 0.4

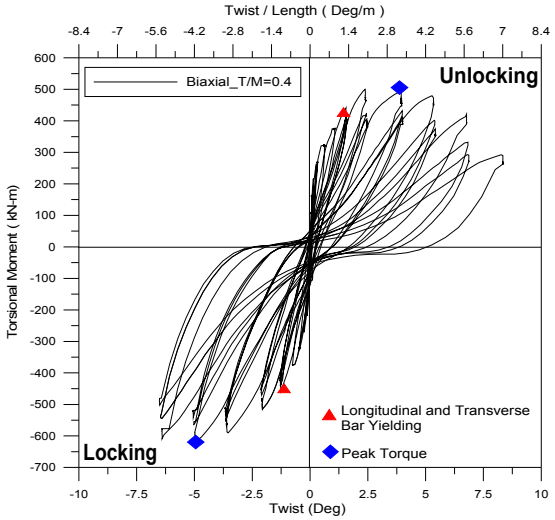

Fig. 4-28 Torsional Hysteresis Curves under Biaxial T/M Ratio of 0.4

(a) Cracking (b) Yielding (c) Peak (d) Final failure

Fig. 4-29 Damage Progression and Failure Modes under Biaxial T/M Ratio of 0.4

The column under the T/M ratio of 0.4 was observed to have the more inclined cracks than the one under the T/M ratio of 0.2. After the yield loading level, the severe cracking led to progressive concrete cover spalling off at a specific distribution which was determined by the T/M ratios. The column at the high T/M ratio of 0.4 was observed with more torsion failure mode, of which the concrete cover spalled along two-thirds the height of the column, the core concrete severely crushed and longitudinal bar buckled as shown in Fig. 4-29. The column at the low T/M ratio of 0.2 experienced flexure dominated failure with less concrete spalling, lower plastic hinge location, core concrete degradation, and longitudinal reinforcement buckling as shown in Fig. 4-26. Concrete cover spalling distribution for these two columns under biaxial combined loading were observed to be higher than those under uniaxial combined loading, which indicated that the bidirectional bending moment magnified the torsion effect resulting in earlier and more severe concrete cover spalling. However, these two specimens under biaxial combined loading gained less core concrete crushing compared to the ones under uniaxial combined loading due to the fact that most of the bending moment was resisted about the

strong axis, which would release the core concrete damage about the week axis and then lag the whole core concrete crushing till the final failure.

4.3. Discussion of Test Results

The response of columns under combined loading with respect to hysteresis behavior, load-displacement and torsional moment-twist envelopes, displacement and twist profiles, longitudinal and transverse strain variation, principal tensile and shear strains, bending moment-curvature behavior along the column, ductility capacity, damage characteristics, and energy dissipation characteristics are compared with respect to several test parameters in the following sections.

4.3.1. Flexural and Torsional Hysteresis Behavior

The flexural and torsional hysteresis behavior of columns under various T/M ratios was compared with respect to different cross sectional shapes and transverse reinforcement configurations.

4.3.1.1 Square Columns with Octagonal and Square Ties under Combined Loading

Fig. 4-30 and Fig. 4-31 present the hysteretic load-displacement and torsional moment-twist curves of square columns with octagonal and square ties under various T/M ratios. Based on the comparison, the flexural and torsional stiffness degradation was amplified by the combined loading. Also the torsional stiffness degraded more rapidly than the flexural stiffness due to the more severe diagonal shear cracking and more concrete cover spalling. It clearly indicates that the yielding and peak torsional moment and corresponding rotation decreased along with decreased T/M ratios; similarly the yielding and peak lateral load and displacement capacity were reduced by the combination of flexure and torsion. Also the deterioration of capacities in columns is

substantial in the first two loading cycles and becomes less significant along with more loading cycles.

At the post-peak stage, the torsional strength degradation was more than flexural strength degradation due to more concrete core crushing. The pinching effect of flexural hysteresis was magnified by combined loading along with increasing T/M ratios, which indicated the reduced flexural energy dissipation. The significant pinching effect for the torsional hysteresis of all square columns showed that torsional energy dissipation capacity was always less than the flexural energy dissipation capacity.

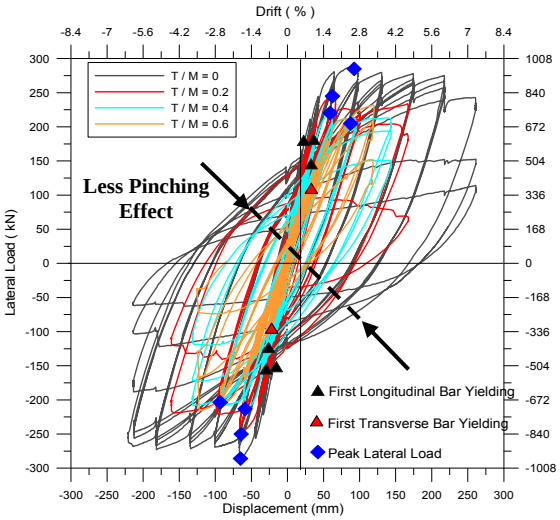

Fig. 4-30 Flexural Hysteresis Comparison for Square Columns under Combined Loading

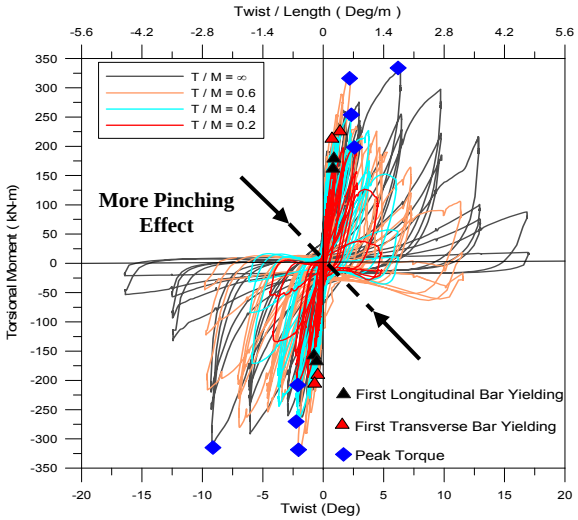

Fig. 4-31 Torsional Hysteresis Comparison for Square Columns under Combined Loading

4.3.1.2 Oval Columns with Interlocking Spirals under Uniaxial Combined Loading

The hysteretic load-displacement and torsional moment-twist curves of oval columns with interlocking spirals under uniaxial loading about the weak axis were compared in Fig. 4-32 and Fig. 4-33. At the post-cracking stage, the oval columns experienced more flexural and torsional stiffness degradation under combined loading. Also the severe concrete cracking and more concrete cover spalling from the torsion effect caused the torsional stiffness to degrade more rapidly than the flexural stiffness after the cracking

load. The flexure effect reduced the torsional moment required to cause yielding of the transverse reinforcement and also the peak torsional component. Similarly, the torsion effect reduced the bending moment required to cause yielding of the longitudinal reinforcement and the peak component of bending moment. In addition, the yielding rotation decreased along with decreased T/M ratios; similarly the yielding displacement was reduced by the combination of flexure and torsion. At post-peak stage, the flexural strength degraded gradually with increasing ductility levels and the torsional strength degraded significantly with more rotation due to more concrete core crushing. However, the torsional stiffness and strength degradation in oval columns with interlocking spirals was less than the degradation in square column due to the better confinement from interlocking spirals and the corresponding increase of concrete core strength.

As in the square columns, the pinching effect of flexural hysteresis in oval columns was magnified by increasing T/M ratios, which in turn reduced flexural energy dissipation capacity. The pinching effect for torsional hysteresis in oval columns was less than the one in square columns because the interlocking spirals provided better confinement to core concrete resulting in more energy dissipation. The locking and unlocking effects were observed from the asymmetry of torsional hysteresis curves, owning to the winding/unwinding interaction mechanism of two interlocking spirals to the core concrete and the asymmetric distribution of additive shear stress from combined flexure and torsion over the cross section.

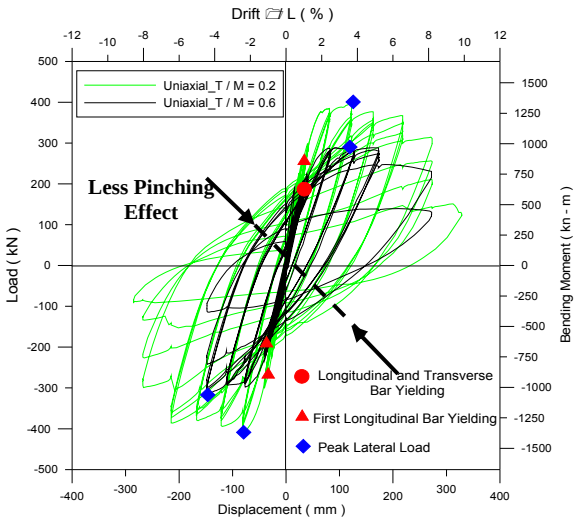

Fig. 4-32 Flexural Hysteresis Comparison for Oval Columns under Uniaxial Combined Loading

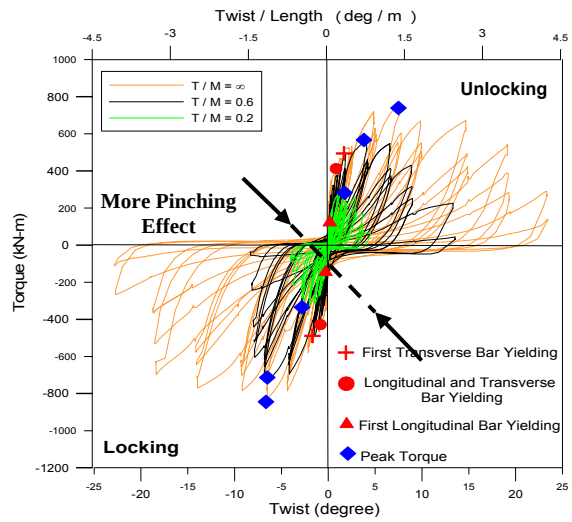

Fig. 4-33 Torsional Hysteresis Comparison for Oval Columns under Uniaxial Combined Loading

4.3.1.3 Oval Columns with Interlocking Spirals under Biaxial Combined Loading

The hysteretic load-displacement and torsional moment-twist curves of the oval column with interlocking spirals under biaxial loading about the 35° axis to the week axis were compared in Fig. 4-34 and Fig. 4-35. Flexural and torsional stiffness degradation was amplified by the combined loading effect and the torsional stiffness degraded more rapidly than the flexural stiffness after the cracking load. As compared to the oval column under uniaxial loading, the stiffness degradation was accelerated by the biaxial loading. The yielding and peak bending moments were reduced by an increase of the T/M ratios; and the yielding and peak torsional moments decreased along with a decrease of the T/M ratios. In addition, the displacement and twist capacities were affected by combined loading as shown in the comparisons. The torsional strength degraded significantly after the concrete cover completely spalled, which was more than the degradation in the oval column under biaxial loading. However, the torsional stiffness and strength degradation in oval columns under biaxial loading was still less than the degradation in square columns due to the better confinement from interlocking spirals. As in the square

columns, the pinching effect of flexural hysteresis in oval columns was magnified by increasing the T/M ratios, which in turn reduced the flexural energy dissipation capacity. The pinching effect for torsional hysteresis in oval columns under biaxial loading was greater than the one under the uniaxial loading due to the rapid stiffness degradation. Moreover, the torsional hysteresis curves under biaxial loading showed more asymmetric features during positive and negative loading cycles because biaxial combined loading enlarged the locking and unlocking effects compared to uniaxial combined loading. Moreover, the biaxial lateral load accelerated the damage progression and reduced the flexural strength of each individual direction.

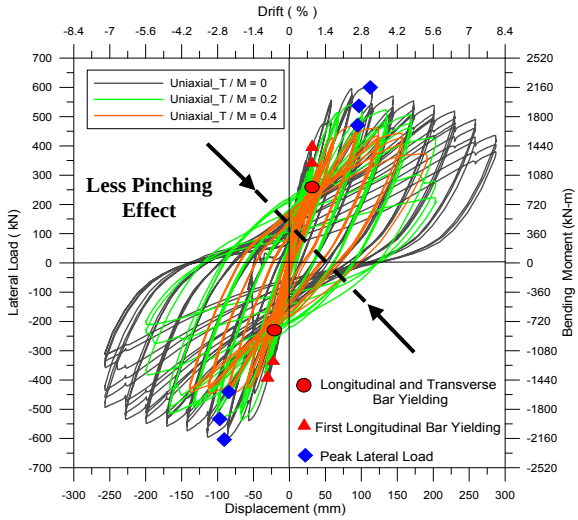

Fig. 4-34 Flexural Hysteresis Comparison for Oval Columns under Biaxial Combined Loading

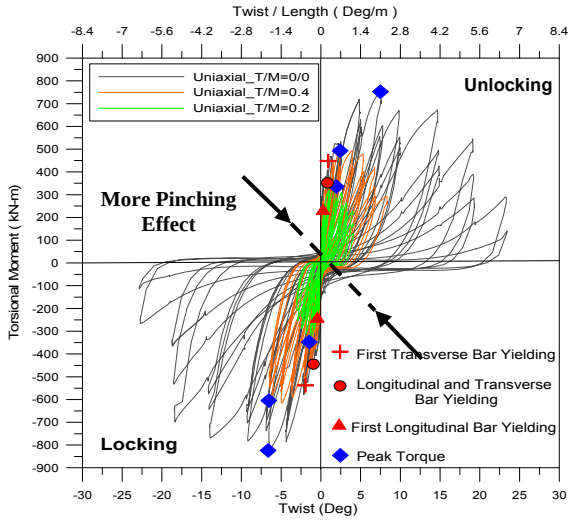

Fig. 4-35 Torsional Hysteresis Comparison for Oval Columns under Biaxial Combined Loading

4.3.2. Lateral Load-Displacement and Torsion Moment-Twist Envelopes

The envelope of hysteresis curves is determined by connecting the peak load or torsional moment points in the first loading cycle at each ductility level, which indicates the similar trends of a load-deformation relationship of members under monotonic loads. The load-deformation envelopes are easily used to conduct the comparison of

experimental results. The lateral load-displacement and torsional moment-twist envelopes of square and oval columns at various T/M ratios are compared in the following sections.

4.3.2.1 Square Columns with Octagonal and Square Ties under Combined Loading

The lateral load-displacement envelopes under combined loading at various T/M ratios are plotted and compared in Fig. 4-36. The flexural and torsional strength decreased because of the combined loading effect identically to the various T/M ratios. Also, the columns experienced strength and stiffness degradation along with increasing load cycles at each ductility level. It was found that the intensity of stiffness degradation dropped along with more applied loading cycles. The yielding displacement increased and the corresponding lateral load decreased along with an increase in the T/M ratio. For columns under pure flexure and combined loading at T/M ratios of 0.2 and 04, the envelopes indicated that the lateral load could be maintained for a few more ductility levels even after the peak load. However, the column under the high T/M ratio of 0.6 failed right after reaching the peak load due to the greater torsion effect.

The torsional moment-twist envelopes under combined loading at various T/M ratios are plotted and compared in Fig. 4-37. The torsional strength and stiffness under combined loading degraded significantly along with the increased bending moment level. Also the strength and stiffness dropped with an increase in the loading cycles at each ductility level for all the columns. The secondary torsional stiffness under combined loading degraded faster than that under pure torsion due to the flexure effect. In addition, the torsional strength was reduced rapidly after the peak torque because the concrete cover almost completely spalled and the core concrete had crushed at peak load stage, which provided limited torque resistance.

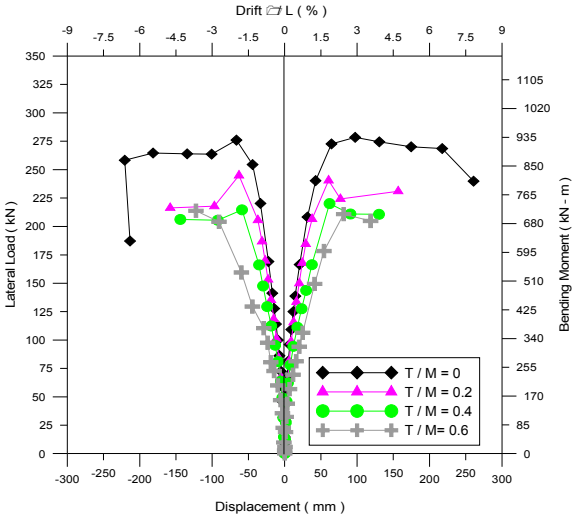

Fig. 4-36 Lateral Load - Displacement Envelopes for Square Columns under Combined Loading

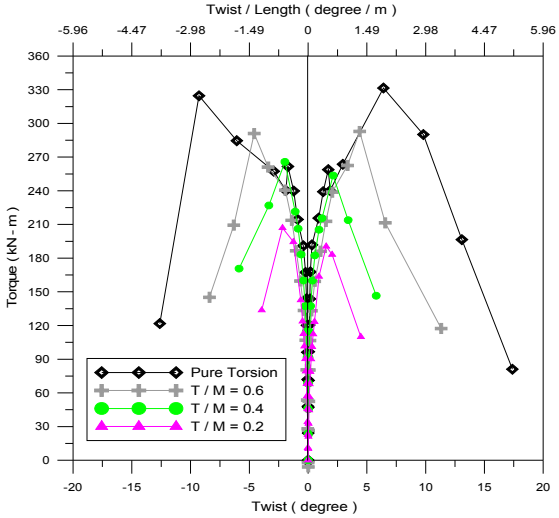

Fig. 4-37 Torsional Moment -Twist Envelopes for Square Columns under Combined Loading

4.3.2.2 Oval Columns with Interlocking Spirals under Combined Loading

The lateral load-displacement and torsional moment-twist envelopes under combined loading at various T/M ratios are plotted and compared in Fig. 4-37. The flexural strength was reduced and stiffness degradation was magnified due to the effect of combined loading, which depended on the various T/M ratios. As T/M ratios increased, the yielding displacement increased and the yielding lateral load decreased due to the torsion effect. For columns under flexure and shear and combined loading at low T/M ratios of 0.2, the envelopes indicated that the lateral load could be maintained at a certain level with slight reduction after the peak load stage with a few more ductility applied. However, the column under the high T/M ratios of 0.4 and 0.6 failed right after reaching the peak load due to the greater torsion effect. Also the oval columns under biaxial loading had larger flexural strength since the load was applied about the axis deviating from weak axis, which equivalently enlarged the dimension of the cross section. The envelopes of oval columns demonstrated better ductile response than in the square columns, which owed to the better transverse confinement from the spirals.

The torsional strength and stiffness under combined loading degraded significantly along with increasing bending moment level. The secondary torsional stiffness under combined loading degraded faster than that under pure torsion due to the flexure portion as in the square columns. The torsional strength was reduced significantly after the peak torque resulted from the severe concrete cover and core damage, which could not provide more torque resistance. The columns under biaxial combined loading gained larger lateral peak load compared to uniaxial combined loading mainly resulting from the large bending moment resistance about the strong axis and the asymmetric feature of the oval cross section. In order to investigate the biaxial loading effect, the decoupled yielding and peak bending moments about the weak axis of the specimens at various T/M ratios under biaxial loading were calculated by multiplying $sin35^{\circ}$ and compared to the yielding and peak bending moment about the weak axis under uniaxial loading as shown in Table 2.

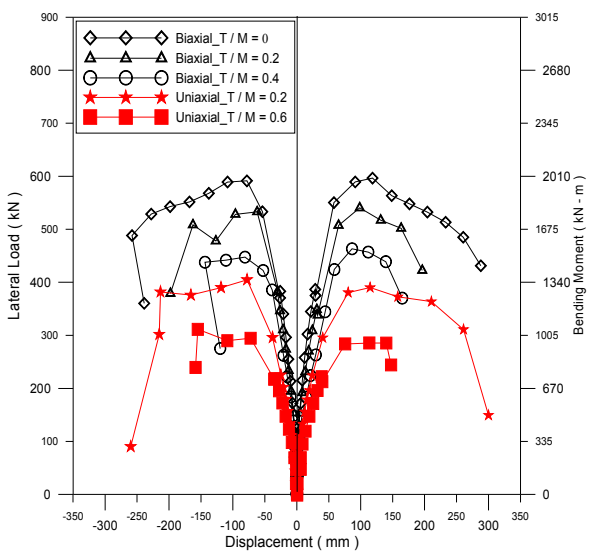

Fig. 4-38 Lateral Load - Displacement Envelopes for Oval Columns under Combined Loading

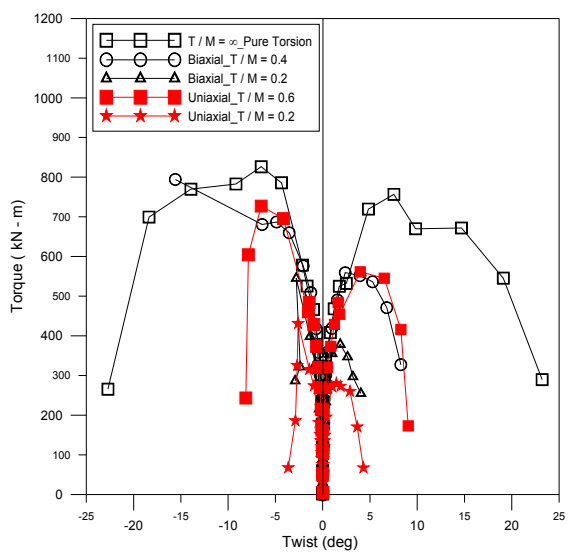

Fig. 4-39 Torsional Moment -Twist Envelopes for Oval Columns under Combined Loading

Table 4-1 Comparison on Yield and Peak Bending Moments about Weak Axis for Biaxial and Uniaixal Combined Loading

		Flexure and Shear T/M=0	T/M= 0.2 (Cracking Condition for Uniaxial Loading) T/M= 0.2 (Cracking Condition for Biaxial Loading)	T/M=0.4 (Balance Condition for Biaxial Loading) T/M= 0.6 (Balance Condition for Uniaxial Loading)
		M (kN-m)	M (kN-m)	M (kN-m)
Biaxial Combined Loading	Yield	743	698	670
	Peak	1147	1039	895
Uniaxial Combined Loading	Yield	864	751	746
	Peak	1333	1308	970
Biaxial / Uniaxial	Yield	0.86	0.92	0.90
	Peak	0.86	0.80	0.92

Based on the comparison, it can be concluded that the biaxial lateral loading magnified the torsion effect on flexural strength deterioration and reduced the peak bending moment by 10%~20%. Current seismic design for RC components under biaxial lateral combined loading is based on the flexural strength about the weak and strong axes independently without considering the interaction effect, which overestimates the strength and ductility capacity for RC members. The locking and unlocking effects from interlocking spirals can be reflected from the asymmetric feature of envelopes, which should be considered during the design progress for combined loading.

4.3.3. Displacement and Twist Profiles along the Column

The displacement and rotation of columns were captured by the string transducer systems at multiple locations along the height of the columns. Horizontal displacement was measured by averaging the displacements measured by the string transducers, and twist was measured by taking the difference between the string transducer measurements

and dividing them by the distance between the transducers as discussed in Chapter 3. The displacement and twist profiles along the column are discussed in following section.

4.3.3.1 Square Columns with Octagonal and Square Ties under Combined Loading

The observed displacement distribution along the height of the columns under combined loading at various T/M ratios is presented in Fig. 4-40. It indicated that more significant stiffness degradation and less displacement was attained due to the additional torsional moment effect at both the yielding and peak states. And this torsional moment effect was more evident at the peak stage than at the yielding stage, which is caused by the severe concrete cover spalling and concrete core crushing at the peak stage. In addition, the twist profile along the height of the columns is shown in Fig. 4-41. According to the comparison of the twist profile before the yielding stage, torsional stiffness did not show significant degradation until the yielding of transverse reinforcement. It was found that stiffness degradation was more prominent at the middle height of the column under pure torsion and at the lower portion of the column under other combined loading after the yielding of transverse reinforcement. Lesser degradation

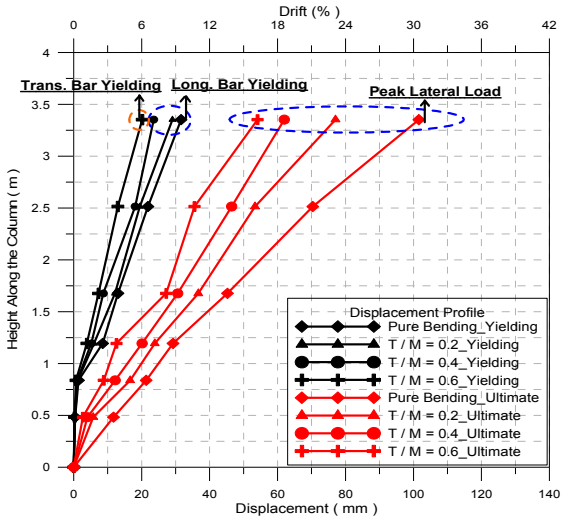

Fig. 4-40 Displacement Profile along the Height of Square Columns

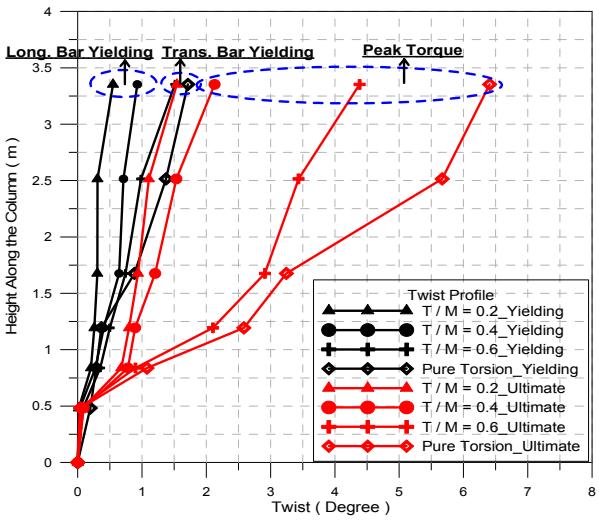

Fig. 4-41 Twist Profile along the Height of Square Columns

in torsional strength and stiffness was observed at the top and bottom due to the enhancement of the loading block and foundation. The column with flexure dominant failure obtained larger displacement and less twist capacity; while the column with torsion dominant failure obtained larger twist and less displacement capacity.

4.3.3.2 Oval Columns with Interlocking Spirals under Combined Loading

The observed displacement distribution along the height of the columns under uniaxial and biaxial combined loading at various T/M ratios is presented in Fig. 4-42. It indicated that more intense stiffness degradation and less displacement was attained due to the additional torsional moment effect at both the yielding and ultimate stages for columns under combined loading. And this torsional moment effect was amplified at the peak state due to the more concrete cover spalling and the plastic hinge formation with core concrete crushing. The specimens, tested at T/M ratios of 0.2 and 0.4 under biaxial combined loading, obtained more stiffness degradation and less displacement capacity compared to the specimens tested at T/M ratios of 0.2 and 0.6 under biaxial combined loading respectively, which validated that biaxial combined loading magnified the torsional moment effect on the damage progression. In addition, the twist profile along the height of the columns is shown in Fig. 4-43. According to the comparison of the twist profile at the yielding stage, torsional stiffness did not show significant degradation at the yielding of longitudinal reinforcement for the column under lower T/M ratios, which experienced flexural dominated failure modes; while it showed significant degradation at the yielding of transverse reinforcement for the column under higher T/M ratios of 0.6 and ∞, which was failed at the torsion dominated mode. It was found that stiffness degradation after the yielding of transverse reinforcement was more prominent at the

middle height of the column under pure torsion and at the lower location of column under other combined loading. The columns under biaxial combined loading was achieved with less twist capacity compared to the ones under uniaxial combined loading because of less core concrete crushing at the plastic hinge as discussed above. The column with flexure dominant failure obtained larger displacement capacity and smaller twist capacity; while the column with torsion dominant failure obtained larger twist capacity and smaller displacement capacity.

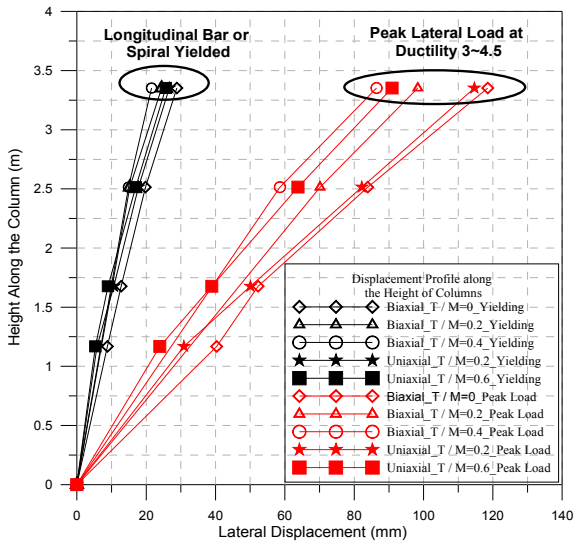

Fig. 4-42 Displacement Profile along the Height of Oval Columns

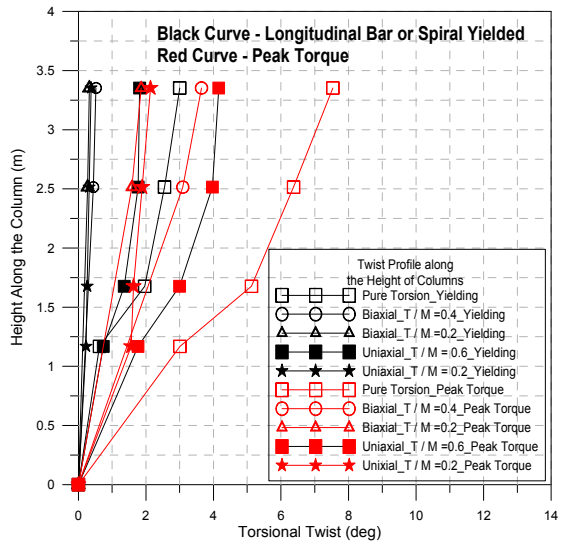

Fig. 4-43 Twist Profile along the Height of Oval Columns

4.3.4. Bending Moment-Curvature Behavior under Combined Loading

Moment-curvature analyses are widely used to assess the nonlinear force-displacement response of an RC member displaying flexure-dominated behavior subjected to inelastic deformation demands under seismic loads. In this study, the curvature under combined loading was calculated according to the LVDT rosettes at the bottom of column. The combined loading effect on the bending moment and curvature behavior are discussed in following section.

4.3.4.1 Square Columns with Octagonal and Square Ties under Combined Loading

The curvature was calculated according to the record of LVDT sets at 50 mm from the concrete base block. The bending moment-curvature curves for square columns under different combined loading conditions are compared in Fig. 4-44. It was found that the yielding curvature increased with respect to increases in the applied T/M ratios due to the more stiffness degradation from higher torsion. Also increasing torsional moment changes the damage characteristics in a column resulting in different flexural response under combined loading. The curvature corresponding to peak load decreased significantly along with increased torsion level because it altered the plastic hinge upwards and resulted in the concrete core deteriorating rapidly before the curvature further developed. As a result, the bending moment curvature behavior of RC columns under combined loading mainly depends on the T/M ratios, which should be taken into account for moment-curvature analysis.

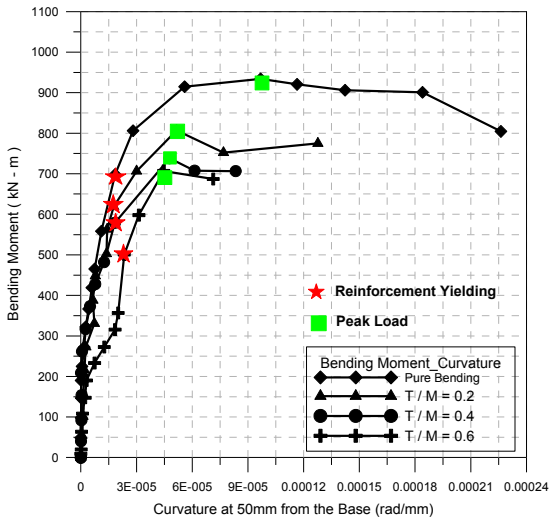

Fig. 4-44 Bending Moment Curvature of Square Columns under Combined Loading

4.3.4.2 Oval Columns with Interlocking Spirals under Combined Loading

The curvature was calculated according to the record of LVDT sets at 150 mm from the concrete base block. The bending moment-curvature curves for oval columns under

uniaixal and biaxial combined loading are compared in Fig. 4-45. As shown in the comparison, the yielding curvature increased with the increasing T/M ratios for all the columns due to the more flexural stiffness degradation from the torsion effect. Also the torsion effect changes the flexural response in a column under combined loading, resulting in less lateral displacement and curvature. And the curvature at the peak stage decreased along with the increasing torsion level because of the alteration of the plastic hinge and rapid concrete core crushing before the curvature further developed. The columns under biaxial loading obtained less curvature at the bottom of the columns than the ones under uniaxial loading, which owed to the biaxial combined loading about the stronger axis. In addition, the oval columns generally experienced less curvature than the square columns because of cross sectional dimension size.

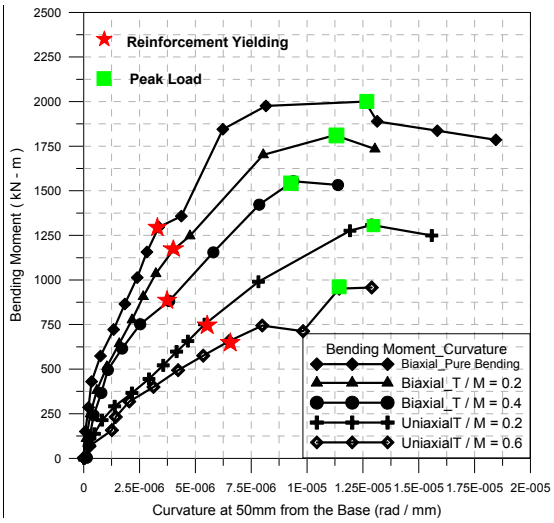

Fig. 4-45 Bending Moment Curvature of Oval Columns under Combined Loading

4.3.5. Damage Characteristics

The cyclic response of the RC column under combined loading was mainly affected by such parameters such as aspect ratio, thickness of concrete cover, longitudinal/transverse reinforcement ratio and configuration, strength of concrete, reinforcement, and loading conditions (T/M ratios). Due to the influence of multiple

parameters, the damage characteristics and failure modes of RC columns under combined loading are very complex. The main sequential damage states under combined flexure, shear, and torsion loading can be categorized as follows: (1) flexural and inclined cracks; (2) longitudinal and transverse reinforcement yielding; (3) concrete cover spalling; (4) crushing of diagonal concrete strut; (5) longitudinal reinforcement buckling and rupturing, and transverse reinforcement rupturing.

4.3.5.1 Square Columns with Octagonal and Square Ties under Combined Loading

Flexural and Inclined Cracking - For an RC column under pure flexure, the horizontal flexural cracks will occur in perpendicular to the longitudinal axis of the member when the principal tensile stresses in concrete reach the tensile strength of the concrete. Then the flexural cracks will develop and extend along with the increasing loads. The RC columns under combined flexure, shear, and torsion would experience diagonal concrete cracking, which is inclined to the transverse axis with angles depending on the level of the T/M ratios. The compressive concrete strut would form along the inclined cracks. Severe inclined crack significantly increased the transverse strain with an increase in the applied T/M ratios, and the flexural cracking resulted in larger longitudinal strain with a reduction in applied T/M ratios. For the columns tested in this study, the angle of cracks with respect to the transverse axis varied from 45° under pure torsion to 0° under flexure and shear. In addition, the flexural cracks concentrated at the lower portion of the column and inclined cracks can develop along the whole column. The observed cracking angle of all the columns with respect to the transverse axis was presented in Fig. 4-46.

Longitudinal and Transverse Reinforcement Yielding - The combined axial and shear forces and torsional and bending moment resulted in complex longitudinal and transverse

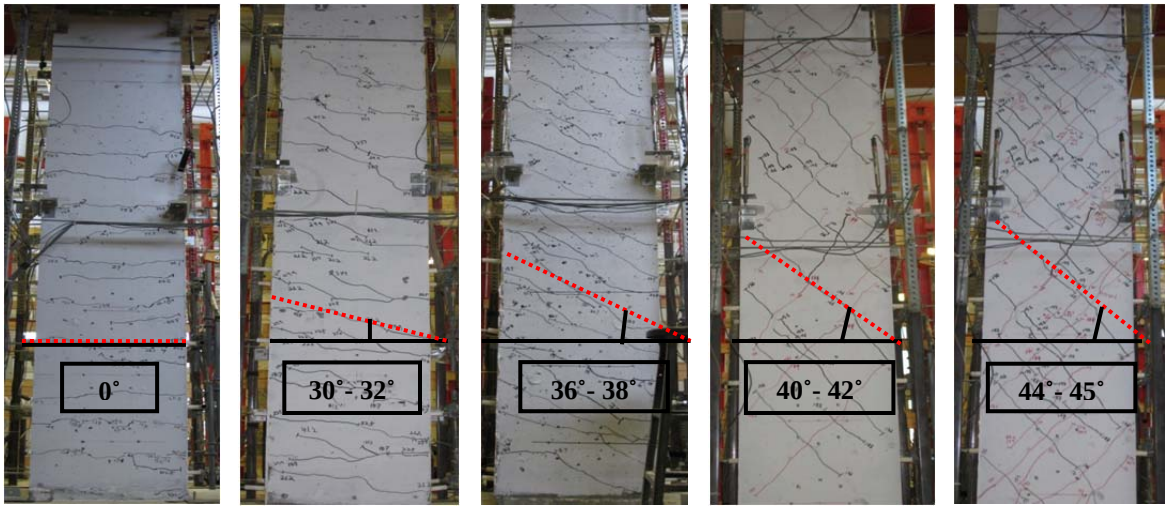

T / M = 0 T / M = 0.2 T / M = 0.4 T / M = 0.6 T / M = ∞

Fig. 4-46 Effect of Combined Loading on Crack Inclination and Distribution

strain combination and yielding mechanism, which could produce different damage sequences and failure modes. The longitudinal and transverse strain variation at plastic hinge zone could be affected by various T/M ratios under combined loading. Normally the RC members have elastic response before the first yielding of the longitudinal reinforcement for flexure dominant failure. Under combined loading including torsion, the location and sequence of longitudinal reinforcement yielding was mainly determined by the applied T/M because the torsional moment induced uniform tensile strain in all longitudinal bars; while the pure bending moment resulted in compressive and tensile strain of longitudinal bars at two opposite sides. The combination of longitudinal strain by cyclic torsional and bending moment caused complex yielding mechanism such as the longitudinal bar yielding first at two opposite sides of the cross section and then progressive yielding on the other two sides. The combined loading finally resulted in larger longitudinally tensile strain on one side of the cross section and less longitudinally compressive strain on another side. The typical longitudinal strain of reinforcement at the plastic hinge of columns under different T/M ratios are summarized and compared in Fig.

4-47. It clearly indicated that the longitudinal strain of reinforcement at the plastic hinge was strengthened significantly along with increasing T/M ratios, which was because the higher torsional moment contributed to developing longitudinally tensile strain of the reinforcement over the whole cross section.

In addition, significant shear forces or torsion would cause the yielding of transverse reinforcement, which indicated an onset of significant degradation of torsional stiffness. Also the torsional resistance under combined loading would not be enhanced too much after transverse reinforcement yielding since the core concrete lost the effective confinement. The experimental study also indicated that even a small ratio of torsional and bending moment would bring the yielding of transverse reinforcement forward for an RC column under combined loading (Li and Belarbi, 2010). The strain history of typical transverse reinforcement for columns at damage zone was plotted and compared in Fig. 4-48.

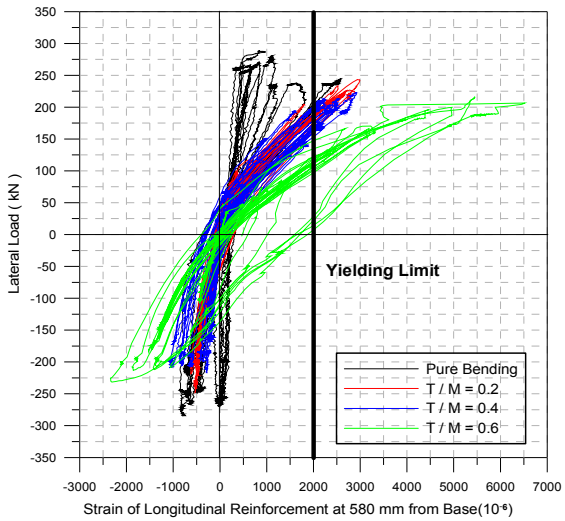

Fig. 4-47 Effect of Combined Loading on Strain Variation of Longitudinal Reinforcement

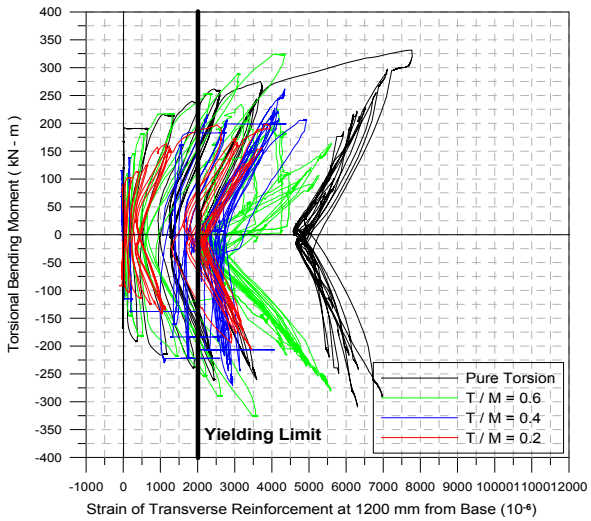

Fig. 4-48 Effect of Combined Loading on Strain Variation of Transverse Reinforcement

As shown in the figures, the torsional moment of combined loading was mainly resisted by the tensile force of transverse reinforcement, which resulted in uniformly

large tensile transverse strain and limited compressive transverse strain over the whole cross section. Additionally the strain of transverse reinforcement increased considerably along with the increase of T/M ratios providing more confinement to the concrete core to resist torsional moment.

Concrete Cover Spalling - The concrete cover spalling intensity under torsional loading is proportional to the compressive stresses in the concrete cover, the cover thickness, and the area of the splitting plane occupied by the reinforcement and is inversely proportional to the concrete tensile strength and size of the section. In addition, the concrete cover is observed to spall off before the peak torsional moment is reached. Under flexural loading, the concrete cover spalling is determined by such parameters as the cover-to-lateral dimension ratio, transverse reinforcement ratio, the axial load ratio, and the aspect ratio. The timing of spalling is important from a design point of view since the shear flow path is related to the dimension of the stirrups and the concrete cover. Whether it occurs before or after a column reaches the peak torsional load determines the effective cross-sectional dimensions to be used in the design calculations. If spalling occurs before peak load, only the concrete core section should be considered in the calculation of the ultimate capacity of the RC members. The combined loading including torsion could result in spalling of the cover even at the lesser load level than the theoretical concrete strength. The concrete cover spalling typically occurs when the concrete cover approaches the ultimate strain caused by two sets of severe shear cracking in opposite diagonal directions. Finally the separation between the concrete cover and concrete core is induced by the interfacial failure between them. Spalling of the concrete cover along the columns under combined loading will generally occur after excessive

yielding of reinforcement and prior to reaching the peak load, which induces significant stiffness degradation. In addition, the concrete cover spalling location and length are related to the loading conditions such as the torsional and bending moment ratio, which determines the minimum length confinement by transverse reinforcement from a design point of view. Under combined loading, concrete cover spalling occurs due to shear flow characteristics and changes in the shear flow direction. In general, the spalling of the concrete cover represents moderate damage that can be repaired without substantial members' replacement. The observed concrete cover spalling length increased significantly with the increasing T/M ratio as shown in Fig. 4-49.

Crushing of the Diagonal Concrete Strut - The compressive and tensile internal components from increasing applied combined loading can be resisted by the diagonal concrete compression struts as a compressive element and by steel reinforcements as a tension element after concrete cover spalling and transverse reinforcement yielding. The concrete compression struts crushing are developed once the concrete core exceeds the compressive strength. However, the diagonal compressive strength of concrete is much lower than the normal compressive strength under combined loading due to the softening effect from a smeared reinforced concrete point of view. The crushing of the diagonal strut is almost the ultimate damage limit state as it represents the failure of the RC member. The typical concrete core crushing locations and modes for square columns are presented in Fig. 4-50. It indicated that the location of concentrated concrete core crushing moved upward along with the increasing T/M ratios due to the torsion effect.

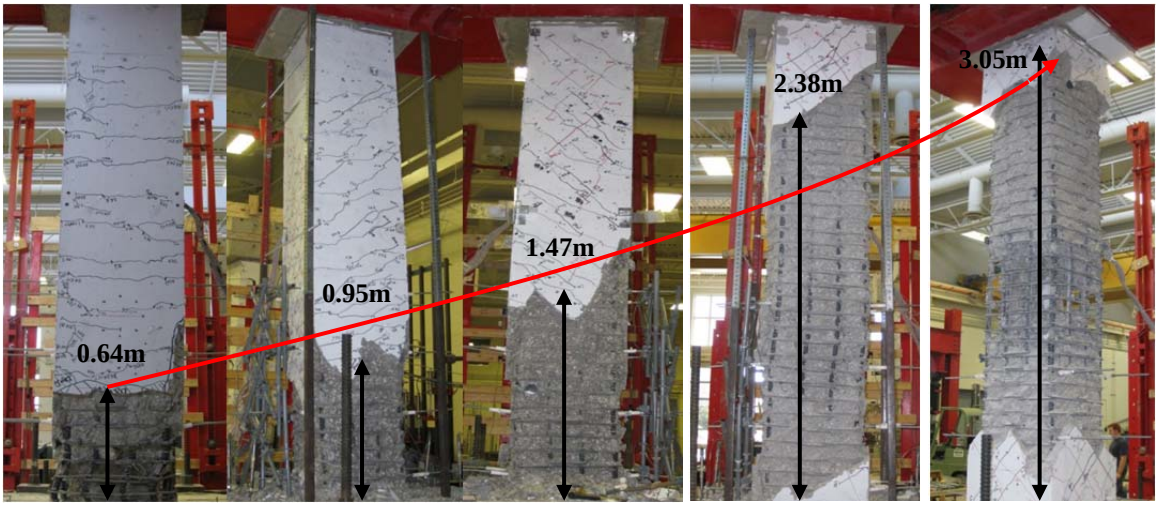

T / M = 0 T / M = 0.2 T / M = 0.4 T / M = 0.6 T / M = ∞

Fig. 4-49 Effect of Combined Loading on Concrete Cover Spalling Distribution

Reinforcement Buckling and Rupturing - After severe spalling of the concrete cover and significant degradation of the concrete core at post-peak stage, the longitudinal and transverse reinforcement were exposed without any confinement and protection from the concrete. The longitudinal bars then began to buckle or rupture due to the cyclic compressive or tensional force from combined loading. The buckling and rupturing of longitudinal bars was typically observed in the flexural plastic-hinge zone for all the RC square columns in this study. In addition, the transverse bars ruptured due to the excessive transverse stress or strain from the confinement effect. However, the length of the buckled longitudinal bar increased with the level of applied torsion. This buckling is a final damage limit state because it represents the collapse of the structure. Meanwhile the transverse bars would rupture due to the transverse confinement strain exceeding the limit strain of reinforcement. The observed typical longitudinal bar buckling and transverse or longitudinal bar rupturing are presented in Fig. 4-51.

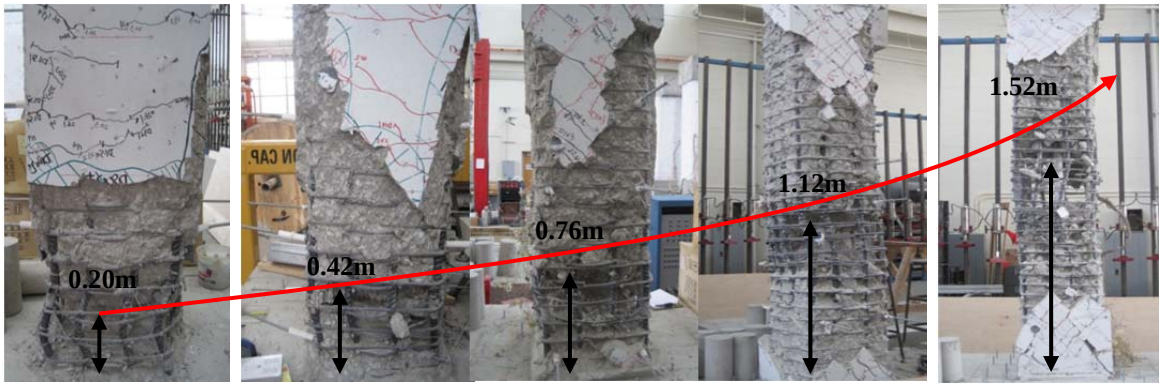

T / M = 0 T / M = 0.2 T / M = 0.4 T / M = 0.6 T / M = ∞

Fig. 4-50 Effect of Combined Loading on Concrete Core Crushing

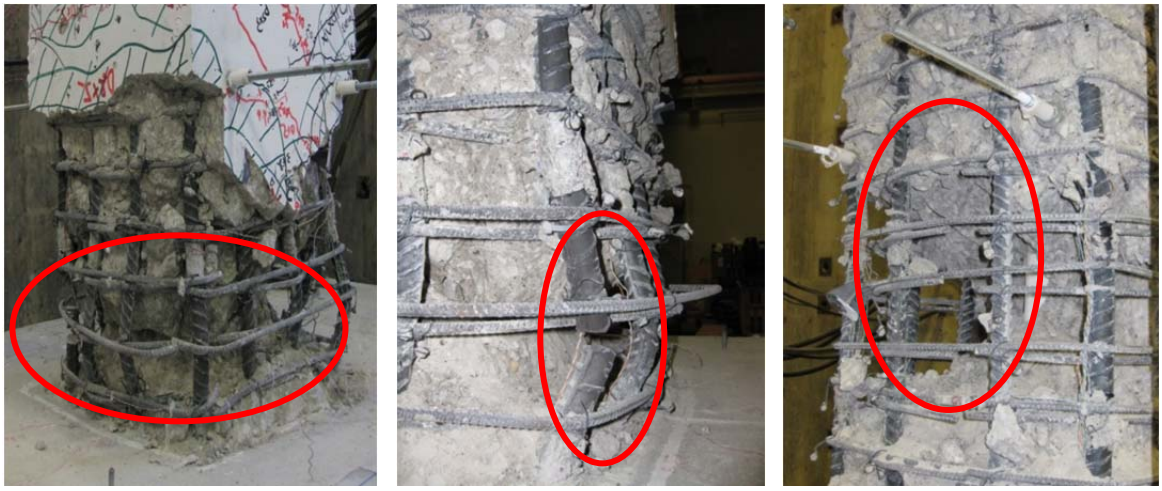

(a) Longitudinal Bars Buckle (b) Transverse Bars Rupture (c) Transverse Bar Rupture

Fig. 4-51 Typical Longitudinal and Transverse Reinforcement Failure Modes

Damage Progression of the Column under Various T/M ratios - The RC square columns under combine loading at T/M ratios of 0, 0.2 and 0.4 experienced flexure dominant failure mode; and the columns under pure torsion and the T/M ratio of 0.6 failed in the torsion dominant mode. The sequential damage limit states are different among the columns at different T/M ratios as shown in Table 4-2. A higher portion of the torsional moment level caused the damage progression such as severe shear cracking, transverse reinforcement first yielding, early concrete spalling before peak load and final failure by concrete crushing; while a higher portion of the bending moment level resulted

in the damage progression such as horizontal and inclined flexural cracking, longitudinal reinforcement first yielding, lagged concrete cover spalling and failure by buckling and fracture of longitudinal bars.

Table 4-2 Damage Progression and Characteristics of Square Columns under Combined Loading

No.	T/M= ∞	T/M= 0.6	T/M= 0.4	T/M= 0.2	T/M=0
1	Inclined Cracks (44˚- 46˚)	Inclined Cracks (40˚ - 42˚)	Inclined and Flexural Cracks at The Bottom	Horizontal Flexure Cracks at The Bottom	Horizontal Flexure Cracks at The Bottom
2	①	Big Shear Crack ①	Inclined Cracks (36˚ - 38˚)	Inclined Cracks (28˚ - 30˚)	Inclined Cracks At Side Faces
3	③	③⑤	Big Shear Crack ①②	②	②
4	⑤⑥	④②	④③⑤	①④③⑤	④③
5	Failure by ⑩	Failure by ⑥⑦⑩	Failure By ⑦⑨⑩	Failure by ⑦⑧⑨⑩	Failure by ⑦⑧⑨⑩

Note: ① Transverse Reinforcement Yield; ② Longitudinal Reinforcement Yield; ③ Concrete Spalling; ④ Peak Lateral Load; ⑤ Peak Torque; ⑥ Dowel Action of Longitudinal Bar; ⑦ Buckling of Longitudinal Bars; ⑧ Rupture of Longitudinal Bars; ⑨ Rupture of Transverse Reinforcement; ⑩ Severe core concrete crushing

4.3.5.2 Oval Columns with Interlocking Spirals under Combined Loading

Flexural and Torsional Cracking - For the oval columns tested in this study, flexural cracks occurred first and then the inclined cracks, which were normal to the direction of the principal tensile stress, developed at a higher portion of the column. The mechanism of concrete cracking in oval columns under combined loading is the same as in the square columns. The cracks of columns under biaxial loading occurred more likely around all the faces; while the one under uniaxial loading concentrated on the interlocking region of two side faces. The observed cracking distribution and angle of all the columns with respect to the transverse axis was presented in Fig. 4-52, which indicated that the cracking angle increased from 0˚ to 45˚ as the T/M ratio increased from 0 to ∞.

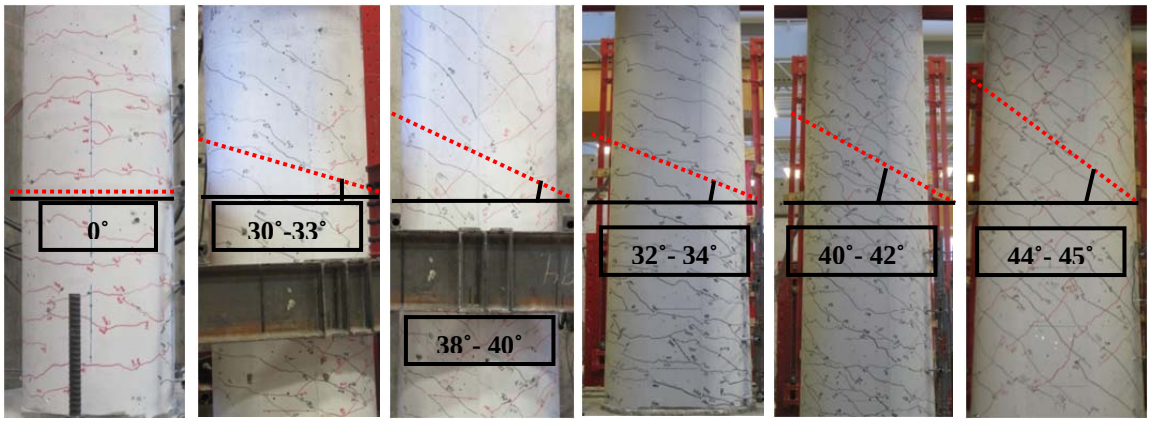

Biaxial T / M = 0 | Biaxial T / M = 0.2_ | Biaxial T / M = 0.4 | Uniaxial T / M = 0.2 | Uniaxial T / M = 0.6 | T / M = ∞

Fig. 4-52 Effect of Uniaxial and Biaxial Combined Loading on Crack Inclination and Distribution

Longitudinal and Transverse Reinforcement Yielding - The typical longitudinal strain of reinforcement for columns under uniaxial and biaxial combined loading at different T/M ratios are summarized and compared in Fig. 4-53 and Fig. 4-54. The longitudinal reinforcement strain at the plastic hinge zone was increased significantly by the combined loading effect. This was because the higher torsional moment contributed to developing a longitudinally tensile strain of reinforcement over the whole cross section after the concrete cover spalling off and the concrete core degradation. On average, the longitudinal strain for columns under uniaxial loading was larger than the one under biaxial loading because the uniaxial loading was applied about the weak axis resulting in a larger longitudinal deformation. In addition, all longitudinal reinforcement over the cross section of the column under biaxial loading yielded at post-peak stage due to the bending moment can be divided into two portions about the strong and weak axis, respectively.

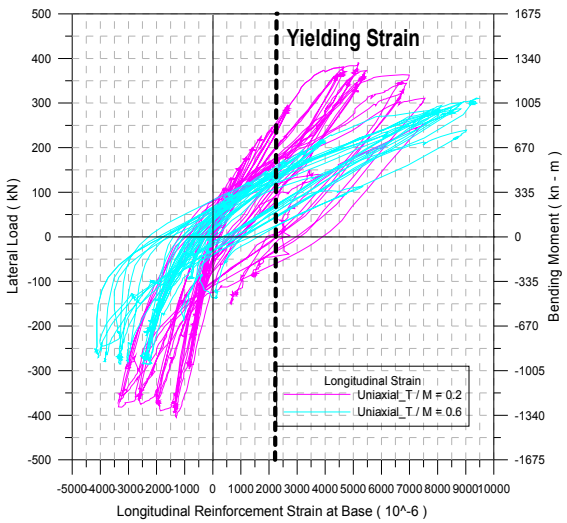

Fig. 4-53 Effect of Uniaxial Combined Loading on Longitudinal Bar Strain

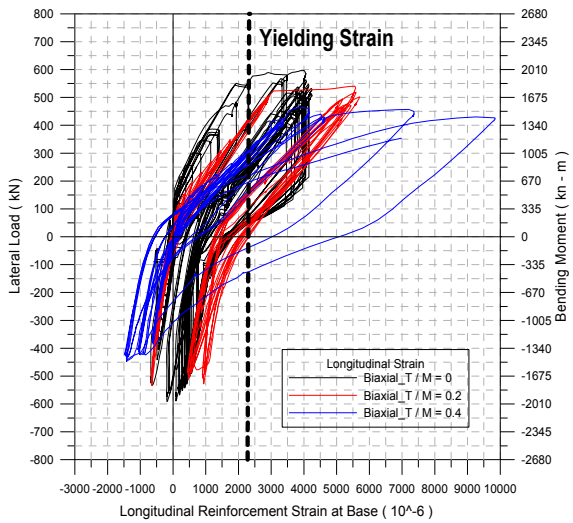

Fig. 4-54 Effect of Biaxial Combined Loading on Longitudinal Bar Strain

The strain history of transverse reinforcement for columns at the plastic hinge zone are plotted and compared in Fig. 4-55 and Fig. 4-56. The torsional moment of combined loading was mainly resisted by the tensile force of interlocking spirals, which resulted in uniformly large tensile transverse strain and limited compressive transverse strain over the whole cross section as shown in the figures. Therefore the strain of spirals increased considerably along with the increase of the T/M ratios providing more confinement to the concrete core to resist the torsional moment. In addition, the spirals achieved higher transverse strain in the locking direction compared to the unlocking direction, which provided more confinement to the core concrete and higher torque resistance. The biaxial combined loading magnified the locking and unlocking effect of spirals, which resulted in a larger transverse reinforcement strain in spirals.

Concrete Cover Spalling - Under flexure and shear, spalling typically occurs when the concrete at the cover approaches the crushing strain. Under combined loading, the spalling of the concrete cover occurs due to shear flow characteristics and changes in the shear flow direction. Finally the separation between the concrete cover and the concrete

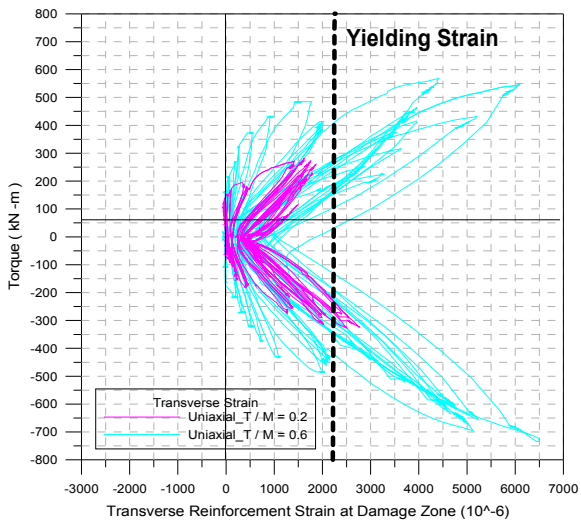

Fig. 4-55 Effect of Uniaxial Combined Loading on Spiral Strain

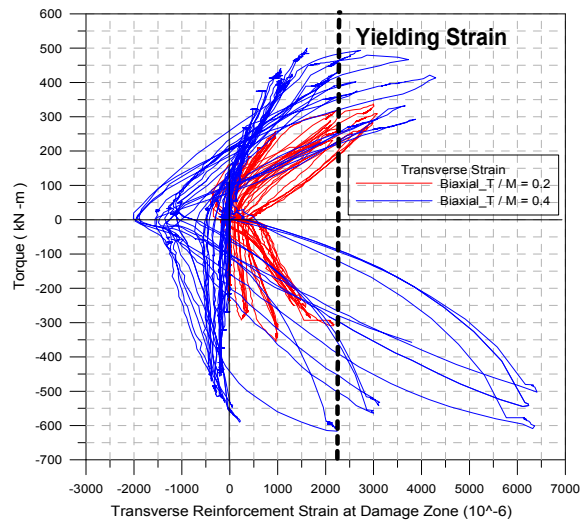

Fig. 4-56 Effect of Biaxial Combined Loading on Spiral Strain

core is induced by the interfacial failure between them from the change in direction of the compressive stresses in the concrete cover and the differences in the mechanical behavior of the concrete core and the cover. Spalling of the concrete cover along the columns under uniaxial and biaxial combined loading will generally occur after excessive yielding of reinforcement and prior to reaching the peak load, which induces significant stiffness degradation. Under combined loading, the observed concrete cover spalling length and intensity increased with increasing the T/M ratio, and biaxial loading did not show a significant effect on spalling distribution compared to uniaxial loading as shown in Fig. 4-57. The columns under low T/M ratios failed in flexure dominant mode with smaller concrete cover spalling length, and the columns under the high T/M ratio failed in torsion dominant mode with larger concrete cover spalling length.

Crushing of the Diagonal concrete Strut -_After concrete cover spalling, the severe concrete cracking divided the concrete into a diagonal concrete strut. The crushing of the diagonal concrete strut indicated severe damage of columns which represents the failure of the RC member. The typical concrete core crushing modes for uniaxial and biaxial

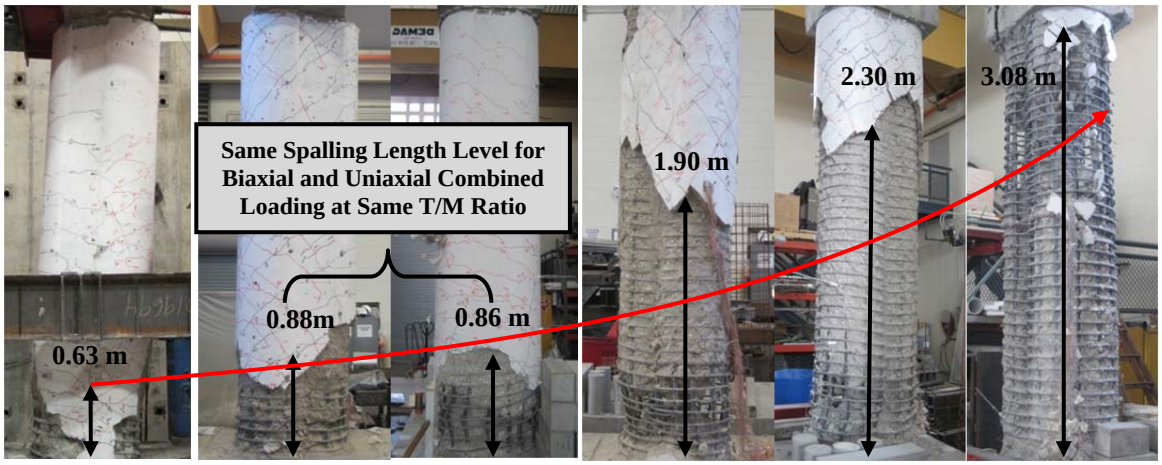

Pure Bending	Biaxial	Uniaxial	Biaxial	Uniaxial	Pure Torsion
T/M=0	T/M=0.2	T/M=0.2	T/M=0.4	T/M=0.6	T/M=∞

Fig. 4-57 Effect of Uniaxial and Biaxial Combined Loading on Concrete Cover Spalling Distribution

combined loading are presented in Fig. 4-58. The core concrete experienced more severe crushing with increased T/M ratios from 0 to ∞ due to the torsion effect, and the biaxial combined loading magnified the torsion effect to cause more concrete crushing compared to uniaxial combined loading. The concrete core crushing locations for uniaxial and biaxial combined loading are compared in Fig. 4-59. For columns under flexure and shear and combined loading, the locations of concrete core crushing shifted upwards along with increasing T/M ratios. The uniaxial and biaxial loading had less effect on the concrete core crushing locations.

Reinforcement Buckling and Rupture - The reinforcement then begins to buckle or rupture due to the nature of cyclic loading during an earthquake. The formation and mechanism of reinforcement buckling and rupturing in oval columns under combined loading were as same as to the square columns. This buckling or fracture is the final damage limit state because it represents the collapse of the structure. The observed typical longitudinal bar buckling and fracture are presented in Fig. 4-60. No transverse rupturing was observed in oval column.

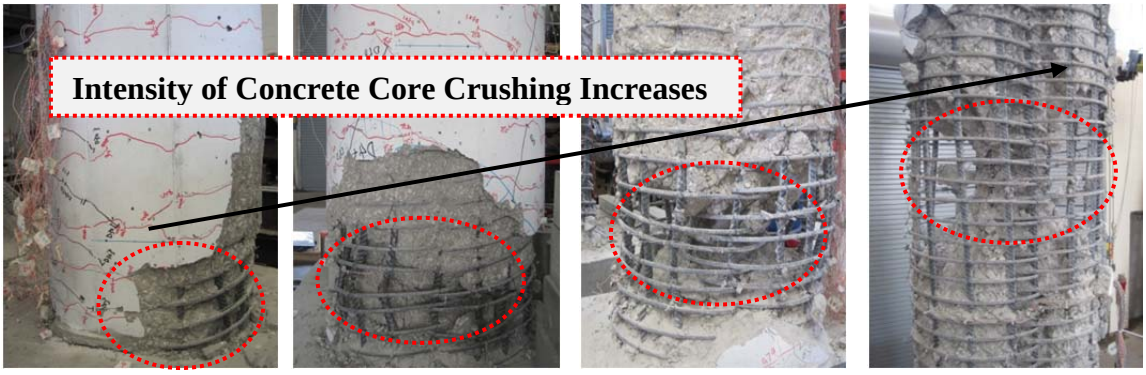

Pure Bending T/M=0 | Uniaxial Combined Load | Biaxial Combined Load | Pure Torsion T/M=∞

Fig. 4-58 Concrete Core Crushing Characteristics under Biaxial and Uniaixal Combined Loading

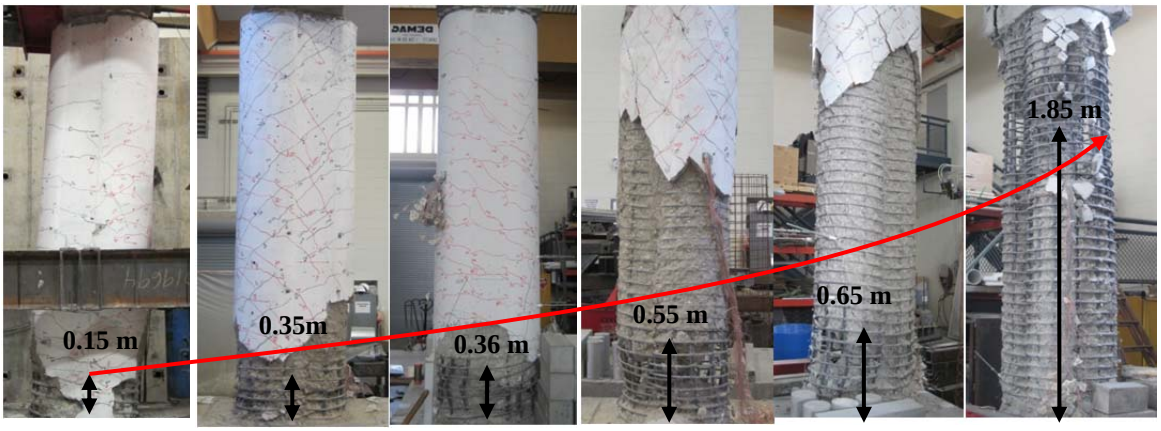

Pure Bending T/M=0 | Biaxial T/M=0.2 | Uniaxial T/M=0.2 | Biaxial T/M=0.4 | Uniaxial T/M=0.6 | Pure Torsion T/M=∞

Fig. 4-59 Effect of Uniaxial and Biaxial Combined Loading on Concrete Core Crushing Locations

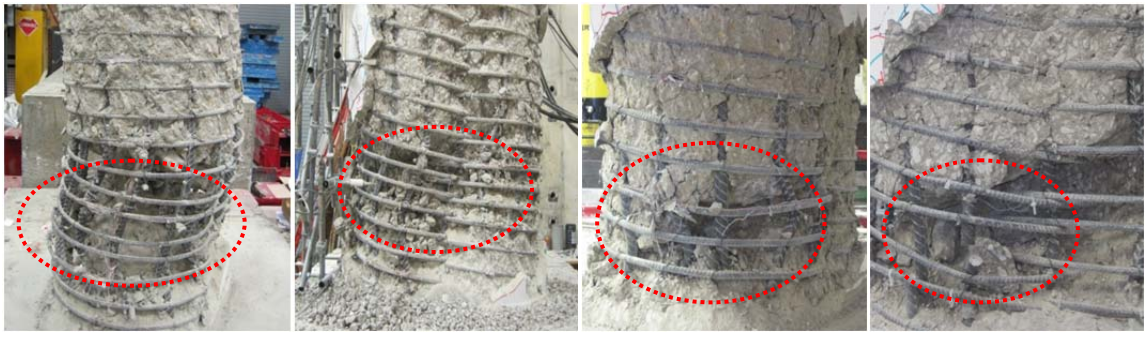

(a) Longitudinal Reinforcement Buckling (b) Longitudinal Reinforcement Fracture

Fig. 4-60 Typical Longitudinal Reinforcement Failure Modes

Damage Progression of the Column at Various T/M ratios - The oval columns under uniaxial and biaxial combined loading at low T/M ratios of 0.0, 0.2 and 0.4 experienced

flexure dominant failure mode; while the columns under pure torsion and a T/M ratio of 0.6 failed in torsion dominant failure mode. Larger T/M ratios caused the damage progression such as severe shear cracking, transverse reinforcement first yielding, early concrete spalling before peak load and final failure by concrete crushing; while the lower T/M ratios resulted in the damage progression such as horizontal and inclined flexural cracking, longitudinal reinforcement first yielding, lagged concrete cover spalling and failure by buckling and fracture of longitudinal bars. The sequential damage limit states, which mainly depend on the response and failure mode of members, are different among the columns at different T/M ratios as shown in Table 4-3.

Table 4-3 Damage Progression and Characteristics for Oval Columns under Combined Loading

No.	T/M= ∞	Uniaxial Loading T/M= 0.6	Biaxial Loading T/M= 0.4	Biaxial and Uniaxial Loading T/M= 0.2	Biaxial Loading T/M=0
1	Inclined Cracks (44˚- 45˚)	Inclined Cracks (40˚- 42˚)	Inclined and Flexural Cracks at the Bottom	Horizontal Flexural Cracks at the Bottom	Horizontal Flexural Cracks at the Bottom
2	Big Shear Crack ①	Big Shear Crack①	Shear Cracks (38˚- 40˚)	Shear Cracks (30˚-33˚)	Shear Cracks At Side Faces
3	③⑤	③	②①	②	②
4	⑥	④②⑤	④③⑤	①④③⑤	④③①
5	Failure by ⑨	Failure by ⑥⑦⑨	Failure by ⑦⑨	Failure by ⑦⑧⑨	Failure by⑦⑨

Note: ① Transverse Reinforcement Yield; ② Longitudinal Reinforcement Yield; ③ Concrete Spalling; ④ Ultimate Lateral Load; ⑤ Ultimate Torque; ⑥ Dowel Action of Longitudinal Bar; ⑦ Buckling of Longitudinal Bars; ⑧ Rupture of Longitudinal Bars; ⑨ Severe core concrete crushing

4.3.5.3 Observed Damage Characteristics Comparison

In this section, the observed concrete cover spalling length, concrete cover crushing depth, and severe damage zone location are summarized and discussed. The definitions of

the damage characteristics are shown in Fig. 4-61 and Fig. 4-62. The concrete cover spalling length was taken as the largest length of concrete cover spalling on all the faces of the columns. The concrete core crushing depth was measured from the original outer surface to the deepest spot of concrete core crushing. The height of the severe damage zone was defined as the distance from the base of column to the severe concrete core crushing location.

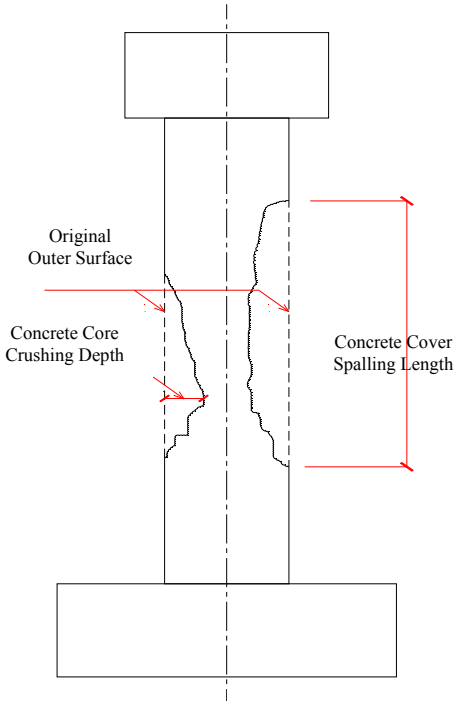

Fig. 4-61 Definition of Spalled Length and Concrete Core Crushing Depth

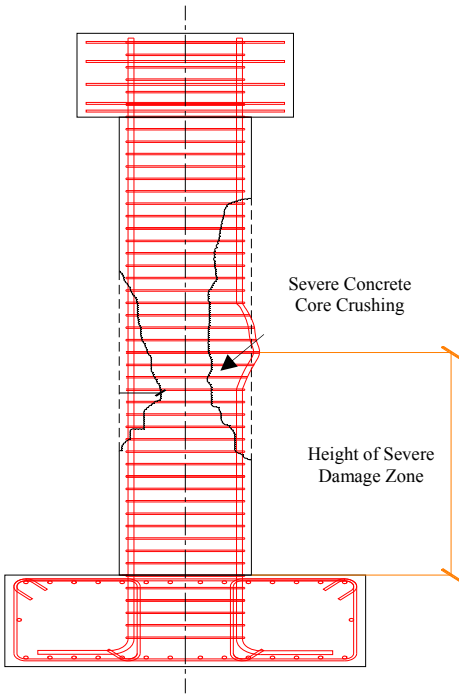

Fig. 4-62 Definition of the Height of Severe Damage Zone

Square Column - The quantified typical damage characteristics for square columns under combined loading are summarized in Table 4-4. The length of the concrete cover spalling and the height of the severe damage zone were increased along with increasing the applied torsional moment. The torsion effect also deteriorated the concrete core crushing according to the comparison of the concrete core crushing depth. For the column under the lower T/M ratios, half of the concrete core crushed at the final failure stage; for the column under the higher T/M ratios, the whole concrete core completely crushed at

the final failure stage. For the columns with flexure dominant failure mode, all longitudinal reinforcement over the cross section yielded after the concrete core was crushed; for the columns with torsion dominant failure mode, more than half of the longitudinal reinforcement over the cross section yielded due to the excessive longitudinal strain by the torsional moment. In addition, the longitudinal reinforcement buckling and rupturing or transverse reinforcement rupturing more likely happened in the column with the lower T/M ratios of 0, 0.2, and 0.4 due to the larger cyclic compression and tension force under flexure.

Table 4-4 Summaries of Quantified Typical Damage Characteristics for Square Columns

T/M	Concrete Damage		Reinforcing Steel Damage				Damage Location (mm)
	Spalled Length (mm)	Core Crushing Depth (mm)	No. of Yielded Long. Bars	No. of Buckled Long. Bars	No. of Ruptured Long. Bars	No. of Ruptured Ties	
0	640	>160	12/12	11/12	4/12	4	200
0.2	950	>160	12/12	10/12	2/12	3	420
0.4	1470	>182	10/12	10/12	0/12	2	760
0.6	2380	>280	9/12	4/12	0/12	1	1120
∞	3050	>280	7/12	2/12	0/12	1	1520

Oval Column - The quantified typical damage characteristics for oval columns under combined loading are summarized in Table 4-5. It was found that the length of the concrete cover spalling and height of the severe damage zone were affected by the combined loading effect which was identified to various T/M ratios. The columns with a larger torsion effect were also observed with more concrete core crushing depth. For the column under lower T/M ratios, one-third of the concrete core crushed at the final failure stage; for the column under higher T/M ratios, more than two-thirds of the concrete core crushed at final failure stage. For the columns with flexure dominant failure mode, the longitudinal reinforcement around the cross sectional circumference yielded after the

concrete core crushed; for the columns with torsion dominant failure mode, more than half of the longitudinal reinforcement over the cross section circumference yielded due to the excessive longitudinal strain by torsional moment. In addition, two of the longitudinal reinforcement in the interlocking region of columns under uniaxial loading showed yielding since they were located far from the neutral axis of the cross section; and none of the longitudinal reinforcement in the interlocking region of columns under biaxial loading yielded since they were located close to the neutral axis of the cross section. The longitudinal reinforcement buckling and rupturing more likely happened in the column with the lower T/M ratios due to the larger cyclic compression and tension force under flexure. None of the spirals was observed to rupture at the final failure stage.

However, the differences between the height of severe damage zone locations in oval columns, under flexure and shear and combined loading, were less than the differences in the square columns due to the fact that interlocking spirals provided better transverse confinement and improved the torsional stiffness and strength degradation at post-peak stage, which in turn equivalently altered the torsion dominant failure modes to the flexure dominant failure modes and generally lowered the height of the concrete core crushing. However, the location of the severe damage zone in the oval column under pure torsion was much higher than the one in the square column. This phenomenon was caused by the larger stiffness of the oval column from the larger dimension size and better transverse confinement, which corresponded to the stiffness redistribution along the column, top locking blocks and the loading base and resulted in the severe damage zone shifting up towards the weaker top loading block. It was found that the location of the torsional

damage zone was also affected by the relative stiffness between the column and boundary constraints, which should be considered in the future design process.

Table 4-5 Summaries of Quantified Typical Damage Characteristics for Oval Columns

T/M Ratios	Concrete Damage		Reinforcing Steel Damage				Damage Location (mm)
	Spalled Length (mm)	Core Crushing Depth (mm)	No. of Yielded Long. Bars	No. of Buckled Long. Bars	No. of Ruptured Long. Bars	No. of Ruptured Trans. Bar	
Biaxial0	630	>60	>16/20	7/20	4/20	0	150
Biaxial 0.2	880	>120	>16/20	10/20	4/20	0	350
Biaxial 0.4	1900	>260	>14/20	8/20	2/20	0	550
Uniaxial 0.2	860	>80	>10/20	9/20	5/20	0	360
Uniaxial 0.6	2300	>240	>10/20	8/20	1/20	0	650
∞	3080	>300	>6/12	2/20	0/20	0	1850

4.3.6. Ductility Capacity and Locking and Unlocking Effect

4.3.6.1 Ductility Capacity Definition

The lateral displacement and twist deformation along the length of a column under combined loading are shown in Fig. 4-63. The flexural displacement distribution is essentially linear before the yielding of the longitudinal bars under the tensile forces from combined flexure, shear and torsion; thereafter, it becomes nonlinear. The yielding of the longitudinal reinforcement, the subsequent concrete cover spalling and concrete core crushing result in the formation of a flexural plastic-hinge. The column under flexure dominant failure mode typically forms a plastic-hinge zone at the bottom portion where the maximum bending moment occurs as shown Fig. 4-63 (a). The plastic hinge would develop upwards to the height of L_P, defined as the plastic hinge length, along with an increasing applied load. The flexural displacement distribution above the plastic hinge can be assumed to be linear. The twist distribution of columns tested under pure torsion

or combined loading including torsion is essentially linear before inclined cracking, becoming nonlinear thereafter, as shown in Fig. 4-63 (b).

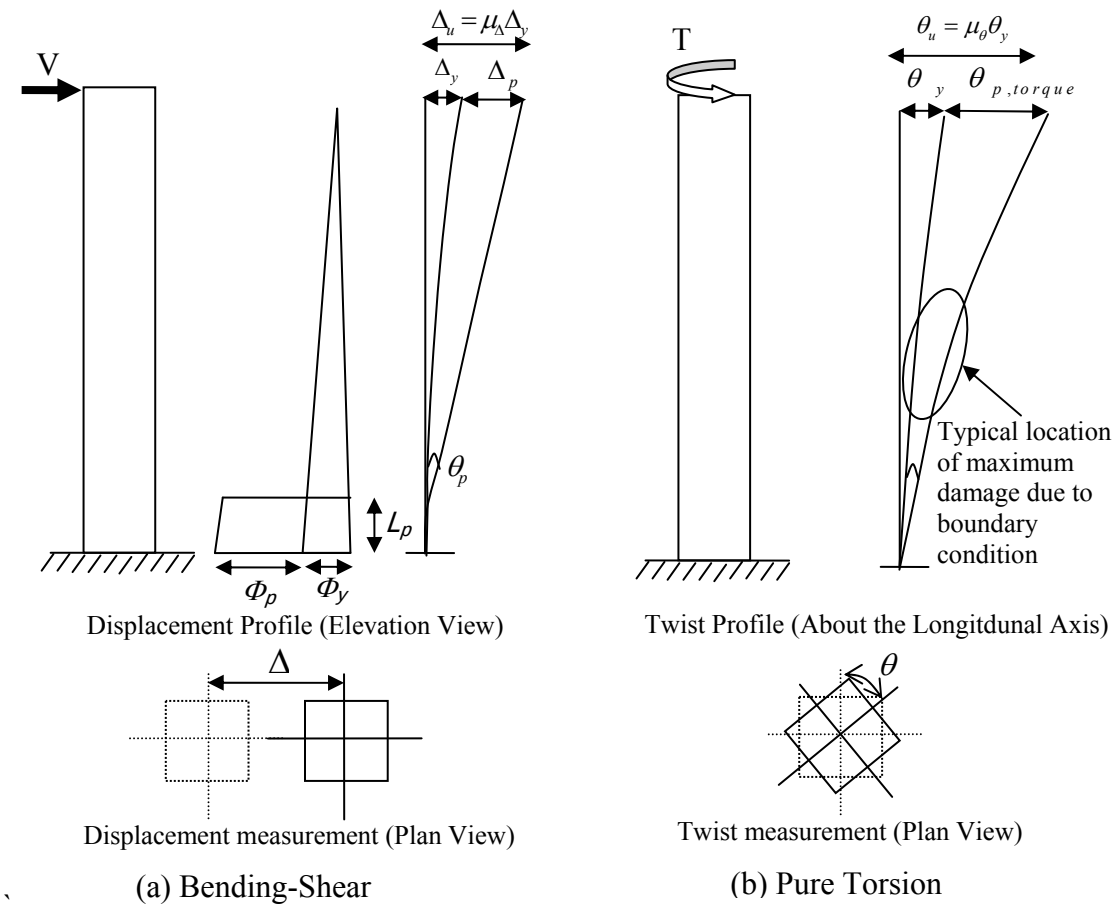

(a) Bending-Shear (b) Pure Torsion

Fig. 4-63 Displacements/Twist Distribution along the Length of Column

The seismic design codes specify that the structure or members should be capable of undergoing substantial inelastic deformations without loss of strength, which is noted as ductile behavior. Under flexure and shear, total flexural displacement Δ_t after yielding was composed of yielding displacement Δ_y and plastic displacement Δ_p. The yielding displacement Δ_y was calculated by the average displacement of two actuators once the first longitudinal reinforcement was captured to yield. The total lateral displacement Δ_t at each load level after yielding was also calculated by the average displacement from the two top string transducer. The yielding load level was taken as ductility level one and

then the instant displacement ductility Δ_θ after yielding could be calculated from the ratio of the instant total displacement to the yielding displacement as given by

$$\mu_\Delta = \frac{\Delta_t}{\Delta_y}. \tag{4-1}$$

Under pure torsion, similarly, total twist deformation θ_t after yielding was composed of yielding displacement θ_y and plastic displacement θ_p. The yielding twist θ_y was calculated by the ratio of subtraction of the two actuators' displacement to the distance between the two actuators when the first transverse reinforcement was captured to yield. The total twist deformation θ_t at each load level after yielding was calculated by the ratio of subtraction of the two top transducers' displacement to the distance between them. The yielding load level was taken as ductility level one and then the instant twist ductility μ_θ after yielding could be calculated from the ratio of the instant total twist deformation to the yielding twist deformation as given by

$$\mu_\theta = \frac{\theta_t}{\theta_y}. \tag{4-2}$$

In our test, both lateral displacement and twist deformation are included in the columns under combined flexure, shear, and torsional loads. The yielding load or deformation was captured by monitoring whatever the first yielding of longitudinal and transverse reinforcement. Then the instant displacement or twist ductility level after yielding can be measured and calculated based on the displacement data from the actuators or string line transducers. The ductility capacity μ_m was considered as the ratio of ultimate displacement/rotation to yielding displacement/rotation, where the ultimate displacement/rotation was determined based on the ultimate load (80% of peak load).

4.3.6.2 Locking and Unlocking Efficient Definition

As discussed above, the transverse reinforcement performed more active confinement to the concrete core after transverse yielding. Under pure torsion, the ties in square columns behaved in the same way during positive and negative cycles; the two spirals in oval columns were locked together with each other during the negative cycles of twisting and unlocked in the positive cycles of twisting. The locking and unlocking effect could either enhance the confinement to the concrete core contributing to the strength of it or reduce the confinement effect on the concrete core. Under combined loading, one side of the cross section is always subjected to higher additive shear stress from combined flexure and torsion, leading to more damage and less load resistance. As a result, this locking and unlocking effect and asymmetric features of additive shear stresses cause the torsional moment of oval columns in the negative cycles to be much higher than the positive cycles of loading, especially at higher ductility levels. The asymmetric feature of torsional response can be evaluated by the ratio of the difference between positive and negative peak torque to the positive peak torque, which was notated as the locking and unlocking coefficient as expressed by

$$\kappa = \frac{\left| T_{peak-} - T_{peak+} \right|}{T_{peak+}}, \tag{4-3}$$

where κ is the locking and unlocking coefficient, T_{peak-} is the peak torque during the negative loading cycles, and T_{peak+} is the peak torque during the positive cycles. Therefore, the locking and unlocking efficient included not only locking and unlocking effect from spirals but also the asymmetric features of additive shear stresses from combined shear and torsion.

4.3.6.3 Comparison on Locking and Unlocking Efficient and Ductility Capacity

The peak torque in positive and negative cycles, locking and unlocking coefficient, and ductility capacity in square columns are summarized in Table 4-6. There is no locking and unlocking effect from the ties in square columns. Therefore, very small locking and unlocking efficient were obtained in all the square columns, which were introduced only by the asymmetric features of additive shear stresses from combined shear and torsion. Also the asymmetric feature of peak torque in square columns was increased along with decreasing T/M ratios because the lower T/M ratios with more shear forces under combined loading resulted in more asymmetrically additive shear stresses inside the outer shear flow zone, which in turn increased the locking and unlocking efficient. In addition, all the square columns with octagonal and square ties achieved adequate ductility capacity of more than four which is required by seismic design codes. The flexural and torsional deformation capacities were reduced by the combined loading effect. Moreover, the combined loading did reduce the ductility capacity compared to pure torsion and pure flexure and shear cases. However, the ductility capacities for columns under combined loading were attained at the same level of 4.5 and not affected by varying T/M ratios.

Table 4-6 Comparison on Peak Torque, Locking and Unlocking Coefficient and Ductility Capacity in Square Columns

Square Columns	S-H/B(6)-T/M(0.2)		S-H/B(6)-T/M(0.4)		S-H/B(6)-T/M(0.6)		S-H/B(6)-T/M(∞)	
Peak Torque (kN-m)	+	-	+	-	+	-	+	-
	191	201	254	264	313	308	332	327
Locking and Unlocking Coefficient κ	0.0523		0.0393		0.0160		0.0151	
Ductility Capacity	4.5		4.5		4.5		8.0	

The peak torque in positive and negative cycles, locking and unlocking coefficient, and ductility capacity in oval columns under combined uniaxial and biaxial loading are summarized in Table 4-7. The large locking and unlocking efficient were achieved in all the oval columns, which were caused by not only by the locking and unlocking effect from interlocking spirals but also by the asymmetric features of additive shear stresses from combined shear and torsion. The locking and unlocking efficient in the oval columns was larger than the one in the square columns due to the winding and unwinding actions of interlocking spirals. The asymmetric feature of peak torque in the oval columns under combined loading was more intense than the pure torsion case since combined loading introduced the asymmetrically additive shear stresses distribution from combined shear and torsion. Also the locking and unlocking efficient under combined loading was increased along with decreasing T/M ratios because the lower T/M ratios with more shear forces under combined loading resulted in a more asymmetric feature of additive shear stresses inside the outer shear flow zone, which in turn increased the locking and unlocking efficient. In addition, the uniaxial combined loading amplified the locking and unlocking efficient by 10%-20% compared to the biaxial combined loading.

All the oval columns with interlocking spirals achieved much more ductility capacity than the cases in square columns because the interlocking spirals improved the transverse confinement to concrete core. As in the square columns, the combined loading did reduce the ductility capacity of oval columns compared to pure torsion and pure flexure and shear cases. However, the ductility capacities for columns under combined loading were attained at the similar level of six and not affected by varying T/M ratios.

Table 4-7 Comparison on Peak Torque, Locking and Unlocking Coefficient and Ductility Capacity in Oval Columns

Oval Columns	O-H/B(5.5)-T/M(0.2)-U		O-H/B(5.5)-T/M(0.6)-U		O-H/B(5.5)-T/M(∞)-U		O-H/B(5.5)-T/M(0.2)-B		O-H/B(5.5)-T/M(0.4)-B	
Peak Torque (kN-m)	+	-	+	-	+	-	+	-	+	-
	280	360	562	727	757	827	322	378	509	624
Locking and Unlocking Coefficient	0.286		0.294		0.100		0.174		0.2259	
Ductility Capacity μ_m	8.0		5.5		10.0		6.0		5.5	

4.3.7. Energy Dissipation Characteristics

Energy dissipation capacity is an important parameter in assessing the strength and stiffness degradation of reinforced concrete members subjected to cyclic loading of a structure. Energy dissipation is developed in RC members through crack formation, internal friction due to plastic deformation of the reinforcement, and friction resulting from sliding of the concrete struts. The dissipated flexural and torsional energy in the tested columns are defined as the area enclosed by the load-displacement and torque-rotation hysteresis curve respectively as demonstrated in Fig. 4-64. Additionally the equivalent ratio, which is derived based on their hysteretic response and hysteretic energy dissipated under fully reversed cyclic loading, can also be used to represent the energy dissipation of individual RC members under cyclic loads. All the equations and parameters defined for energy dissipation calculation are listed in Table 4-8. The flexural energy dissipation capacity is mainly determined by the strength of the concrete and longitudinal reinforcement, inelastic deformation of reinforcement in plastic hinge, and the arrangement of longitudinal reinforcement. The torsional energy dissipation capacity is affected by the concrete cover, the strength of concrete and transverse reinforcement, and configuration of transverse reinforcement. The dissipated flexural and torsional

energy of all the columns for each individual loading cycle and the accumulations of the dissipated energy are discussed in the following section.

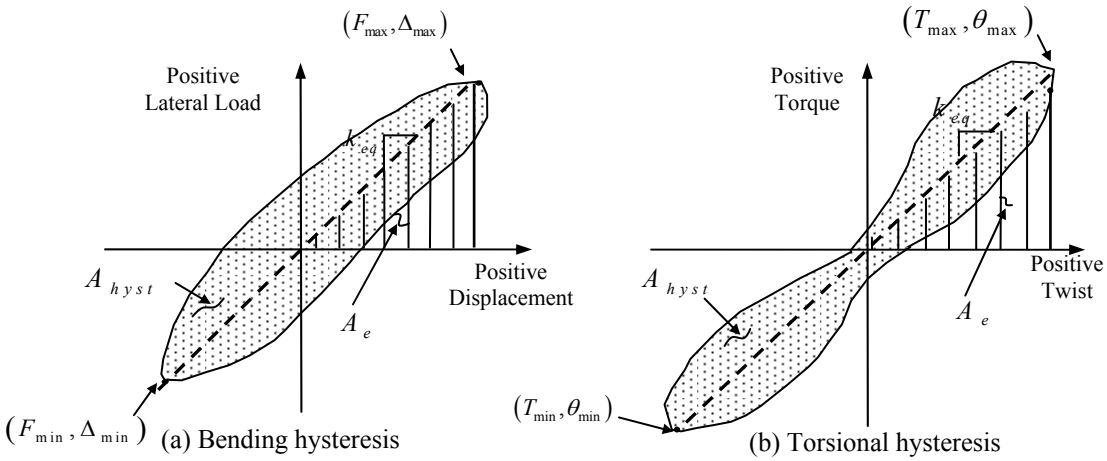

Fig. 4-64 Energy Dissipation and Equivalent Definition of Parameters

Table 4-8 Parameters for Energy Dissipation and Equivalent Damping Ratio

Parameters	Torsional Hysteresis	Flexural Hysteresis
Energy Dissipation	$E_{D,torsion} = A_{hyst,torsion}$ (4-4)	$E_{D,flexure} = A_{hyst,flexure}$ (4-5)
Average Peak Moment/Force	$T_m = \frac{1}{2}(T_{max} - T_{min})$ (4-6)	$F_m = \frac{1}{2}(F_{max} - F_{min})$ (4-7)
Average Peak Twist/ Displacement	$\theta_m = \frac{1}{2}(\theta_{max} - \theta_{min})$ (4-8)	$\Delta_m = \frac{1}{2}(\Delta_{max} - \Delta_{min})$ (4-9)
Effective Stiffness	$k_{eff,torsion} = \frac{T_m}{\theta_m}$ (4-10)	$k_{eff,flexure} = \frac{F_m}{\Delta_m}$ (4-11)
Strain Energy in Equivalent System	$A_{e,torsion} = \frac{k_{eff,torsion}}{2}(\theta_m)^2$ (4-12)	$A_{e,flexure} = \frac{k_{eff,flexure}}{2}(\Delta_m)^2$ (4-13)
Equivalent Damping System	$\xi_{eq,torsion} = \frac{A_{hyst,torsion}}{4\pi A_{e,torsion}}$ (4-14)	$\xi_{eq,flexure} = \frac{A_{hyst,flexure}}{4\pi A_{e,flexure}}$ (4-15)

4.3.7.1 Square Columns with Square and Octagonal Ties under Combined Loading

The dissipated flexural and torsional energy for each individual loading cycle and the accumulations of the dissipated energy are plotted in Fig. 4-65 through Fig. 4-72. For all the columns, the dissipated flexural energy at each load cycle was maintained at a low

level before the reinforcement yielding because they behave as an elastic response as shown in Fig. 4-65, Fig. 4-67, Fig. 4-69, and Fig. 4-71. Thereafter the flexural energy dissipated at the first load cycle of each ductility significantly increased along with the increasing ductility level until final failure. However, the dissipated flexural energy decreased along with the more applied loading cycle at each ductility, which indicated the strength and stiffness degradation.

All the columns started to dissipate torsional energy after concrete cover cracking, which was also the onset of inelastic torsional response. The torsional energy dissipation had well developed at the yielding stage since the concrete cover started spalling, which significantly contributed to torsional resistance. For the column tested under pure torsion with dominated tensional failure, the dissipated torsional energy dramatically increased at the peak torque stage with complete concrete cover spalling and continued to increase up to the higher ductility with more crushing of core concrete, and then decreased for the further more imposed ductility level until the ultimate failure as shown in Fig. 4-65. This fact indicated that torsional energy dissipation can be developed more after peak torque state with the contribution from the transverse confinement of spirals and dowel action of longitudinal reinforcement. For the columns tested under a combined loading at T/M ratios of 0.2, 0.4, and 0.6, the torsional energy increased along with more loading cycles up to the ultimate failure stage as the same trend as the flexural energy dissipation. Also the dissipated torsional energy decreased along with more applied loading cycle at each ductility due to the strength and stiffness degradation.

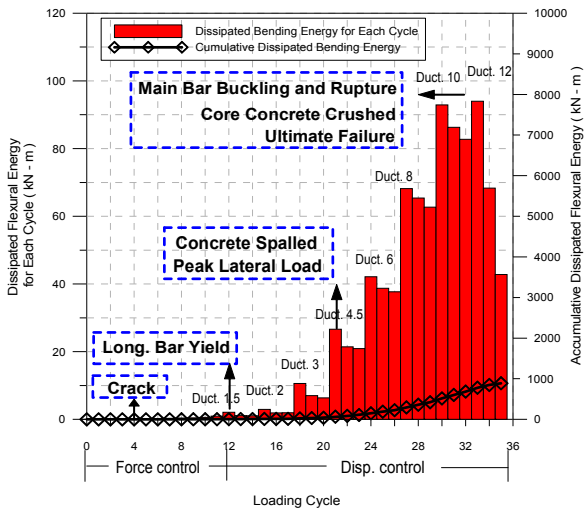

Fig. 4-65 Dissipated Flexural Energy under T/M=0

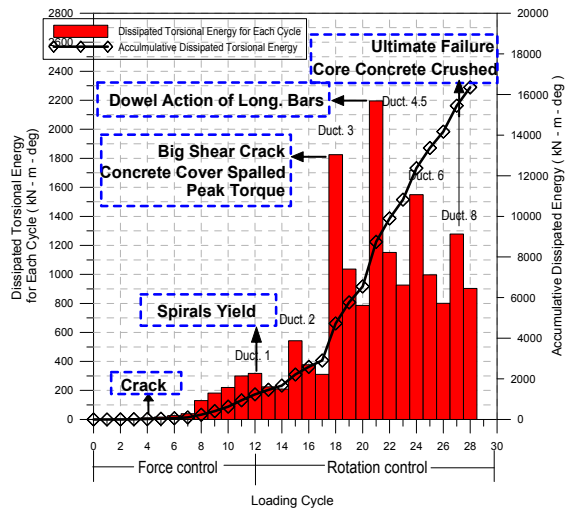

Fig. 4-66 Dissipated Torsional Energy under T/M=∞

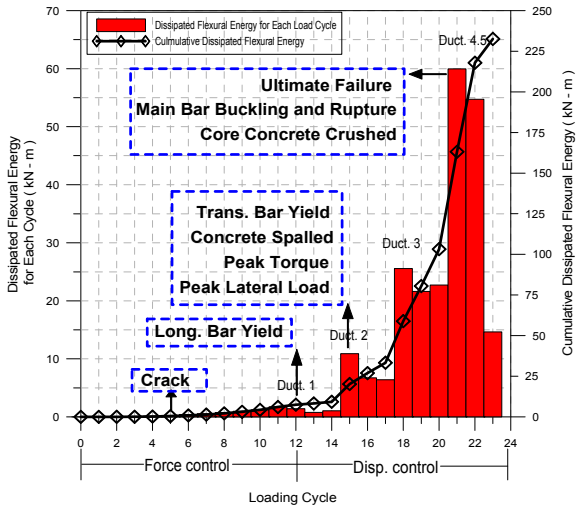

Fig. 4-67 Dissipated Flexural Energy under T/M=0.2

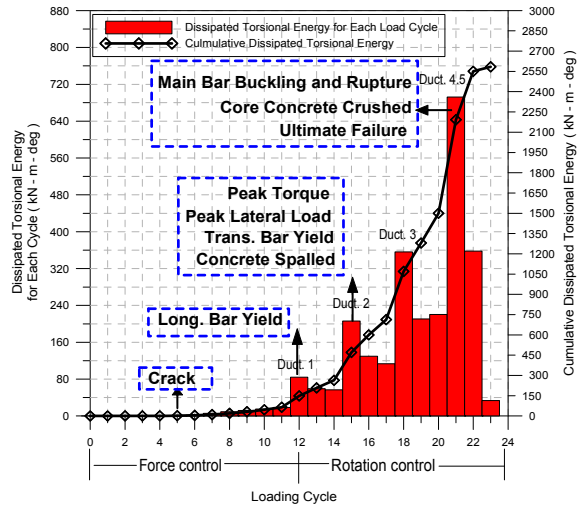

Fig. 4-68 Dissipated Torsional Energy under T/M=0.2

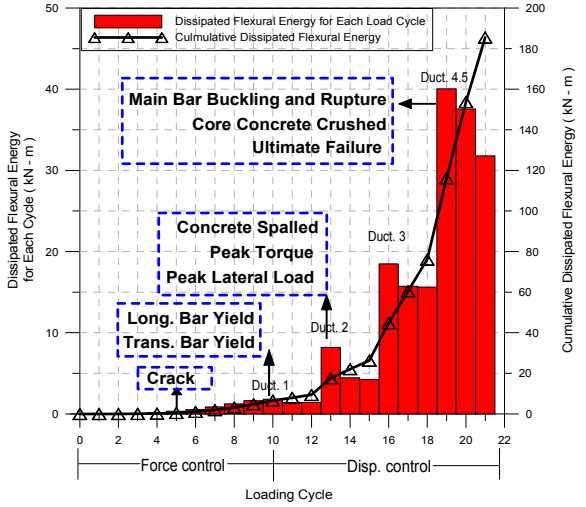

Fig. 4-69 Dissipated Flexural Energy under T/M=0.4

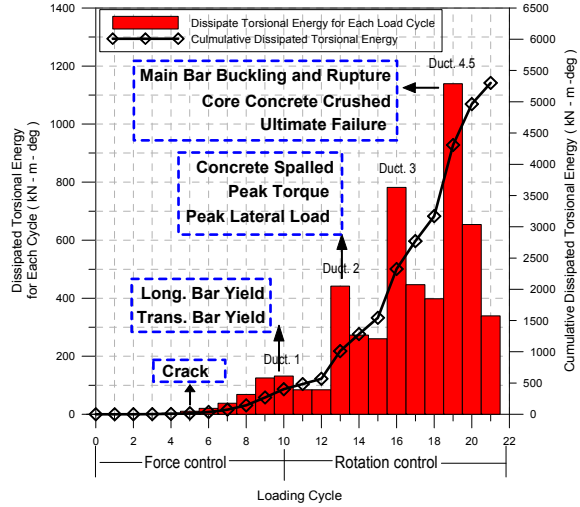

Fig. 4-70 Dissipated Torsional Energy under T/M=0.4

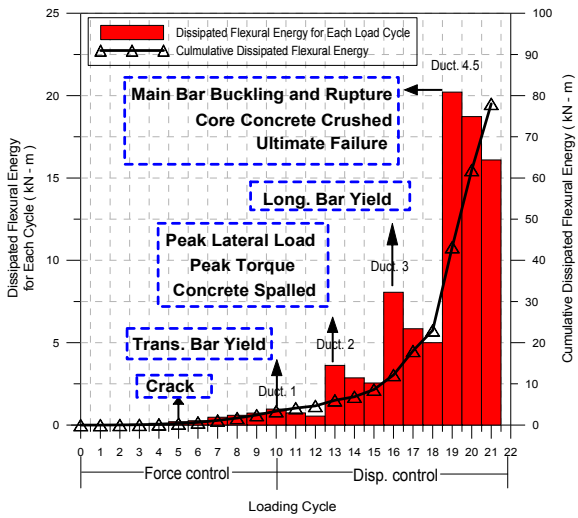

Fig. 4-71 Dissipated Flexural Energy under T/M=0.6

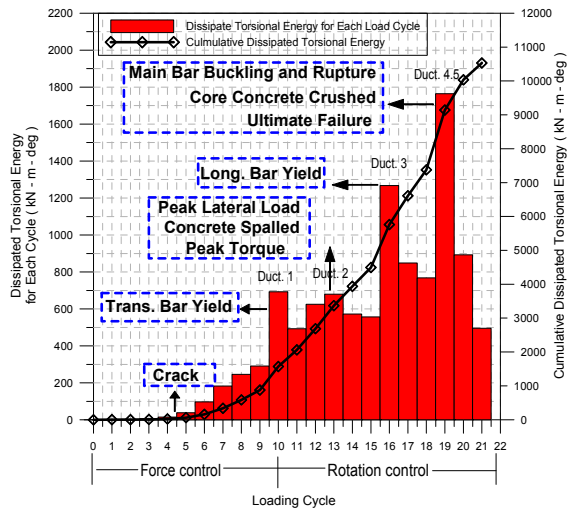

Fig. 4-72 Dissipated Torsional Energy under T/M=0.6

The cumulative dissipated flexural and torsional energy at the first load cycle of each ductility level for all the columns were plotted and compared in Fig. 4-73 and Fig. 4-74. It was found that the dissipated flexural energy decreased significantly as the T/M ratio increased due to torsion effect, which led to a less displacement ductility capacity, severer concrete cracking, more stiffness degradation and concrete core crushing; and the dissipated torsional energy decreased as the T/M ratio decreased due to the flexural effect such as flexural crack, buckling of longitudinal reinforcement and core concrete crushing. For all the columns, the energy dissipation rate versus deformation ductility increased along with the increase in the T/M ratio, which indicated that the torsional moment in columns under combined loading accelerated the energy dissipation due to the more rapid and greater stiffness degradation from the torsion effect. In addition, larger displacement ductility and flexural energy dissipation are required to yield the transverse reinforcement along with decreasing T/M ratios, and larger rotation ductility and torsion energy dissipation are required to yield the longitudinal reinforcement because of torsion dominated failure mode.

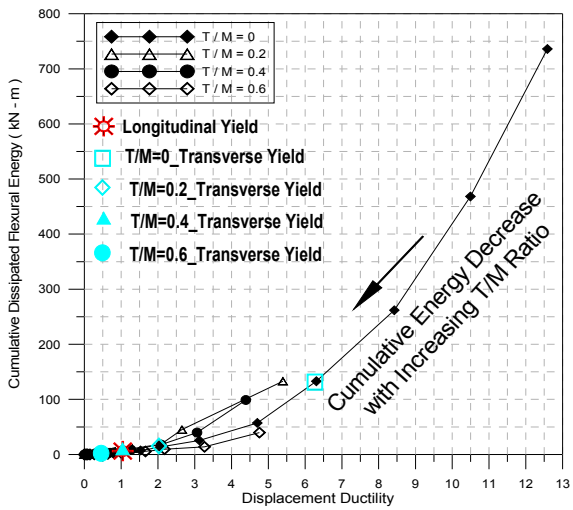

Fig. 4-73 Comparison of Cumulative Flexural Energy Dissipation under Combined Loading

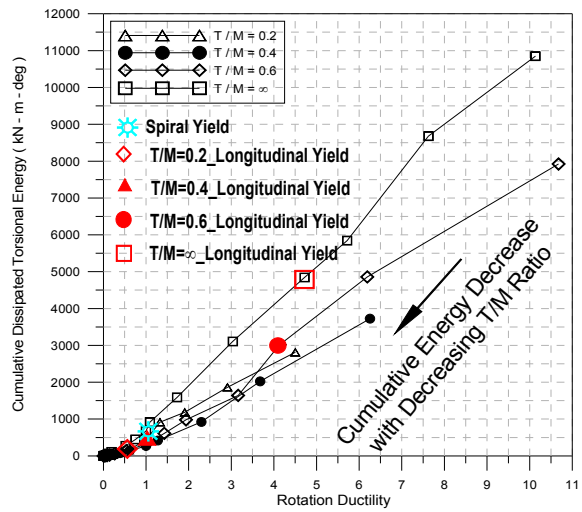

Fig. 4-74 Comparison of Cumulative Torsional Energy Dissipation under Combined Loading

4.3.7.2 Oval Columns with Interlocking Spirals under Combined Loading

For the columns tested under biaxial pure flexure and shear, the dissipated flexural energy was low at each load level before the reinforcement yielding due to the elastic response as shown in Fig. 4-75. Thereafter the energy dissipated at the first cycle of each ductility significantly increased along with the increasing ductility level up to the ultimate flexure dominated failure. For the column tested under pure torsion with dominated tensional failure, the dissipated torsional energy at the first cycle of each ductility increased until it reached the peak torque state with totally concrete cover spalling and continued to develop at a higher ductility with more contributions from transverse reinforcement, concrete core, and longitudinal reinforcement, and it finally dropped down at the ultimate failure as shown in Fig. 4-76. This fact indicated the column can dissipate more torsional energy after peak torque state with the contribution from transverse confinement of spirals and dowel action of longitudinal reinforcement. For the columns tested under biaxial combined loading at T/M ratios of 0.2 and 0.4, both dissipated flexural and torsional energy at each cycle significantly increased after reinforcement

yielding up to the ultimate flexure dominated failure with core concrete crushing and longitudinal bar buckling as shown in Fig. 4-77 through Fig. 4-80. For the column tested under uniaxial combined loading at a T/M ratio of 0.2, the dissipated flexural and torsional energy developed the same as the one under biaxial combined loading at a T/M ratio of 0.2 as shown in Fig. 4-81 and Fig. 4-82 since they both experienced similar damage progression with flexure dominated failure mode. However, the column tested under uniaxial combined loading at a T/M ratio of 0.6 was observed to be in the torsion dominated failure mode, which resulted in dissipated torsional energy at the first cycle of each ductility increasing along with the increase of the ductility level until it reached peak torque and then decreasing for the more imposed ductility level as shown in Fig. 4-83 and Fig. 4-84. This is because torsional stiffness severely degraded after the concrete cover totally spalled and then the peak torque was achieved, which reduced the energy dissipation of RC members. However, the dissipated flexural and torsional energy for all the columns decreased with the loading cycle increase at each ductility resulting from the degradation of stiffness.

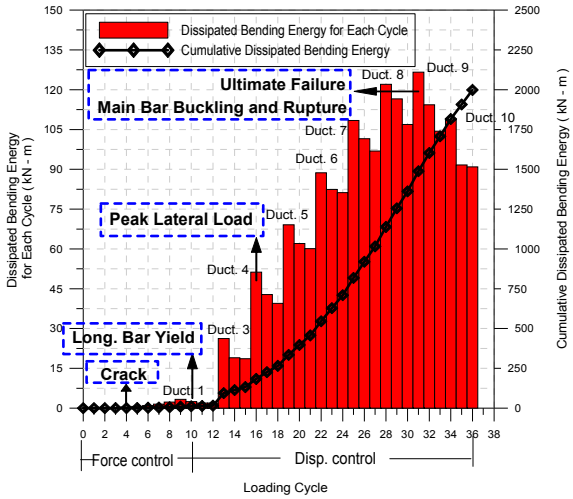

Fig. 4-75 Dissipated Flexural Energy under Biaxial T/M=0

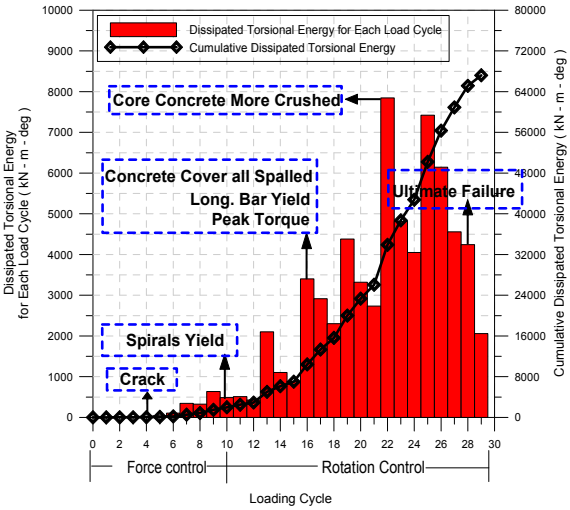

Fig. 4-76 Dissipated Torsional Energy under T/M=∞

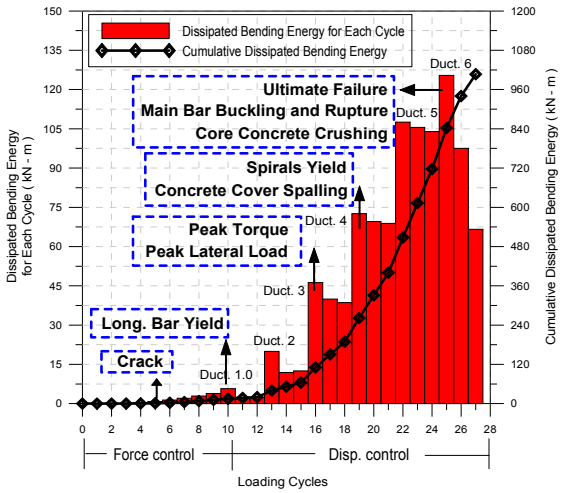

Fig. 4-77 Dissipated Flexural Energy under Biaxial T/M=0.2

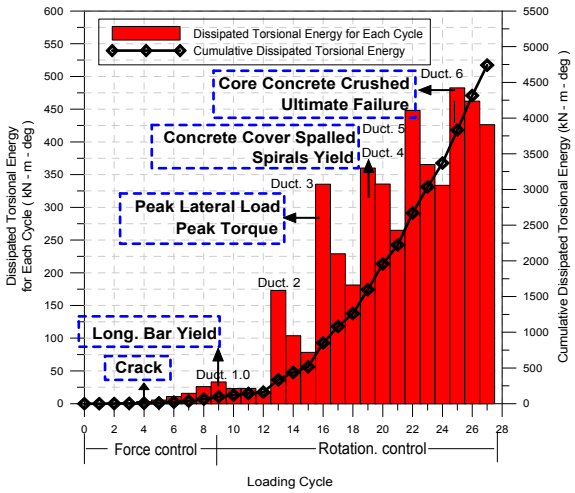

Fig. 4-78 Dissipated Torsional Energy under Biaxial T/M=0.2

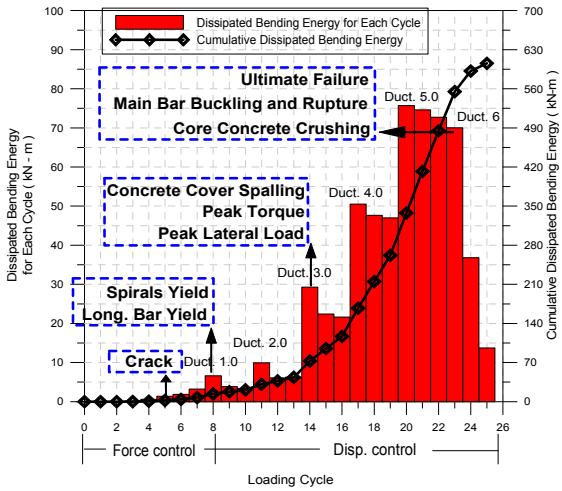

Fig. 4-79 Dissipated Flexural Energy under Biaxial T/M=0.4

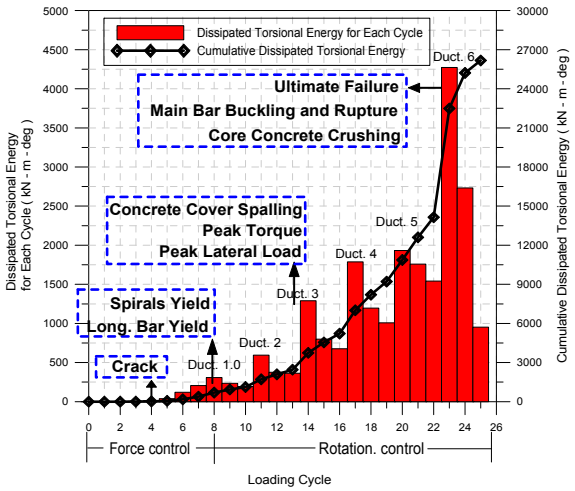

Fig. 4-80 Dissipated Torsional Energy under Biaxial T/M=0.4

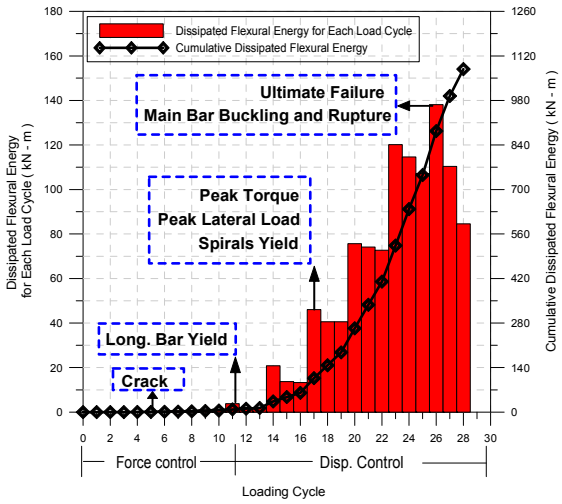

Fig. 4-81 Dissipated Flexural Energy under Uniaxial T/M=0.2

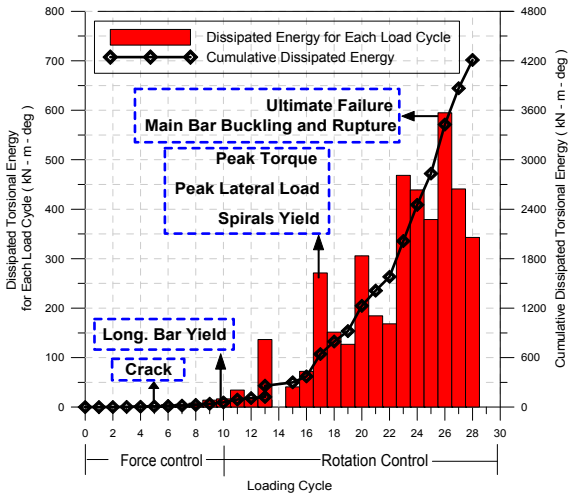

Fig. 4-82 Dissipated Torsional Energy under Uniaxial T/M=0.2

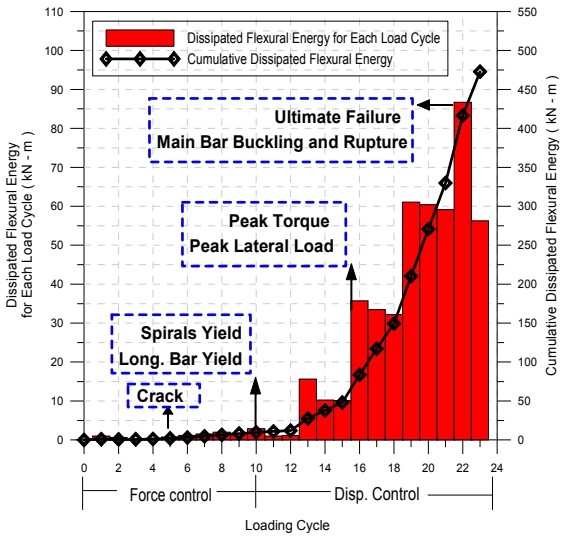

Fig. 4-83 Dissipated Flexural Energy under Uniaxial T/M=0.6

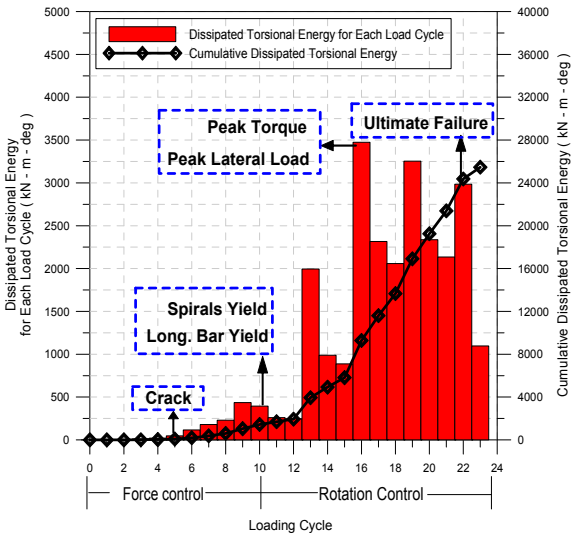

Fig. 4-84 Dissipated Torsional Energy under Uniaxial T/M=0.6

The cumulative dissipated flexural and torsional energy for oval columns under uniaxial and biaxial combined loading was plotted and compared in Fig. 4-85 through Fig. 4-90. For the columns under both uniaxial and biaxial combined loading, it can be concluded that the dissipated flexural energy decreased significantly as the T/M ratio increased because the greater torsion effect caused less displacement ductility capacity, more severe inclined crack, more stiffness degradation and torsional plastic hinge formation; also the dissipated torsional energy decreases as the T/M ratio decreased due to the flexure effect such as flexural crack, buckling of longitudinal bar and core concrete crushing. As in the square columns, the energy dissipation rate versus deformation ductility increased along with the increase in the T/M ratio, which indicates that torsional moment in the column under combined loading accelerated the energy dissipation. In addition, larger displacement ductility and more flexural energy dissipation are required for columns at lower T/M ratios to yield the interlocking spirals because of the less torsion effect on the spirals reaction; and larger rotation ductility and more torsion energy

dissipation are required for columns at higher T/M ratios to yield the longitudinal reinforcement because of torsion dominated failure mode.

The cumulative flexural and torsional energy dissipation under uniaxial and biaxial combined loading was compared in Fig. 4-89 and Fig. 4-90. At the same T/M ratio condition, the biaxial combined loading reduced the displacement ductility and flexural energy dissipation capacity compared to the uniaxial combined loading, which indicated that the interaction of two directionally lateral loading magnified the torsion effect on the flexural response of RC members. Also the biaxial combined loading reduced torsional energy dissipation capacity compared to the uniaxial combined loading because of that the interaction of the two directionally lateral loading accelerated flexural stiffness and strength degradation on each other, which resulted in more flexure effect on torsional behavior of RC member combined loading.

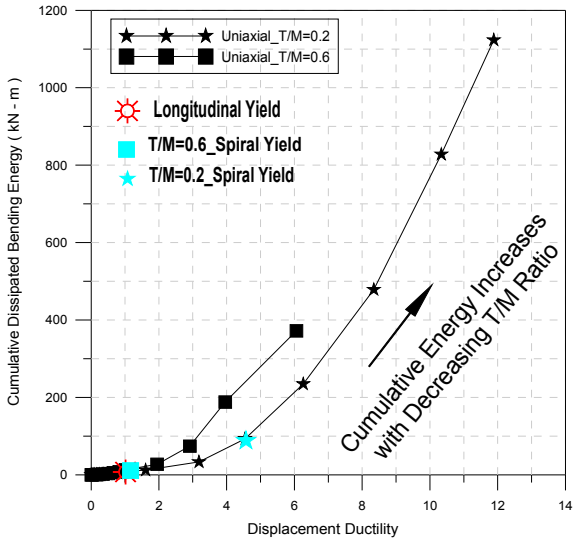

Fig. 4-85 Comparison of Cumulative Flexural Energy Dissipation under Uniaxial Combined Loading

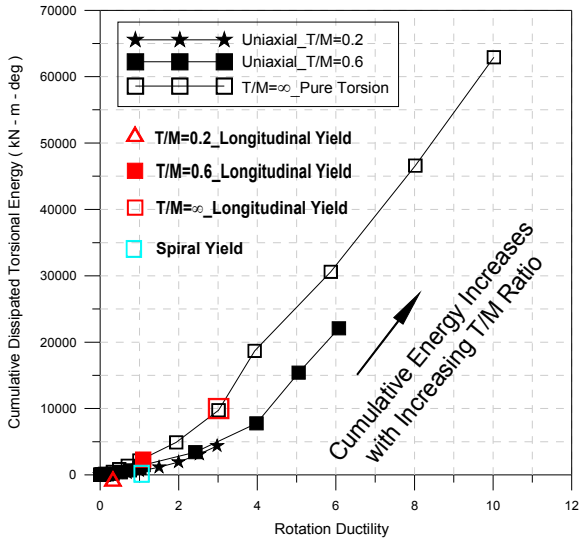

Fig. 4-86 Comparison of Cumulative Torsional Energy Dissipation under Uniaxial Combined Loading

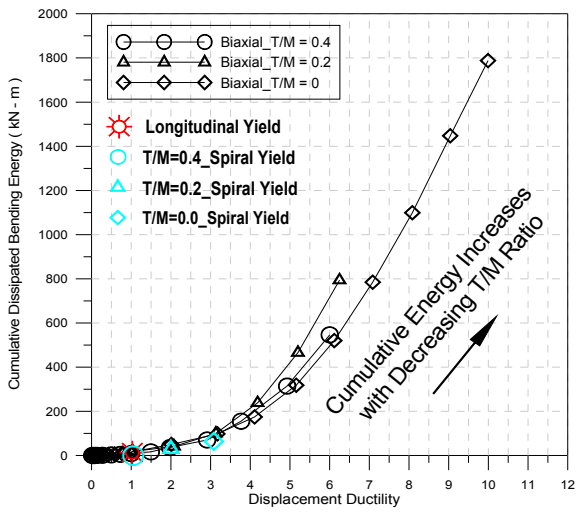

Fig. 4-87 Comparison of Cumulative Flexural Energy Dissipation under Biaxial Combined Loading

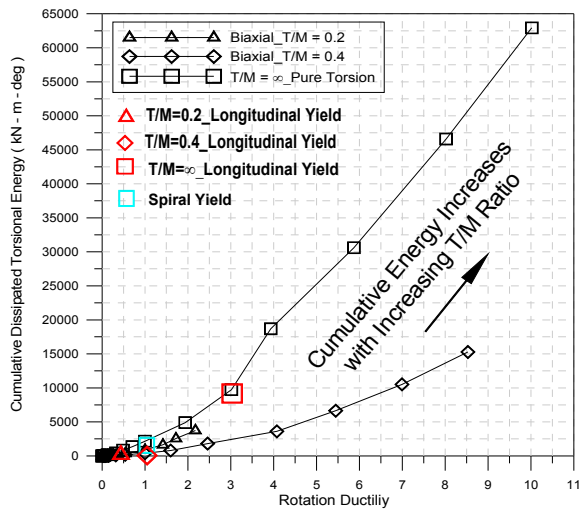

Fig. 4-88 Comparison of Cumulative Torsional Energy Dissipation under Biaxial Combined Loading

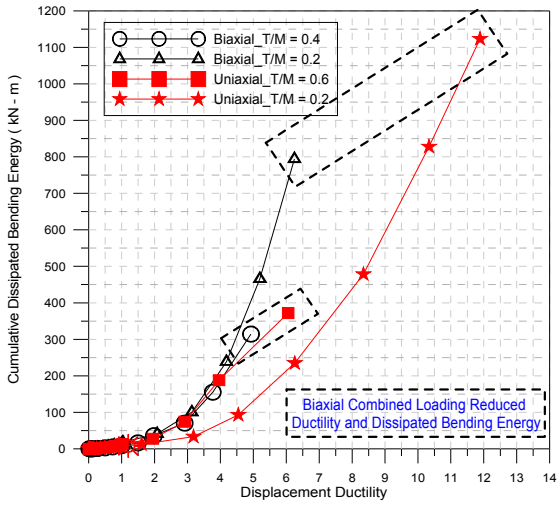

Fig. 4-89 Comparison of Cumulative Flexural Energy Dissipation under Uniaxial and Biaxial Combined Loading

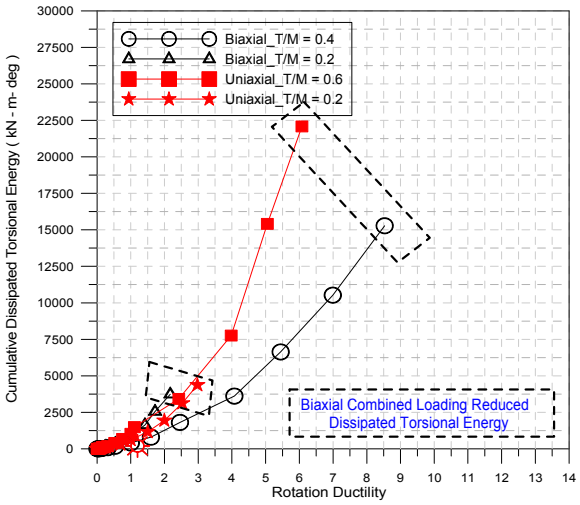

Fig. 4-90 Comparison of Cumulative Torsional Energy Dissipation under Uniaxial and Biaxial Combined Loading

4.4. Interaction Diagram of Flexure and Torsion

The interaction diagram of flexure and torsion can be used to discuss about the combined loading effect on flexural and torsional strength at different load stages with respect to flexural and inclined torsional cracking, longitudinal and transverse reinforcement yielding, and peak bending and torsional moment. The interaction diagrams of flexure and torsion for square and oval columns are established and discussed in following section.

4.4.1. Square Columns with Octagonal and Square Ties

The interactive features between flexure and torsion depends on a number of factors, such as the amount of transverse and longitudinal reinforcements, the aspect ratio of the section, and the concrete strength. The bending and torsional moment loading curves during testing and the interaction diagrams between torsional and bending moment at different loading stages are plotted according to the test results in Fig. 4-91 and Fig. 4-92. The bending and torsional moment loading curves were established by connecting all the peak load points of each ductility level, with respect to the bending and torsional moment. During the process of testing, it was noted that the T/M ratio was maintained close to the desired constant ratio in all the columns up to the peak torsional moment. Soon after the peak torsional strength, the desired loading ratio could no longer be kept constant because torsional stiffness and strength degraded much more significantly than flexure. The columns under combined loading at T/M ratios of 0.2 and 0.4 failed by flexure dominant mode and reached their torsional and flexural strength at the same ductility level; while the column under a T/M ratio of 0.6 failed by torsion dominant mode due to the high torsion level and reached its torsional strength prior to flexural strength. The interaction diagram are determined at peak torsional moment, or peak lateral loads and the corresponding lateral load or bending moment depending on which one was achieved first. The interaction diagrams as shown can be categorized into a number of loading stages, namely, flexural cracking, inclined torsional cracking, longitudinal yielding, transverse yielding and peak torsional or bending moment. The longitudinal reinforcement yielded before the transverse reinforcement for columns with flexure dominant failure mode, and the transverse reinforcement yielded before the

longitudinal reinforcement for the torsion dominant mode. Also, the longitudinal and transverse reinforcement yielded at the same load stage for a T/M ratio of 0.4 as shown in Fig. 4-92, in which the intersection of longitudinal and reinforcement curves fell on the T/M ratio of 0.4. The torsional strength and bending moment strength at different load stages were reduced due to the effect of combined bending and torsion. For the columns under pure torsion and a T/M ratio of 0.6, it was observed that the torsional yielding stage and peak state almost occurred simultaneously, which concluded that transverse reinforcement ratio and designed configuration being adequate from a confinement design point of view may not satisfy design criteria in the presence of torsional loading.

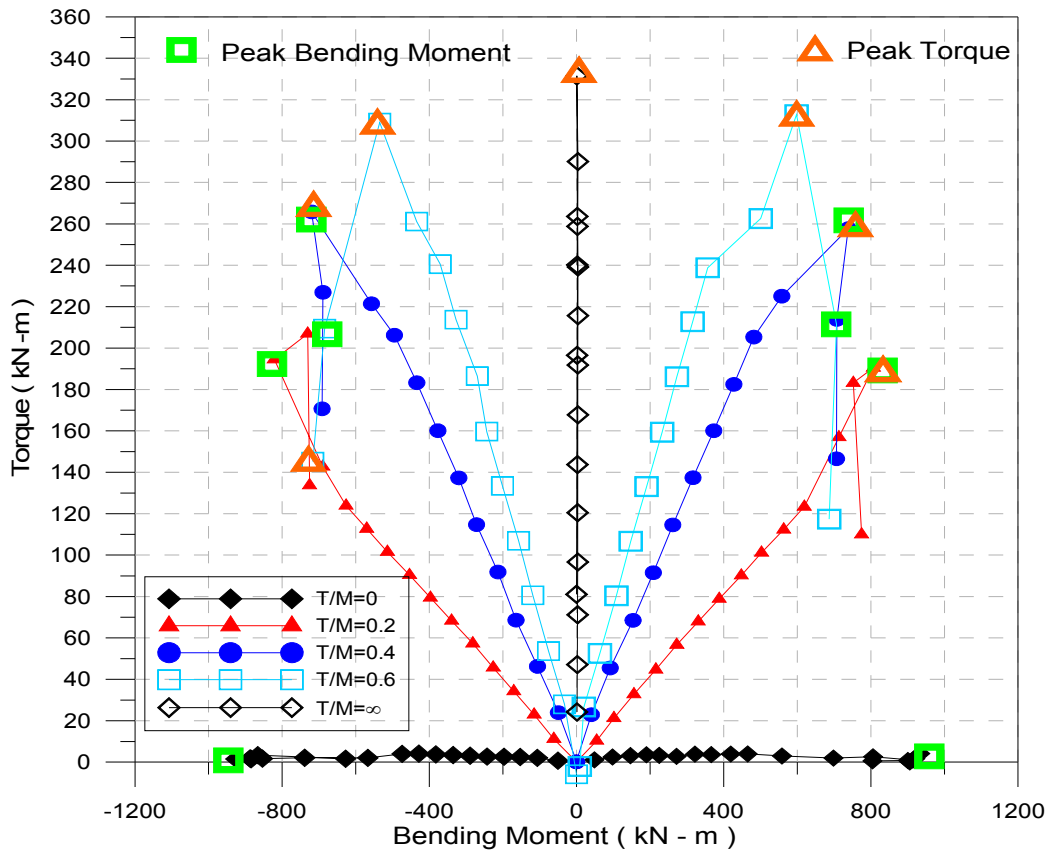

Fig. 4-91 Torsional and Bending Moment Loading Curves for Square Columns

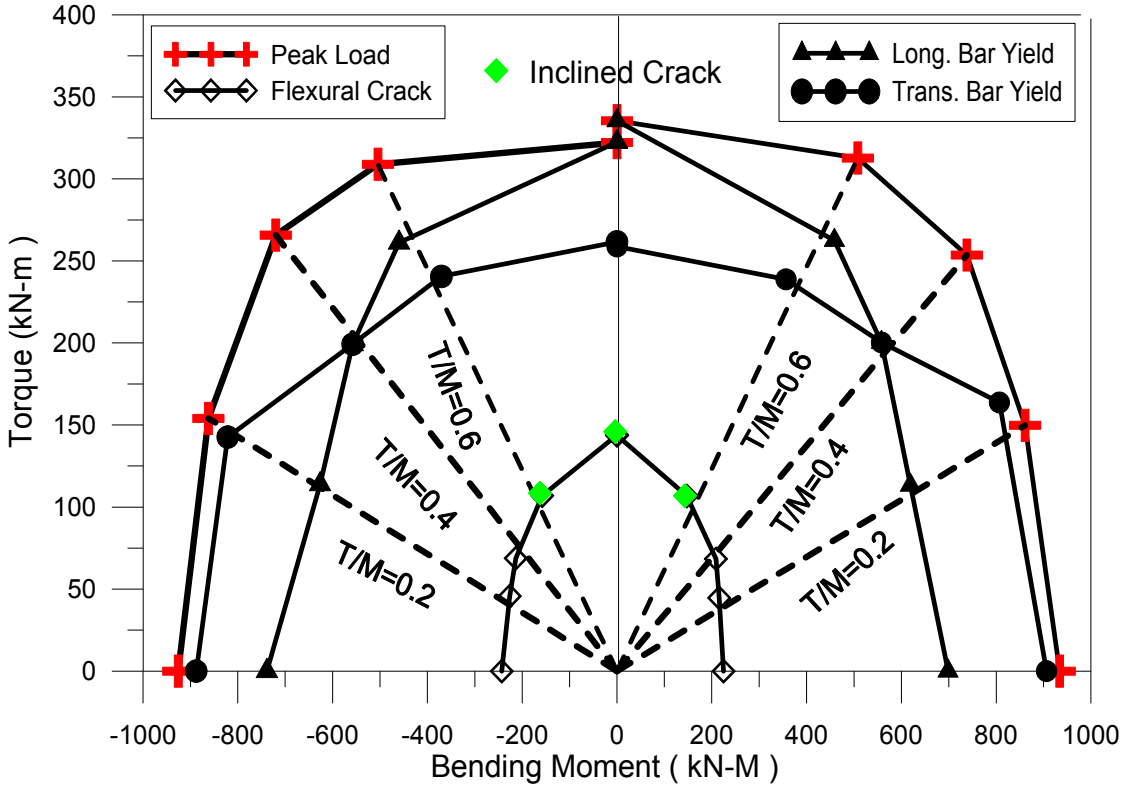

Fig. 4-92 Torsion-Moment Interaction Diagram at Different Loading Stages

4.4.2. Oval Columns with Interlocking Spirals

The bending and torsional moment loading curves during testing and the interaction diagrams between torsional and bending moments at peak stages are plotted in Fig. 4-93 and Fig. 4-94 according to the test results under uniaxial and biaxial combined loading. The bending and torsional moment loading curves for oval columns were established by connecting all the peak load points of each ductility level as in the square columns. During the loading process, it was noted that the T/M ratio was maintained close to the desired constant ratio in all the columns until either peak lateral load or torsional moment was achieved. Thereafter, the desired loading ratio could no longer be kept constant because of significant degradation in both flexural or torsional stiffness and strength. Under combined loading at T/M ratios of 0.2 and 0.4, the columns failed by flexure-

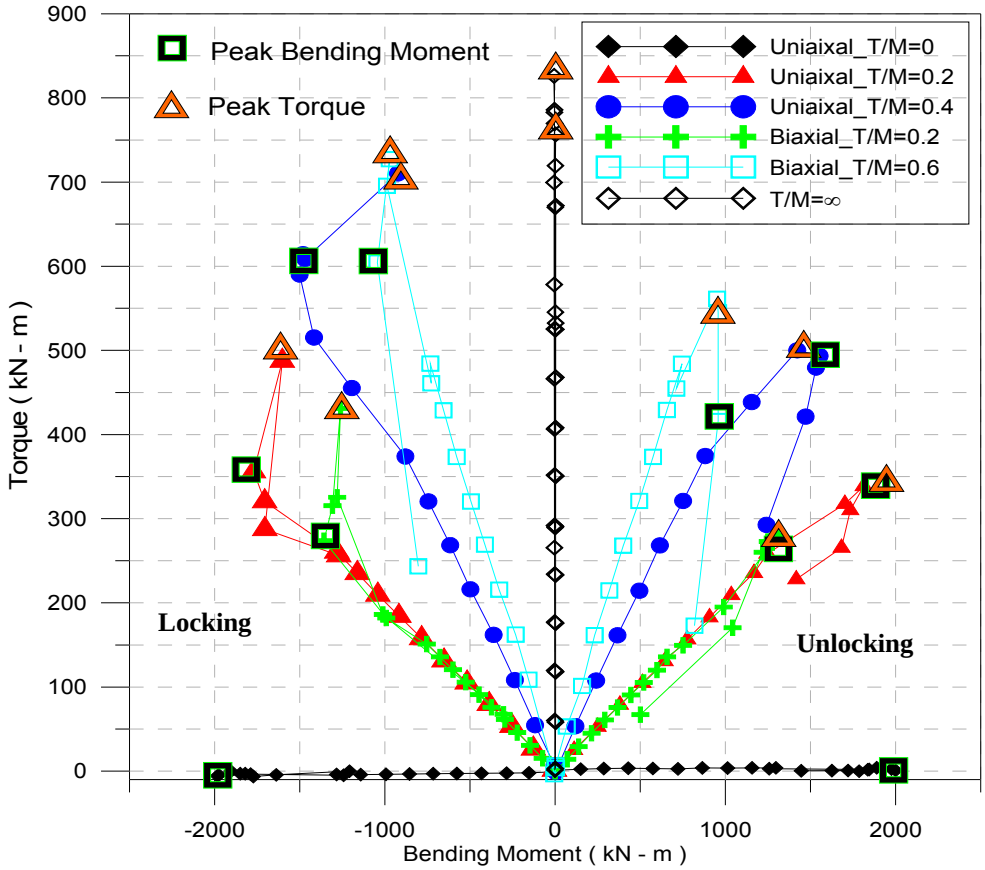

Fig. 4-93 Torsional and Bending Moment Loading Curves for Oval Columns

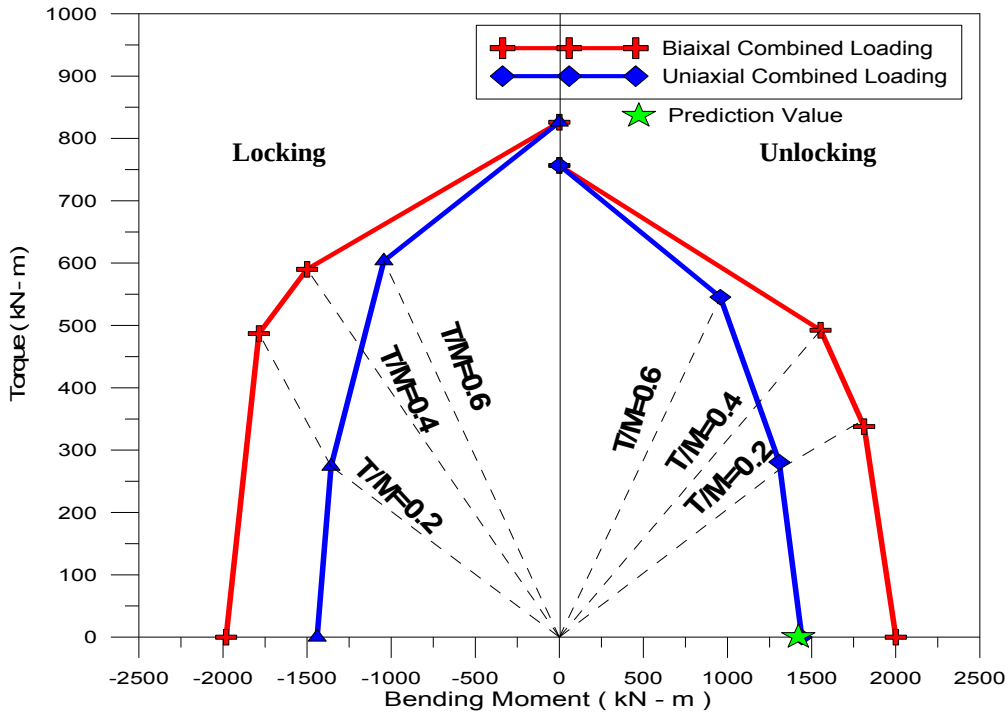

Fig. 4-94 Torsion-Moment Interaction Diagram at Peak Loading Stages under Uniaxial and Biaxial Combined Loading

dominant mode with less concrete cover spalling and earlier longitudinal reinforcement yielding and reached their torsional and flexural strength at the same ductility level in positive loading cycles. They reached their flexural strength prior to torsional strength in negative cycles due to the locking effect in spirals, which increased the torsional strength and ductility capacity. This means that the locking effect postponed the torsional damage in negative loading cycles at a high ductility level. However, the column with a T/M ratio of 0.6 failed in the torsion dominant mode with excessive concrete cover spalling and earlier transverse reinforcement yielding, and reached its torsional strength prior to flexural strength in both positive and negative loading cycles. The interaction diagram are established based on either peak torsional moment or peak lateral loads and the corresponding lateral load or bending moment depending on which one was achieved first. The original zero states and the peak load states are connected by radial lines specified at different T/M ratios. The effect of combined loading on flexural cracking and longitudinal yielding is not significant for the T/M ratio of 0.2. However, combined loading have a pronounced effect on spiral yielding and peak torsional strength for other T/M ratios. The torsional capacity as well as the bending moment capacity decreased due to the effect of combined bending and torsion. In addition, the biaxial combined loading magnified the locking and unlocking effect compared to the uniaxial combined loading, which can be addressed according to the intensity difference of the asymmetric nature on interaction diagrams.

4.5. Concluding Remarks

This section presented the test results for square and oval columns under flexure and shear, pure torsion, and combined flexure, shear and torsion. The square columns with

octagonal and square ties were tested under combined loading at T/M ratios of 0, 0.2, 0.4, 0.6 and ∞; the oval columns with interlocking spirals were tested under pure torsion, uniaxial combined loading at T/M ratios of 0.2 and 0.6, and biaxial combined loading at T/M ratios of 0, 0.2 and 0.4. The test results provide useful information to investigate the cyclic behavior of RC columns under combined loading including torsion. First, the lateral load-displacement and torsional moment-twist hysteresis curves, plastic hinge location, concrete cover spalling, and damage progression under combined loading were presented in this section; second, the effects of cross sectional shape, transverse configurations, and T/M ratios on the deformation distribution along the columns, strength and stiffness degradation, locking and unlocking efficiency, failure modes and energy dissipation characteristics under combined loading were discussed; third, the bending and torsional moment loading curves and interaction diagrams of torsional and bending moments were established according to test data from different loading stages. The test results support the following conclusions:

4.5.1. Flexural and Torsional Hysteresis Curves

Hysteretic load-displacement and torsional moment-twist curves of RC columns provided the strength and deformation at different loading stages with respect to concrete cracking, reinforcement yielding, peak load, and deformation capacity. The pinching effect of flexural hysteresis was magnified by combined loading along with increasing T/M ratios, which indicated the reduced flexural energy dissipation. The significant pinching effect for the torsional hysteresis of all columns showed that torsional energy dissipation capacity was always less than the flexural energy dissipation capacity. The interlocking spirals in oval columns provided better transverse confinement, which

lessened the pinching effect of hysteresis as comparing to square columns. In addition, the pinching effect of flexural and torsional hysteresis was magnified by biaxial combined loading in oval columns compared to uniaxial combined loading.

4.5.2. Flexural and Torsional Stiffness and Strength Degradation

In columns under combined loading, the flexural and torsional stiffness started degrading after concrete cracking and deteriorated more rapidly after peak load stages. Also the torsional stiffness degraded faster than the flexural stiffness due to the severer inclined torsional cracking and more concrete cover spalling and concrete core crushing. The flexural strength and displacement capacity of the columns under combined loading decreased with increasing T/M ratios due to the torsion effect. Similarly, the decrease of the T/M ratio caused reduced torsional strength and ultimate twist capacity from the flexure effect.

Compared to square columns, the oval columns with interlocking spirals mitigated the stiffness and strength degradation in flexural and torsional response. Also the biaxial combined loading magnified the stiffness and strength degradation as comparing to uniaxial combined loading. In addition, the deterioration of stiffness and strength is substantial in the first two loading cycle and becomes less significant in the last cycle.

4.5.3. Damage Characteristics and Failure Mode

- The flexural damage of RC columns under flexure and shear was initiated by flexural concrete cracking and yielding of reinforcement. Then the formation of a flexural plastic hinge and concrete cover spalling at the base of the column caused significant lateral stiffness and strength degradation. The final flexure dominant failure was observed by concrete core crushing and buckling or rupturing of reinforcement. Interlocking spirals

in the oval columns did not significantly affect the flexural damage progression by compared to square columns. But the biaxial lateral load in the oval columns accelerated the damage progression and reduced the flexural strength of each individual direction.

- The damage progression of the RC columns under pure torsion started with two sets of perpendicular inclined torsional cracks and continued with concrete cover spalling along the entire-height of column. Finally the torsional plastic hinge formatted with severe core concrete degradation near the mid-height of the column, which was significantly different from the typical flexural damage characteristics. This locking and unlocking effect in the oval columns was observed and reflected in the asymmetric nature of the torsional hysteresis curve for positive and negative cycles. However, there was no locking and unlocking effect in the square columns with ties. The location of a severe damage zone in the oval columns under pure torsion was much higher than the one in the square columns.

- The combined loading including torsion altered the damage patterns of the RC columns. The columns under combined loading at low T/M ratios of 0.2 and 0.4 experienced flexure dominant failure mode; while the columns at the higher T/M ratio of 0.6 failed in torsion dominant failure mode. The columns with large T/M ratios experienced the damage progression in sequence of severe torsional inclined cracking, transverse reinforcement first yielding, early concrete spalling before peak load, and final failure by completely concrete crushing while the columns with lower T/M ratios resulted in the damage progression such as horizontal and inclined cracking, longitudinal reinforcement first yielding, lagged concrete cover spalling and failure by buckling and rupturing of longitudinal bars and less concrete core crushing. The length of concrete

cover spalling was increased with an increase in T/M ratios. Biaxial loading did not show a significant effect on spalling distribution compared to uniaxial loading; however it magnified the damage states at the same ductility compared to uniaxial combined loading due to more torsion effect. In addition, the location of the plastic zone shifted upwards from the base of the column along with the increased applied T/M ratio.

- The depth of concrete core crushing in the column at lower T/M ratios almost reached half of the cross sectional dimension at the final failure stage; for the column under higher T/M ratios, the whole concrete core completely crushed at final failure stage. The biaxial combined loading in the oval columns amplified the concrete core damage compared to uniaxial combined loading. All the longitudinal reinforcement over the cross section yielded after the concrete core was crushed in the columns with flexure dominant failure mode; more than half of the longitudinal reinforcement over the cross section yielded in the columns with torsional dominant failure mode. In addition, the longitudinal reinforcement buckling and rupturing or transverse reinforcement rupturing more likely happened in the column with lower T/M ratios of 0.2 and 0.4 due to the larger cyclic compression and tension force under flexure. None of the spirals in the oval columns was observed to rupture at the final failure stage.

4.5.4. Ductility Capacity and Locking and Unlocking Effect

- Very small locking and unlocking efficient were obtained in all the square columns caused by the asymmetric features of additive shear stresses from combined shear and torsion. For square columns, lower T/M ratios with more shear forces under combined loading resulted in more asymmetrically additive shear stresses and increased the locking and unlocking efficient.

- Interlocking spirals in oval columns introduced a large locking and unlocking effect in torsional response. The locking and unlocking action of spirals together with the asymmetrically additive shear stresses from combined shear and torsion increased the locking and unlocking efficient. In addition, the biaxial combined loading amplified the locking and unlocking efficient by 10% - 20% compared to the uniaxial combined loading.
- The flexural and torsional deformation capacities were reduced by the combined loading effect. The combined loading did reduce the ductility capacity compared to pure torsion and pure flexure and shear cases. The interlocking spirals enhanced the ductility capacity in oval columns. However, the ductility capacities for columns under combined loading were not significantly affected by varying T/M ratios.

4.5.5. Flexural and Torsional Energy Dissipation

- Dissipated flexural energy decreased significantly as the T/M ratio increased due to the torsion effect and the dissipated torsional energy decreased as the T/M ratio decreased due to the flexure effect. For all the columns, the energy dissipation rate versus the deformation ductility increased along with the increase in the T/M ratio. In addition, larger displacement ductility and flexural energy dissipation are required to yield the transverse reinforcement along with the decreasing T/M ratios and larger rotation ductility and torsion energy dissipation are required to yield the longitudinal reinforcement.
- Then interlocking spirals in oval columns improved flexural and torsional energy dissipation as compared to square columns with ties. The biaxial combined loading reduced flexural and torsional energy dissipation capacity compared to the uniaxial

combined loading due to the magnified the torsion effect from the interaction of two directionally lateral loading.

4.5.6. Interaction Diagrams of Bending and Torsional Moment

- Interaction diagrams between torsional and bending moments at different loading stages can be established based on the test results. For all the columns, the yielding and peak torsional moment and corresponding rotation decreased along with decreasing T/M ratios; similarly the yielding and peak lateral load and displacement capacity were reduced by the combination of flexure and torsion.
- For square columns, lower T/M ratios of 0.2 and 0.4 resulted in the flexure dominant mode and achieved torsional and flexural strength at the same ductility level; while a higher T/M ratio of 0.6 failed the columns by torsion dominant mode and reached its torsional strength prior to flexural strength.
- For oval columns with lower T/M ratios of 0.2 and 0.4, they reached torsional and flexural strength at the same ductility level in positive loading cycles and reached their flexural strength prior to torsional strength in negative cycles due to the locking effect in spirals, which increased the torsional strength and ductility capacity. However, the oval column with a T/M ratio of 0.6 reached its torsional strength prior to flexural strength in both positive and negative loading cycles.

Chapter 5 Damage Assessment for RC Bridge Columns under Combined Loading Including Torsion

5.1. Introduction

The combined loading including torsion during earthquake excitations will affect the seismic performance of reinforced concrete (RC) bridge columns and result in complex damage progression and failure mode in these columns. In recent years, a few experimental studies were performed on RC bridge columns under combined shear, flexure and torsion (Rasmussen and Baker 1995, Suda et al. 1997, Otsuka et al. 2004, Tirasit and Kawashima 2007, Browning et al. 2007, Belarbi and Prakash, 2009, Arias-Arias-Acosta and Sanders 2010). However, very few experimental results are reported in the literature on the damage assessment of RC bridge columns under cyclic combined loading including torsion. In order to assess the damage progression, a proper damage index model accounting for the hysteretic behavior under combined loading should be developed to quantify different damage limit states. Then the performance of the RC bridge columns under cyclic combined loading can be evaluated from the hysteresis curves using the damage indices, which can be adopted to facilitate repair or retrofit decisions. A few studies (Park et al. 1984 and 1985, Kunnath et al 1992 and 1997, Williams and Sexsmith 1995, Williams et al. 1997, Rao et al. 1997, Chung and Meyer 1987 and 1989, Kratzig et al. 1989, Sadeghi et al. 1993, Meyer et al. 1994, Borzi and Elnashai 2000, Hindi and Sexsmith 2001, Khashaee 2005) were conducted to investigate the development of damage indices based on flexural behavior.

In addition, Jeong and Elnashai (2006) developed the damage index for RC buildings with planar irregularities taking into account three-dimensional responses. A method to

combine the local damage indices were proposed to verify their experimental results with conventional damage indices. Suriya and Belarbi (2009) tested twelve circular RC bridge columns under various T/M ratios to investigate the interaction effects of proposed decoupled flexural and torsional damage indices (Suriya, 2010). However, no experimental and analytical study was conducted to assess the coupled damage characteristics of RC bridge columns under combined loading. In order to establish the damage assessment criteria for RC bridge columns under combined loading, the RC columns were tested under combined loading with various T/M ratios. Accordingly, decoupled torsional and flexural damage index models are proposed based on flexural and torsional hysteresis curves.

However, the flexural and torsional damage characteristics of RC columns during an earthquake were coupled with each other. Therefore a unified equivalent damage index model should be proposed to couple the flexural and torsional actions for combined loading in this section, which can quantify the various damage limit states. Finally the quantified damage index models are correlated to the categorized damage limit states to assess the damage of RC columns under combined loading.

5.2. Research Review on Damage Index Models

Most of the previous damage index models were based on flexural failure modes. This experimental and analytical study aims to modify and extend the existing damage indices for flexural failure mode to the complex failure mode under combined loading. The damage assessment process of RC bridge columns under combined loading can be established through three steps: first, decoupled torsional and flexural damage index models for combined loading must be developed to identify the implications of combined

loading from the perspective of damage characteristics; second, a unified equivalent damage index model should be proposed to couple the flexural and torsional actions for combined loading, which can quantify the various damage limit states; third, unified damage index models are developed to quantify the various damage limit states, which can be correlated to the categorized structural damage implication and repair requirement. To achieve these objectives, the experimental data are used to validate the proposed damage index models and the main results are presented in following sections.

In the damage assessment progress, the non-dimensional parameter known as "damage index" can be used to perform a quantitative assessment of various damage states under earthquake excitations. In the earlier study, noncumulative damage indices can be simply evaluated based on displacement ductility or inter-story drift under monotonic loading, which do not consider the strength or stiffness degradation and energy dissipation under cyclic loading. However, the damage to a structure or its components is caused by the cyclic loading or deformation under combined loading conditions during an earthquake. The RC members suffered both strength and stiffness degradation under cyclic loading, and the local damage characteristics in theses members are cumulative in nature during various damage limit states. Therefore the hysteretic energy-dissipation-based or cyclic-displacement-based damage indices were used to account for all these cumulative and deteriorative natures. These damage indices can be used to assess the damage progression of the structure or components and inform retrofit decisions in disaster planning and post-earthquake assessment.

5.2.1. Noncumulative Damage Indices

For the RC members under monotonic loading, the traditional and simple damage indices are mostly used to evaluate the damage states according to the ratio of ultimate displacement achieved to yield displacement, which is defined as ductility given by

$$\mu_\Delta = \frac{\Delta_u}{\Delta_y}, \tag{5-1}$$

where Δ_u is the maximum displacement, Δ_y is the yield displacement, and μ_Δ is the displacement ductility at different loading states. And the inter-story drift, the difference between the roof and floor displacement, has also been used as a damage indicator for monotonic loading.

In addition, the damage limit can also be indicated by the degradation of stiffness at a given load level proposed by Banon et al. (1981), which is defined as the ratio of initial stiffness to the secant stiffness corresponding to the maximum displacement in a given loading cycle. Recently, the formula of this indicator has been modified by Roufaiel and Meyer (1987) in terms of stiffness or flexibility at the initial, ultimate and failure stage respectively as expressed by

$$D_k = \frac{k_f}{k_u} \times \frac{(k_u - k_0)}{(k_f - k_0)}, \tag{5-2}$$

where D_k is the damage index in terms of stiffness, k_f is the secant stiffness at failure, k_u is the secant stiffness at the ultimate displacement, and k_0 is the initial tangent stiffness;

$$D_f = \frac{f_m - f_0}{f_u - f_0}, \tag{5-3}$$

where D_f is the damage index in terms of flexibility, f_0 is the pre-yield flexibility, f_m is the secant flexibility at a given load, and f_u is the secant flexibility at the ultimate load. However, these damage indices does not account for the cumulative nature of various damage limit states due to excluding the effect of cyclic loading.

5.2.2. Ductility or Displacement-Based Cumulative Damage Indices

In order to reflect the cumulative damage characteristics of members under cyclic loading, Banon et al. proposed an approach to measure the cumulative ductility for all the loading cycles as given by

$$D = \sum_i \frac{|\Delta_{m,i} - \Delta_y|}{\Delta_y} = \sum_i (\mu_i - 1), \tag{5-4}$$

where $\Delta_{m,i}$ is the maximum displacement in cycle i, μ_i is ductility in cycle i. This ductility based cumulative damage index includes both the elastic and plastic response under cyclic loads.

Stephens and Yao (1987) proposed a damage index based on the increments of plastic displacement, which is given by

$$D = \sum \left(\frac{\Delta_p^+}{\Delta_f}\right)^{1-br}, \tag{5-5}$$

where Δ_p^+ and Δ_p^- are positive and negative plastic displacement increments for each full loading cycle, r is the ratio of Δ_p^+ and Δ_p^-, Δ_f is the positive plastic displacement increments at the failure cycle and b is a constant with a recommended value of 0.77.

Later on a simple damage model was developed by Wang and Shah (1987) to take into account the accumulation of damage by assuming its exponentially proportional relationship to the damage already incurred as given by

$$D = \frac{exp(s\alpha) - 1}{exp(s) - 1}, \tag{5-6}$$

$$\alpha = c \sum_i \frac{\Delta_{m,i}}{\Delta_f}, \tag{5-7}$$

where c and s are constants recommended by 0.1 and 1.0 respectively for a well-reinforced member.

5.2.3. Energy-Based Cumulative Damage Indices

Structural members dissipated energy under seismic loading due to inelastic deformation showing both strength and stiffness degradation. The energy dissipation ratio at different loading levels can be taken as a damage indicator. Meyer and Garstka (1988 and 1993) proposed an accumulative damage index by normalizing the dissipated energy at each loading cycle with respect to the dissipated energy under monotonic loading. So the damage index varies from '0' responding to zero displacement to '1' responding to the ultimate displacement. The governing equations for this index are expressed by

$$D = D^+ + D^- - D^+ \times D^-, \tag{5-8}$$

$$D^{\pm} = \frac{\sum_i E_{p,i}^{\pm} + \sum_i E_i^{\pm}}{E_f^{\pm} + \sum_i E_i^{\pm}}, \tag{5-9}$$

where D is the overall damage index, $\pm$ is positive or negative phase of cyclic deformation, $D^{\pm}$ are the damage indices in positive and negative phase, $E_{p,i}$ is the energy dissipated by primary half-cycle, $E_{s,i}$ is the energy dissipated by follower half-cycle, and E_f is the maximum energy dissipated under the monotonic load.

5.2.4. Energy and Cyclic Displacement-Based Cumulative Damage Indices

The numbers of equivalent yield excursions was proposed by Zahrah and Hall (1984) to assess the damage in structures. This damage index includes the maximum hysteretic energy demand, displacement ductility and yield strength of the member as calculated by

$$N_{ex} = \frac{E_{hm}}{Q_y u_y(\mu_\Delta - 1)}, \tag{5-10}$$

where N_{eq} is the numbers of equivalent yield excursions, u_y is yield displacement, E_{hm} is the maximum hysteretic energy demand and Q_y is yield strength of structure, and μ_Δ is the displacement ductility.

Hwang and Scribner (1984) proposed the damage index that stiffness and energy dissipation along with displacements in a given loading cycle were adopted to represent cumulative damage characteristics of members under cyclic loading. The main disadvantage of this damage index is the difficulty to quantify the damage limit states since it significantly depends on the cross sectional property and loading history and its maximum value is not unit one as the index proposed by Park and Ang. The calculative formula for this damage index is expressed as

$$D = \sum_{i=1}^{M} \Delta E_{h,i} \frac{K_{m,i}}{K_0} \frac{u_{m,i}^2}{u_y^2}, \tag{5-11}$$

where i is the cycle number, M is the total number of yield cycles, K_0 is the pre-yield stiffness, $u_{m,i}$ is the maximum displacement in the ith loading cycle, K_{mi} is the secant stiffness corresponding to $u_{m,i}$, $\Delta E_{h,i}$ is the hysteretic dissipated energy in the ith load cycle, and u_y is the yielding displacement.

Park and Ang (1985) proposed the reasonably practical flexural damage index, which was expressed as a linear combination of normalized displacement and dissipated energy as given by

$$D = \frac{u_m}{u_u} + \frac{\beta E_{hm}}{Q_y u_u} = \frac{\mu}{\mu_u} + \frac{\beta E_{hm}}{Q_y u_y \mu_u}, \tag{5-12}$$

where u_m is maximum displacement achieved in the loading cycle, u_u is ultimate displacement under monotonic load, u_y is yield displacement, μ is the displacement ductility, μ_u is ultimate displacement ductility, β is constant accounting for the effect of cyclic load, E_{hm} is maximum hysteretic energy demand, and Q_y is yield strength of the structure or members. The park and Ang model takes the ductility ratio as the primary variable and normalized cumulative energy as the secondary item. The empirical strength degradation factor β depends on the value of shear and axial forces in the section and on the total amount of longitudinal and confining reinforcement and varies from 0.05 to 0.15 accounting for the effect of the cyclic load, which indicates that more weight is given to the displacement ductility term than the energy dissipation term. The main advantage of the Park and Ang damage index model is its simplicity and physical intuition as it varies from '0' corresponding to no damage to '1' corresponding to near collapse. It has been reported in the previous work that the damage index goes slightly higher than the limit value of 1. Park and Ang also suggested the specific damage classification based on calibration against a considerable amount of observed seismic damage shown in Table 5-1.

Table 5-1 Damage Index Classification based on Calibration

Damage Index	Interpretation in Terms of Damage State
D < 0.1	No damage or localized minor cracking
0.1≤ D < 0.25	Minor damage-light cracking throughout
0.25 ≤ D < 0.40	Moderate damage-severe cracking, localized spalling
0.4 ≤ D < 1.00	Severe damage-concrete crushing, reinforcement exposed
D ≥ 1.0	Collapse

Rao et al. (1998) proposed a local damage index model for RC elements under cyclic loading, which is consistent with accepted definitions of ductility and takes into account at least two equal amplitude cycles at each displacement level. The damage index model was based on the existing Park and Ang damage model and calculated by

$$D = \frac{\mu_{cy-\delta}}{\mu_{st}} + \beta \frac{\sum E_{cy-\delta}}{\sum kE_{st-\delta}}, \tag{5-13}$$

where D is the damage index ranging from '0' to '1', μ_{st} is the static ductility ratio, $\mu_{cy-\delta}$ is the cyclic displacement ratio in multiples of yield displacement ($1 \leq \mu_{cy-\delta} \leq \mu_{cy}$ and $\mu_{cy} \leq \mu_{st}$), β is the element response factor with an average value of 1.25, $\sum E_{cy-\delta}$ is energy dissipated a cyclic displacement δ, $\sum E_{cy-st}$ is energy dissipated at corresponding static displacement δ, k is the constant of flexural capacity between tension to compression face, and δ is the cyclic displacement level under consideration. This equation has been modified to account for the known design variables such as cyclic and monotonic ductility indices. The energy terms have also been modified to account for the true cyclic cumulative and monotonic energy dissipation at a given value of displacement δ. The factor k is equal to 2 in the denominator and accounts for symmetric energy dissipation under a single complete cyclic loop consisting of a positive phase and a negative phase of monotonic loading. In the case of asymmetric reinforcement of longitudinal reinforcement, this factor can be fixed between 1 and 2 based on the strengths in the respective directions.

5.2.5. Fatigue-Based Cumulative Damage Indices

Jeong and Iwan (1988) proposed a damage index model under cyclic loading based on the well-known Miner's rule in terms of the numbers of loading cycles and the ductility level, which was expressed by

$$D = \sum_i \frac{n_i \mu_i}{n_f \mu}, \tag{5-14}$$

where n_i is the number of cycles at given amplitude to ductility level μ_i, and n_f is the number of cycles to failure at a specified ductility factor μ.

A fatigue-based damage model was proposed by Kunnath (1997) by varying the procedure from Mander and Cheng (1995). The linear strain variation along with the section was assumed to obtain the plastic strain amplitude as expressed by

$$\varepsilon_p = \emptyset_p \bar{d}/2, \tag{5-15}$$

where ε_p is the plastic strain amplitude, $\emptyset_p$ is the plastic curvature, and $\bar{d}$ is the distance between the center of compressive and tensile longitudinal reinforcement. In addition, the neutral axis of the section does not always stay at the center of the cross section during the cyclic loading process. However, the plastic strain amplitude of the main reinforcement becomes equal to twice $\emptyset_p \bar{d}/2$ after one completed loading cycle with the same displacement or curvature at both of the opposite lateral directions if the section strains vary linearly and the main reinforcement is located outside of the neutral axis. In addition, the plastic hinge strain amplitude was recalibrated by his experimental results based on the research from the Mander et al. (1994) and expressed by

$$\varepsilon_p = 0.0065(2N_f)^{-0.436}, \tag{5-16}$$

where N_f is the number of complete loading cycles at the appearance of the first fatigue on reinforcement.

The corresponding plastic rotation θ_p is assumed to be located at the center of the plastic hinge length L_p by neglecting shear and then the $\emptyset_p$ can be expressed as

$$\emptyset_p = \frac{\theta_p}{L_p} = \frac{\delta_p/(h-0.5L_p)}{L_p}, \tag{5-17}$$

where, δ_p is the plastic displacement, and h is the member length. The number of cycles at failure N_f was derived from Eq. (5-14) through Eq. (5-16) and given by

$$N_f = 2\left(\frac{0.065L_p(h-0.5L_p)}{\delta_p \bar{d}}\right)^{1/0.436}. \tag{5-18}$$

Finally, the cumulative damage D for circular flexural RC columns is given by

$$D = \sum_i \frac{1}{2N_f} = \sum_i \frac{1}{4\left(\frac{0.065L_p(h-0.5L_p)}{\delta_p \bar{d}}\right)^{1/0.436}}. \tag{5-19}$$

5.3. Proposed Decoupled Flexural and Torsional Damage Index Models

Previous damage index models were limit calibrated with respect to observed damage in laboratory tests or post-earthquake investigations. In addition, these indices are based primarily on flexural failure mechanisms. Therefore reasonable validation of the physical meaning of damage indices under combined loading is necessary for understanding the various damage states under combined loading including torsion. The damage limit states of RC columns under combined loading couple flexural and torsional damage characteristics. However, the cyclic flexural and torsional responses are represented by analytical or experimental flexural and torsional hysteresis curves, respectively. Therefore the decoupled flexural and torsional damage index models for combined loading including torsion must be developed to identify the implications of flexural and torsional hysteresis from the perspective of damage assessment, which can be used to distinguish the effect of the flexural and torsional response from the combined loading condition.

5.3.1. Decoupled Flexural Damage Index under Combined Loading

The Park and Ang (1985) model is the best known and most widely used damage index, which can be used for RC columns to quantify the flexural damage under combined loading as expressed by

$$FDI_{\text{P.A.Flexure,Combined}} = \frac{u_m}{u_u} + \beta \frac{E_{hm}}{Q_y u_u}. \tag{5-20}$$

The parameters needed to calculate $FDI_{\text{P.A.Flexure,Combined}}$ damage index include the maximum displacement in a cycle, the yielding lateral force, ultimate displacement corresponding to ultimate lateral load, and the flexural energy dissipation in the given loading cycle. This study assumed that ultimate failure was reached when a reduction in strength of at-least 10% was achieved. However, some tests were stopped for safety reasons when the longitudinal reinforcement ruptured, where the reduction of strength was less than 10%. So the ultimate failure was taken at the cycle of the rupture of longitudinal reinforcement. The definition of parameters is described in Fig. 5-1.

The damage index model proposed by Hwang and Scribner (1984) was modified by normalization with respect to totally cumulative flexural energy dissipated under flexure ($E_{Total,Flexure}$) to predict the flexural damage index under combined loading as given by

$$FDI_{H.S.Flexure,Combined} = \frac{\sum_{i=1}^{M} \Delta E_{h,i} \frac{K_{m,i} u_{m,i}^2}{K_0 \quad u_y^2}}{E_{Total,Flexure}}. \tag{5-21}$$

The parameters needed to calculate $FDI_{H.S.Flexure,Combined}$ damage index include the maximum displacement in each loading cycle, the maximum stiffness in each loading cycle, the yielding displacement and stiffness, the flexural energy dissipation in each loading cycle and the totally cumulative flexural energy dissipation during all the loading cycles. The definitions of parameters are described in Fig. 5-2.

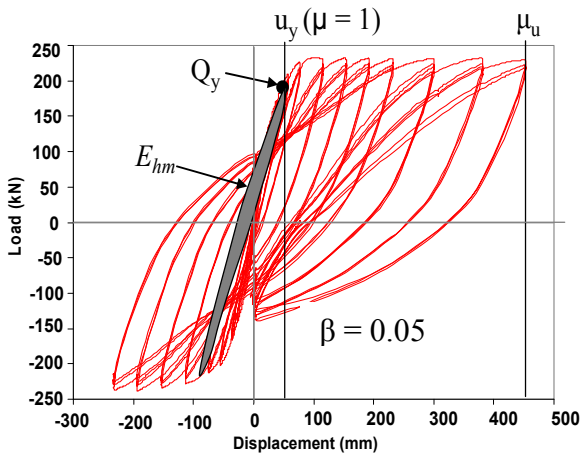

Fig. 5-1 Parameters for Flexural Park and Ang Damage Index

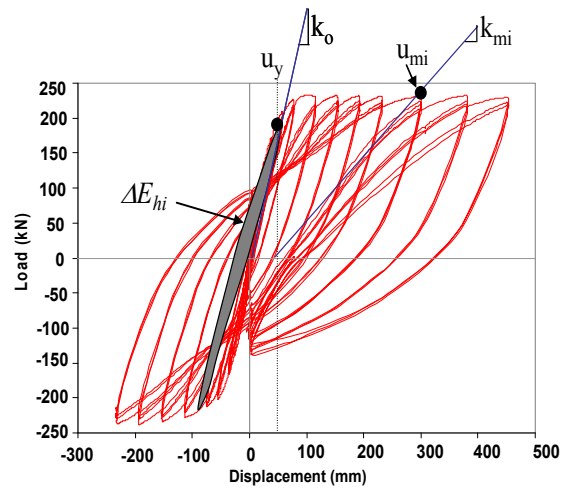

Fig. 5-2 Parameters for Modified Flexural Hwang and Scribner Damage Index

5.3.2. Torsional Damage Index for Combined Loading

In this study, the cumulative damage index model proposed by Park and Ang (1985) was modified and extended to predict the progression of the torsional damage state under pure torsion and combined loading and the normalization-modified Hwang and Scribner (1984) model was also used to quantify the various torsional damage states. The following equations are thus proposed for torsional damage indices under pure torsion and combined loading as expressed by

$$\boldsymbol{TDI}_{\mathbf{P.A.Torsion,Combined}} = \frac{\boldsymbol{\theta_m}}{\boldsymbol{\theta_u}} + \boldsymbol{\beta}\frac{\boldsymbol{E_{hm}}}{\boldsymbol{T_y\theta_u}}, \tag{5-22}$$

$$\boldsymbol{TDI}_{\boldsymbol{H.S.Torsion,Combined}} = \frac{\sum_{i=1}^{M}\Delta E_{h,i,T}\frac{K_{m,i,T}}{K_{0,T}}\frac{\theta_{m,i,T}^2}{\theta_{y,T}^2}}{E_{Total,Torsion}}. \tag{5-23}$$

The parameters for calculating the torsional damage index include the maximum twist in a given cycle, yielding torsional moment, ultimate twist corresponding to ultimate torsional moment, the maximum twist in each loading cycle, the maximum torsional stiffness in each loading cycle, the yielding twist and torsional stiffness, and the torsional

energy dissipation in each loading. The definitions of these parameters are shown in Fig. 5-3 and Fig. 5-4.

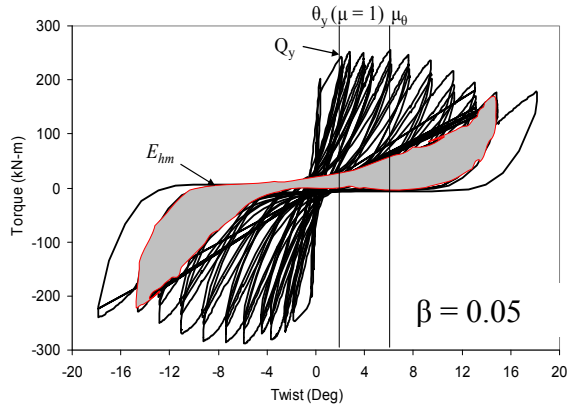

Fig. 5-3 Parameters for Modified Torsional Park and Ang Damage Index

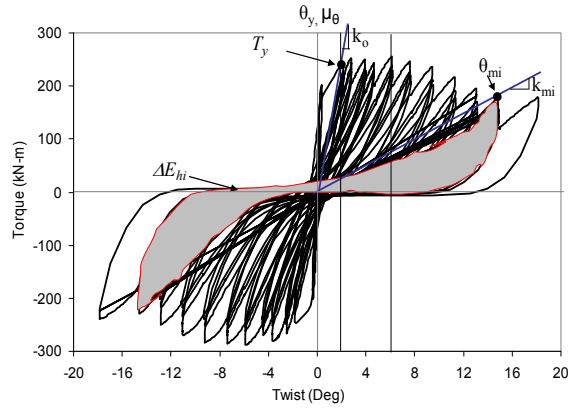

Fig. 5-4 Parameters for Modified Torsional Hwang and Scribner Damage Index

5.4. Validation of Proposed Damage Index Models

The proposed damage index models for combined loading are validated by the hysteretic response of RC columns through the experimental program. The verification of the proposed damage index models and the combined loading effect on these models are discussed in the following section.

5.4.1. Square Columns under Combined Loading

The flexural and torsional damage indices for square columns were calculated according to two proposed damage index models from flexural and torsional hysteresis under pure flexure, pure torsion and combined loading. All the damage index values are plotted up to the ultimate failure states. It is clearly shown that the Park and Ang damage index model can well predict the progressions of damage limit states for both flexure and torsion as shown Fig. 5-5 and Fig. 5-6. The proposed torsional damage index values using the Park and Ang approach for torsional hysteresis works as well as for flexure. In both cases, the progression of damage index by Park and Ang approach was linear with a

ductility level up to the ultimate failure state. The damage index value varied from '0', corresponding to no damage, to '1' or a little higher than '1', corresponding to near collapse. The structural damage characteristics such as reinforcement yielding, peak load, concrete cover spalling and concrete core crushing can be represented by various damage index values as shown in the figures. The damage index value at the each ductility maintained the same level along with increasing loading cycles, which is a disadvantage for indicating the progression of damage in each increasing load cycle at the same ductility level. The flexural displacement ductility capacity dropped from 12.5 for pure flexure to 4.5, 4.5 and 4.0 under the T/M ratio 0.2 and 0.4 and 0.6, respectively. Therefore the flexural damage index curve with respect to displacement ductility obtained an increasing slope with the increasing T/M ratio, which indicated that the progression of flexural damage is amplified with an increase in the T/M ratio by more concrete cover spalling and concrete core crushing. And the torsional rotation ductility at the ultimate state dropped from 10 to 9.5, 5 and 3 when the T/M ratio decreased from ∞

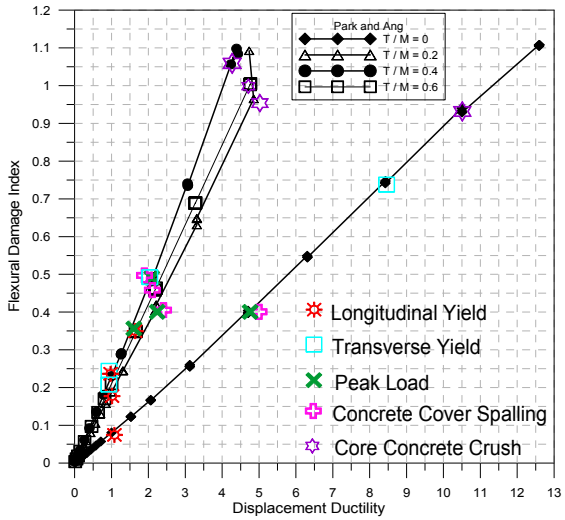

Fig. 5-5 Park and Ang Flexural Damage Index for Square Columns under Combined Loading

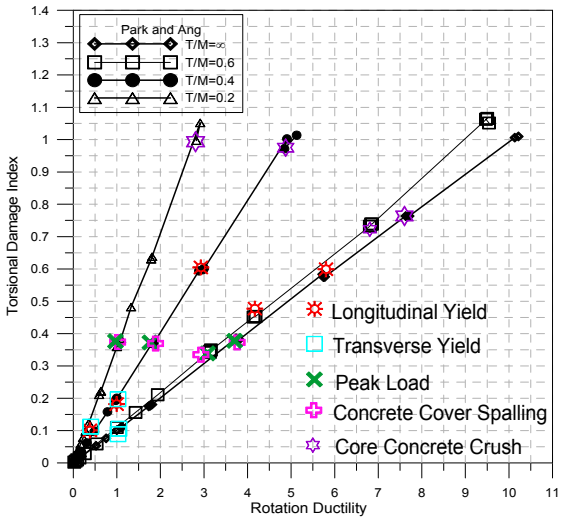

Fig. 5-6 Modified Park and Ang Torsional Damage Index for Square Columns under Combined Loading

to 0.6, 0.4 and 0.2, which also indicated the progression of torsional damage is amplified by the flexure effect from severe buckling and rupturing of the longitudinal reinforcement.

The flexural and torsional damage index by the modified Hwang and Scribner approach increased with the progressive ductility up to failure state as shown in Fig. 5-7 and Fig. 5-8, which are much higher than the ones by the Park and Ang approach. The modified Hwang and Scribner damage index versus ductility become highly non-linear after concrete cover spalling for the flexural response, and after yielding of the transverse reinforcement for the torsional responses. In addition, the damage index value of this modified model increased step by step as more loading cycles were imposed at the each ductility level, which was an advantage in demonstrating the progression of damage and stiffness degradation along with increasing load cycles within the same ductility level. The ultimate flexural damage indices dropped from 13 for pure flexure to 5.5, 4.5, and 7.5 for T/M ratios of 0.2, 0.4, and 0.6 respectively. At the given ductility level, the columns with higher T/M ratios obtained larger damage index values compared to the one with lower T/M ratios, which indicated the amplification and acceleration of flexural damage limit states due to the torsion effect. For the torsional hysteresis, the ultimate torsional damage indices were 3.75, 3.15, 1.8, and 1.1 with respect to the T/M ratios of ∞, 0.6, 0.4, and 0.2, respectively. Though the ultimate torsional damage index value decreased with more flexure, the flexural effect degraded the rotation ductility capacity and amplified the torsional damage states during the progression of damage.

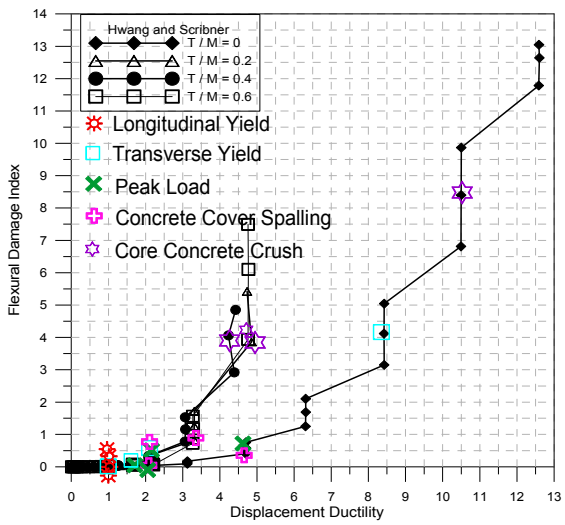

Fig. 5-7 Modified Hwang and Scribner Flexural Damage Index for Square Columns under Combined Loading

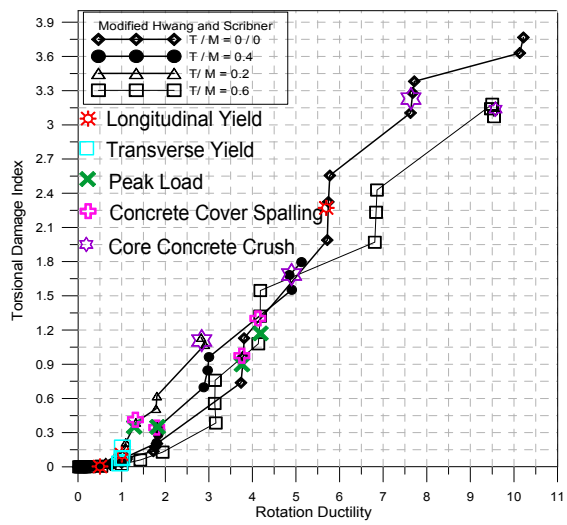

Fig. 5-8 Modified Hwang and Scribner Torsional Damage Index for Square Columns under Combined Loading

5.4.2. Oval Columns under Uniaxial Combined Loading

The Park and Ang damage index model was used to present the damage progression of oval columns under uniaxial combined loading for both flexural and torsional hysteresis as shown Fig. 5-9 and Fig. 5-10. The linear trends of the damage index along with the ductility level were the same as the ones in the square columns. The flexural displacement ductility capacity dropped from 10.5 to 4.5 for a T/M ratio of 0.2 and 0.6, respectively. Therefore the flexural damage index curve with respect to displacement ductility obtained an increasing slope along with an increasing T/M ratio, which showed that flexural damage progression was amplified with an increase in the T/M ratio for flexural responses. And the torsional rotation ductility at the ultimate state dropped from 9.5 to 6 and 2.5 when the T/M ratio decreased from ∞ to 0.6 and 0.2, which also indicated that the progression of torsional damage is amplified by the flexure effect. It can predict the progression of damage for both the flexural and torsional failure dominant columns under combined loading, which can be tracked throughout the course of inelastic loading.

The flexural and torsional damage index by the modified Hwang and Scribner approach increased with the progressive ductility up to the ultimate value, which is much higher than the ones by the Park and Ang approach as shown in Fig. 5-11 and Fig. 5-12.

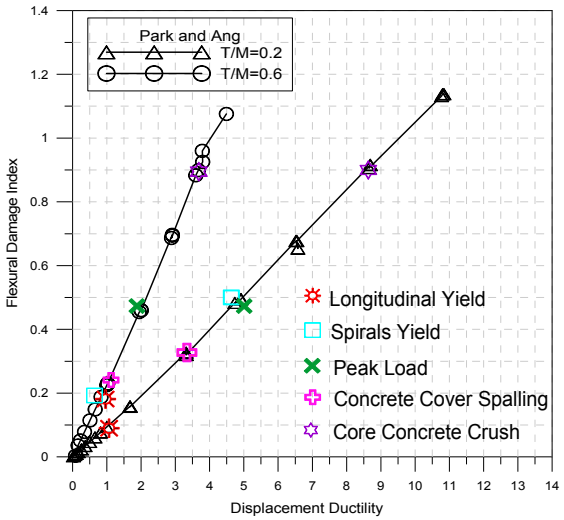

Fig. 5-9 Park and Ang Flexural Damage Index for Oval Columns under Uniaxial Combined Loading

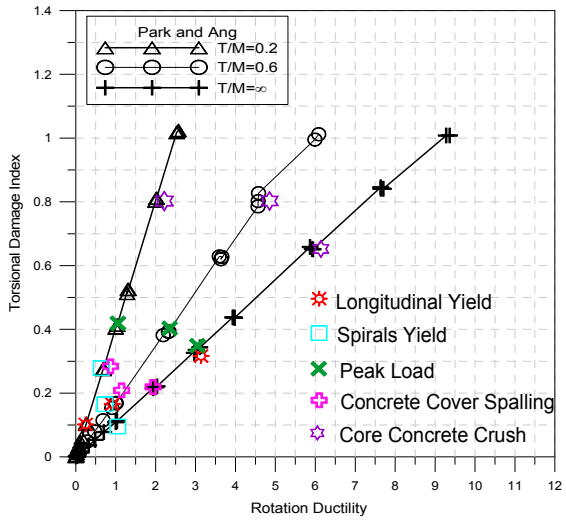

Fig. 5-10 Modified Park and Ang Torsional Damage Index for Oval Columns under Uniaxial Combined Loading

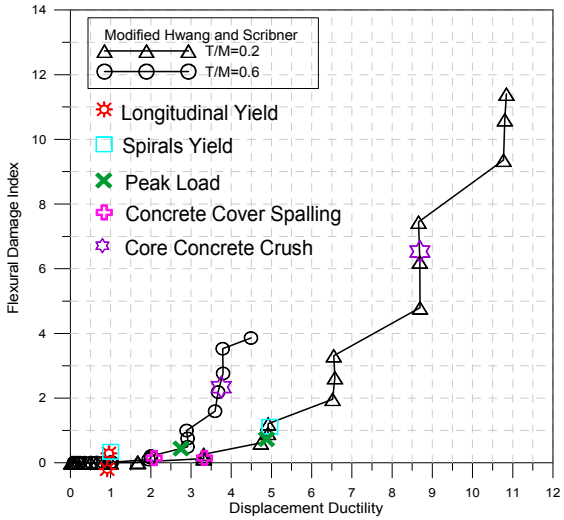

Fig. 5-11 Modified Hwang and Scribner Flexural Damage Index for Oval Columns under Uniaxial Combined Loading

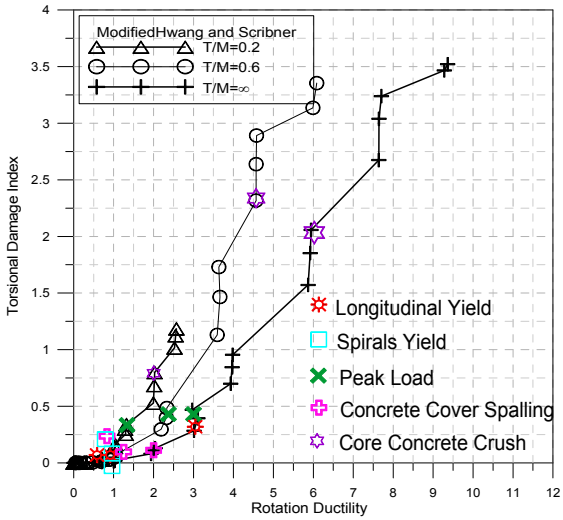

Fig. 5-12 Modified Hwang and Scribner Torsional Damage Index for Oval Columns under Uniaxial Combined Loading

For the flexural hysteresis, the flexural damage index by the modified Hwang and Scribner approach significantly increased and became highly non-linear after spalling of concrete cover up to the ultimate damage state. Though the ultimate flexural damage

indices dropped from 11.5 to 4 for T/M ratios of 0.2 and 0.6 respectively, the column loaded with larger torsional moment (T/M=0.6) obtained larger flexural damage index as compared to the column at a T/M ratio of 0.2 at the same displacement ductility, indicating the amplification and acceleration of flexural damage limit states due to he torsion effect. For the torsional hysteresis, the torsional damage index by the modified Hwang and Scribner approach rapidly developed and became highly non-linear after yielding of the transverse spirals. The ultimate torsional damage indices were 3.6, 3.25, and 1.35 with respect to the T/M ratios of ∞, 0.6 and 0.2, respectively. Though the ultimate torsional damage index value decreased along with more flexure, the flexural effect degraded the rotation ductility capacity and amplified the torsional damage states during the progression of damage. In addition, the flexural and torsional damage index values at the ultimate state significantly differ for the same columns.

5.4.3. Oval Columns under Biaxial Combined Loading

The flexural and torsional damage index values for oval columns under biaxial combined loading were calculated by the Park and Ang damage index model as plotted in Fig. 5-13 and Fig. 5-14. The linear relationship between damage index and ductility level provided simple and reliable indication of sequential failure stages of the RC columns. The flexural displacement ductility capacity dropped from 10 for pre-flexure and shear to 6 and 5.5 for a T/M ratio of 0.2 and 0.4, respectively. The combined loading effect on the reduction of ductility capacity resulted in amplification of flexural damage progression with an increase in the T/M ratio for flexural responses. The torsional rotation ductility at the ultimate state dropped from 9.5 to 5.5 and 2.5 when the T/M ratio decreased from ∞

to 0.4 and 0.2. So the columns with low T/M ratios experienced more damage as compared to the columns with high T/M ratios at the same torsional ductility level.

The flexural and torsional damage indices by the modified Hwang and Scribner approach were calculated and plotted along with the ductility level as shown in Fig. 5-15 and Fig. 5-16. The modified Hwang and Scribner damage index values are much higher than the ones from the Park and Ang approach. As in the case of uniaxial loading, the flexural damage index by the modified Hwang and Scribner approach became highly non-linear after concrete cover spalling up to the ultimate damage state. The ultimate flexural damage index dropped from 9 for pure flexure and shear to 6.5 and 5.5 for T/M ratios of 0.2 and 0.4, respectively. The column loaded with larger T/M ratios obtained larger flexural damage index as compared to the column at the T/M ratio of 0.2 at the same displacement ductility. This amplification and acceleration of flexural damage limit

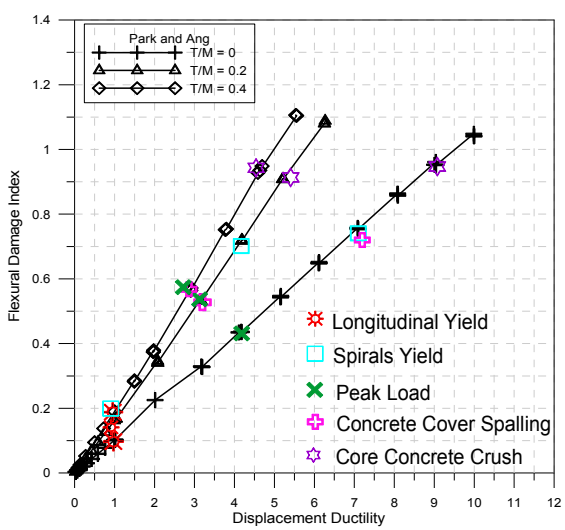

Fig. 5-13 Park and Ang Flexural Damage Index for Oval Columns under Biaxial Combined Loading

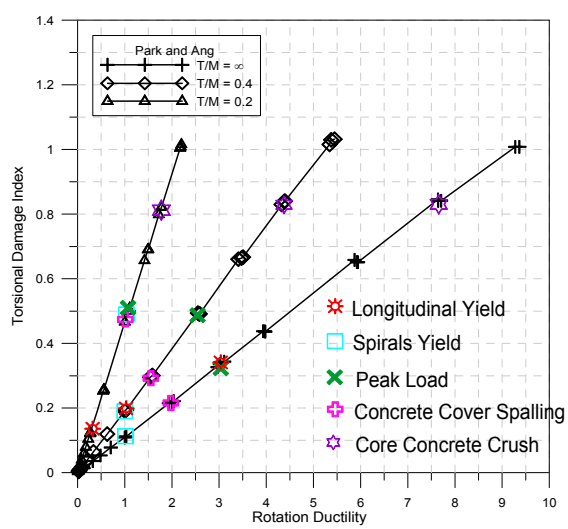

Fig. 5-14 Modified Park and Ang Torsional Damage Index for Oval Columns under Biaxial Combined Loading

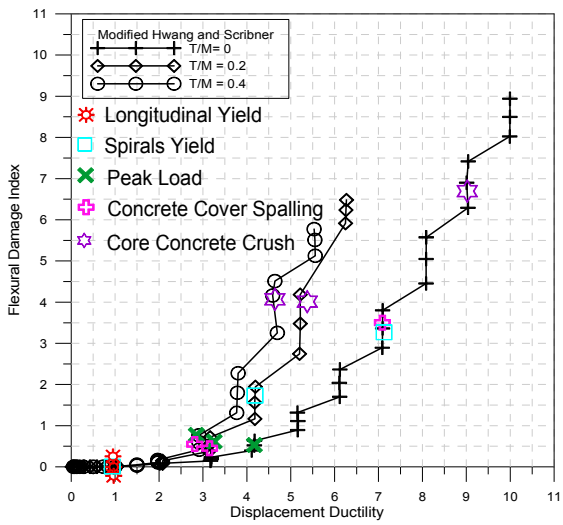

Fig. 5-15 Modified Hwang and Scribner Flexural Damage Index for Oval Columns under Biaxial Combined Loading

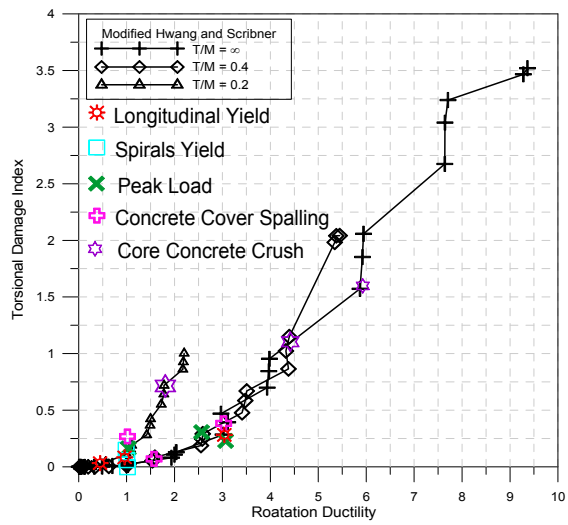

Fig. 5-16 Modified Hwang and Scribner Torsional Damage Index for Oval Columns under Biaxial Combined Loading

states under the combined loading were caused by the torsion effect. For the torsional hysteresis, the torsional damage index by the modified Hwang and Scribner approach rapidly increased with highly non-linear trends after yielding of the transverse spirals. The ultimate torsional damage indices were 3.6, 2.0, and 1.0 with respect to the T/M ratios of ∞, 0.4, and 0.2 respectively. Though the ultimate torsional damage index value decreased along with increase of the T/M ratios, the flexural load degraded the rotation ductility capacity and amplified the torsional damage states during the progression of damage.

5.4.4. Transverse Confinement Effect

In order to study the transverse confinement effect, the damage indices of square columns under T/M ratios of 0.2, 0.6 and ∞ are selected to compare to the ones in the oval columns under uniaixal combined loading at T/M ratios of 0.2, 0.6 and ∞. The damage index values for square and oval columns from two proposed models are plotted and compared in Fig. 5-17 through Fig. 5-20.

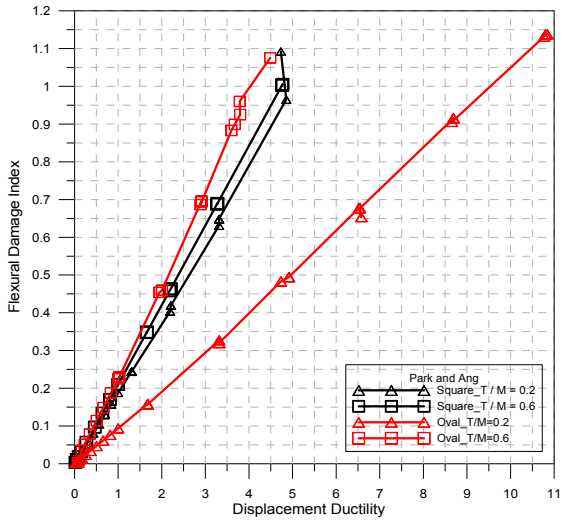

Fig. 5-17 Park and Ang Flexural Damage Index Comparison for Square and Oval Columns

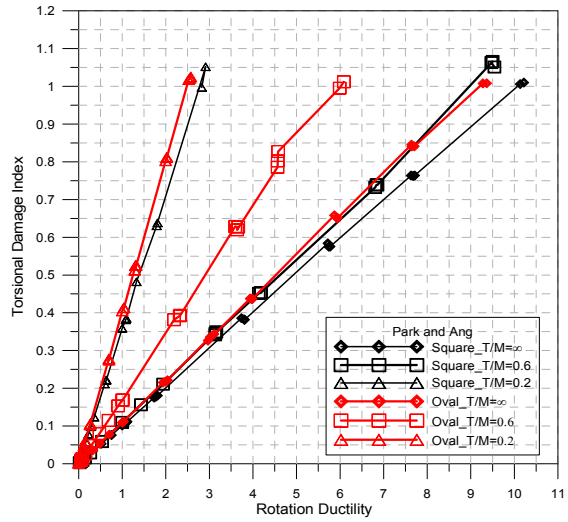

Fig. 5-18 Modified Park and Ang Torsional Damage Index Comparison for Square and Oval Columns

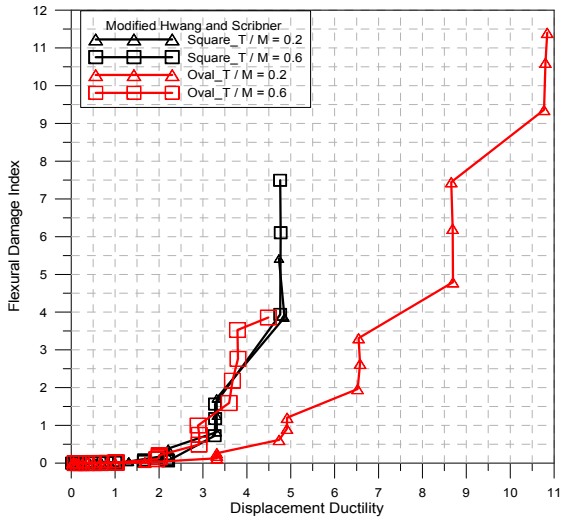

Fig. 5-19 Modified Hwang and Scribner Flexural Damage Index Comparison for Square and Oval Columns

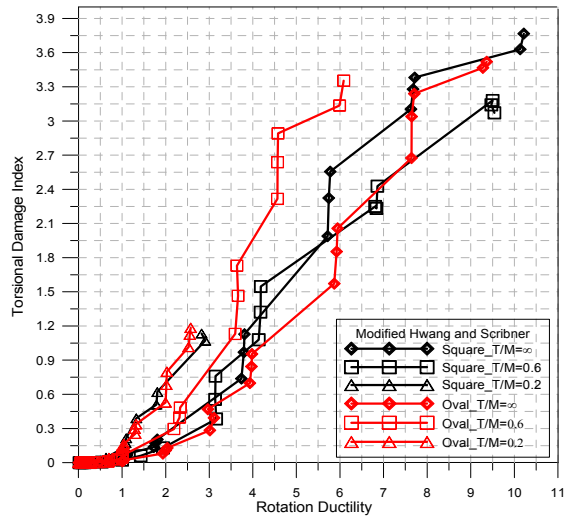

Fig. 5-20 Modified Hwang and Scribner Torsional Damage Index Comparison for Square and Oval Columns

The flexural damage indices for oval columns were smaller as compared to the square columns at the same ductility level, which indicated that interlocking spirals provided better transverse confinement and reduced concrete core crushing to mitigate the flexural damage at higher displacement ductility levels. With respect to torsional damage, the square and oval columns both experienced severe stiffness and strength degradation at high rotation ductility levels so there was no big difference in the torsional damage index

values for these two different transverse confinement configurations. However, the square column under the T/M ratio of 0.6 seems to obtain lower torsional damage index as compared to the oval column under a T/M ratio of 0.6 at the same rotation ductility. This exceptional case was caused by the slight overloading at yielding stage for this square column, which resulted in unexpected earlier transverse reinforcement yielding and in turn unexpected larger rotation ductility. In general, the better transverse confinement effect from interlocking spirals contributed to mitigating the damage progression of RC bridge columns under combined loading.

5.4.5. Biaxial and Uniaxial Loading Effect

In order to study the biaxial and uniaxial loading effect, the damage indices of oval columns under uniaxial combined loading at T/M ratios of 0.2 and 0.6 were selected to compare to the ones in oval columns under biaxial combined loading at T/M ratios of 0.2 and 0.4, as shown in Fig. 5-21 through Fig. 5-24. For flexure dominant failure, the column under biaxial combined loading at a T/M ratio of 0.2 obtained both larger flexural and torsional damage indices than the ones under uniaxial combined loading at a T/M ratio of 0.2. These amplified damage indices can be explained by less ductility capacity and more damage under biaxial combined loading. For the columns under higher T/M ratios of 0.4 and 0.6, the biaxial combined loading accelerated and amplified the torsional damage progression resulting in larger torsional damage index values; however, no significant difference in flexural damage index values was observed between biaxial and uniaxial combined loading since more torsional damage occurred in these columns with more torsion effect. Therefore, the amplification of damage progression under biaxial combined loading can be reflected by the proposed damage index model prediction.

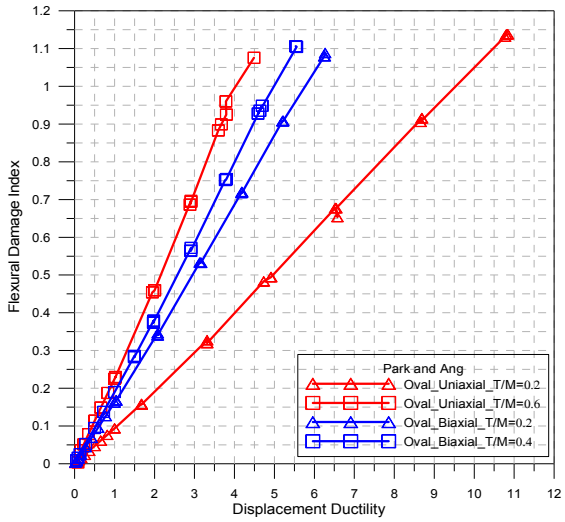

Fig. 5-21 Park and Ang Flexural Damage Index Comparison for Biaxial and Uniaxial Combined Loading

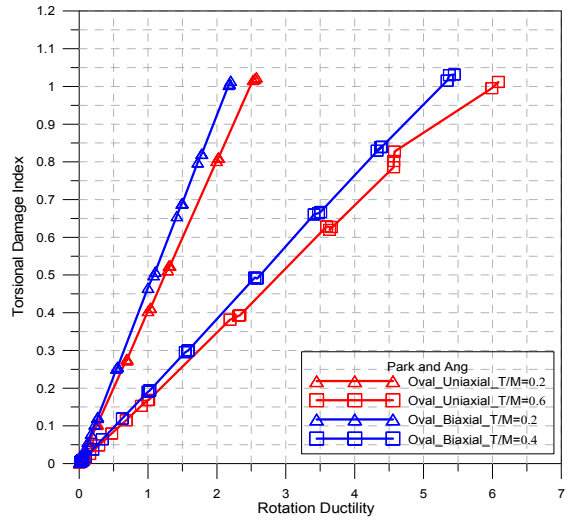

Fig. 5-22 Modified Park and Ang Torsional Damage Index for Biaxial and Uniaxial Combined Loading

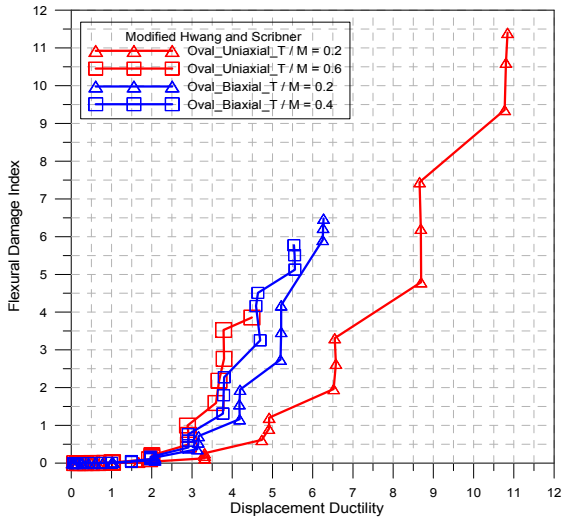

Fig. 5-23 Modified Hwang and Scribner Flexural Damage Index for Biaxial and Uniaxial Combined Loading

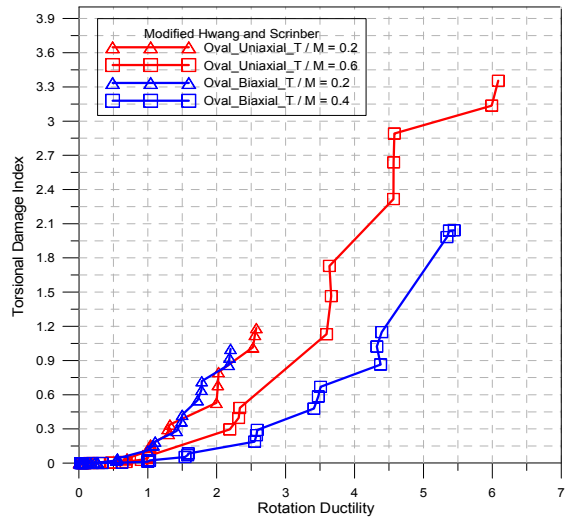

Fig. 5-24 Modified Hwang and Scribner Torsional Damage Index for Biaxial and Uniaxial Combined Loading

5.5. Interaction of Flexural and Torsional Damage Indices

Schematic framework for the damage assessment or damage-based design approach for RC columns under combined loading is shown in the Fig. 5-25. The interaction relationship between decoupled flexural and torsional damage index should be used to conduct further damage assessment and design procedure. Due to the physical intuition and simpleness, the damage progression predictions from the Park and Ang approach

were adapted to establish the interaction diagram and propose an empirical model for flexural and torsional damage index interaction under combined loading.

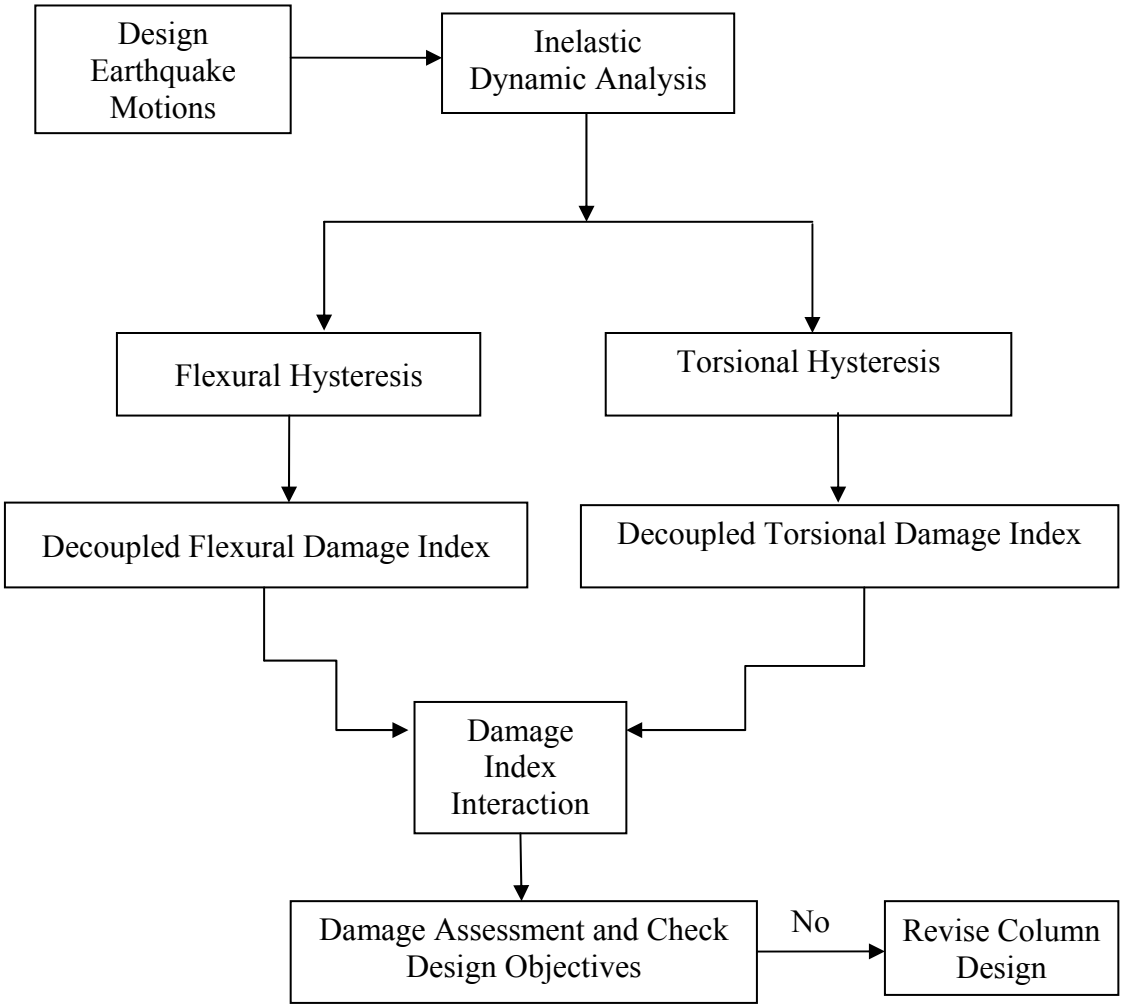

Fig. 5-25 Framework of Damage Assessment and Damage-based Design for RC Columns under Combined Loading

5.5.1. Interaction Diagram of Damage Index for Square Columns

The interaction between the flexural and torsional moment depended on a number of factors, such as the amount of transverse and longitudinal reinforcement, the aspect ratio of the section, and concrete strength. The interaction diagrams for flexural and torsional damage index of square columns are plotted in Fig. 5-26 based on the Park and Ang approach. The interaction diagram indicated a linear relationship between flexural and

torsional damage indices. For all the square columns, the interaction diagrams merged with each other before concrete cover spalling rapidly developed along the column. Thereafter, the warping effect of the square cross section accelerated the concrete cover spalling and introduced significant torsional stiffness and strength degradation, which demerged the interaction diagrams depending on different failure modes. For columns under a balanced T/M ratio of 0.4, the torsional and flexural damage index reached the value of '1' simultaneously at ultimate failure. The column under a lower T/M ratio of 0.2 experienced flexure dominant failure mode resulting in the flexural damage index reaching the value of '1' just before the torsional damage index reached the value of '1' at the ultimate failure stage. The column under the higher T/M ratio of 0.6 experienced torsion dominant failure mode and the torsional damage index reachedthe value of '1' just before the flexural damage index reached the value of '1' at the ultimate failure stage.

However, all these linear diagrams obtained around a 45˚ slope, which concluded that the transverse reinforcement ratio was adequate from both the confinement design point of view and damage assessment specifications under combined loading. Based on the comparison of interaction diagrams under various T/M ratios, it was observed with a limited combined loading effect on the interaction behavior of the torsional and flexural damage indices. In addition, this interaction diagram can be split into five different zones with specific damage index levels, namely, concrete cracking, reinforcement yielding, concrete cover spalling, concrete core crushing and reinforcement buckling and rupturing as shown in Fig. 5-26.

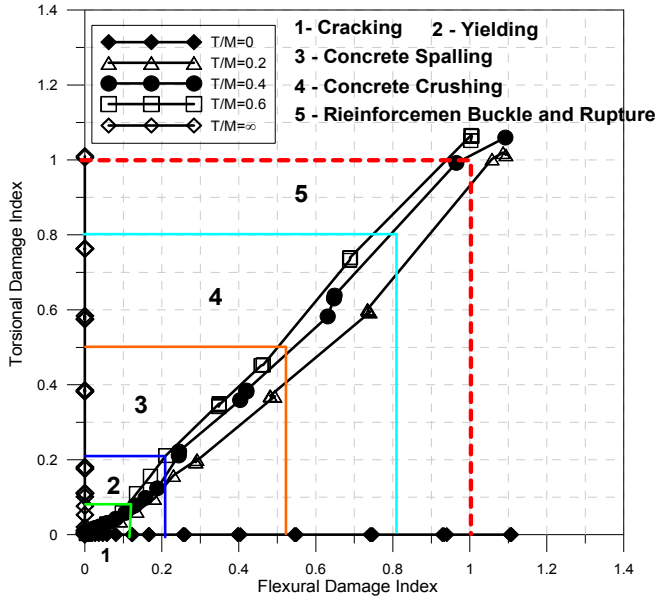

Fig. 5-26 Interaction Diagrams of Flexural and Torsional Damage Indices of Square Columns

5.5.2. Interaction Diagram of Damage Index for Oval Columns

The interaction diagrams for the flexural and torsional damage indices of oval columns are plotted in Fig. 5-27 based on the Park and Ang approach. The interaction diagram had an almost linear relationship between flexural and torsional damage indices as the same as the interaction diagram in the square columns. The interaction diagrams of torsional and flexural damage for all the oval columns merged with each other before the concrete cover totally spalled, which was postponed as compared to square columns, and thereafter the significantly torsional stiffness and strength degradation demerged the interaction diagrams depending on different failure modes. The columns under T/M ratio of 0.2 and 0.4 experienced the torsion dominant failure mode and achieved the flexural damage index value of '1' first before the ultimate torsional damage index; the column under the higher T/M ratio of 0.6 experienced torsion dominant failure mode reaching the flexural damage index value of '1' first and then the torsional damage index value of '1' at ultimate failure stage. However, all these linear diagrams had around a 45° slope,

which concluded that the transverse reinforcement ratio was adequate from both the confinement design point of view and damage assessment specifications under combined loading. Also it showed a limited combined loading effect on the interaction behavior of torsional and flexural damage indices. Biaxial and uniaxial loading did not affect the interaction relationship of torsional and flexural damage indices.

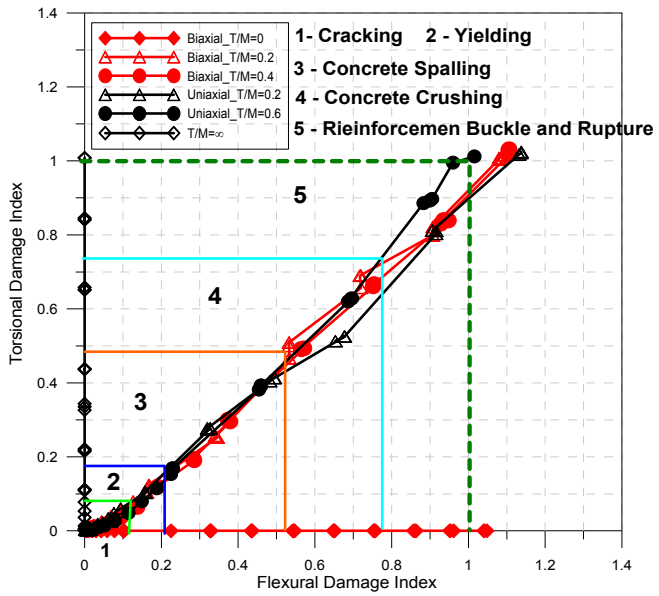

Fig. 5-27 Interaction Diagrams of Flexural and Torsional Damage Indices of Oval Columns

Moreover, this interaction diagram can be split into five different zones with specific damage index levels, namely, concrete cracking, reinforcement yielding, concrete cover spalling, concrete core crushing and reinforcement buckling and rupturing as shown in Fig. 5-27. The oval columns used in this study had the same longitudinal and transverse reinforcement ratios and different transverse reinforcement configurations as compared to square columns. However, all the columns showed similar trends of interaction relationship of torsional and flexural damage indices throughout the whole inelastic response history, which indicated that transverse reinforcement configurations showed no effect on the interaction diagrams.

5.5.3. Empirical Model for Interaction of Flexural and Torsional Damage Index

In this study, the main variables are cross-sectional shape, transverse reinforcement configurations and T/M ratios. In order to establish the empirical model to predict the interaction of flexural and torsional damage indices, the experimental results from Suriya and Belarbi (2008) was used in this study to consider other variables on this interaction relationship such as circular cross section, transverse reinforcement ratios and aspect ratios. The test matrix for their experimental study is summarized in Table 5-2.

Table 5-2 Test Matrix for Experimental Program from Suriya and Belarbi (2008)

Column Name		ρ_l (%)	ρ_t (%)	H/D	Spiral Design For Torsion	T/M Ratio
Circular Column	H/D(6)-T/M(0.0)/0.73%	0.73	2.1	6	Low	0
	H/D(6)-T/M(0.1)/0.73%	0.73	2.1	6	Low	0.1
	H/D(6)-T/M(0.2)/0.73%	0.73	2.1	6	Low	0.2
	H/D(6)-T/M(0.4)/0.73%	0.73	2.1	6	Low	0.4
	H/D(6)-T/M(∞)/0.73%	0.73	2.1	6	Low	∞
	H/D(6)-T/M(0.2)/1.32%	1.32	2.1	6	Moderate	0.2
	H/D(6)-T/M(0.4)/1.32%	1.32	2.1	6	Moderate	0.4
	H/D(3)-T/M(0.0)/1.32%	1.32	2.1	3	Moderate	0
	H/D(3)-T/M(0.2)/1.32%	1.32	2.1	3	Moderate	0.2
	H/D(3)-T/M(0.4)/1.32%	1.32	2.1	3	Moderate	0.4
	H/D(3)-T/M(∞)/1.32%	1.32	2.1	3	Moderate	∞

For experimental results from Suriya and Belarbi (2008), the damage index values generated from the Park and Ang approach were used to create the diagrams of interaction of flexural and torsional damage indices. The effect of transverse spiral reinforcement ratio and T/M ratios on the interaction relationship of torsional and flexural damage indices is shown in Fig. 5-28. With a low transverse spiral reinforcement ratio of 0.73%, the columns experienced the torsion failure mode as the torsional damage index reached the value of '1' before the flexural damage index. This relationship shows that a transverse reinforcement ratio that is adequate from a confinement design point of view

may not satisfy performance specifications under torsional loading. Even with an increase in the transverse spiral reinforcement ratio, the columns reached the torsional damage index value of '1' just before the flexural damage index reached '1'. However, the increase in the transverse spiral reinforcement ratio led to less torsion failure mode involved by more transverse confinement. In addition, with an increase in the transverse spiral reinforcement ratio, the flexural damage index values and progression of damage were nearly the same for various levels of the T/M ratios.

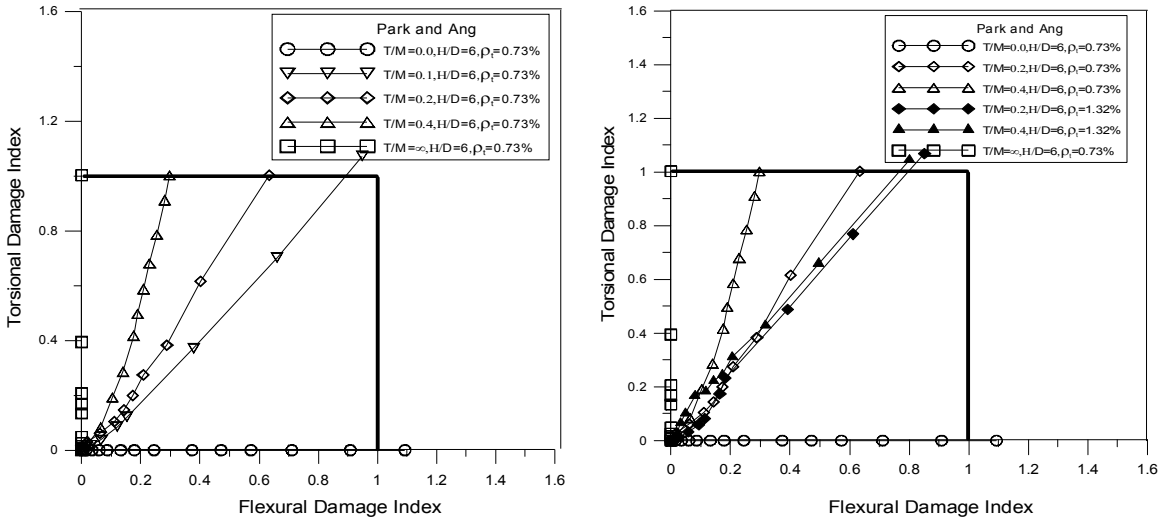

Fig. 5-28 Effect of Transverse Spiral Reinforcement Ratio and T/M Ratios on Interaction Diagrams of Flexural and Torsional Damage Index Model (Suriya 2010)

For circular columns with a low transverse reinforcement ratio of 0.73%, the slopes of interaction diagrams were significantly affected by T/M ratios since they experienced torsion dominant failure; however, the slopes of interaction diagrams for circular columns with a higher transverse reinforcement ratio of 1.32% were not affected by the T/M ratios since they experienced more flexural damage. The effect of aspect ratio or shear span on flexural and torsional damage index interaction is presented in the Fig. 5-29. Lower aspect ratio or shear span altered the failure mode from torsion dominant to flexure

dominant. The flexural damage index reached the value of '1' before the torsional damage index reached the same value.

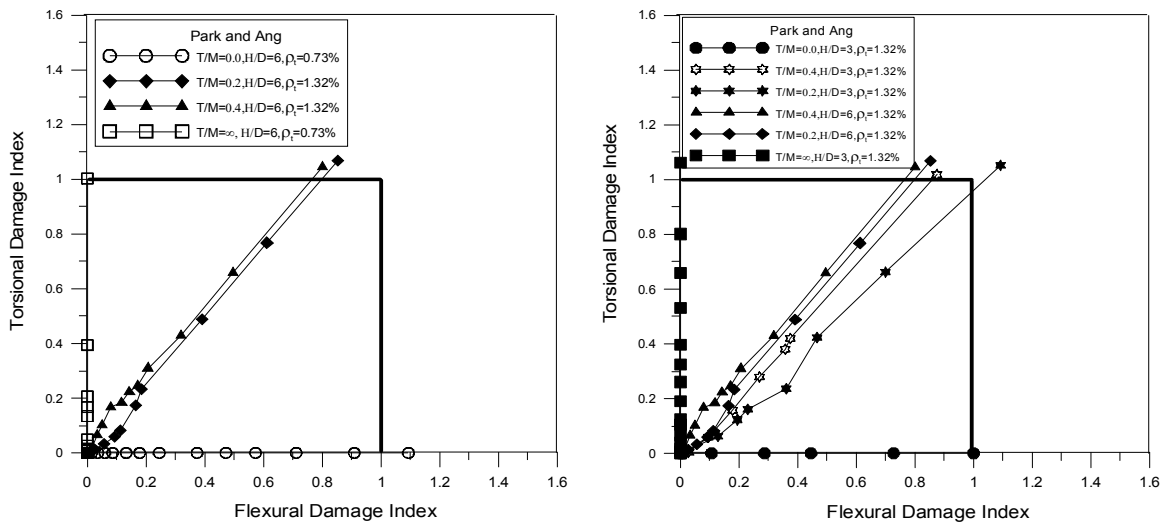

Fig. 5-29 Effect of Aspect Ratios on Interaction Diagrams of Flexural and Torsional Damage Index Model (Suriya 2010)

Using experimental results from this study and Suriya and Belarbi (2008), an empirical model was developed to predict the interaction of torsional and flexural damage indices. Due to the nearly linear relationship of interaction diagrams from experimental results, the equation was derived through combining multi-factor line regression and polynomial regression by the Ordinary Least Square (OLS) method, which incorporated the main variables such as transverse reinforcement ratio and configurations, cross sectional shape, aspect ratios and T/M ratios. The equation expression and parameters description are summarized in Eq. 5-24 and Table 5-3. The equation can be expressed by

$$FDI = \lambda_1 \left[\lambda_2 \left(\frac{T}{M}\right)^3 - \lambda_3 \left(\frac{T}{M}\right)^2 + \lambda_4 \left(\frac{T}{M}\right) \right] \times (\rho_t) \times \left(\frac{H}{D}\right) \times TDI - 0.0111\lambda_5, \qquad (5\text{-}24)$$

where *TDI* refers to the torsional damage index, *FDI* represents the flexural damage index, ρ_t is the transverse reinforcement ratio in percent, $\frac{H}{D}$ represents the aspect ratios, λ_1 is a correction factor for the aspect ratios, λ_2, λ_3 and λ_4 are the correlation factors with

T/M ratios and transverse reinforcement ratio, and λ_5 is the correlation factors with cross sectional shapes. The correction factor λ_1 accommodates the various aspect ratios and varies in a linear relationship from '2' to '1' for aspect ratio from '3' to '6'. The correlation factor λ_5 is taken as '3', '2', '1' for square, oval and circular columns, respectively.

Table 5-3 Parameters Determination of Empirical Model for Interaction Diagrams of Torsional and Flexural Damage Index under Combined Loading

Cross Section	λ_1		λ_2		λ_3		λ_4		λ_5
Square	H/D=6	1.0	3.72		4.0		1.3		3.0
Oval	H/D=5.5	1.09	2.76		3.14		1.1		2.0
Circular	H/D=6	1.0	ρ_t=1.32	0	ρ_t=1.32	1.96	ρ_t=1.32	1.2	1.0
	H/D=3	2.0	ρ_t=0.73	28.3	ρ_t=0.73	16.78	ρ_t=0.73	4.0	

Using the proposed empirical model, the interaction relationship of decoupled torsional and flexural damage indices under combined loading can be predicted with respect to a different cross sectional shape, transverse reinforcement ratio and configurations, aspect ratios, and T/M ratios. The comparisons of empirical prediction and experimental results are presented in Fig 5-30 through Fig. 5-33. The proposed empirical model provided the foundation toward development of a damage-assessment approach for RC bridge columns under combined loading. The above empirical equation is applicable for circular, square and oval columns with specific ranges in transverse reinforcement ratio, aspect ratio and T/M ratios. The predictions were reasonably accurate for the columns with transverse reinforcement ratios of 0.73% and 1.32%, aspect ratios varying between 3 and 6 and T/M ratios varying between 0.2 and 0.6. In the plotted diagram, the correlation coefficient R-squared values are also shown along with

the prediction, which are used to estimate the fitness of regression curves to the experimental data. All the R-squared values ranged between '0.96' and '0.99', which indicated an accurate prediction. The comparisons demonstrated that the model accurately predicted the change from torsional-dominant behavior to flexural-dominant behavior with an increase in the spiral reinforcement ratio. In addition, the predicted interaction diagrams of oval column had smaller average slope as compared to the square and circular columns, which indicated that interlocking spirals enhanced torsional capacity and prohibited the torsional dominant failure mode.

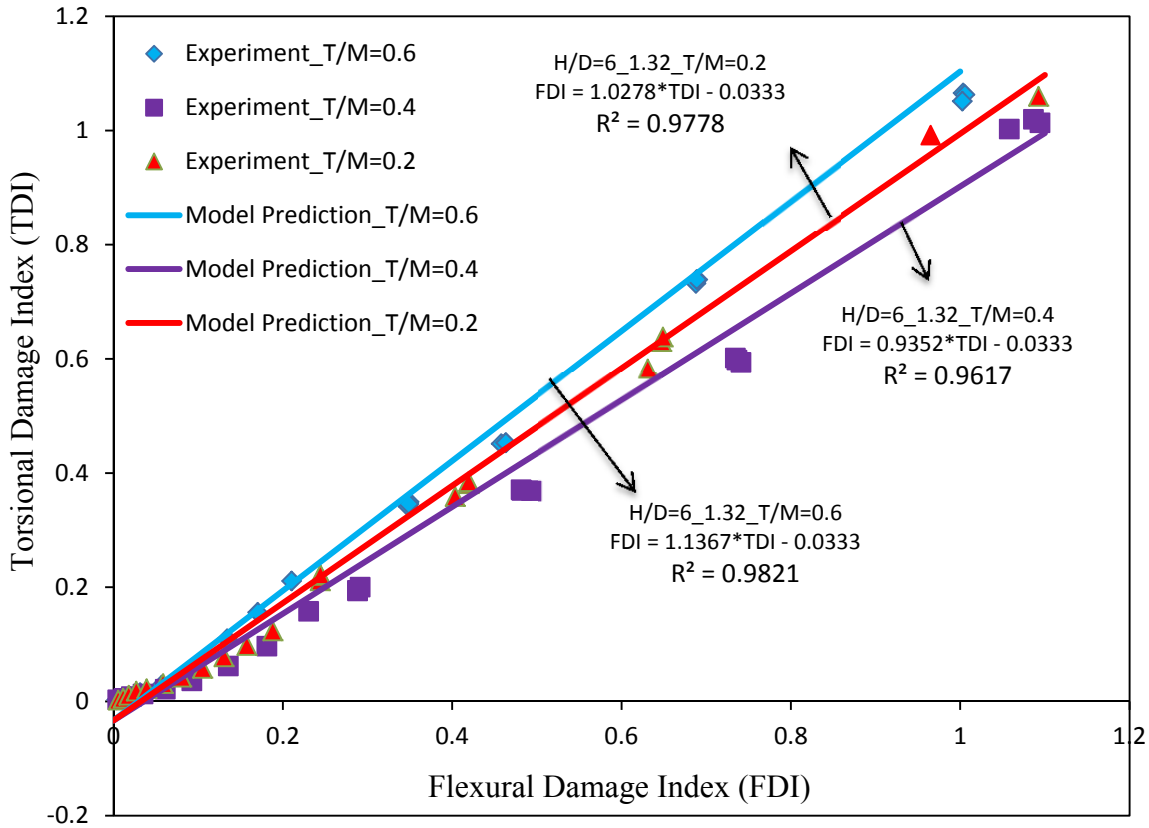

Fig. 5-30 Empirical Model Prediction for Square Columns

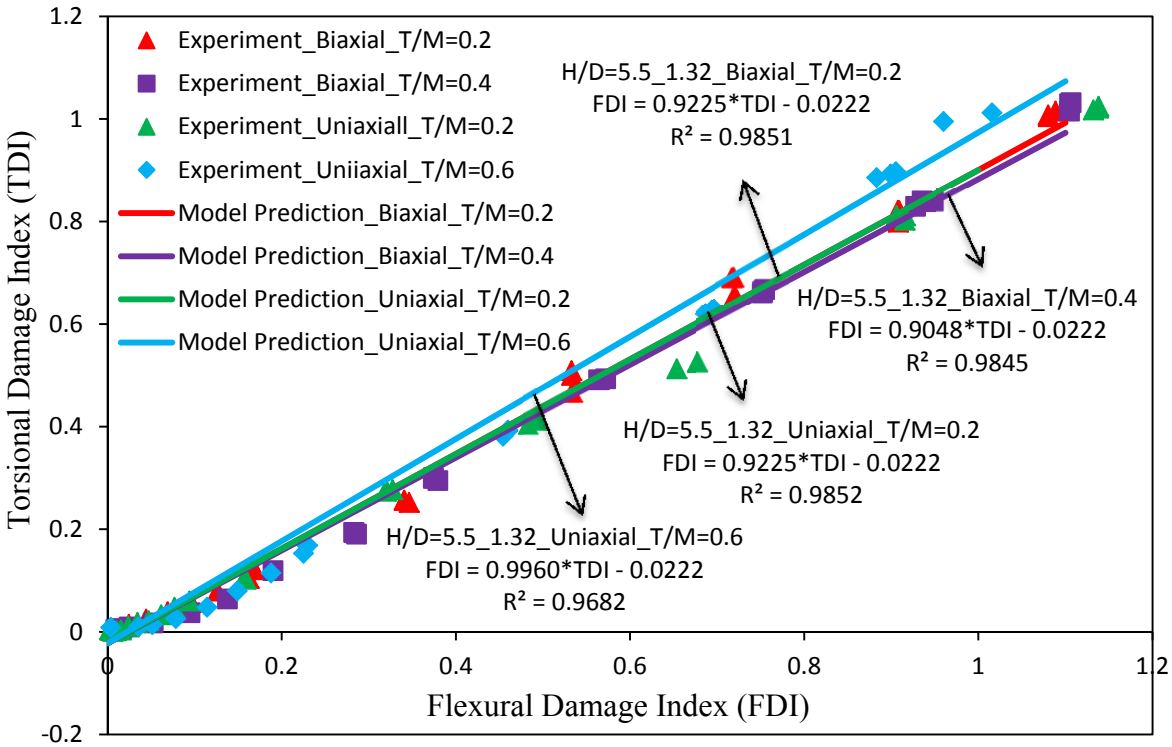

Fig. 5-31 Empirical Model Prediction for Oval Columns

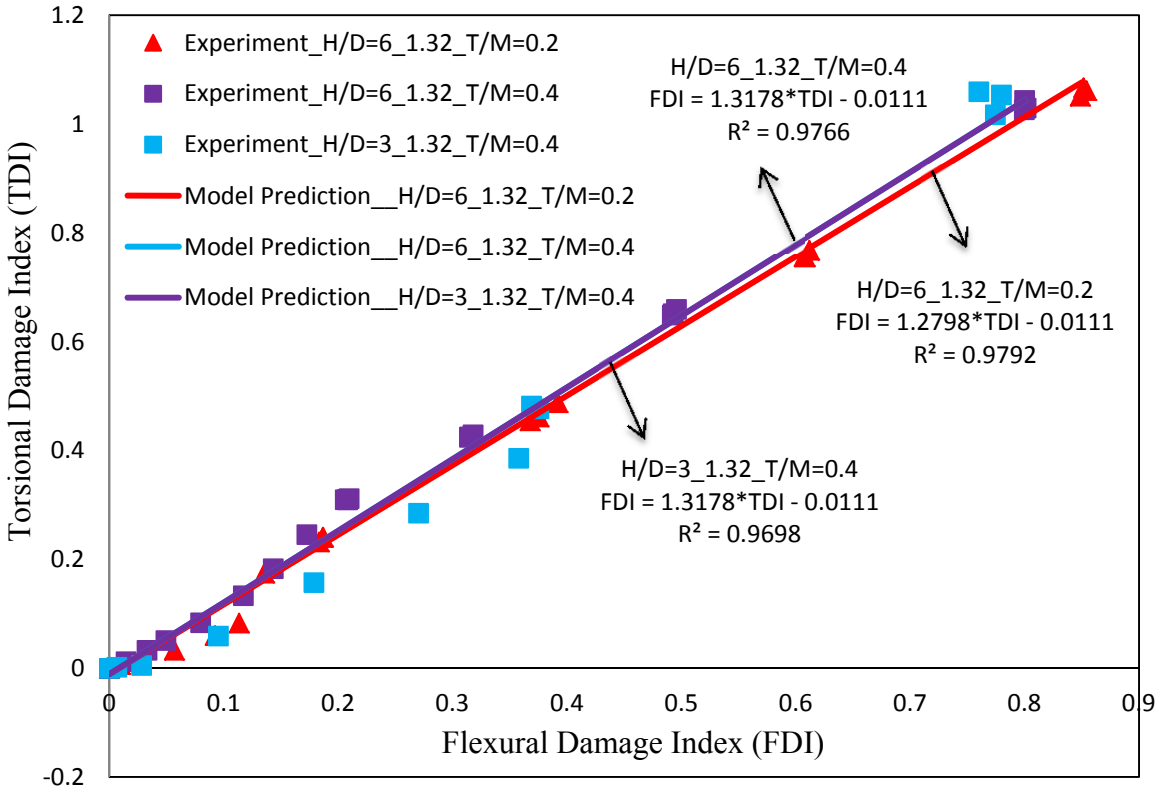

Fig. 5-32 Empirical Model Prediction for Less Reinforced Circular Columns

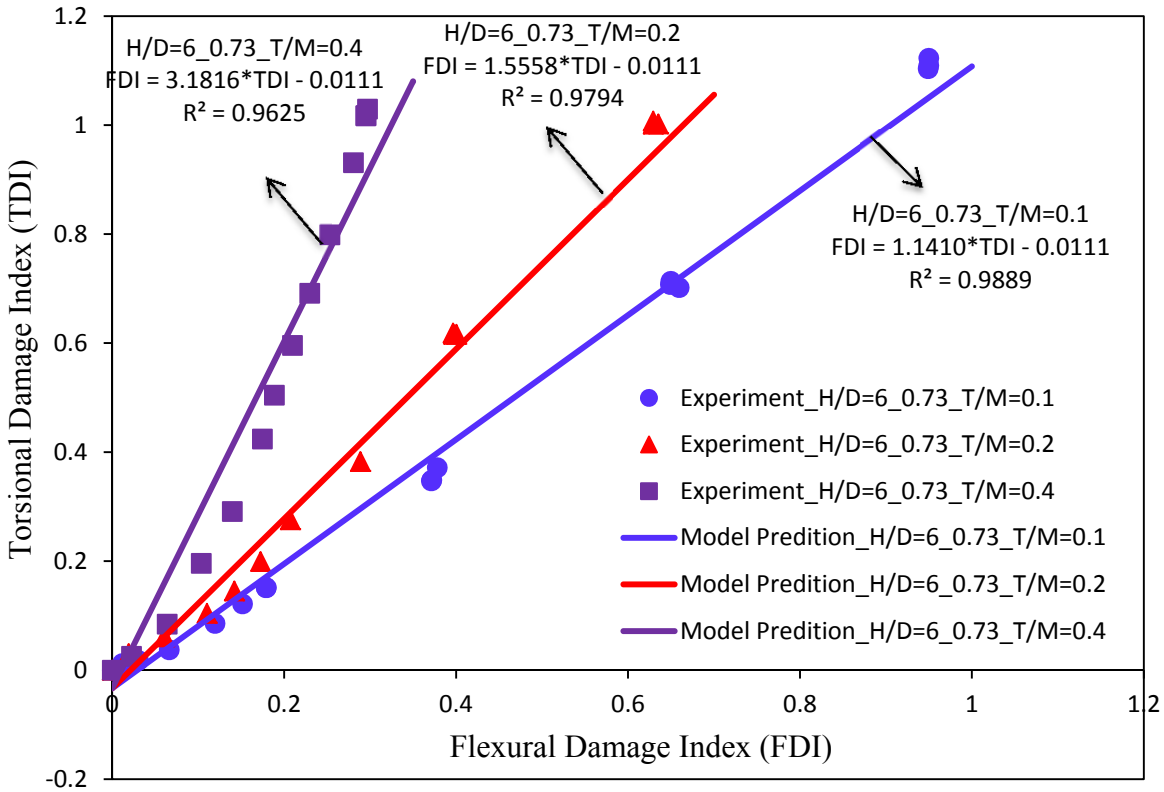

Fig. 5-33 Empirical Model Prediction for Moderate Reinforced Circular Columns

Moreover, all the interaction points for columns with a moderate amount of transverse reinforcement (ρ_t = 1.32%) are plotted in Fig. 5-34. Based on the comparison, the effects of aspect ratios and T/M ratios on the interaction diagrams are so limited, and the cross sectional shape and transverse reinforcement configuration effect are pronounced. Therefore three simplified empirical equations can be achieved for the square, circular and oval columns with moderate transverse reinforcement ratios by neglecting the aspect and T/M ratios. The simplified empirical equations and corresponding R-squared values are shown in Fig. 5-34. The equations can be expressed as

$$FDI = \chi_1 TDI - 0.0111\chi_2, \tag{5-25}$$

where χ_1 and χ_2 are the correction factors accommodating cross sectional shapes and transverse reinforcement configurations. For the RC columns with a moderate transverse

reinforcement ratio, the factor χ_1 can be taken as 0.9, 1.0 and 1.3 and χ_2 can be taken as 2.0, 3.0, and 1.0 for oval, square and circular columns with specific transverse configurations, respectively. The factor χ_1 represents the slope of the simplified interaction diagram. The oval columns with interlocking spirals and square columns with double ties provided better transverse confinement to lessen the torsional failure and achieved larger χ_1 compared to circular columns with single spirals. The columns used in this study had a constant longitudinal ratio of 2.10%. Thus, the results of the proposed equation are applicable only to those columns with a longitudinal reinforcement ratio of approximately 2%. The proposed equation could be improved with further experimental and analytical study to incorporate more parameters such as concrete strength, concrete cover thickness, bending moment to shear ratio, and so on.

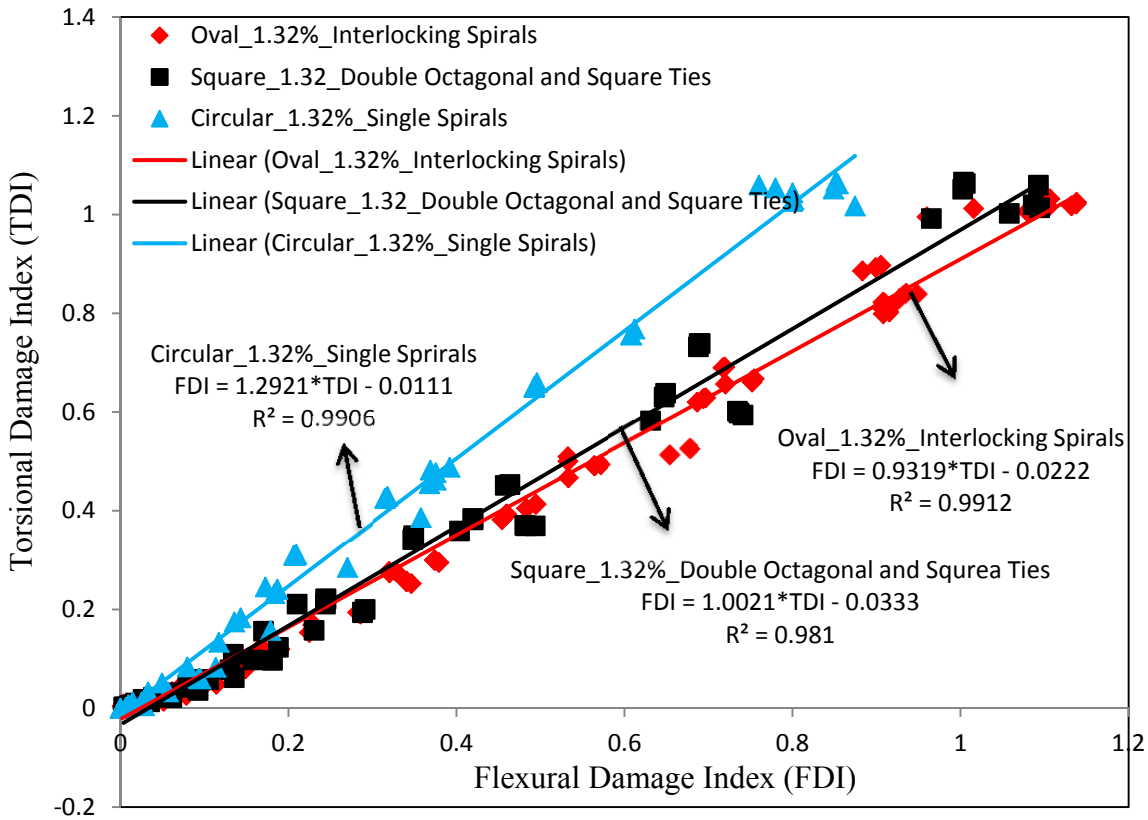

Fig. 5-34 Simplified Empirical Model for Moderate Reinforced Columns with Different Cross Sectional Shapes and Transverse Reinforcement Configurations

5.6. Proposed Unified Equivalent Damage Index Model

Based on the Park and Ang approach, decoupled flexural and torsional damage index models for combined loading had been developed to identify the flexural and torsional damage from flexural and torsional hysteretic behavior. The decoupled flexural and torsional damage indices can distinguish the effect of flexural and torsional behavior from the combined loading condition. However, the decoupled torsional and flexural damage indices should united with each other to correlate with observed damage limit states during the test. The damage index ranged from '0' to '1' along with the increasing ductility levels/ So the ductility value at each load level was intentionally normalized by the ductility capacity, which resulted in a ductility ratio also ranging from '0' to '1'. The unification process was conducted by a weight scheme of T/M ratios to calculate non-dimensional unified equivalent damage index (UEDI) and equivalent ductility ratio (UEDR) under combined loading since the torsional and flexural damage were coupled with each other during the process of combined loading. The weight ratios of bending moment (m) and torsional moment (t) can be determined by the T/M ratios, which are supposed to be a unit in summation during the unification process. Fig. 5-35 shows the sketching of the unification process for torsional and flexural damage indices. The unified damage index values can be split into different ranges corresponding to different observed damage limit states. The UEDI and UEDR are calculated by

$$UEDI = m \times FDI_{Combined\ Loading,Flexure} + t \times TDI_{Combined\ Loading,Torsion}, \quad (5\text{-}26)$$

$$UEDR = m \times \frac{\mu_{\Delta}}{\mu_{\Delta,u}} + t \times \frac{\mu_{\theta}}{\mu_{\theta,u}}, \quad (5\text{-}27)$$

$$m = 1/\ (1 + T/M), \quad (5\text{-}28)$$

$$t = 1 - m\ , \quad (5\text{-}29)$$

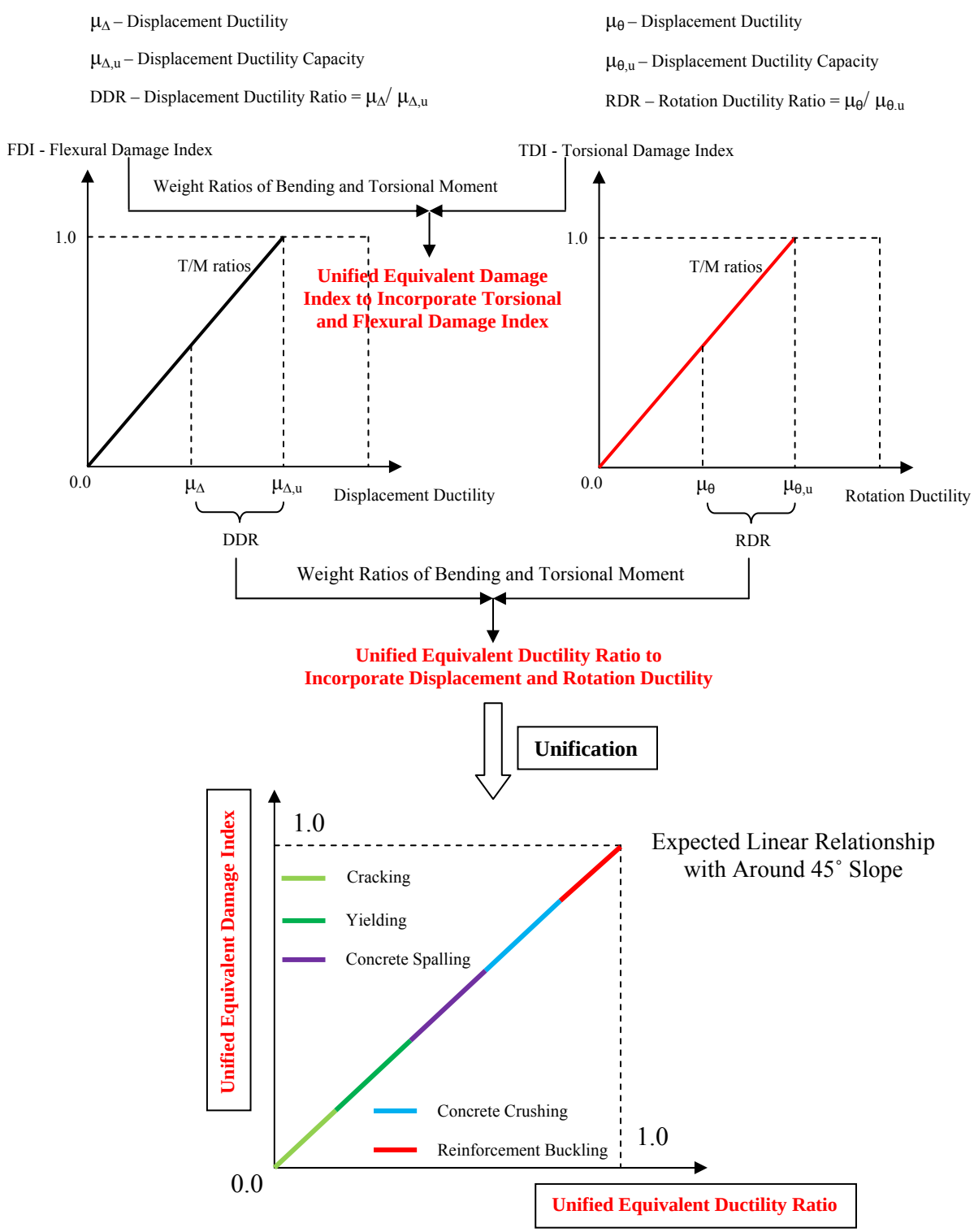

Fig. 5-35 Sketching of the Unification Process for Torsional and Flexural Damage Index

where T/M is the ratio of torsional and bending moment, m is the weight ratio of bending moment, t is the weight ratio of torsional moment, $FDI_{Combined\ Loading,Flexure}$ is the flexural damage index under combined loading, $TDI_{Combined\ Loading,Torsion}$ is the torsional damage index under combined loading, μ_{Δ} is the displacement ductility at given load level, $\mu_{\Delta,u}$ is the displacement ductility capacity at ultimate stage, μ_{θ} is the rotation ductility at given load level, and $\mu_{\theta,u}$ is the rotation ductility capacity at ultimate stage.

The relationship between UEDI and EDR under each ductility level can be plotted as shown in Fig. 5-36 and Fig. 5-37. The unified equivalent damage indices for all the columns under combined loading are linear with corresponding equivalent ductility ratios at a slope of around 45 degrees and the values of proposed UEDI and EDR both vary from 0 to 1. The proposed unified equivalent system is simple and intuitive to be read due to the unification process, which can be used to perform damage assessment for RC bridge columns under combined loading.

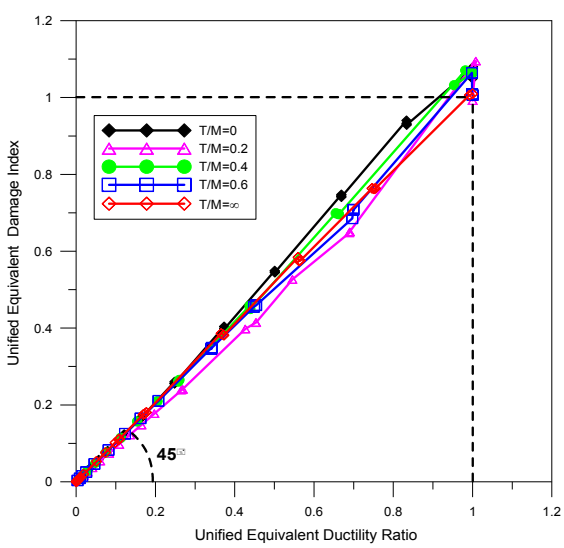

Fig. 5-36 Unified Equivalent Damage Index for Square Columns under Combined Loading

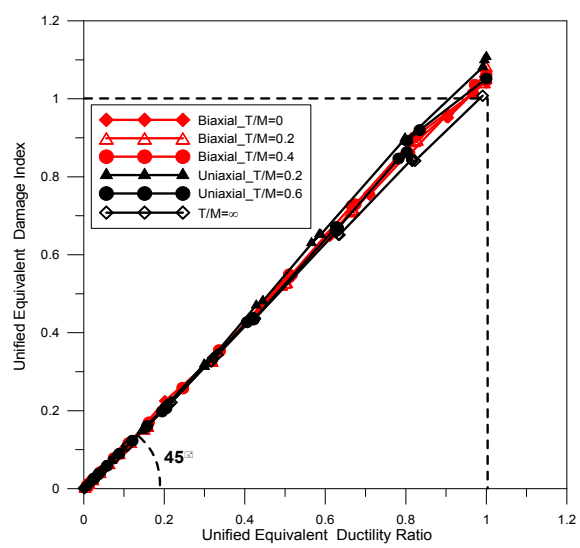

Fig. 5-37 Unified Equivalent Damage Index for Oval Columns under Combined Loading

5.7. Damage Assessment using Unified Equivalent Damage Index Model

The damage characteristics of RC columns under combined loading can be categorized into flexural and inclined cracks, longitudinal and transverse reinforcement yielding, concrete cover spalling, crushing of diagonal concrete struts, longitudinal reinforcement buckling and rupturing, and transverse reinforcement rupturing as discussed in Section 4.3.5. The progression of these damage states can be quantified and assessed by the proposed unified equivalent damage index model from a practical point of view. Lehman and Moehle (2001) have categorized damage states based on flexural tests on RC columns. Based on their study, the damage states under combined loading can also be categorized into no damage, minor damage, moderate damage, severe damage, and failure, which corresponded to the specific structural implications. In addition, different repair criteria are required for different damage states.

In this study, the damages states were defined by specifying unified equivalent damage indices into five different regions to quantify the damage assessment for these columns. The division regions of the unified equivalent damage index for square columns under combined loading are presented in Fig. 3-38. The quantified damage limit states and corresponding structural implications and repairs requirements are summarized in Fig. 3-39 and Tables 5-4. The damage limit states with a damage index less than 0.1 is categorized into no damage or localized minor cracking requiring no cosmetic or structural repair. The damage index range of 0.10 and 0.25 indicated minor damage such as lightly cracking, initial debonding of concrete cover at specific location of column and yielding of reinforcement, which required cosmetic repair and no necessary structural repairs. Moderate damage state represents severe cracking and localized concrete cover

spalling when the damage index is between 0.25 and 0.5, where the existing RC members should be repaired essentially in place without other substantial demolition or replacement. The excessive concrete cover spalling, exposed reinforcement, and onset of core concrete crushing indicates the severe structural damage with a damage index between 0.5 and 0.9 requiring substantial structural repair or replacement of columns. The core concrete crushed and reinforcement buckled or ruptured when the damage index was higher than 0.9 which means no feasibility to repair.

The division regions of the unified equivalent damage index for oval columns under combined loading are presented in Fig. 3-40. The quantified damage limit states, corresponding structural implications, and repairs requirement are summarized in Fig. 3-41 and Tables 5-5. The damage limit states was identified as no damage or localized

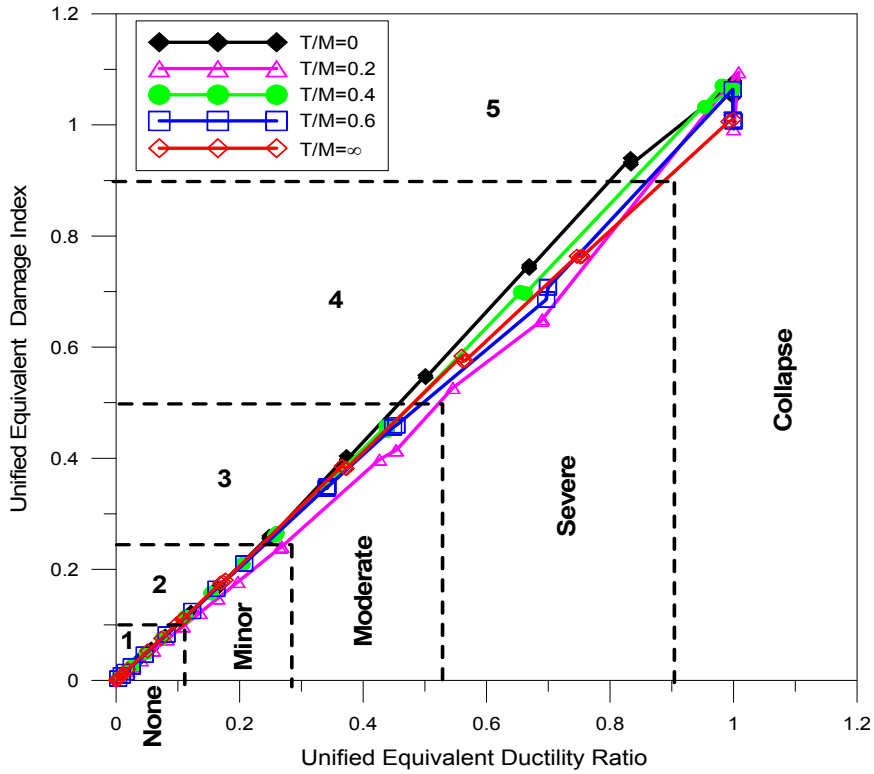

Fig. 5-38 Division Region of Unified Equivalent Damage Index for Square Columns under Combined Loading

None Damage Minor Damage Moderate Damage Severe Damage

Fig. 5-39 Typical Categorization of Damage States of Square Columns under Combined Loading

Table 5-4 Correlation of Damage States with Unified Damage Index under Combined Loading

Range of EUDI	Damage Limit States (Description)	Repairs Requirement
< 0.1	No damage or localized minor flexural or torsional cracking along the height of column	No cosmetic or structural repair
0.1~ 0.25	Insignificant damage - more cracking throughout column, yielding of reinforcement and initial debonding of concrete cover	Cosmetic repair and no structural repairs necessary
0.25 ~ 0.5	Moderate damage - Severe cracking along the column and localized concrete cover spalling	Repair the damaged members in place without substantial demolition
0.5 ~ 0.9	Severe damage - Complete concrete cover spalling, exposed reinforcement, and onset of concrete core crushing	Substantial structural repair or replacement of the damaged members
> 0.9	Failure- Totally concrete core crushing, and reinforcement buckling or rupturing	No feasibility to repair

minor cracking with a damage index of less than 0.08, which required no cosmetic or structural repair. When the damage index varied from 0.08 to 0.22, the columns obtained minor damage such as lightly cracking, initial debonding of concrete cover and first yielding of reinforcement, which required cosmetic repair but no necessary structural repairs. Severe concrete cracking, localized concrete cover spalling and plastic hinge formation were observed when the damage index is between 0.22 and 0.55, which was identified as moderate damage and needed essential repairs in place without other

substantial demolition or replacement. Severe structural damage was observed with the damage index falling between 0.55 and 0.9, which meant excessive concrete cover spalling and initial concrete core crushing. In this situation, the RC systems required substantial structural repair or replacement of columns. Then the concrete core crushed and reinforcement buckled or ruptured when the damage index was higher than 0.9 which means structural failure and no feasibility to repair.

5.8. Concluding Remarks

This section has emphasized the importance of a damage assessment approach of RC bridge columns. Decoupled torsional and flexural damage index models were proposed by the modified Park and Ang and Hwang and Scribner approaches to study the progression of damage under combined loading. In addition, interaction between flexural

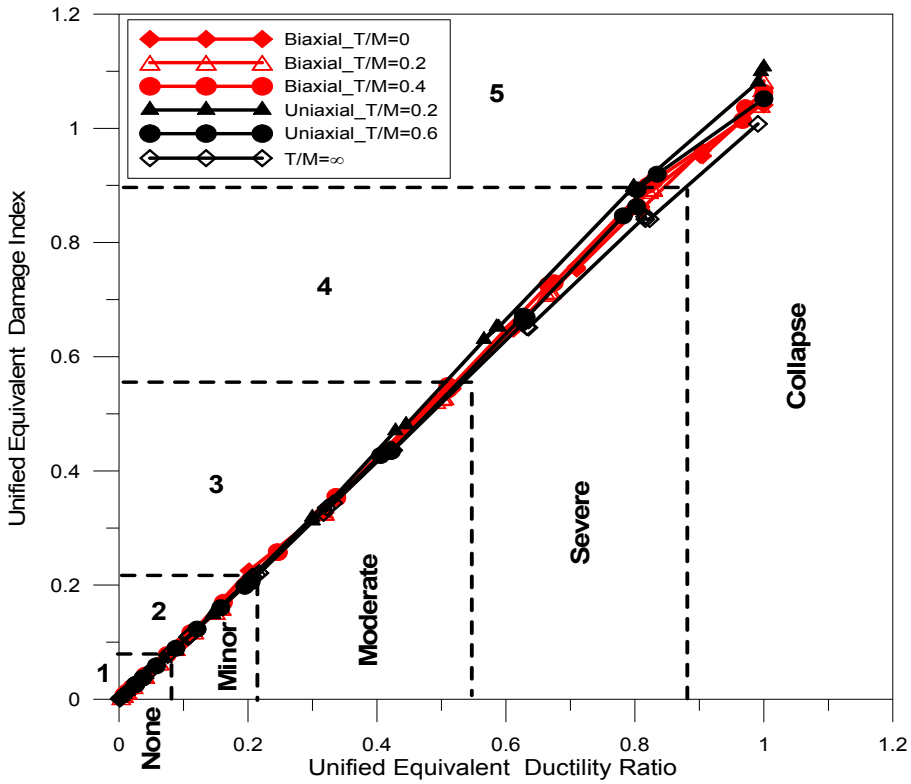

Fig. 5-40 Division Region of Unified Equivalent Damage Index for Oval Columns under Combined Loading

None Damage Minor Damage Moderate Damage Severe Damage

Fig. 5-5 Typical Categorization of Damage States of Oval Columns under Combined Loading

Table 5.8-1 Correlation of Damage States with Unified Damage Index under Combined Loading

Range of EUDI	Damage Limit States (Description)	Repairs Requirement
< 0.08	No damage or localized minor flexural or torsional cracking along the height of column	No cosmetic or structural repair
0.08~ 0.22	Insignificant damage - more cracking throughout column, yielding of bar and initial debonding of concrete cover	Cosmetic repair and no structural repairs necessary
0.22 ~ 0.55	Moderate damage - Severe cracking along the column and localized concrete cover spalling	Repair the damaged members in place without substantial demolition
0.55 ~ 0.9	Severe damage - Complete concrete cover spalling, exposed reinforcement, and onset of concrete core crushing	Substantial structural repair or replacement of the damaged members
> 0.9	Failure- Totally concrete core crushing, and reinforcement buckling or rupturing	No feasibility to repair

and torsional damage index models was studied by interaction diagrams. Thereafter non-dimensional unified equivalent damage index (UEDI) and equivalent ductility ratio (UEDR) under combined loading were calculated through the unification process by a weight scheme of T/M ratios, which were used to quantify the damage states for assessment. Based on the results of this study, the following concluding remarks are drawn:

- Decoupled torsional and flexural damage index models from the Hwang and Scribner approach was modified by normalizing with total energy dissipation capacity from hysteresis curves for all columns under combined loading. The damage index value of this modified model increased step by step as more loading cycles were imposed at the each ductility, which is an advantage in demonstrating the progression of damage and stiffness degradation along with loading cycles within a given loading level. Though, the models predicted the progression of damage well, the flexural and torsional damage index values at the ultimate state significantly differs for the same columns.
- The park and Ang approach can be modified and extended to calculate the decoupled torsional and flexural damage index according to torsional and flexural hysteretic response of columns, respectively. It can predict the progression of damage for both the flexural and torsional failure-dominated column under combined loading. The damage models were physically intuitive and easy to quantify the different damage characteristics from '0' indicating no damage to '1' indicating near collapse. So the damage process of a particular column under combined loading can be tracked throughout the course of inelastic loading.
- Interlocking spirals in oval columns provided better transverse confinement and reduced concrete core crushing to mitigate the flexural damage at higher displacement ductility levels as compared to the square columns with ties. In addition, the biaxial combined loading accelerated and amplified the torsional damage progression resulting in larger torsional damage index values; however, no significant difference in flexural damage index values was observed between biaxial and uniaxial combined loading since more torsional damage occurred in these columns with more torsion effect.

- An empirical model was proposed, through combining multi factor line regression and polynomial regression by the Ordinary Least Square (OLS) method, to predict the interaction relationship of torsional and flexural damage indices. The empirical equation incorporated the main variables such as transverse reinforcement ratio, cross sectional shape, aspect ratios and T/M ratios. The comparisons demonstrated that the model accurately predicted the interaction diagrams of RC columns with specific design requirements.
- The decoupled torsional and flexural damage indices can be unified by a weight scheme of T/M ratios and equivalent ductility ratios, which identify with the coupled torsional and flexural damage during the process of combined loading. The unified equivalent damage indices (UEDI) of the columns under combined loading are linear with corresponding equivalent ductility ratios (EDR) at a slope of around 45 degrees and the values of proposed UEDI and EDR both vary from '0', indicating no damage, to '1', indicating collapse.
- The damage states under combined loading can be categorized into no damage, minor damage, moderate damage, severe damage, or collapse with the specific structural implications. The proposed unified equivalent damage index model can specify the range of damage index value into different regions to quantify and assess these damage states.

Chapter 6 Analytical Studies on Torsion-Flexure-Shear Interaction Using Mechanical Models

6.1. Introduction

Reinforced concrete members can be subjected to torsional moments in addition to flexural moments, axial load, and shear forces during earthquake excitations. For most design situations, flexural moment and shear forces are considered primary effects, whereas torsion is regarded as secondary. Using the limit states approach, the design process requires an understanding of the failure interaction relationship under combined flexure, shear, and torsion. In this study, the failure interaction curves for combined loading involving flexure, shear and torsion was proposed using mechanical models basing on the flexural theory, modified compression field theory (MCFT), and softened truss model (STM). The privacy of predictions was confirmed by the experimental results.

The methodology of this analytical investigation are as follows: (i) modify and extend the existing models to predict the flexural capacity for square and oval RC cross sections under flexure and constant axial load by incorporating confinement models of concrete, (ii) use MCFT to predict the shear capacity for square and oval RC cross sections under shear and constant axial load, (iii) develop the existing STM to predict the torsional capacity for square and oval RC cross sections under torsion and constant axial load, and (iv) validate the torsion, bending and shear force interaction diagrams of experimental results by proposing semi-empirical formulations in terms of the flexural, shear and torsional strength under a constant axial load ratio. The failure interaction curves under

combined flexure, shear force, and torsional moments are proposed based on modifying the semi-empirical relationship from Elfgren (1974).

6.2. Flexure Theory for Bending Capacity and Load-Displacement Response

Analytical models are required to predict the bending moment capacity and load-displacement response of RC bridge columns under flexure. Conventional flexure theory can be applied for the moment-curvature analysis and bending moment capacity prediction. Then the displacement or deflection can be calculated based on the curvature distribution along the height of the columns. The flexure theory for bending moment capacity and load-displacement response prediction is discussed in the following section.

6.2.1. Moment-Curvature Analysis and Bending Capacity Prediction

After concrete cracking, the applied bending moment is resisted by an internal force couple consisting of resultant compression force and resultant tension force at the critical section, which can be calculated by integrating the compressive and tensile stresses along the cross section depth induced by the applied bending moment in concrete and reinforcement parts. In this theory, it is assumed that the plane sections remain plain after bending, and the tensile strength of concrete is negligible since the internal tension is provided entirely by the longitudinal reinforcement located below the neutral axis at failure stage. These assumptions are used to build up the equilibrium conditions and compatibility equations. Then the flexural response of RC members can be predicted by combining the equilibrium and compatibility conditions with the material stress-strain relationships.

6.2.1.1 Compatibility Conditions

The geometric hypothesis of "plane section remains plane" is the basis of engineering beam theory under flexure. Under this hypothesis, the concrete strain obtained a linear distribution along the depth of the cross section and can be determined by strain at the top face and the strain at the bottom face. Then the neutral axis location will be determined based on a triangular similarity relationship, which corresponds to the depth of the concrete compression zone. In addition, the curvature of the cross section, which is equal to the change in slope per unit length or strain gradient along the cross section, can be evaluated. The compatibility conditions are shown in Fig. 6-1.

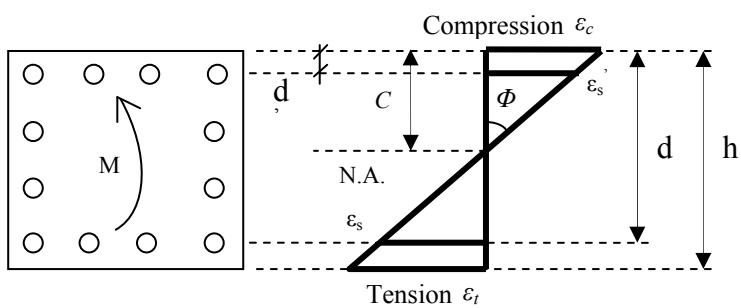

Fig. 6-1 Strain Distribution under Compatibility Conditions

The depth of concrete compression zone is given by

$$C = \frac{\varepsilon_c h}{\varepsilon_c - \varepsilon_t}, \tag{6-1}$$

where C is the depth of the concrete compression zone, ε_c is the compressive strain at the bottom face taken as negative, ε_t is the tensile strain at the top face taken as positive, and h is the depth of the whole cross section. The curvature can be calculated by

$$\Phi = \frac{\varepsilon_c}{C}, \tag{6-2}$$

where Φ is the curvature of the cross section. In addition, the strain of each reinforcement layer can be determined by this compatibility condition. For example, the top compressive and bottom tensile reinforcement strain can be expressed by

$$\varepsilon_s = \frac{d-C}{C}\varepsilon_c \ , \tag{6-3}$$

$$\varepsilon_s' = \frac{C-d'}{C}\varepsilon_c \ , \tag{6-4}$$

where ε_s and ε_s' are the strains for top and bottom reinforcement layer respectively, and d' is the distance from the extreme top face and center of the top reinforcement layer. Then the strain of concrete and reinforcement at any location of the cross section can be determined based on the above compatibility conditions.

6.2.1.2 Equilibrium Conditions

The stress variation over the depth of the cross section is determined by the strain profile and stress-strain relationship, which will be discussed in the next section. The stresses can be integrated over the section to obtain the internal bending moment M and axial force N. The stresses and stress resultants are shown in Fig. 6-2. The compressive forces (F_s') and tensile forces (F_s) in reinforcement layers are calculated based on the corresponding reinforcement strain. The resultant compressive forces from concrete block (C_c) can be determined by the integration of concrete stress (σ_c) distribution along the compression zone.

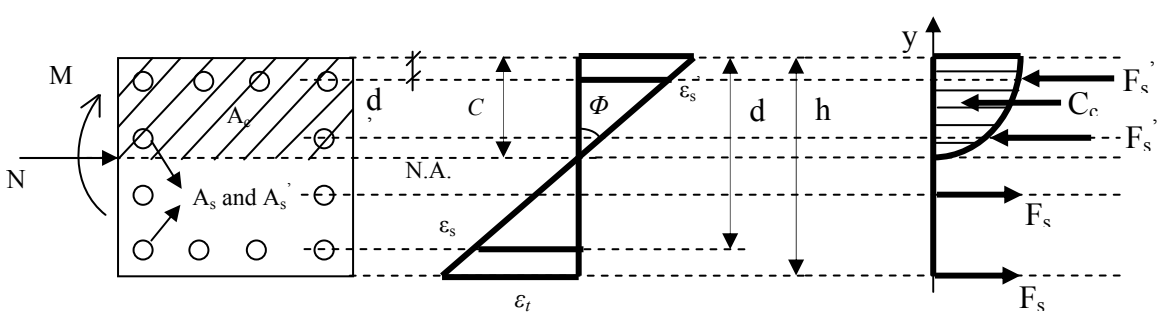

Fig. 6-2 Strain Distribution under Compatibility Conditions

The required sectional forces M and N can be calculated as follows:

$$N = \int_{\frac{h}{2}-C}^{h/2}\left[b_{c(y)}\sigma_{cc(y)} + (b_{(y)} - b_{c(y)})\sigma_{cu(y)}\right]dy + \sum_{i=1}^{n} A_{si}f_{si} \ , \tag{6-5}$$

$$\sigma_{cc(y)} = f_{cc}(\varepsilon_y) \ , \tag{6-6}$$

$$\sigma_{cu(y)} = f_{cu}(\varepsilon_y) \ , \tag{6-7}$$

$$\varepsilon_y = \frac{\varepsilon_c}{C}(y - \frac{h}{2} + C) \ , \tag{6-8}$$

$$M = \int_{\frac{h}{2}-C}^{h/2} \left[b_{c(y)}\sigma_{cc(y)} + (b_{(y)} - b_{c(y)})\sigma_{cu(y)} \right] y dy + \sum_{i=1}^{n} A_{si} f_{si} y_i \ , \tag{6-9}$$

where $b_{(y)}$ is the total width variation along the depth of compression zone, $b_{c(y)}$ is the width variation for the confined portion along the depth of compression zone, $\sigma_{cc(y)}$ is the confined concrete stress-strain relationship along the depth of compression zone, $\sigma_{cu(y)}$ is the unconfined concrete stress-strain relationship along the depth of the compression zone, A_{si} is the area of reinforcement with the distance y_i from the centroidal axis, and f_{si} is the stress of reinforcement with the distance y_i from the centroidal axis.

6.2.1.3 Unconfined and Confined Concrete Stress-Strain Relationship

For the concrete cover, an unconfined parabolic stress-strain curve is assumed for normal strength concrete in the moment-curvature analysis as shown in Fig. 6-3. Mander's model (1988) for unconfined concrete was adopted in this concrete cover region until the concrete strain reached the spalling strain ε_{sp}. The concrete stress in the spalling region is considered as zero after the spalling strain, which meant ceasing to carry any stress. Mander et al. (1984) have proposed a unified stress-strain approach for confined concrete applicable to both circular and rectangular shaped transverse reinforcement based on an equation suggested by Popovics (1973). Later on, Mander (1998) proposed modified the stress-strain model accounting for the influence of various

types of confinement by defining an effective lateral confining stress, which is dependent on the configuration of the transverse and longitudinal reinforcement.

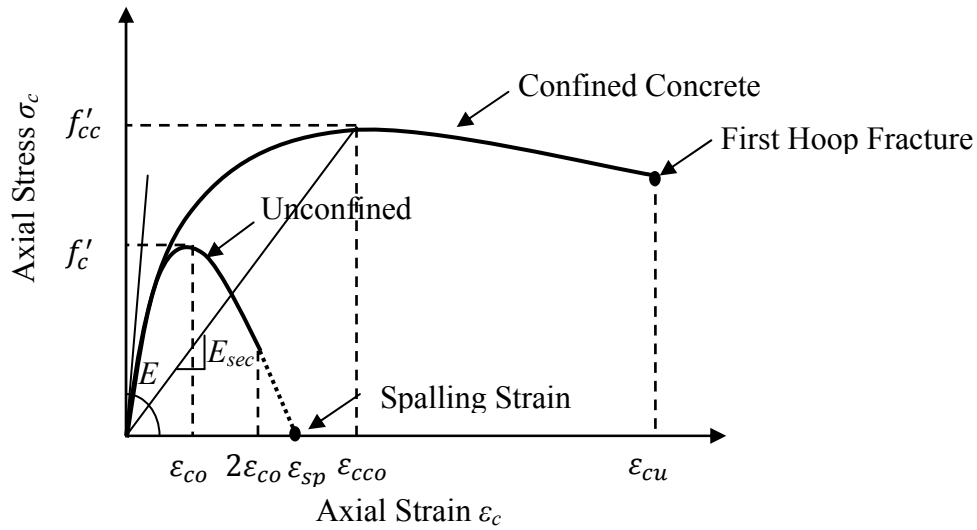

Fig. 6-3 Stress-Strain Model for Confined and Unconfined Concrete in Compression

For unconfined concrete in the spalling region, a parabolic stress-strain curve is assumed in our study since the used concrete is normal strength concrete. The unconfined concrete stress is expressed as

$$f_c = f_c^{'}[2(\frac{\varepsilon_c}{\varepsilon_{co}}) - (\frac{\varepsilon_c}{\varepsilon_{co}})^2] \quad \text{when} \quad \varepsilon_c \le 2\varepsilon_{co}, \tag{6-10}$$

where f_c is the unconfined concrete compressive stress, $f_c^{'}$ is the unconfined concrete compressive strength, ε_c is the unconfined concrete compressive strain, and ε_{co} is the unconfined concrete strain corresponding to compressive strength taken as 0.002. To defined the stress-strain relationship of the concrete cover in the spalling region, the descending portion, where $\varepsilon_c \ge 2\varepsilon_{c0}$, is assumed to be a straight line following the tangent trend at $\varepsilon_c = 2\varepsilon_{c0}$ and to reach zero stress at specific strain around 0.005, which is defined as spalling strain, ε_{sp} .

Under a slow (quasi-static) strain rate and monotonic loading, the confined concrete compressive stress f_{cc} is given as follows:

$$f_{cc} = \frac{f_{cc}^{'} xr}{r - 1 + x^{r}}, \tag{6-11a}$$

$$x = \frac{\varepsilon_{cc}}{\varepsilon_{cco}}, \tag{6-11b}$$

$$\varepsilon_{cco} = \varepsilon_{co}[1 + 5(\frac{f_{cc}^{'}}{f_{c}^{'}} - 1)], \tag{6-11c}$$

$$r = \frac{E_c}{E_c - E_{\sec}}, \tag{6-11d}$$

$$E_c = 5000\sqrt{f_c^{'}}(MPa), \tag{6-11e}$$

$$E_{\sec} = \frac{f_{cc}^{'}}{\varepsilon_{cco}} \tag{6-10f}$$

where f_{cc} is the confined concrete compressive stress, $f_{cc}^{'}$ is the compressive strength of confined concrete, ε_{cc} is the confined concrete compressive strain, ε_{cco} is the confined concrete strain corresponding to the compressive strength, E_c is the tangent modulus of elasticity of the uncombined concrete, and $E_{\sec}$ is the secant stiffness of confined concrete corresponding to compressive strength.

6.2.1.3.1 Effective Lateral Confining Pressure and the Confinement Effectiveness

The maximum transverse pressure from the confining transverse reinforcement can only be applied effectively on the concrete core with full confinement development from the arching action, which is assumed to occur between the levels of transverse reinforcement in the form of a second-degree parabola with an initial tangent slope of 45°. Thus the area of ineffectively confined concrete will be largest at the midway point between the levels of the transverse reinforcement and the area of effectively confined

concrete core will be smallest. In addition, the area of the confined concrete is defined as the area of the concrete within the center lines of the perimeter transverse reinforcement. The effective lateral confining pressure is then introduced to derive the effectively confined concrete core, which is given as follows:

$$f_l^{'} = f_l k_e, \tag{6-11a}$$

$$k_e = \frac{A_e}{A_{cc}}, \tag{6-11b}$$

$$A_{cc} = A_c(1-\rho_{cc}), \tag{6-11c}$$

where $f_l^{'}$ is the effective lateral confining pressure from the transverse reinforcement, f_l is the uniformly distributed lateral confining pressure over the surface of the concrete core from the transverse reinforcement, k_e is the confinement effectively coefficient, A_e is the area of the effectively confined concrete core, A_{cc} is the area of the confined concrete , A_c is the area of the core section enclosed by center lines of the perimeter transverse reinforcement, and ρ_{cc} is the ratio of the longitudinal reinforcement area to the concrete core area.

6.2.1.3.2 Confinement Effectiveness for Cross Sections Confined by Spirals

By assuming an arching action between the levels of transverse reinforcement to be in the form of a second-degree parabola with an initial tangent slope of 45°, the area of an effectively confined concrete core at midway between the levels of spirals can be calculated by

$$A_e = \frac{\pi}{4} D_s (D_s - \frac{s^{'}}{2}) = \frac{\pi}{4} D_s^2 (1 - \frac{s^{'}}{2D_s}), \tag{6-12}$$

$$A_{cc} = \frac{\pi}{4} D_s^2 (1-\rho_{cc}), \tag{6-13}$$

where $s^{'}$ is the clear vertical spacing of transverse reinforcement and D_s is the diameter of spirals between reinforcement center. By substituting Eq. (6-12) and Eq. (6-13) into Eq. (6-11 b), the confinement effectiveness coefficient for spirals can be calculated by

$$k_e = \frac{(1-\frac{s^{'}}{2D_s})}{1-\rho_{cc}}. \tag{6-14}$$

By assuming that the tensile forces from yielding transverse reinforcement resulted in the uniform lateral stress on the concrete core, the lateral confining pressure can be calculated as follows:

$$f_l = \frac{2f_{yt}A_{sp}}{sD_s} = \frac{1}{2}\rho_t f_{yt}, \tag{6-15}$$

$$\rho_t = \frac{A_{sp}\pi D_s}{\frac{\pi}{4}D_s^2 s} = \frac{4A_{sp}}{D_s s}, \tag{6-16}$$

$$f_l^{'} = \frac{1}{2}k_e\rho_t f_{yt}, \tag{6-17}$$

where ρ_t is the ratio of transverse reinforcement volume to confined concrete core volume, A_{sp} is the area of single transverse spiral, and k_e is given by Eq. (6-14). In this study, the oval RC columns were reinforced by two interlocking spirals, which can be simply considered as two single spirals overlapping and acting with each other over the cross section. The area of effectively confined concrete core A_e and the area of the confined concrete A_{cc} were taken as the summation of the ones in two single spirals for simplification. Thus the effective lateral confining pressure calculation procedure for interlocking spirals is the same for single spirals.

6.2.1.3.3 Confinement Effectiveness for Square Sections Confined by Hoops

For square cross sections, the arching action occurs not only between layers of transverse hoops in the vertical direction but also between longitudinal reinforcement in the horizontal direction. The effectively confined area of concrete core at each hoop level is considered as the area of concrete core subtracting the area of the ineffectively confined concrete in the form of second-degree parabolas with an initial tangent slope of 45°, which can be calculated by

$$A_i = \sum_{i=1}^{n} \frac{(w_i^{'})^2}{6}, \tag{6-18}$$

where A_i is the ineffective confined concrete, and $w_i^{'}$ is the ith clear distance between adjacent longitudinal reinforcement. Thus the area of effectively confined concrete core at the mid-way point between the levels of transverse reinforcement is expressed as

$$A_e = (B_c^2 - A_i)(1 - \frac{s^{'}}{2B_c})^2, \tag{6-19}$$

$$A_{cc} = B_c^2 (1 - \rho_{cc}), \tag{6-20}$$

where B_c is the core dimension to the centerlines of perimeter transverse ties. By substituting Eq. (6-19) and Eq. (6-20) into Eq. (6-11 b), the confinement effectiveness coefficient for square ties can be calculated by

$$k_e = \frac{(1 - \sum_{i=1}^{n} \frac{(w_i^{'})^2}{6B_c^2})(1 - \frac{s^{'}}{2B_c})^2}{(1 - \rho_{cc})}. \tag{6-21}$$

Finally, lateral confining stress on the concrete core is taken as the total transverse reinforcement yielding forces divided by the vertical area of confined concrete, which is given as

$$f_l = \frac{f_{yt} A_{st}}{sB_c} = \rho_t f_{yt}, \tag{6-22}$$

$$\rho_t = \frac{A_{st}}{sB_c}, \tag{6-23}$$

$$f_l^{'} = k_e \rho_t f_{yt}, \tag{6-24}$$

where A_{st} is the total area of transverse ties at each reinforcement level. In this study, square and octagonal ties were used in the square cross section. Thus A_{st} was simply taken as the total area of square and octagonal ties at each reinforcement level since the octagonal ties were closely located to square ties excepting at the four corners.

6.2.1.3.4 Compressive Strength of Confined Concrete

Mander (1988) used the "five-parameter" multiaxial failure surface (William and Warnke 1975) to describe a specified ultimate strength surface for multiaxial compressive stresses of confined concrete. The calculated ultimate strength surface based on the triaxial tests of Schickert and Winkler (1979) was adopted in his study. Finally the general solution of the multiaxial failure criterion in terms of the lateral confining stresses were proposed by placing the concrete in triaxial compression with equal effective lateral confining stresses $f_l^{'}$ from spirals or ties. The confined compressive strength is given by

$$f_{cc}^{'} = f_c^{'}(-1.254 + 2.254\sqrt{1 + \frac{7.94 f_l^{'}}{f_c^{'}}} - 2\frac{f_l^{'}}{f_c^{'}}. \tag{6-25}$$

Rather than computing the complicated strain energy balance for the confinement reinforcing, the ultimate strain of confined concrete can be simply calculated by (Priestley et al., 1996)

$$\varepsilon_{cu} = 0.004 + 1.4 \rho_t f_{yt} \frac{\varepsilon_{su}}{f_{cc}^{'}}, \tag{6-26}$$

where ε_{su} is the ultimate strain of the reinforcement model. This equation simplifies the computations and provides a slightly more conservative result.

6.2.1.4 Reinforcement Stress-Strain Relationship

The typical experimental stress-strain curve of reinforcement is shown in Fig. 6-4 (a), which experienced a short yielding plateau after yielding and significantly strain hardening at a higher strain level. Therefore, the stress-strain relationship with these characteristics was used in this study for both the transverse and longitudinal reinforcement as given by

$$f_s = E_s \varepsilon_s \qquad \varepsilon_s \le \varepsilon_y, \qquad \text{(6-27 a)}$$

$$f_s = f_y \qquad \varepsilon_y \le \varepsilon_s \le \varepsilon_{sh}, \qquad \text{(6-27 b)}$$

$$f_s = f_y[1.5 - 0.5(\frac{0.12 - \varepsilon_s}{0.112})^2 \qquad \varepsilon_{sh} \le \varepsilon_s \le \varepsilon_{cu}, \qquad \text{(6-27 c)}$$

where E_s is the modulus of elasticity of reinforcement, f_s and ε_s are the stress and strain in the reinforcement, and f_y is the yielding strength of the reinforcement. The model is plotted in Fig. 6-4 (b), in which ε_{sh} is taken as 0.008, ε_{su} is taken as 0.12, and f_u is the stresses corresponding to ultimate strain ε_{su}.

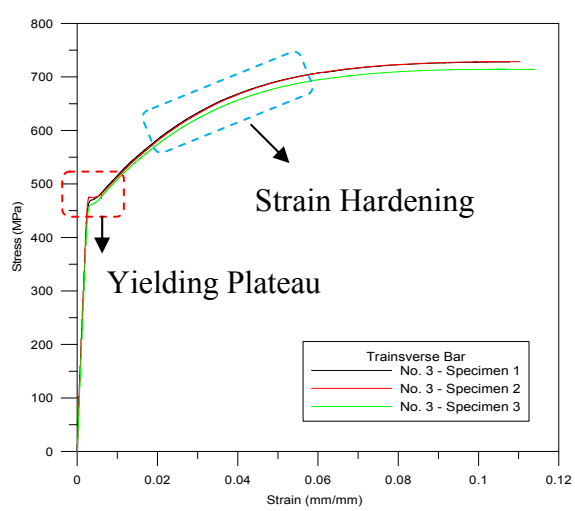

(a) Typical Experimental Stress-Strain Curves for Monotonic Loading

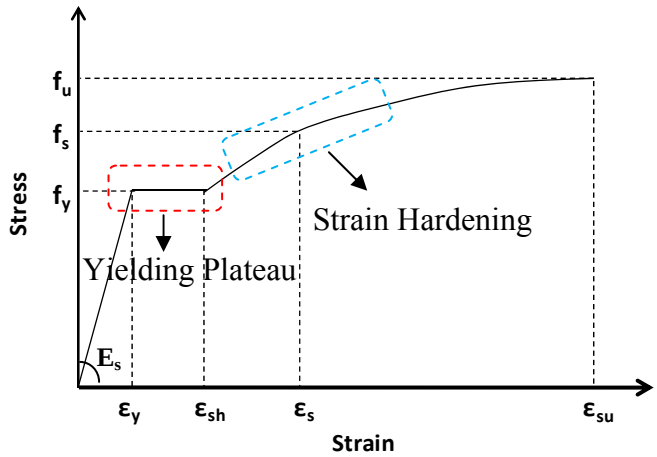

(b) Adopted Model

Fig. 6-4 Material Models for Reinforcement

6.2.1.5 Solution Procedure for Moment-Curvature Prediction

The moment-curvature analysis was performed by iterating the extreme compressive concrete strain ε_c at the top face from the initial zero value to the ultimate strain capability of the concrete at equal increment value. For each of the iteration, the neutral axis was determined by iterating through the section depth until the internal axial force was balanced with the external axial load, that is, to satisfy the compatibility and equilibrium conditions. The forces for compressive concrete can be obtained by integration over the depth of the compressive zone based on the concrete stress-strain relationship. The forces for reinforcement can be calculated from the reinforcement strain from compatibility conditions and the reinforcement stress-strain relationship. Then the bending moment and corresponding curvature can be calculated at each concrete strain level. The value of ε_c should be limited to 0.0035 mm/mm for unconfined concrete or the ultimate compression strain for the confined core concrete as defined in Eq. (6-26). The first yield moment corresponds to the first yielding of the longitudinal bar on the tension side of the section.

The following information must be given in the calculation: cross section dimensions, quantity and configurations of reinforcement, reinforcement material properties, and concrete material property. The solution procedure for moment-curvature analysis is shown in Fig. 6-5. Thereafter the whole curve of moment-curvature and bending moment capacity can be calculated along with the increase of concrete strains.

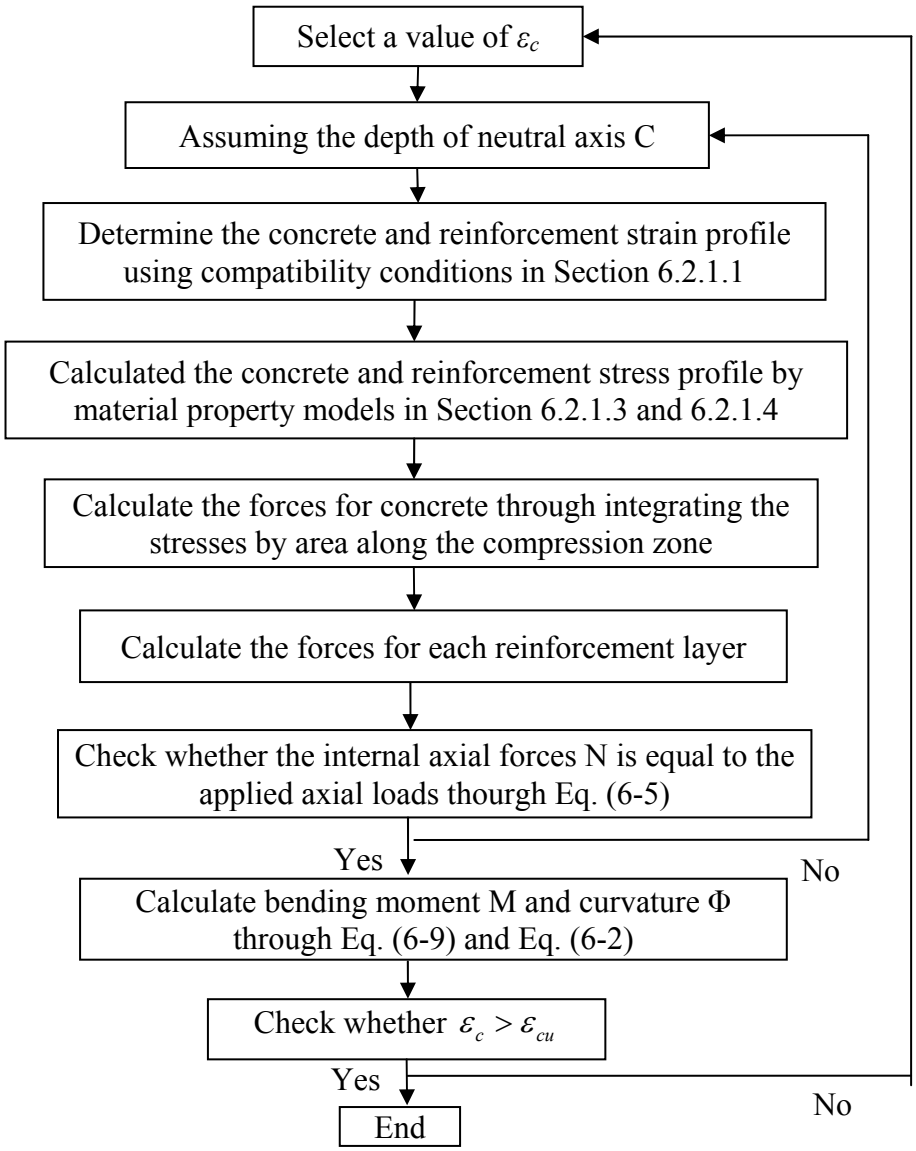

Fig. 6-5 Solution Procedure for Moment-Curvature Analysis

6.2.2. Lateral Load-Displacement Response

The moment-curvature relationship at the sectional level can be obtained from the above Section 6.2.1. In this study, the lateral load is applied at the top end of a cantilever column as shown in Fig. 6-6 (a) and results in a linear bending moment distribution *M(z)* along the column as shown in Fig. 6-6 (b). Based on the bending moment distribution and calculated moment-curvature relationship, a non-linear sectional curvature profile *Φ(z)* along the column is established. Once the curvature distribution is obtained, the deflection slope at any location can be calculated by integrating the curvature along the height of the column, based on fact that the change of slope between any two points along the column is equal to the area under the curvature diagram between these two points as shown in Fig. 6-6 (c). Moreover, the deflection or deviation of any two points is calculated by the product of slope and distance between these two points. Thus lateral displacement Δ_{BA} at the top end can be captured by integrating the slope profiles along with the height of the column as shown in Fig. 6-6 (d).

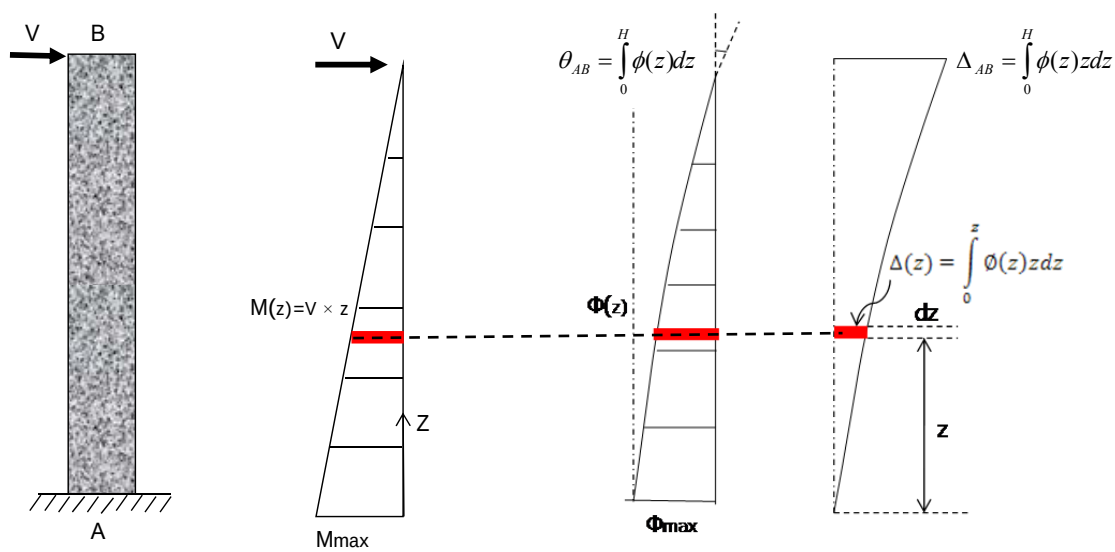

(a) Lateral Load (b) Bending Moment (c) Curvature Profile (d) Deflection

Fig. 6-6 Load-Displacement Response Prediction Procedure

The change of slope between 'A' and 'B' points is the area under curvature diagram along the whole column, which can be calculated by integration as given by

$$\theta_{AB} = \int_0^H \phi(z)dz\,, \tag{6-28}$$

where θ_{AB} is the change of slope between 'A' and 'B', H is the height of the column, and $\phi(z)$ is the curvature distribution along the column. Also the top end displacement can be captured by integrating the slope profiles along with the height of column as given by

$$\Delta_{AB} = \int_0^H \phi(z)zdz\,, \tag{6-29}$$

where Δ_{AB} is the lateral displacement at the top end.

In this analytical study, the column was divided into amounts of elements along the total height for convenience in performing the integration numerically as shown in Fig. 6-7. The element 'i' is selected to present a typical element with a width of $\Delta z_i = z_{i+1} - z_i$. Once the location of the element 'i' is determined, the bending moment M_i and M_{i+1} and curvature ϕ_i and ϕ_{i+1} can be calculated from the moment-curvature relationship along the column height. The curvature distribution along the width of the element is assumed to be simply linear due the very small width Δz_i. Then the deviation in this element can be easily expressed by

$$\Delta_i = \frac{1}{2}(\phi_i z_i + \phi_{i+1} z_{i+1})\Delta z_i\,, \tag{6-30}$$

where Δ_i is the deviation in the element 'i', z_i and z_{i+1} represent the location of the two nodes in the element 'i', Δz_i is the width of the element 'i', ϕ_i and ϕ_{i+1} are curvatures at the two nodes in the element 'i'. Therefore, the lateral displacement Δ_{BA} at the top end is calculated by the summation of all the elements as expressed by

$$\Delta_{BA} = \sum_{i=1}^{n} \frac{1}{2}(\phi_i z_i + \phi_{i+1} z_{i+1})\Delta z_i \ , \tag{6-29}$$

where n is the amount of elements along the column. In this study, the column was divided into 264 elements along the column resulting in the element width of 0.5 inch. The calculation procedure is illustrated in Fig. 6-7.

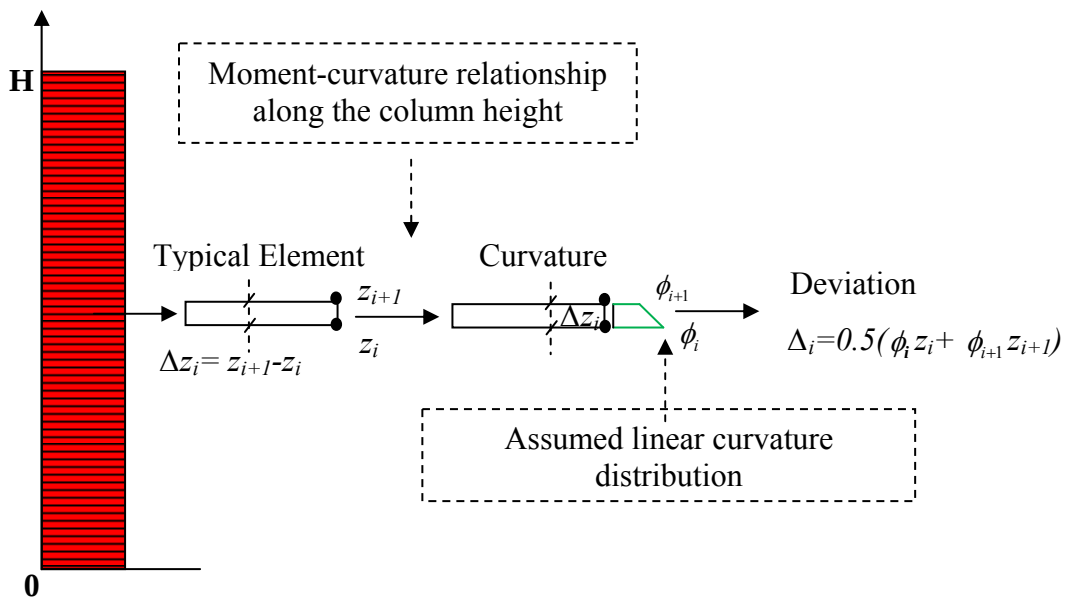

Fig. 6-7 Lateral Displacement Calculation Procedure in Numerical Integration

6.2.3. Analytical Prediction and Experimental Result Comparison

The sectional moment-curvature analysis was conducted for RC square and oval columns under flexure and shear at constant axial load ratio. Using the analytical moment-curvature analysis results, the lateral load-displacement curves can be predicted using the numerical integration method as discussed above. The analytical predictions and experimental results are compared in following section.

6.2.3.1 Comparison for Square Column under Flexure and Shear

At a constant axial load ratio of 7%, the moment-curvature curve prediction of the square columns under flexure and shear is presented in Fig. 6-8. The experimental and analytical moment-curvature curves perfectly agreed with each other before

reinforcement yielding. At post-yielding stage, the stiffness degradation in analytical prediction was less than the stiffness degradation in the experimental results, which might be caused by a difference between the reinforcement coupon test results and the adopted model for reinforcement. However, the measured stiffness at post-yielding stage was around 90% of the calculated effectively secant stiffness, which was acceptable. At peak load, the flexural strength from the prediction was around 97% of the experimental flexural strength. At post-peak stage, the experimental strength degradation was much less than the strength degradation in the prediction, which was a result of the conservative estimation of compressive behavior for confined concrete with square ties. Also the predicted curvature capacity is around 15% less compared to the experimental results due to the less predicted confinement from the square ties. Lateral displacement at the tip of the column, where the horizontal force was applied during the test, was predicted based on the moment-curvature analysis as shown in Fig. 6-9.

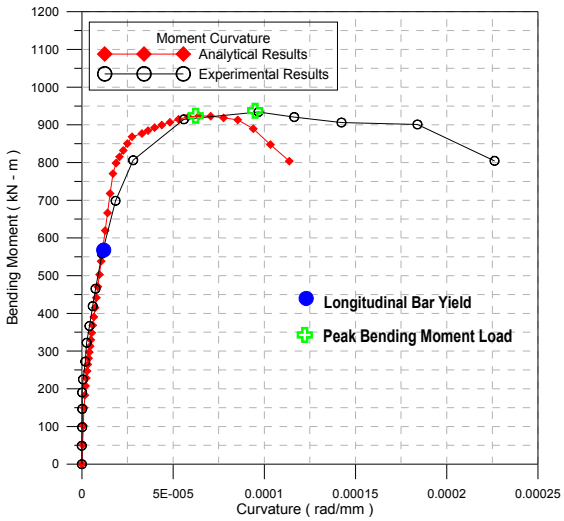

Fig. 6-8 Analytical and Experimental Moment-Curvature Comparison for Square Column under Flexure and Shear

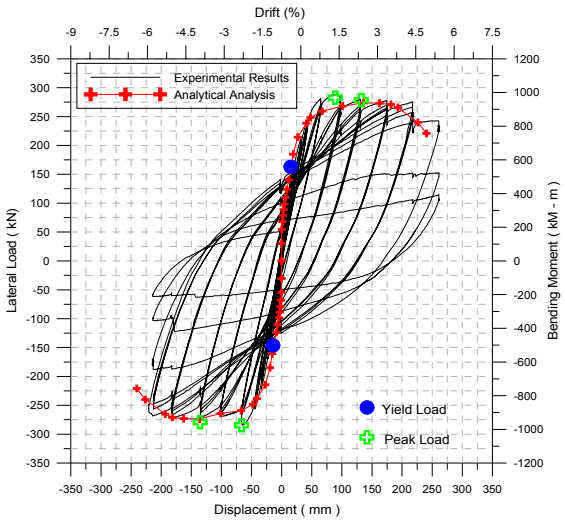

Fig. 6-9 Analytical and Experimental Load-Displacement Comparison for Square Column under Flexure and Shear

The predicted displacement capacity was about 5% smaller than the experimental results, which was caused by the smaller curvature capacity in the prediction. Shear

deformation and bond slip of reinforcement are not considered in the prediction; therefore, the predicted lateral displacements are approximate.

6.2.3.2 Comparison for Oval Column under Biaxial Flexure and shear

At a constant axial load ratio of 7%, the moment-curvature curve prediction of the oval column under biaxial flexure and shear is presented in Fig. 6-10. At pre-cracking stage, the analytical moment-curvature curves perfectly agreed with the experimental results. At post-cracking stage, the stiffness degradation in the analytical prediction was a little less than the stiffness degradation in the experimental results due to the adopted reinforcement model. The measured stiffness at post-yielding stage was smaller than the calculated effectively secant stiffness due to the overestimation of confined concrete strength under a lower strain level in analytical study. At peak load, the flexural strength from the prediction was around 98% of the experimental flexural strength. At post-peak stage, the experimental strength degradation perfectly agreed with the strength degradation in the prediction, which indicated the accurate prediction for compressive behavior of confined concrete with spirals at the high strain levels. Also the predicted curvature capacity was much greater than the measured curvature capacity, which might be caused by not only the overestimation of ultimate strain in confined concrete with spirals but also the loss of instrumentation at higher curvature level. Lateral displacement at the tip of the column was predicted based on the moment-curvature analysis as shown in Fig. 6-11. The lateral load-displacement curves in analytical analysis can well predict the experimental results before reinforcement yielding. At post-yielding stage, however, the displacement in analytical analysis was about 5% -25% less than the experimental results, which was caused by the strain penetration into the base of the tested columns to

amplify the lateral displacement response during testing. Also the shear deformation and bond slip of reinforcement are not considered in the prediction; therefore, the predicted lateral displacements are approximate.

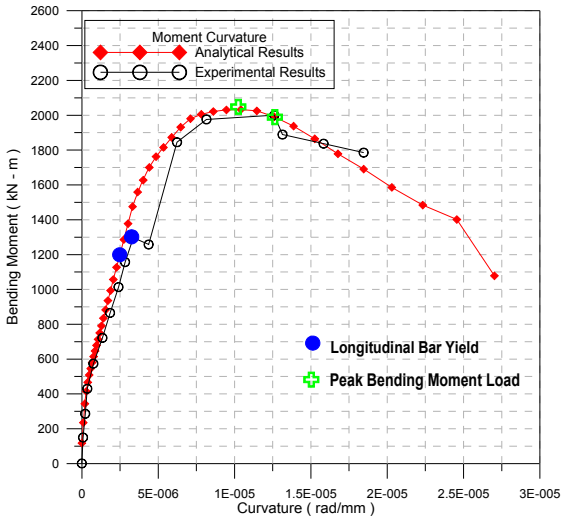

Fig. 6-10 Analytical and Experimental Moment-Curvature Comparison for Oval Column under Biaxial Flexure and Shear

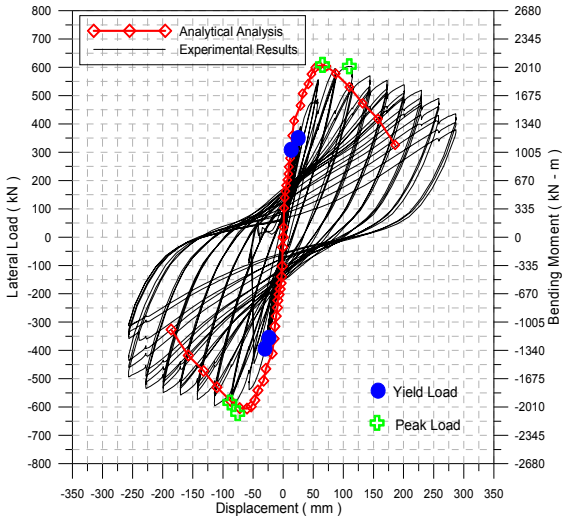

Fig. 6-11 Analytical and Experimental Load-Displacement Comparison for Oval Column under Biaxial Flexure and Shear

6.2.3.3 Analytical Results for Oval Column under Uniaxial Flexure and shear

At a constant axial load ratio of 7%, the moment-curvature curve prediction of the oval column under uniaxial flexure and shear is presented in Fig. 6-12. At pre-cracking stage, the analytical moment-curvature curve is linear with slight stiffness degradation. At post-cracking stage, the obvious stiffness degradation was observed with a nearly linear moment-curvature relationship. After reinforcement yielding, the stiffness degradation was significantly developed due to increasing deformation. The curvature at post-yielding stage was smaller than the calculated effectively secant stiffness due to the overestimation of confined concrete strength under the lower strain level in analytical analysis. The flexural strength was predicted at a lateral load of 425 kN. At post-peak stage, the strength degraded gradually due to the confinement of spirals. Lateral displacement at the tip of the column was predicted based on the moment-curvature

analysis as shown in Fig. 6-13. The predicted lateral displacement capacity for the oval column under uniaxial flexure and shear was larger than the predicted one under biaxial flexure and shear due to a larger curvature capacity.

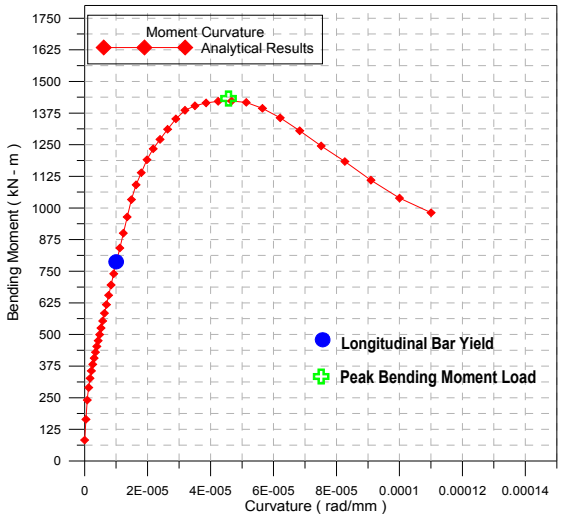

Fig. 6-12 Analytical and Experimental Moment-Curvature Comparison for Oval Column under Flexure and Shear

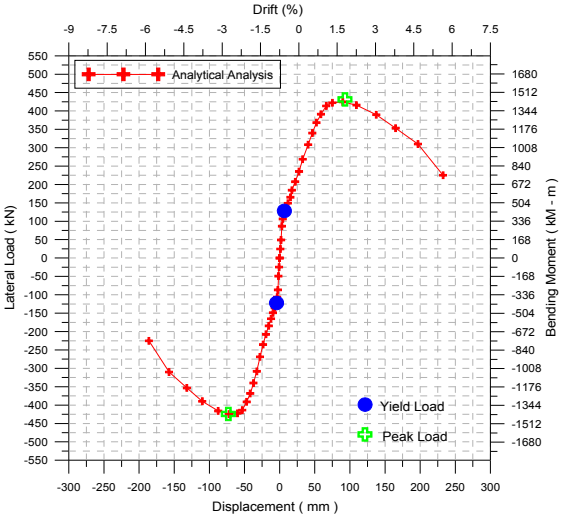

Fig. 6-13 Analytical and Experimental Load-Displacement Comparison for Oval Column under Flexure and Shear

6.3. MCFT Model for Shear Capacity

Based on the literature review, there are reliable tools or models to predict pure shear capacity for RC elements (Vecchio and Collins, 1986, Belarbi and Hsu 1994; Pang and Hsu, 1995). Among well-established analytical models, the MCFT offers good predictions for RC members, which quantified and introduced the effects of concrete softening under tensile strain and tension stiffening under uniaxial stress to account for existing tensile stresses in the concrete between the cracks (Collins and Mitchell 1993, Rahal and Collins (1995a). The MCFT method was developed by observing the response of a large number of reinforced concrete elements loaded in pure shear or in shear combined with axial stress; and can predict the shear strength of RC elements with an average shear strength ratio of 1.01 and a coefficient of variation (COV) of only 12.2%. In this study, the prediction of shear capacity relied on the computer program Response

2000 which can be used for RC sectional analysis using MCFT. The equilibrium, compatibility and stress-strain relationships used by the MCFT are briefly summarized in Fig. 6-14. In the MCFT approach, θ is the angle between the x-axis and the direction of the principal compressive average strain, which also represents the angle of concrete cracking. These average strains are measured over base lengths which are equal to or greater than the crack spacing. Then average stresses are calculated considering effects both at and between the cracks, which are distinct from stresses calculated at cracks. A detailed description of MCFT is provided by Vecchio and Collins, 1988 and Collins and Mitchell, 1993.

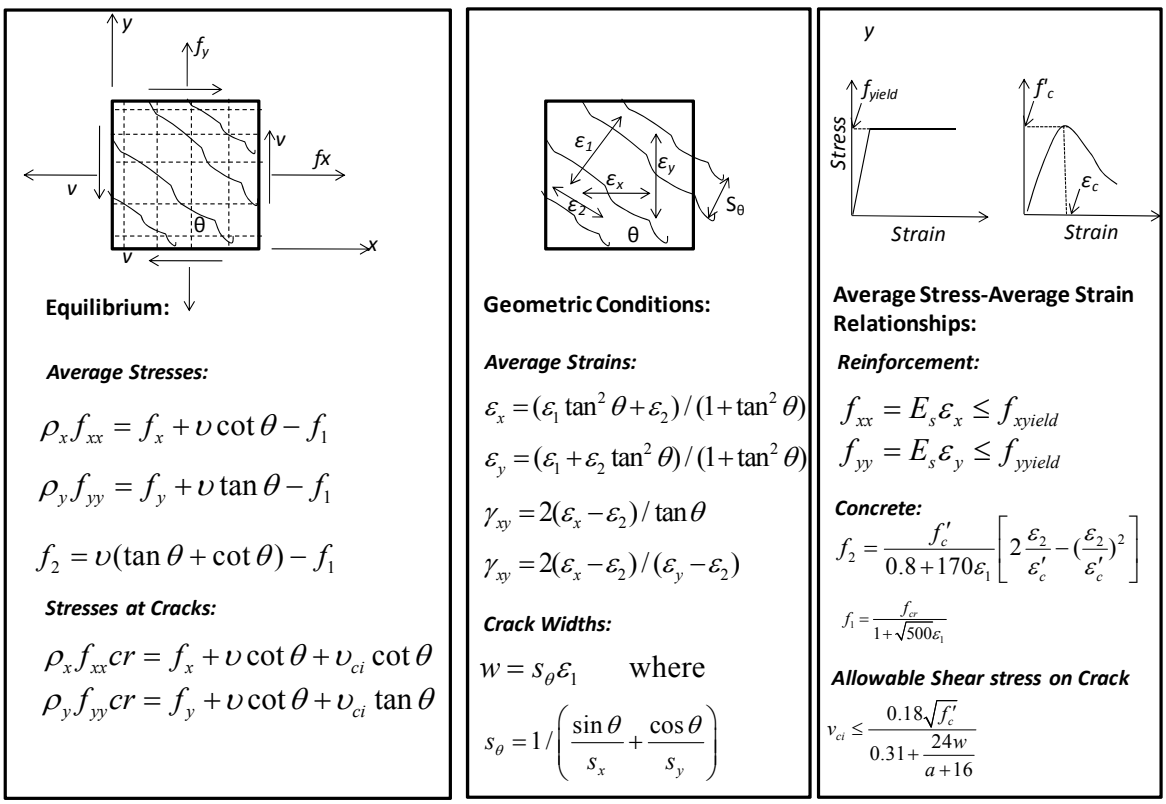

Fig. 6-14 MCFT for Shear Behavior (Concepts from Collins and Mitchell, 1993)

Evan Bentz (2000) developed Response 2000 at the University of Toronto as a part of his doctoral dissertation work, supervised by Professor Michael P. Collins. This two-dimensional sectional analysis program for RC beams and columns can predict the

strength and ductility of RC members subjected to shear, moment, and axial loads, which can also be considered to apply simultaneously to investigate the interaction relationship between them. Response 2000 can provide the shear strength of beams and columns with various cross sectional shapes and transverse reinforcement configurations. Bentz (2000) considered each cross-section as a stack of biaxial element and assumed that "plane sections remain plane, and that there is no transverse clamping stress across the depth of the elements." For given axial loads, the cracking angle, the average stresses and the average strains can be calculated from the given equilibrium equations in terms of average stresses, the given compatibility equations in terms of average strains, and the given average stress-strain relationships. Then shear stress distribution and the shear strength of a section can be derived if just one biaxial element within the web of the section is considered and the shear stress is assumed to remain constant over the depth of the web. The typical Response 2000 model of the beam section is shown in Fig. 6-15.

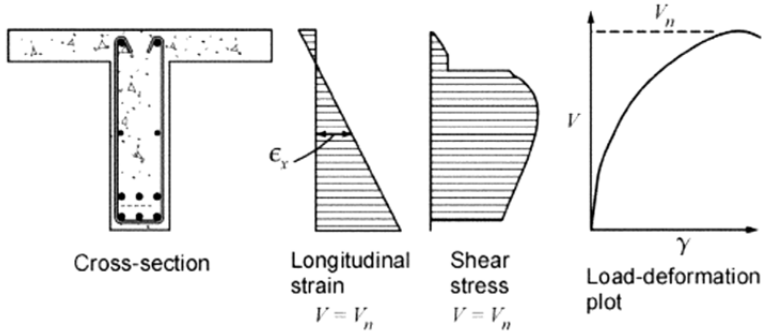

Fig. 6-15 Response 2000 Model of Typical Beam Section

The shear strength predictions of square and oval columns using Response 2000 are shown in Fig. 6-16. The shear and deformation relationship remained almost linear before reinforcement yielding, where the shear resistance was taken as yielding shear strength. The oval column obtained larger yielding shear strength than the square column; but they had the similar shear strain. Also the oval column experienced a longer yielding plateau

than the square column due to a larger concrete section and reinforcement configurations. At post-yielding stage, the shear resistance developed with both concrete and reinforcement contribution. Thereafter, the concrete was observed with severe shear crack and transverse reinforcement significantly contributed to shear resistance. The oval column achieved peak shear strength at 2025 kN, which was almost twice compared to the square column due to the larger cross section and greater amounts of transverse reinforcement.

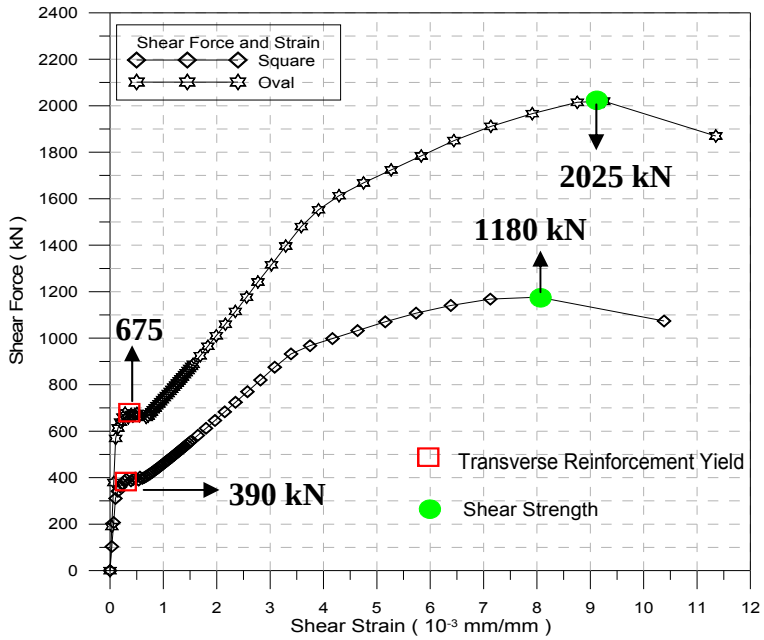

Fig. 6-16 Predictions of Shear Strength using Response 2000

6.4. STM Model for Torsional Capacity

This section describes the analytical model development for predicting the torsional moment-twist behavior of square and oval RC members based on the original STM. The proposed model uses the basic equilibrium and compatibility equations for the STM and includes the effect of concrete tension stiffening (TS-STM) to improve the prediction of RC members at the cracking state as well as to reduce the overestimation of the peak torsional moment. In order to account for the concrete acting in tension, a stress-strain

relationship for concrete in tension should be incorporated into the model. Also the shear flow zone determination should be adjusted to account for the transition range between the uncracked and cracked stages (Greene, 2006). Greene (2006) validated the tension-stiffening incorporation in the analytical model for RC members under pure torsion using the test data available in the literature. The proposed TS-STM adopts the equilibrium and compatibility equations developed for an RC panel under a membrane stress field.

6.4.1. Governing Equations for TS-STM

For an RC member subjected to a torsional moment, the TS-STM is comprised of equilibrium equations, compatibility conditions, and constitutive laws for concrete and reinforcement. All the required equations are described in the following sections.

6.4.1.1 Equilibrium Equations

Under in-plane stress conditions, the stresses in reinforced concrete membrane elements are shown in Fig. 6-17 and Fig. 6-18. The basic governing equations for in-plane shear issue are based on this condition. The coordinate system designed with *l-t* axes represents the directions of the longitudinal and transverse reinforcement; the coordinate system designed with *d-r* axes represents the directions of the principal compression and tension stresses and strains in reinforced concrete as shown in Fig. 6-17. The *d* axis is inclined at an angle θ to the longitudinal reinforcement. For cracked members with the development of diagonal cracks, the reinforced concrete forms a truss action by the concrete struts being subjected to compression and the reinforcement acting as tension links. Accordingly, the normal applied stresses σ_l and σ_t, and the shear stress τ_{lt}, can be carried by the superposition of concrete stress σ_d and σ_r, and reinforcement stresses $\rho_t f_t$ and $\rho_l f_l$, as shown in Fig. 6-18. The two-dimensional equilibrium equations

relates with average compressive and tensile stresses in the concrete, average internal stresses in the longitudinal and transverse reinforcement, and the average applied stresses, which are with respect to the angle of inclination of the *d*-axis for the *l*-axis as shown in Fig. 2-20 (a). The three basic equilibrium equations are expressed by Eq. (2-8) though Eq. (2-10). The torsional moment induced by internal shear stress can be expressed as Eq. (2-4).

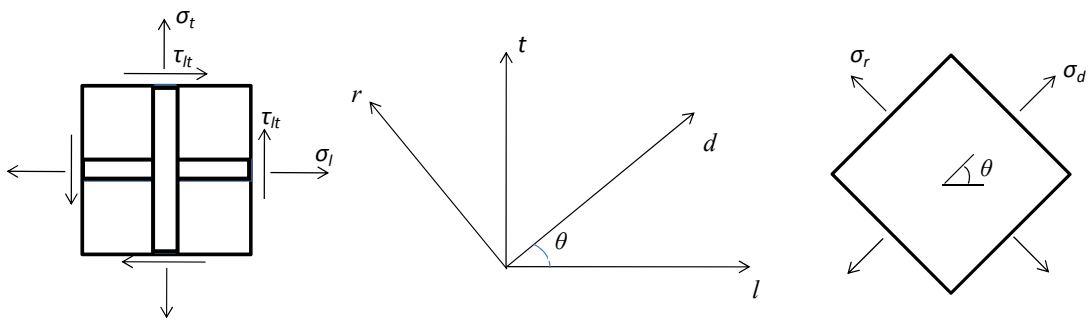

Fig. 6-17 Definition of Coordinate System and Stresses in Reinforced Concrete

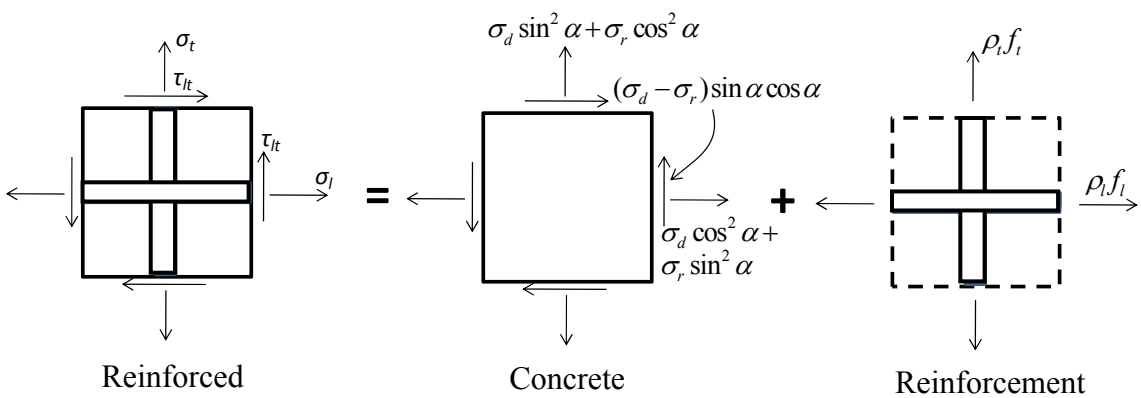

Fig. 6-18 Superposition of Concrete Stresses and Reinforcement Stresses

6.4.1.2 Compatibility Conditions

The three basis two-dimensional compatibility equations describe the relationship between the average strains with respect to d-r and l-t coordinate systems. Therefore the transformation of average strains along the *l-t* coordinate system into the *d-r* principal axes is performed based on the membrane element behavior as expressed by Eq. (2-11) through Eq. (2-13). The relationship between shear strain in the assumed tube wall and

the angle of twist can be derived from the compatibility condition of warping effect as expressed by Eq. (2-14). In addition, the angle of twist also produces warping in member walls for square columns resulting in both compression and bending in the compression concrete struts. The bending curvature of the compression concrete strut can be calculated by Eq. (2-15). In order to establish reasonable solution algorithm, the inclination θ of the diagonal compression, representing the principal strain direction, can be given in Eq. (2-16) by combining the two compatibility equations Eq. (2-11) and Eq. (2-12). The strains along the coordinate axes, ε_d, ε_l, ε_t and ε_r, are related by a compatibility condition as given by

$$\varepsilon_r = \varepsilon_l + \varepsilon_t - \varepsilon_d . \tag{6-30}$$

6.4.1.3 Thickness of Shear Flow Zone

Accurate estimation of the thickness of shear flow zone, t_d, establishes the foundation to extend the two-behavior of two-dimensional membrane elements to a three-dimensional member under torsion. The estimation of t_d is better established for rectangular sections than for circular sections. In the original STM, the thickness of the shear flow zone is assumed to extend into the member from the outer surface to the neutral axis, within which the strain distribution is assumed to be linear as shown in Fig. 2-26 (b) and (d) based on Bernoulli's plane section hypothesis used in the bending theory. However the curvature of the concrete strut should be uncoupled from the thickness of the of shear flow zone before the member was fully cracked (Greene 2006). Before concrete cracking, an uncracked or slightly cracked member can be modeled by allowing the neutral axis to approach the center of the member without requiring an increase in the thickness of the shear flow zone. The thickness of the shear flow zone in

an uncracked section, t_{d0}, represents the effective thickness of thin tube at cracking, which can be calculated by (ACI-318 2008)

$$t_{d0} = \frac{3}{4}\frac{A_{cp}}{p_c}, \tag{6-31}$$

where t_{d0} is the thickness of the shear flow zone in an uncracked section. After additional cracking, the concrete inside the neutral axis acts in tension and is considered ineffective and then the member is assumed to be fully cracked as the concrete and reinforcement acts as a truss. For cracked members, the shear flow zone determination in the proposed model was the same as the definition used in the STM, which can be notated as T_d in this solution procedure and expressed as the same as Eq. (2-27). Also the thickness of shear shear flow zone increases after cracking according to the increase in torsional moment.

According to the above discussion, the model of shear flow zone can be categorized into two cases for the uncracked and cracked members, respectively. The first case describes the model for the uncracked or slightly cracked member as shown in Fig. 6-19 (a), where the thickness of the shear flow zone is taken as the lesser of t_{d0} or half depth of the section; the second case describes the model for a fully cracked member as shown in Fig. 6-19 (b), where the thickness of shear zone is defined as the compression zone depth from the neutral axis to the extreme compression fiber and taken as equal to T_d. The average strain of shear flow zone ε_d is taken as the strain at the center of the shear flow zone as shown in Fig. 6-19. For uncracked members, the average strain of the shear flow zone can be calculated by

$$\varepsilon_d = \frac{\varepsilon_{ds} + \varepsilon_b}{2}, \tag{6-32}$$

$$\varepsilon_b = \varepsilon_{ds} \frac{T_d - t_d}{T_d}, \tag{6-33}$$

where ε_{ds} is the strain at the top surface of cross section, and ε_b is the strain at the bottom location of shear flow zone. For cracked members, the bottom line of the shear flow zone coincides with neutral axis (N.A.), which results in ε_b being equal to zero. The strain at the top surface of the cross section is notated as ε_{ds}, which can be related to ε_d as given by

$$\varepsilon_{ds} = 2\varepsilon_d . \tag{6-34}$$

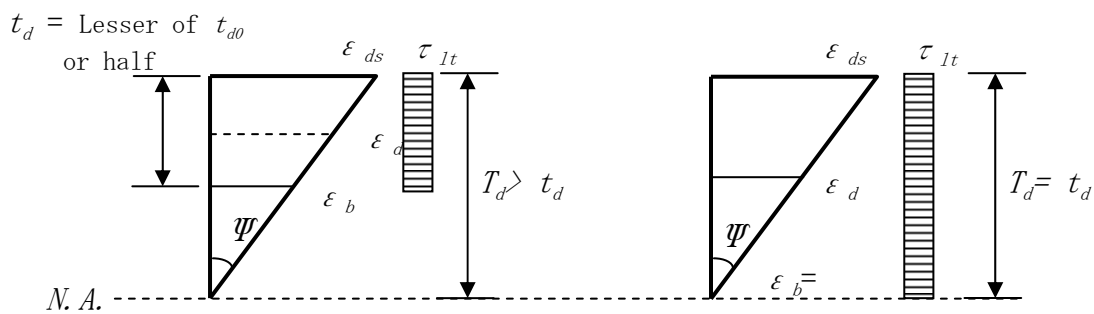

(a) Uncracked Members (b) Cracked Members

Fig. 6-19 Strain and Stress Distribution in Shear Flow Zone

6.4.2. Constitutive Law for Concrete and Reinforcement

6.4.2.1 Concrete Stress-strain Curves under Compression

The analytical models for predicting the behavior of members under shear or torsion are greatly affected by the constitutive laws for concrete and reinforcement. A parabolic stress-strain relationship for a concrete cylinder was used in an early analytical study, which typically overestimated the capacity of such members. Thereafter, new models were developed to quantify the biaxial constitutive relationships for concrete in both compression and tension after Robinson and Demorieux (1972) proposed the concrete compression softening concept. Under uniaxial compression, the behavior of plain concrete can be modeled by the simple parabolic curve. However, the concrete struts in RC members under shear or torsion are subject to a biaxial tension-compression stresses,

which resulted in significantly a different compressive stress-strain response as compared to uniaxial compression. Robinson and Demorieux (1972) conducted a small scale panel test and found that the compressive capacity of the panels was reduced, or softened, by tensile stress in the reinforcement normal to the applied compression. As compared to a non-softened response, the concept of the stress softened response is illustrated in Fig. 6-20 (a). The model developed by Robinson and Demorieux scaled down the compressive stress with increases in the maximum shear strain without quantifying the softening effect. Until the development of research facilities for testing large-scale shear panels, the understanding of the concrete softening could be investigated in detail. Belarbi and Hsu (1991) and Pang and Hsu (1992) proposed the softening coefficient based on the testing of large scale shear panels. Belarbi and Hsu observed both stress-softening and strain-softening effects, and concluded that the softening coefficient ζ was mainly affected by the principal tensile strain. They proposed a proportional stress and strain softening concept to calculate the average concrete compressive stress as shown in Fig. 6-20 (b). Hsu and Zhang (1998) tested more high-strength panels and incorporated the compressive strength of concrete into the softening coefficient expression as expressed in Eq. (2-32).

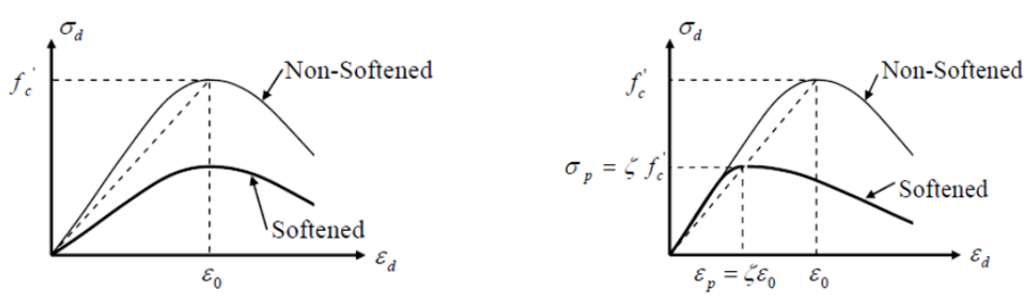

(a) Scaled Softening (b) Proportionally Softening

Fig. 6-20 Softened Stress-Strain Relationship for Concrete in Compression

In addition, the stress-strain relationship of concrete in compression can be analytically expressed by two branches of parabolic curves involving the softening coefficient as expressed by Eq. (2-28). In a simple way, the average stress σ_d of the concrete stress block in Fig. 2-26 (c) can be expressed by a simplified method in Eq. (2-29). The coefficient k_1 can be derived by integrating the stress-strain curve in Eq. (2-28) as expressed in Eq. (2-30).

6.4.2.2 Concrete Stress-Strain Curves under Tension

The original STM for rectangular members (Hsu 1993) disregarded the tension stiffening effect from tensile stress in concrete, which resulted in an unreasonable prediction of full torsional moment-twist response. Though the tensile action in concrete may only have a small effect on the prediction of a member's peak strength, it has a significant effect on the prediction of a member's full load-deformation response. To predict the full response of an RC member accurately, the tensile stress-strain response of concrete should be incorporated into the proposed model. Greene (2006) calculated the tensile stress-strain data in concrete based on the experimental results from the 37 specimens tested under pure torsion. For each experimental data point on the torque-twist curve, a stress--strain point was calculated based on a modified version of the STM. The calculations procedure was similar to the one described by Hsu (1993) by assuming a trial tensile stress σ_r and tensile strain ε_r, and then adjusting the values until calculated torque T and twist θ matched the experimental values. The calculated stress-strain data is plotted in Fig. 6-21 including 280 data points, which indicated that the tensile stress of concrete decreased with increasing tensile strain after cracking. The linear, parabolic and exponential regression curves were used to perform the parameters affecting the study

(Greene 2006). In this study, the exponential tensile stress-strain relationship of concrete was used to account for the tension stiffening effect. Tensile stress-strain relationships of concrete under tension are given by

$$\sigma_r = E_c \varepsilon_r \qquad \varepsilon_r \le \varepsilon_{cr}, \tag{6-35 a}$$

$$\sigma_r = f_{cr} e^{-379.6(\varepsilon_r - \varepsilon_{cr})} \qquad \varepsilon_r > \varepsilon_{cr}, \tag{6-35 b}$$

$$f_{cr} = 0.53 \frac{A_g}{A_{cp}} \sqrt{f_c'}, \tag{6-35 c}$$

where f_{cr} is the cracking stress or tensile strength of concrete, ε_{cr} is the cracking strain of concrete taken as 0.00010, A_g is the gross area of the cross section, and A_{cp} is the total area inside the perimeter of the section. So the effect of hollow and solid cross sections can be evaluated using factor A_g / A_{cp}, which is equal to unit one in this study. In addition, it is assumed that most of the deformation due to the tensile strain actually occurs at crack locations.

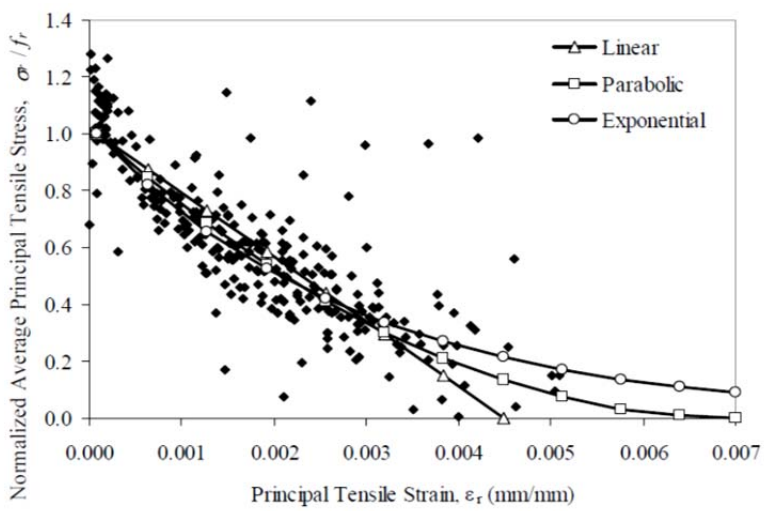

Fig. 6-21 Normalized Data and Proposed Concrete Tensile Strength Models (adopted from Greene, 2006)

Then the shear flow zone can be viewed as sections of concrete struts connected by reinforcement at the cracks, and the curvature in the concrete strut occurs as the concrete sections rotate about the reinforcement as the cracks open and close. The tensile strain of

concrete ε_r can be considered as the tensile strain at $t_d/2$ since the reinforcement is located near mid-depth of the shear flow zone.

6.4.2.3 Reinforcement Stress-Strain Curves

At the post-yielding state, the smeared stress-strain relationship of reinforcement embedded in concrete is difficult to be determined since the reinforcement strain at the cracked sections increases rapidly to reach the strain hardening region of the stress-strain curve. The averaging of the reinforcement strains and the corresponding reinforcement stresses becomes mathematically complex and requires numerical integration. Belarbi and Hsu (1994) proposed a simple bi-linear model of the smeared stress-strain relationship of mild steel embedded in concrete based on testing of large scale shear panels. They found that the yielding point of the average stress-strain curve of mild steel bars embedded in concrete is lower than that of the bare bar. The stress-strain relationship for the longitudinal and transverse reinforcement in this study adopted the simplified bilinear model from Belarbi and Hsu (1994) as expressed by

$$f_s = E_s \varepsilon_s \qquad \varepsilon_s \le \varepsilon_n, \tag{6-36 a}$$

$$f_s = f_y[(0.91 - 2B) + (0.02 + 0.25B)\frac{\varepsilon_s}{\varepsilon_y}] \qquad \varepsilon_s > \varepsilon_n, \tag{6-36 b}$$

$$\varepsilon_n = \varepsilon_y(0.93 - 2B), \tag{6-36 c}$$

$$B = \frac{1}{\rho}\left(\frac{f_{cr}}{f_y}\right)^{1.5}, \tag{6-36 d}$$

where f_y is the yielding stress of reinforcement, and f_s is the stress of reinforcement at the strain of ε_s. In addition, l replaces s in the subscripts of the symbols for longitudinal steel, and t replaces s in the subscripts of the symbols for transverse steel.

6.4.3. Additional Equations and Solution Procedure

This section provides the additional equations needed for calculations and provides an efficient solution procedure to solve the system of equations. In this study, two constant values, σ_l = applied axial stress and σ_t = 0, are used in the solution procedure. Unless explicitly stated in the study, E_s was taken as 200 GPa (ACI 318 2008), the concrete strain at peak stress ε_0 was assumed to be -0.002 mm/mm (Vecchio and Collins 1986) and the average cracking strain ε_{cr} was considered as 0.00010 mm/mm (Belarbi and Hsu 1994, Gopalaratnam and Shah 1985). The ascending branch of concrete in tension was assumed to be linear, and therefore elastic modulus for concrete based on Hooke's Law for linear elastic materials was defined as

$$E_c = \frac{f_{cr}}{\varepsilon_{cr}}, \tag{6-37}$$

where E_c is the elastic modulus of concrete.

The cross section of the square RC member can be defined in terms of the height and width. The equations for cross sectional properties are given by

$$A_{cp} = A_g = b \times b, \tag{6-38}$$

$$p_c = 4 \times b, \tag{6-39}$$

where b is the width of the square cross section. The proposed analytical model is based on the STM model, which involved the warping effect by the compatibility condition as expressed in Eq. (2-14) and Eq. (2-15). Therefore, the sectional dimension for oval RC members was assumed to be idealized as a square cross section by equivalent area criteria. Then the equivalent square cross section was expected to achieve the similar shear flow zone area as the oval cross section. However, the equivalent square cross section overestimates the warping effect from the oval cross section, which was neglected

in this study. The original oval cross section dimension and equivalent square cross section dimension are presented in Fig. 6-22. The equations for equivalent cross sectional properties are given by

$$A_{cp} = A_g = (1+\frac{\pi}{2})B^2, \tag{6-40}$$

$$p_c = (4+\pi)B, \tag{6-41}$$

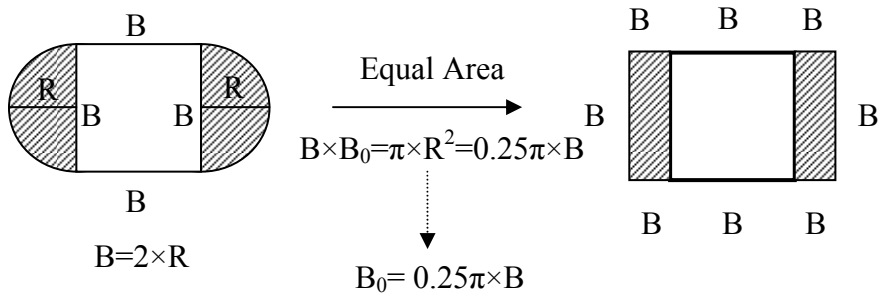

Fig. 6-22 Equivalent Square Cross Section for Oval Members

By combing Eq. (2-16), Eq. (8) and Eq. (9), the stresses along *l* and *r* direction σ_l and σ_t, can be expressed by

$$\sigma_l = \sigma_d(\frac{\varepsilon_r - \varepsilon_l}{\varepsilon_r - \varepsilon_d}) + \sigma_r(\frac{\varepsilon_l - \varepsilon_d}{\varepsilon_r - \varepsilon_d}) + f_l(\frac{A_l}{t_d p_0}), \tag{6-42}$$

$$\sigma_t = \sigma_d(\frac{\varepsilon_r - \varepsilon_t}{\varepsilon_r - \varepsilon_d}) + \sigma_r(\frac{\varepsilon_t - \varepsilon_d}{\varepsilon_r - \varepsilon_d}) + f_t(\frac{A_t}{t_d s}), \tag{6-43}$$

$$\rho_l = \frac{A_l}{t_d p_0}, \tag{6-44}$$

$$\rho_t = \frac{A_t}{t_d s}, \tag{6-45}$$

where ρ_l is the longitudinal reinforcement ratio verse shear flow zone and ρ_t is the transverse reinforcement ratio verse shear flow zone. In order to establish the checking criteria in iteration, the equation for depth of neutral axis can be rewritten by combining Eqs. (2-13), (2-14), (2-15), and (2-27) to eliminate the angle θ as expressed by

$$T_d = \frac{A_0}{2p_0}[\frac{(-\varepsilon_{ds})(\varepsilon_r - \varepsilon_d)}{(\varepsilon_l - \varepsilon_d)(\varepsilon_t - \varepsilon_d)})], \tag{6-46}$$

Given the dimensions of the cross section, the transverse and longitudinal reinforcement amount and configurations, and the material properties, a "displacement-controlled" solution to the equations can be established by trial and error processes and iteration. The initial calculations should be made for constant variables during the solution process. Therefore, A_{cp}, p_c, t_{d0}, ε_{ly}, ε_{ty}, f_{cr}, E_c is calculated according to Eqs. (6-38) or (6-40), (6-39) or (6-41), (6-31), (6-36 c), (6-36 d), (6-35 c), and (6-37). Then the compressive strain ε_{ds} is selected first, which is limited by $0 < \varepsilon_{ds} \leq 0.0035$ mm/mm. Thereafter, an iterative procedure is used to assign the values for concrete tensile stain ε_r and the depth of neutral axis T_d and solve the torque and twist response by the equilibrium equations, compatibility equations, and stress-strain relationships. The solution algorithm for the proposed analytical model is described as following and summarized as a flow chart in Fig. 6-23.

1. Select a value of ε_{ds}.
2. Assume a value of ε_r.
3. Assume a value of T_d.
4. Determine thickness of shear flow zone t_d by taking the minimum one of T_d, t_{d0} or half of the smaller cross section dimension size.
5. Calculate ε_b, ε_d, ζ, k_1, σ_d, σ_r A_0 and p_0 from Eqs. (6-33), (6-32), (2-32), (2-30), (2-29), (6-35), (2-34), and (2-35).
6. Assume a value of longitudinal reinforcement strain ε_l.
7. Calculate the longitudinal reinforcement stress f_l from Eq. (6-36).

8. Calculate the stress σ_l from Eq. (6-42). If the calculated σ_l is not close to the real applied axial load stress within a tolerance, repeat Steps 6 and 7 until convergence is achieved. Then the longitudinal reinforcement strain can be determined.
9. Assume a value of transverse reinforcement strain ε_t.
10. Calculate the transverse reinforcement stress f_t from Eq. (6-36).
11. Calculate the stress σ_t from Eq. (6-43). If the calculated σ_t is not close to zero within a tolerance, repeat Steps 9 and 10 until convergence is achieved. Then the transverse reinforcement strain can be determined.
12. Calculate T_d from Eq. (6-46). If the difference between the assumed and calculated value of T_d is not within tolerance, then repeat Steps 3 to 12 until convergence is achieved.
13. Calculate concrete tensile strain ε_r from Eq. (6-30). If the difference between the assumed and calculated value of ε_r is not within tolerance, then repeat Steps 2 to 13 until convergence is achieved.
14. Calculate θ, τ_{lt}, T, γ_{lt}, Φ, and Ψ from Eqs. (2-16), (2-10), (2-4), (2-13), (2-14), and (2-15).

6.4.4. Torsional Moment Capacity Prediction from TS-STM

Using the proposed model, the predictions of cracking, yielding and peak torque for columns are compared with test results as shown in Fig. 6-24. The predicted cracking torque is only about 5% - 10 % less than the experimental value on average, which is a considerable improvement over the cracking torque predicted by the elastic method using St. Venant's equations or the thin-tube theory. The predicted peak torque is only about 5% larger than the experimental value on average. The predicted twist at cracking was

about 20% greater than the measured values, while the twist at peak torque was about 20% less than measured. The larger twist deformation in the test was caused by cyclic loading with more stiffness degradation at a high load level. Although the prediction of cracking and peak torsional moment proved accurate, the post cracking stiffness and post yield behavior were approximate. In addition, the model predicted that the transverse reinforcement would yield before the longitudinal reinforcement as observed in the experiments. However, the prediction at post-peak stage was not accurate due to the discrepancy between concrete and steel constitutive laws after the peak point, which arises because of disregarding the Poisson Effect in this model. In general, the accurate peak torque prediction can be used for developing the flexure-shear-torsion interaction curves in following section.

6.5. Torsion-Flexure-Shear Interaction Model

Elfgren et al. (1974) developed a three-dimensional interaction surface for members under combined torsion, flexure, and shear, based on three failure modes as discussed in Section 2.3.2.1. In the first mode failure, the top longitudinal reinforcement and the transverse reinforcement yield on the side where the shear and torsional stresses are additive. The second failure mode occurs when the longitudinal and transverse reinforcement on the additive side yield. In the third mode failure, the bottom longitudinal reinforcement and the transverse reinforcement both yield on the additive side. In this study, Elfgren's model would be modified to develop the torsion-flexure-shear interaction model for the RC members with different transverse configurations under cyclic combined loading.

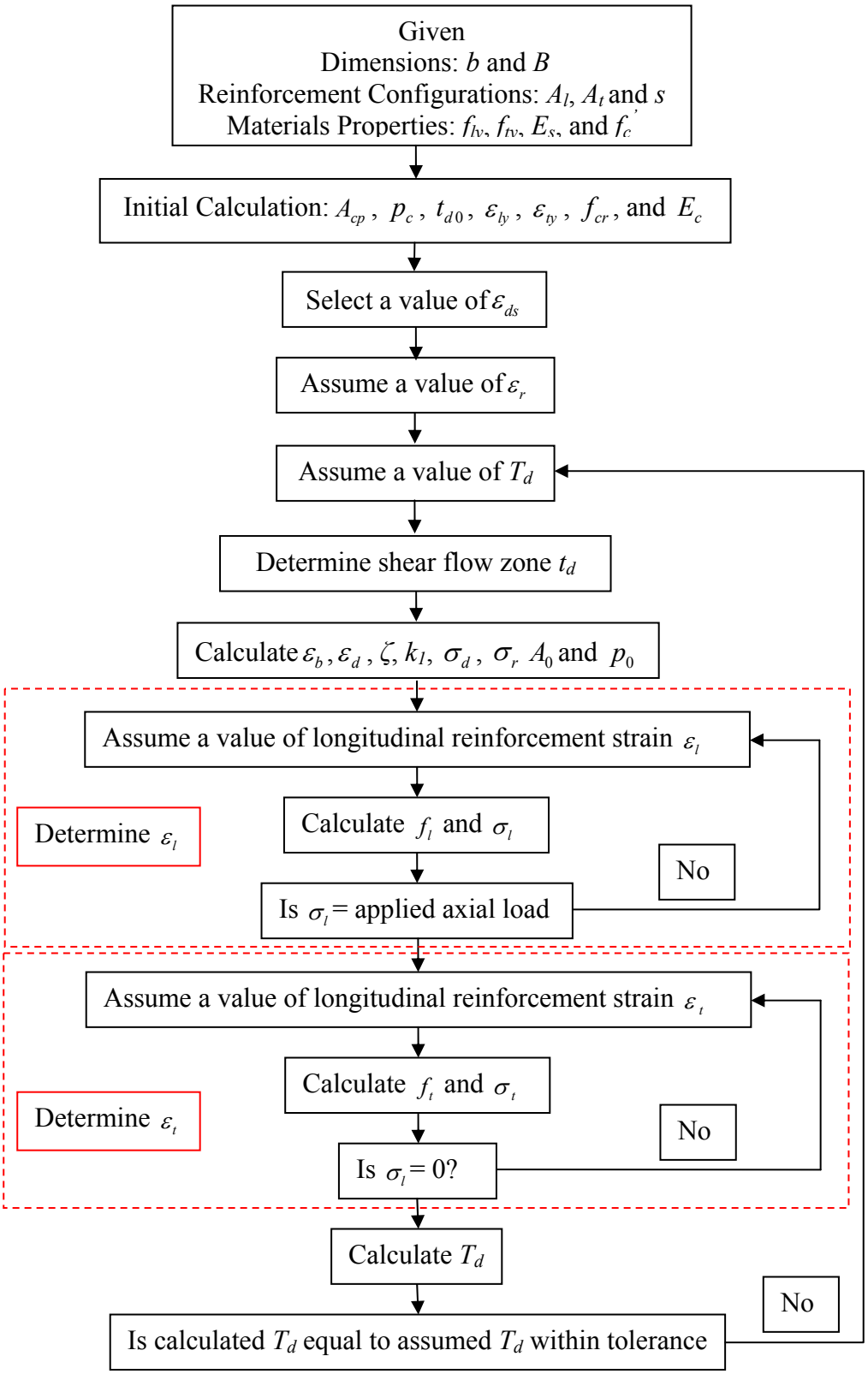

Fig. 6-23 Solution Flow Chart for Proposed Model including Tension Stiffening

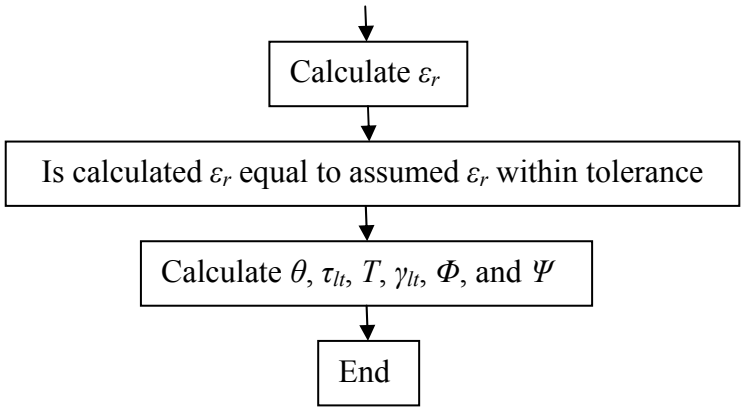

Fig. 6-23 Solution Flow Chart for Proposed Model including Tension Stiffening (cont)

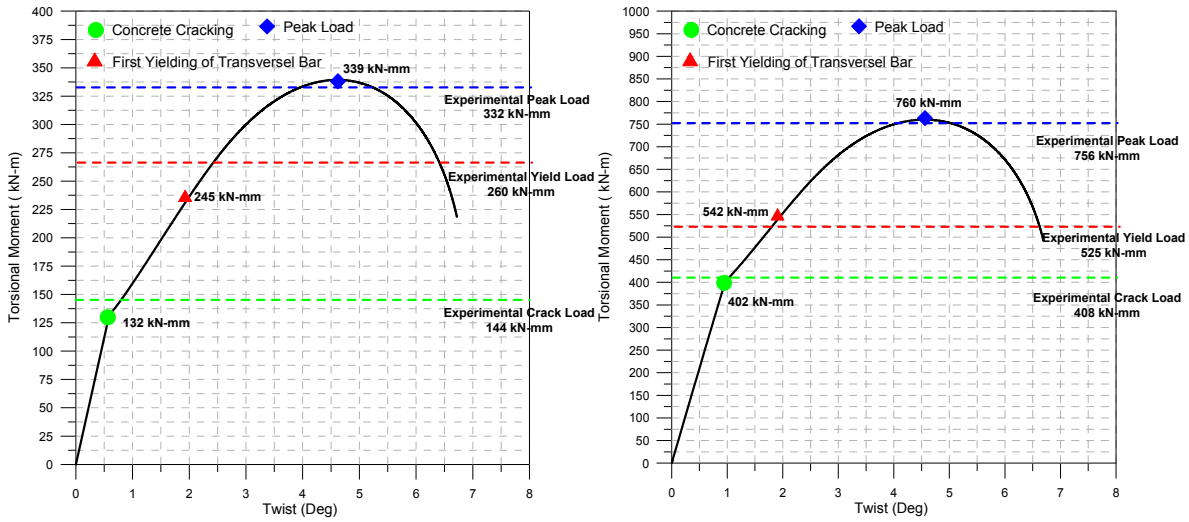

(a) Square Column (b) Oval Column

Fig. 6-24 Torque-Twist Response Prediction using Proposed Model

First, the symmetric reinforcement configurations in this study eliminated the asymmetrical reinforcement configurations effect in Elfgren's model, which was accounted for by the ratio of the force in the top stringers at yielding to the force in the bottom stringers at yielding ($r=A_s^{'} f_y / A_s f_y$). Therefore, the proposed model would not include the asymmetrical reinforcement configurations effect factor. Second, the RC columns were tested by cyclic combined loading in this study and experienced only one failure mode in which both top and bottom longitudinal reinforcement yielded and the transverse reinforcement on the additive side yielded at failure stage. This yielding

mechanism at failure stage can be considered by combining the first and third failure mode in Elfgren's model, which was conducted through squaring the bending moment ratio (M_0/M) to eliminate the positive/negative conventional effect between the first and third failure mode. Third, the damage progression and failure sequence in RC columns under combined loading were affected by the ratio of the transverse and longitudinal reinforcement amount, which should be incorporated into the proposed torsion-flexure-shear interaction model. Also the transverse confinement configurations should be accounted for in the proposed model due to its significant effect on torsional strength and stiffness degradation and deformation capacity.

Under the constant axial load ratio (7%), the flexural, shear and torsional capacity are calculated using the models described in the previous Sections 6.2, 6.3 and 6.4. The proposed the torsion-flexure-shear interaction model can be expressed by

$$(\frac{M}{M_0})^2 + \omega(\frac{V}{V_0})^2 + \omega\lambda(\frac{T}{T_0})^2 = 1, \tag{6-47}$$

where, M is the flexural moment capacity with full interaction found from the cyclic combined loading conditions, M_0 is the flexural moment capacity under constant axial load ratio with no consideration of interaction with torsional moment as per Section 6.2, V is the shear capacity with full interaction found from the cyclic combined loading conditions, V_0 is the shear capacity under constant axial load ratio with no consideration of interaction with flexural and torsional moment from MCFT model in Section 6.3, T is the torsional moment capacity with full interaction found from the cyclic combined loading conditions, T_0 is the torsional moment capacity under constant axial load ratio with no consideration of interaction with bending moment and shear as per Section 6.4,

ω is the amount ratio of transverse reinforcement to longitudinal reinforcement defined as ρ_t / ρ_l, and λ is the factor representing the transverse reinforcement configuration effect taken as 0.9 and 1.75 for ties and interlocking spirals, respectively. The determination of the factor λ was an optimization process using the experimental data, which resulted in the fact that the average calculated values in Eq. (6-47) were most closely to reaching unit one.

The predicted torsion-flexure-shear interaction relationships for square and oval RC columns are plotted in Fig. 6-25. The interaction curved surfaces for oval columns were shifted further from the original zero point compared to the one for the square columns due to the larger cross sectional dimension size. The interaction curved surface for oval column under biaxial loading was rotated about the interaction curve 'AB' in the shear-torsion plane compared to the one for the oval columns under uniaxial loading, which was caused by the larger bending moment capacity under biaxial loading. Therefore, the predicted interaction curved surface coincided with the response of columns in the test. The predicted torsion-flexure-shear interaction curved surface for the square columns are compared to the corresponding tested columns with various T/M ratios of 0.2, 0.4, and 0.6 as shown in Fig. 6-26. The strengths of tested columns were close to the outer interaction curved surface, indicating that the predictions were in perfect agreement with the test results. The predicted torsion-flexure-shear interaction curved surfaces for oval columns are compared to the corresponding tested columns with various T/M ratios of 0.2, 0.4, and 0.6 as shown in Fig. 6-27 and Fig. 6-28. The strengths of the tested columns under uniaxial loading were close to the outer interaction curved surface. For biaxial loading case, the strength of tested columns with a T/M ratio of 0.2 was close to the outer

interaction curved surface, and the strength of the one with a T/M ratio of 0.4 was close to the inner interaction curved surface. This concluded that the model results were in reasonable agreement with the test results and provided conservative prediction.

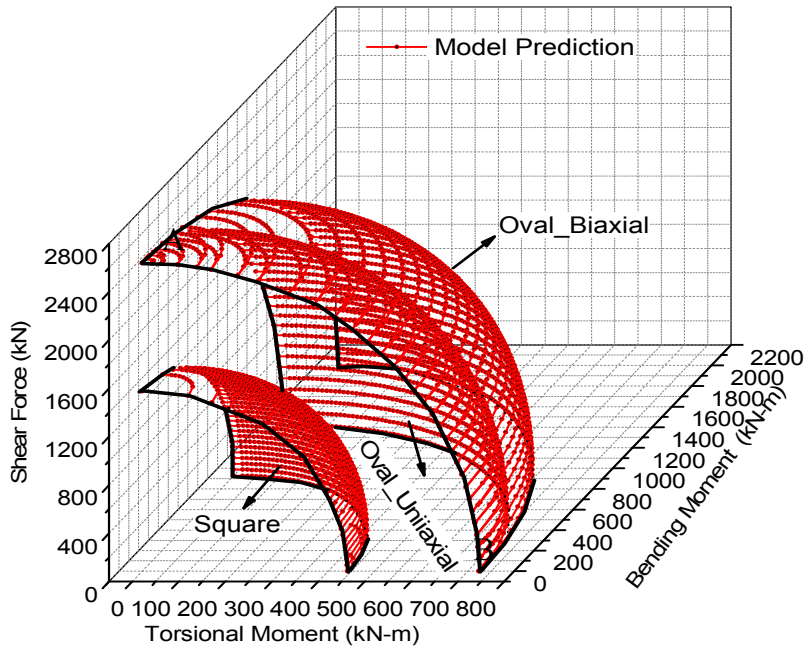

Fig. 6-25 Torsion-Flexure-Shear Interaction Prediction for Square and Oval RC Columns

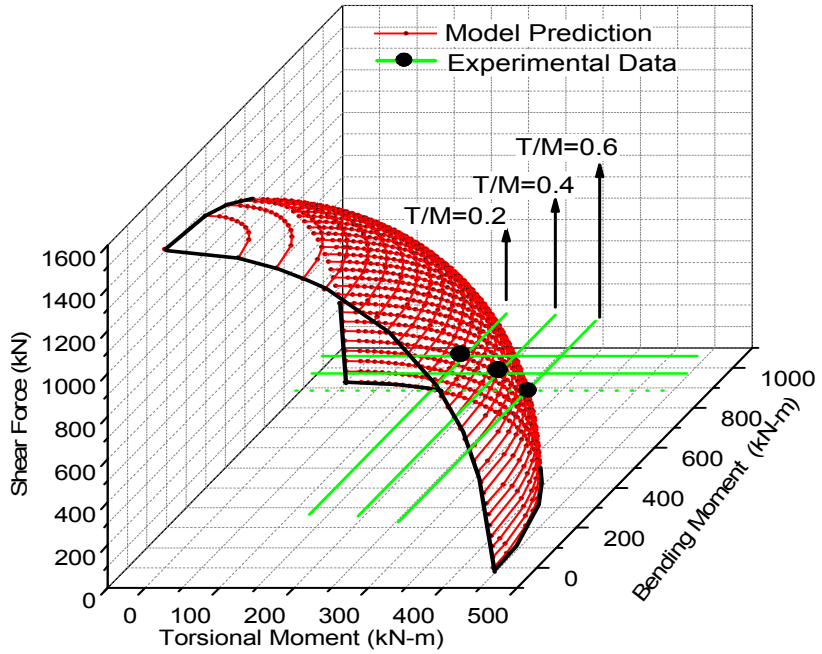

Fig. 6-26 Comparison of Torsion-Flexure-Shear Interaction Curved Surface Prediction and Experimental Results for Square Columns

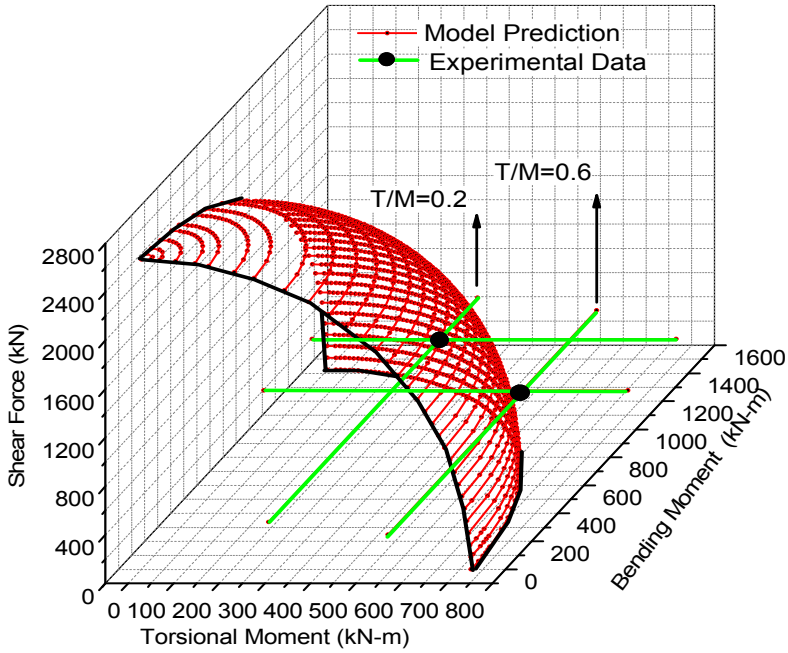

Fig. 6-27 Comparison of Torsion-Flexure-Shear Interaction Curved Surface Prediction and Experimental Results for Oval Columns under Uniaxial Loading

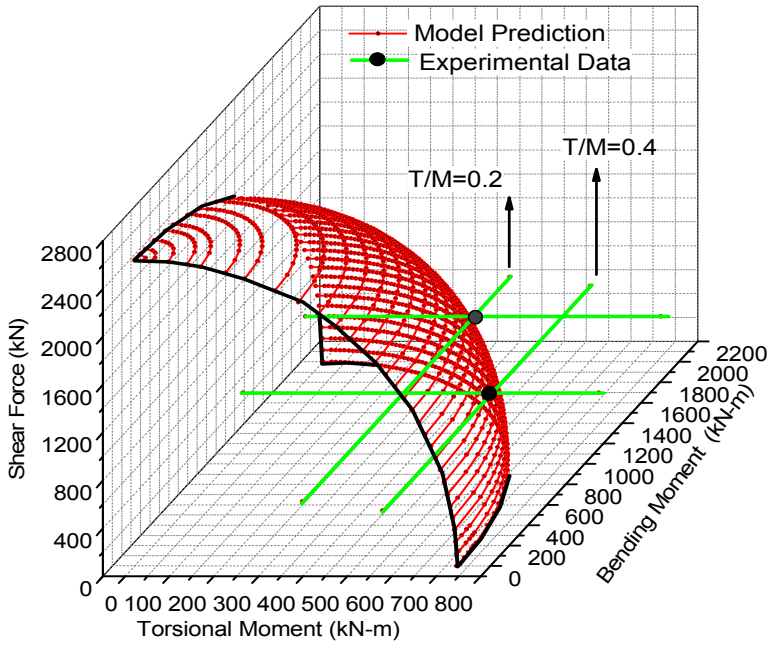

Fig. 6-28 Comparison of Torsion-Flexure-Shear Interaction Curved Surface Prediction and Experimental Results for Oval Columns under Biaxial Loading

In this study, all the columns were tested with a constant ratio of bending moment to shear force (*M/V*), which was the effective loading height of 3.35 m. Therefore, the Eq.

(6-47) can be rewritten to express the torsion-flexure interaction diagram by substituting the constant *M/V* ratio of 3.35 m as given by

$$(\frac{1}{M_0^2}+\frac{0.089\omega}{V_0^2})M^2+(\frac{\lambda\omega}{T_0^2})T^2=1\ . \tag{6-47}$$

The torsion-flexure interaction diagrams, which are the projections of torsion-flexure interaction surfaces, are plotted and compared with the test results in Fig. 6-29. These predicted torsion-flexure interaction diagram achieved good agreement with the test results.

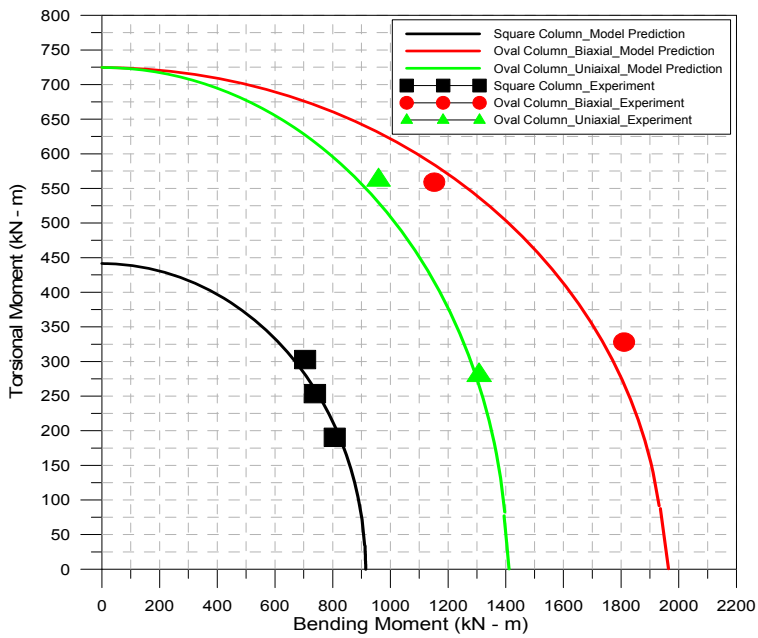

Fig. 6-29 Comparison of Torsion-Flexure Interaction Diagram Prediction and Experimental Results for Square and Oval Columns

In order to validate the proposed model, the predicted torsion-flexure-shear diagrams for circular columns with various transverse reinforcement ratios and aspect ratios were compared with the tested data from Suriya et al. (2009). For circular column with single spirals, the transverse reinforcement configuration factor λ was recommended as 1.2, which was larger than the one for ties and smaller than the one for interlocking spirals. Fig. 6-30 presents the comparison between the predictions and test results for circular

columns. These predicted torsion-flexure interaction diagrams achieved good agreement with the test results, which validated the proposed model for RC columns with different cross sectional shapes, transverse reinforcement amounts, and configurations.

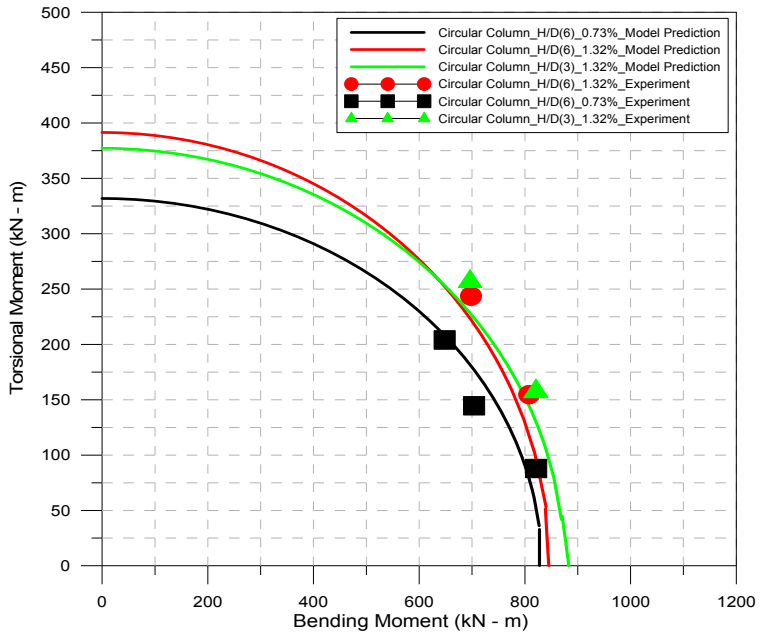

Fig. 6-30 Comparison of Torsion-Flexure Interaction Diagram Prediction and Experimental Results for Circular Columns

6.6. Conclusion Remarks

In this chapter, the torsion-flexure-shear interaction model was developed based on the Elfgren's model. First, the analytical model for well-confined columns under flexure was developed using the existing moment-curvature analysis with some modifications. Second, the MCFT model was used to predict the shear capacity of square and oval columns. Third, the STM model was modified by incorporating the tension-stiffening effect to predict the torsional response of square and oval columns. Then the torsion-flexure-torsion interaction model was established using analytical results from flexural, shear and pure torsion results as a benchmark. Based on the results of this study, the following concluding remarks are drawn:

- Existing moment-curvature analysis was used to predict the bending moment capacity and load-displacement response of RC columns under flexure with a constant axial load. The behavior of confined concrete was incorporated into the model to account for different transverse reinforcement configurations. The predictions of bending moment capacity closely coincide with the experimental results. However, the deformation predictions were smaller than the experimental results.
- The STM model was modified to predict the torsional response of RC columns with a constant axial load by including a tension-stiffening effect and remodeling the thickness of the shear flow zone. The predictions of cracking and peak torsional moment for RC columns with constant axial load were in good agreement with the experimental data. However, the model underestimated the torsional deformation and could better predict the response at post-peak stage once the Poisson's effect was accounted for.
- The proposed torsion-flexure-shear interaction model eliminated the asymmetrical reinforcement configurations effect in Elfgren's model, and combined the first and third failure mode in Elfgren's model to consider the failure mechanism of the columns under cyclic combined loading. The ratio of the transverse and longitudinal reinforcement amounts was introduced to reflect its effect on damage progression and failure sequence in RC columns under combined loading. Also, the transverse confinement factor was determined to account for the effect of transverse confinement on torsional strength and stiffness degradation and deformation capacity. The predictions of the interaction diagrams agreed substantially with the experimental results.

Chapter 7 Conclusion Remarks and Future Recommendations

7.1. Summary

This research study was intended to improve the understanding of the behavior of RC bridge columns under cyclic combined loading including torsion, assess the damage limit states using proposed unified damage index model, and develop analytical model to predict the interaction feature of torsion-flexure-shear loads. The objective of experimental investigation was to determine the combined loading effects on flexural and torsional response in RC bridge columns with respect to strength, stiffness, deformation, ductility, energy dissipation, and damage characteristics, and so on. One of the objectives in analytical study was to develop the decoupled torsional and flexural damage index models based on flexural and torsional hysteresis curves and then couple the flexural and torsional actions for combined loading which can quantify the various damage limit states to assess the damage of RC columns under combined loading. Another objective of analytical investigation was to improve existing models for flexure and torsion under constant axial loads, and establish interaction surface or diagrams from a semi-empirical approach.

7.2. Conclusion Remarks

7.2.1. Experimental Investigation

In the experimental investigation, five square columns reinforced with ties and six oval columns reinforced with interlocking spirals were tested under combined loading at various T/M ratios. The experimental program and results were discussed in Sections 3 and 4. The major conclusions of this experimental work are summarized in the following sections.

7.2.1.1 Flexural and Torsional Hysteresis Curves

The pinching effect of flexural hysteresis was magnified by combined loading along with increasing T/M ratios, which indicated the reduced flexural energy dissipation. The significant pinching effect for the torsional hysteresis of all the columns showed that torsional energy dissipation capacity was always less than the flexural energy dissipation capacity. The interlocking spirals in oval columns provided better transverse confinement, which lessened the pinching effect of hysteresis as comparing to square columns. In addition, the pinching effect of flexural and torsional hysteresis was magnified by biaxial combined loading in oval columns comparing to uniaxial combined loading.

7.2.1.2 Flexural and Torsional Stiffness and Strength Degradation

In columns under combined loading, the flexural and torsional stiffness started degrading after concrete cracking and deteriorated more rapidly after peak load stages. Also the torsional stiffness degraded faster than the flexural stiffness due to the severer inclined torsional cracking and more concrete cover spalling and concrete core crushing.

The flexural strength and displacement capacity of the columns under combined loading decreased with increasing T/M ratios due to the torsion effect. Similarly, the decrease of the T/M ratio caused reduced torsional strength and ultimate twist capacity from the flexure effect. Compared to square columns, the oval columns with interlocking spirals mitigated the stiffness and strength degradation in flexural and torsional response. Also the biaxial combined loading magnified the stiffness and strength degradation as comparing to uniaxial combined loading. In addition, the deterioration of stiffness and

strength is substantial in the first two loading cycles and becomes less significant in the last cycle.

7.2.1.3 Damage Characteristics and Failure Mode

7.2.1.3.1 Damage Characteristics and Failure Mode under Flexure and Shear

The flexural damage of RC columns under flexure and shear was initiated by flexural concrete cracking and yielding of reinforcement. Then the formation of a flexural plastic hinge and concrete cover spalling at the base of the column caused significant lateral stiffness and strength degradation. The final flexure dominant failure was observed by concrete core crushing and buckling or rupturing of reinforcement. Interlocking spirals in the oval columns did not significantly affect the flexural damage progression by compared to the square columns. But the biaxial lateral load in the oval column accelerated the damage progression and reduced the flexural strength of each individual direction.

7.2.1.3.2 Damage Characteristics and Failure Mode under Torsion

The damage progression of the RC columns under pure torsion started with two sets of perpendicular inclined torsional cracks; and continued with concrete cover spalling along the entire-height of the column; finally the torsional plastic hinge formatted with severe core concrete degradation near the mid-height of the column, which was significantly different from the typical flexural damage characteristics. This locking and unlocking effect in the oval columns was observed and reflected in the asymmetric nature of the torsional hysteresis curve for positive and negative cycles. However, there was no locking and unlocking effect in the square columns with ties. The location of severe

damage zone in the oval column under pure torsion was much higher than the one in the square column.

7.2.1.3.3 Damage Characteristics and Failure Mode under Combined Loading

The combined loading including torsion altered the damage patterns of the RC columns. The columns under combined loading at the low T/M ratios of 0.2 and 0.4 experienced flexure dominant failure mode; while the column at a higher T/M ratio of 0.6 failed in torsion dominant failure mode. The columns with large T/M ratios experienced the damage progression in sequence of severe torsional inclined cracking, transverse reinforcement first yielding, early concrete spalling before peak load, and final failure by completely concrete crushing; while the columns with lower T/M ratios resulted in the damage progression such as horizontal and inclined cracking, longitudinal reinforcement first yielding, lagged concrete cover spalling and failure by buckling and rupturing of longitudinal bars and less concrete core crushing. The length of concrete cover spalling was increased with an increase in T/M ratios. Biaxial loading did not show a significant effect on spalling distribution compared to uniaxial loading; however it magnified the damage states at the same ductility compared to uniaxial combined loading due to more torsion effect. In addition, the location of the plastic zone shifted upwards from the base of the column along with the increased applied T/M ratio.

7.2.1.4 Ductility Capacity and Locking and Unlocking Effect

Very small locking and unlocking efficient were obtained in all the square columns caused by the asymmetric features of additive shear stresses from combined shear and torsion. For the square columns, the lower T/M ratios with more shear forces resulted in more asymmetrically additive shear stresses and increased the locking and unlocking

efficient. Interlocking spirals in oval columns introduced the large locking and unlocking effect in torsional response. The locking and unlocking action of spirals together with the asymmetrically additive shear stresses from combined shear and torsion increased the locking and unlocking efficient. In addition, the biaxial combined loading amplified the locking and unlocking efficient by 10% -20% comparing to uniaxial combined loading.

The flexural and torsional deformation capacities were reduced by combined loading effect. The combined loading did reduce the ductility capacity comparing to the pure torsion and the pure flexure and shear cases. The interlocking spirals enhanced the ductility capacity in the oval columns. However, the ductility capacities for the columns under combined loading were not significantly affected by varying T/M ratios.

7.2.1.5 Flexural and Torsional Energy Dissipation

Dissipated flexural energy decreased significantly as the T/M ratio increased due to the torsion effect, and the dissipated torsional energy decreased as the T/M ratio decreased due to the flexure effect. For all the columns, the energy dissipation rate versus the deformation ductility increased along with the increase in the T/M ratio. In addition, larger displacement ductility and flexural energy dissipation are required to yield the transverse reinforcement along with the decreasing T/M ratios, and larger rotation ductility and torsion energy dissipation are required to yield the longitudinal reinforcement. In addition, interlocking spirals in oval columns improved flexural and torsional energy dissipation compared to square columns with ties. The biaxial combined loading reduced flexural and torsional energy dissipation capacity compared to the uniaxial combined loading due to the magnified the torsion effect from the interaction of two directionally lateral loading.

7.2.1.6 Interaction Diagrams of Bending and Torsional Moment

Interaction diagrams between torsional and bending moments at different loading stages can be established based on the test results. For all the columns, the yielding and peak torsional moment and corresponding rotation decreased along with decreasing T/M ratios; similarly the yielding and peak lateral load and displacement capacity were reduced by the combination of flexure and torsion.

For square columns, lower T/M ratios of 0.2 and 0.4 resulted in the flexure dominant mode and achieved torsional and flexural strength at the same ductility level; while a higher T/M ratio of 0.6 failed the columns by torsion dominant mode and reached its torsional strength prior to flexural strength. For oval columns with the lower T/M ratios of 0.2 and 0.4, they reached torsional and flexural strength at the same ductility level in positive loading cycles and reached their flexural strength prior to torsional strength in negative cycles due to the locking effect in spirals, which increased the torsional strength and ductility capacity. However, the oval column with a T/M ratio of 0.6 reached its torsional strength prior to flexural strength in both positive and negative loading cycles.

7.2.2. Analytical Investigation

In analytical investigation, the decoupled torsional and flexural damage index models based were developed based on flexural and torsional hysteresis curves, which can be used to unify the flexural and torsional actions by various T/M ratios for combined loading. Then the unified damage index value can be correlated with different damage limit states with corresponding structural implication to assess the damage of RC columns under combined loading. In addition, a semi-empirical analytical model was proposed to predict the interaction feature of combined loading. The analytical study and

discussion were presented in Sections 5 and 6. The major conclusions of this analytical study are summarized in the following sections.

7.2.2.1 Damage Assessment Based on Damage Index Model

7.2.2.1.1 Decoupled Torsional and Flexural Damage Index Model

Decoupled torsional and flexural damage index models from the Hwang and Scribner approach was modified by normalizing with total energy dissipation capacity from hysteresis curves for all columns under combined loading. The damage index value of this modified model increased step by step as more loading cycles were imposed at the each ductility, which is an advantage in demonstrating the progression of damage and stiffness degradation along with loading cycles within a given loading level. Though, the models predicted the progression of damage well, the flexural and torsional damage index values at the ultimate state significantly differ for the same columns.

The Park and Ang approach can be modified and extended to calculate the decoupled torsional and flexural damage index according to torsional and flexural hysteretic response of columns, respectively. It can predict the progression of damage for both the flexural and torsional failure-dominated column under combined loading. The damage models were physically intuitive and easy to quantify the different damage characteristics from ‘0’ indicating no damage to ‘1’ indicating near collapse. So that the damage process of a particular column under combined loading can be tracked throughout the course of inelastic loading.

Interlocking spirals in oval columns provided better transverse confinement and reduced concrete core crushing to mitigate the flexural damage at higher displacement ductility levels compared to the square columns with ties. In addition, the biaxial

combined loading accelerated and amplified the torsional damage progression resulting in larger torsional damage index values; however, no significant difference in flexural damage index values was observed between biaxial and uniaxial combined loading since more torsional damage occurred in these columns with more torsion effect.

7.2.2.1.2 Interaction Diagram of Torsional and Flexural Damage Index

An empirical model was proposed, through combining multi factor line regression and polynomial regression by the Ordinary Least Square (OLS) method, to predict the interaction relationship of torsional and flexural damage indices. The empirical equation incorporated the main variables such as transverse reinforcement ratio, cross sectional shape, aspect ratios and T/M ratios. The comparisons demonstrated that the model accurately predicted the interaction diagrams of RC columns with specific design requirement.

7.2.2.1.3 Unified Equivalent Damage Index Model

The decoupled torsional and flexural damage indices can be unified by a weight scheme of T/M ratios and equivalent ductility ratios, which identify with the coupled torsional and flexural damage during the process of combined loading. The unified equivalent damage indices (UEDI) of the columns under combined loading are linear with corresponding equivalent ductility ratios (EDR) at a slope of around 45 degrees and the values of proposed UEDI and EDR both vary from ‘0’, indicating no damage, to ‘1’, indicating collapse.

7.2.2.1.4 Unified Damage Assessment Approach

The damage states under combined loading can be categorized into no damage, minor damage, moderate damage, severe damage, or collapse with the specific structural

implications. The proposed unified equivalent damage index model can specify the range of damage index value into different regions to quantify and assess these damage states.

7.2.2.2 Analytical Model for Torsion-Flexure-Shear Interaction Diagrams

7.2.2.2.1 Analytical Study for Flexure under Constant Axial Loads

Existing moment-curvature analysis was used to predict the bending moment capacity and load-displacement response of RC columns under flexure with a constant axial load. The behavior of confined concrete was incorporated into the model to account for different transverse reinforcement configurations. The predictions of bending moment capacity closely coincide with the experimental results. However, the deformation predictions were smaller than the experimental results.

7.2.2.2.2 Analytical Study for Torsion under Constant Axial Loads

The STM model was modified to predict the torsional response of RC columns with a constant axial load by including a tension-stiffening effect and remodeling the thickness of the shear flow zone. The predictions of cracking and peak torsional moment for RC columns with constant axial load were in good agreement with the experimental data. However, the model underestimated the torsional deformation and could better predict the response at post-peak stage once the Poisson's effect was accounted for.

7.2.2.2.3 Analytical Study for Torsion-Flexure-Shear Interaction Diagrams

The proposed torsion-flexure-shear interaction model eliminated the asymmetrical reinforcement configurations effect in Elfgren's model, and combined the first and third failure mode in Elfgren's model to consider the failure mechanism of the columns under cyclic combined loading. The ratio of the transverse and longitudinal reinforcement amounts was introduced to reflect its effect on damage progression and failure sequence

in RC columns under combined loading. Also the transverse confinement factor was determined to account for the effect of transverse confinement on torsional strength and stiffness degradation and deformation capacity. The predictions of the interaction diagrams agreed substantially with the experimental results.

7.3. Future Research Recommendations

Following are recommendations for future research based on the discussion in previous sections:

1) In testing process, the T/M ratio was maintained as specified values. However, there were difficulties in maintaining the ratio due to difference in unloading and reloading stiffness and the nonlinearity after cracking of concrete. Also it is impossible to control the T/M ratio as a constant value once the flexural or torsional strength is reached. Control algorithms could be developed based on the outputs of different sensors for better control over the loading protocol, which could be a scope for further work.

2) The twist-to-displacement ratio would be a test parameter further research to establish a rational relationship between flexural displacement and torsional twist, which can be used in displacement-based design approach.

3) Additional full-reversal cyclic tests on RC columns should be conducted to investigate the effects of various longitudinal and transverse reinforcement ratios, shear spans, axial load ratio, and concrete strength.

4) A parametric study can be conducted to investigate the concrete cover spalling mechanism under combined loading, and to study the effects of different reinforcement ratios and concrete strength on spalling zone distribution.

5) For RC members, the size effect is significant in shear problems. Moreover, torsion is a three dimensional shear problem containing more size effect. However, there have been no studies conducted on the size effect in RC members under combined loading.

6) More tests should be conducted to clarify the shear-dominated behavior of RC bridge columns under combined loading including torsion.

7) The proposed TS-STM model, incorporating with concrete tension stiffening, could be significantly improved to include the Poisson effect and rationally predict the post-peak torsional response. Also the proposed model idealized oval cross section into equivalent square cross section, which introduced more warping effect and might underestimate the torsional capacity of oval columns.

8) The core concrete contributed to the torsional resistance at post-peak stage, which was related to the transverse confinement level. However, the average concrete stress-strain relationship used in current model did not consider this issue.

Reference

American Association of State Highway and Transportation Officials, "*AASHTOLRFD Bridge Design Specifications and Commentary*," SI Units, 2nd Edition, Washington, D.C., 1998, 1091 pages (plus annual updates).

ACI Committee 318, *Building Code Requirements for Reinforced Concrete (ACI 318-71)*, American Concrete Institute, Detroit, MI, 1971.

ACI Committee 318, *Building Code Requirements for Structural Concrete (ACI 318-95) and Commentary (ACI 318 R-95)*, American Concrete Institute, Detroit, MI, 1995.

ACI Committee 318, *Building Code Requirements for Structural Concrete (ACI 318-08) and Commentary (ACI 318 R-05)*, American Concrete Institute, Farmington Hills, MI, 2008.

ACI Committee 445, *A State of the Art Report on Torsion in Structural Concrete*, American Concrete Institute (Submitted).

Ahmad, S.H. and Shah, S.P., "Complete Triaxial Stress-Strain Curves for Concrete," *ASCE Journal of the Structural Division,* Vol. 108, No. ST4, pp. 728-742, 1982.

Akhtaruzzaman, A.A. and Hasnat, A., "Torsion in Concrete Deep Beams with an Opening," *ACI Structural Journal*, Vol. 86, No. 1, pp. 20-25, 1989.

Ang, B.G., Priestley, M.J.N., and Paulay, T., "Seismic Shear Strength of Circular Reinforced Concrete Columns," *ACI Structural Journal,* Vol. 86, No. 1, pp. 45-59, 1989.

Arias-Acosta, J. and D. Sanders, "Shake Table Testing of Bridge Columns under Combined Actions," *SEI Structures Congress*, Orlando Florida, pp. 1805-1816, 2010.

ASTM A 370, *Standard Test Methods and Definitions for Mechanical Testing of Steel Products (ASTM A 370-05)*, ASTM International, West Conshohocken, Pennsylvania, 2005.

ASTM C 31, *Standard Practice for Making and Curing Concrete Test Specimens in the Field (ASTM C 31-03)*, ASTM International, West Conshohocken, Pennsylvania, 2003.

ASTM C 39, *Standard Test Method for Compressive Strength of Cylindrical Concrete Specimens (ASTM C 39-05)*, ASTM International, West Conshohocken, Pennsylvania, 2005.

ASTM C 617, *Standard Practice for Capping Cylindrical Concrete Specimens (ASTM C 617-98)*, ASTM International, West Conshohocken, Pennsylvania, 1998.

Atalay, M.B. and Penzien, J., "The Seismic Behavior of Critical Regions of Reinforced Concrete Components Influenced by Moment, Shear and Axial Force," *Report No. EERC 75-19,* Earthquake Engineering Research Center, University of California, Berkley, 1975.

Badawy, H.E.I., "Plastic Analysis of Reinforced Concrete Curved Beams," *PhD Thesis*, University of Calgary, 238 pages, 1975.

Badawy, H.E.I. and Jordaan, I., "Plastic Analysis of Curved Beams under Point Loads," *Journal of the Structural Division*, *ASCE*, Vol. 103, No. ST7, 1997.

Banon, H., Biggs, J.M., and Irvine, H.M., "Seismic Damage in Reinforced Concrete Members," *Journal of Structural Engineering*, *ASCE*, Vol. 107, No. 9, pp. 1713-1729, 1981.

Baumann, T., "Zur Frage der Netzbewehrung von Flachentragwerken," *Der Bauingenieur*, Vol. 46, No. 6, pp. 367-377, 1972.

Belarbi, A., "Stress-Strain Relationships of Reinforced Concrete in Biaxial Tension-Compression," *Ph.D. Dissertation*, Department of Civil and Environmental Engineering, University of Houston, 471 pages, 1991.

Belarbi, A., and Hsu, T.T.C., "Constitutive Laws of Concrete in Tension and Reinforcing Bars Stiffened by Concrete," *ACI Structural Journal*, Vol. 91, No. 4, pp. 465-474, 1994.

Belarbi, A., Prakash, S.S., and Silva, P., "Flexure-Shear-Torsion Interaction of RC Bridge Columns," *Proceedings of the Concrete Bridge Conference*, St. Louis, USA, Paper No. 6, 2008.

Belarbi, A., Prakash, S.S., and You, Y.M., "Effect of Transverse Spiral Reinforcement on the Seismic Flexural-Shear-Torsional Behavior of Reinforced Concrete Circular Bridge Columns," *Journal of Structural Engineering and Mechanics*, Vol. 33, No. 2, pp. 137-158, 2009.

Bentz, E.C., "Sectional Analysis of Reinforced Concrete Members," *Ph.D. Thesis*, Department of Civil Engineering, University of Toronto, 2000.

Bentzoni, E.C., "Sectional Analysis of Reinforced Concrete Members," *Ph.D. Thesis,* Department of Civil Engineering, University of Toronto, 2000.

Benzoni, G., Priestley, M.J.N., and Seible, F., "Seismic Shear Strength of Columns with Interlocking Spiral Reinforcement," *Proceedings of 12th World Conference on Earthquake Engineering*, Auckland, New Zealand, 8 pages, 2000.

Birkland, C.J., "Strength of Rectangular Beams with Longitudinal Reinforcement in Combined Torsion, Bending, and Shear," *Master's Thesis*, Department of Civil Engineering, University of Washington at Seattle, WA, 1965.

Bishara, A. and Peir, J.C., "Reinforced Concrete Rectangular Columns in Torsion," *Journal of Structural Division*, *ASCE*. Vol. 94, No. ST 12, pp. 1409-1421, 1973.

Borzi, B. and Elnashai, A.S., "Assessment of Inelastic Response of Buildings using Force- and Displacement-based Approaches," *The Structural Design of Tall Buildings*, Vol. 9, pp. 251-277, 2000.

Bredt, R., "Kritische Bemerkungen zur Drehungselastizitat," *Zeitschrift des Vereines Deutscher Ingenieure*, Band 40, No. 28, pp. 785-790; No. 29, pp. 813-817, 1896.

Browning, B., Marvel, L., and Hindi, R., "Torsional Ductility of Circular Concrete Bridge Columns," *ASCE Structures Congress*, May 16-19, Long Beach, California, 2007.

Calderone, A.J., Lehman, D.E., and Moehle, J.P., "Behavior of Reinforced Concrete Bridge Columns Having Varying Aspect Ratios and Varying Lengths of Confinement," *Pacific Earthquake Engineering Research Center Report 2000/08*, 2000.

CALTRANS, Seismic Design Criteria, Version 1.3, pp. 1-101, 2004.

Chung, Y.S., Meyer, C., and Shinozuka, M., "Seismic damage assessment of RC members," *Report NCEER-87-0022*, National Center for Earthquake Engineering Research, State University of New York at Buffalo, 1987.

Chung, Y.S., Meyer, C., and Shinozuka, M., "Damage Model for Reinforced Concrete, Seismic Engineering Research and Practice," *Proceedings of the 1989 ASCE Structures Congress*, San Francisco, CA, pp. 478–487, 1989.

Collins, M.P., "Torque-Twist Characteristics of Reinforced Concrete Beams," *Inelastic and Non-Linearity in Structural Concrete*, University of Waterloo Press, pp. 211-232, 1972.

Collins, M.P. and Chockalingam, S., "Reinforced Concrete Beams under Reversed Cyclic Torsional Loading," *CEB Symposium, Structural Concrete under Seismic Actions*, Rome, Italy, pp. 181-187, 1979.

Collins, M.P., Walsh, P.F., Archer, F.E., and Hall, A.S., "Ultimate Strength of Reinforced Concrete Beams Subjected to Combined Torsion and Bending," *Torsion of Structural Concrete, SP18,* American Concrete Institute, Detroit, pp. 279-402, 1968.

Davey, B.E., "Reinforced Concrete Bridge Piers Under Seismic Loading," *Master of Engineering Report*, Civil Engineering Department, University of Canterbury, Christchurch, New Zealand, February 1975, 107 pages.

Elfgren, L., Karlsson, I., and Losberg, A., "Torsion-Bending-Shear Interaction for Concrete Beams," *Journal of Structural Engineering, ASCE*, Vol. 100, No. ST8, pp. 1657-1676, 1974.

Elfgren, L., "Torsion-Bending-Shear in Concrete Beams: A Kinematic Model, International Association for Bridge and Structural Engineering," *Colloquium Copenhagen 1979: Plasticity in Reinforced Concrete, IABSE Reports*, Vol. 29, Zürich, pp 111-118, 1979.

Elwood, K.J. and Moehle, J.P. "Shake Table Tests and Analytical Studies on the Gravity Load Collapse of Reinforced Concrete Frames," *PEER Report Series*, November 2003.

Ersoy, U., and Ferguson, P.M., "Concrete Beams Subjected to Combined Torsion and Shear—Experimental Trends," *Torsion of Structural Concrete*, *ACI*, Farmington Hills, MI, No. SP-18, pp. 441-460, 1968.

Ewida, A.A., and McMullen, A.E., "Torsion-Shear Interaction in Reinforced Concrete Members," *Magazine of Concrete Research*, Vol. 23, No. 115, pp. 113-122, 1981.

Galal, E.K., and Ghobarah, A., "Flexural and Shear Hysteretic Behavior of Reinforced Concrete Columns with Variable Axial Load," *Engineering Structures*, Elsevier, Vol. 25, pp. 1353-1367, 2003.

Garstka, B., Krätzig, W.B., and Stangenberg, F., "Damage Assessment in Cyclically Loaded Reinforced Concrete Members," Proceedings, *Second EURODYN*, pp. 121-128, 1993.

Gesund, H. and Boston, L.A., "Ultimate Strength in Combined Bending and Torsion of Concrete Beams Containing Only Longitudinal Reinforcement," *Journal of Structural Division*, *ASCE*, Vol. 61, No. 11, pp. 1453-1472, 1964.

Gopalaratnam, V.S. and Shah, S.P., "Softening Response of Plain Concrete in Direct Tension," *ACI Structural Journal*, Vol. 82, No. 3, pp. 310–323, 1985.

Greene, G. G., "Behavior of Reinforced Concrete Girders under Cyclic Torsion and Torsion Combined with Shear: Experimental Investigation and Analytical Models," *Ph.D. thesis*, Department of Civil, Architectural, and Environmental Engineering, University of Missouri at Rolla, Rolla, 227 pages, 2006.

Greene, G.G., and Belarbi, A., "Model for RC Members under Torsion, Bending, and Shear: Part 1: Theory," *Journal of Engineering Mechanics*, *ASCE*, Vol. 135, No. 9, 2009a.

Greene, G.G., and Belarbi, A., "Model for RC Members under Torsion, Bending, and Shear: Part 2: Model Application and Validation," *Journal of Engineering Mechanics, ASCE*, Vol. 135, No. 9, 2009b.

Hachem, M.M., Mahin, S.A., and Moehle, J.P., "Performance of Circular Reinforced Concrete Bridge Columns under Bidirectional Earthquake Loading," *Report No. PEER 2003/06,* Pacific Earthquake Engineering Research Center, University of California, Berkeley, 2003.

Hamilton, M.E., "Strength of T- and L- Section Beams with Longitudinal Reinforcement in Combined Torsion, Bending, and Shear," *Master's thesis*, Department of Civil Engineering, University of Washington at Seattle, WA, 1966.

Hindi, R., Al-Qattawi, M. and Elsharief, A., "Influence of Different Confinement Patterns on the Axial Behavior of R/C Columns," *ASCE Structures Congress*, New York, USA, 2005.

Hindi, R.A. and Sexsmith, R.G., "A Proposed Damage Model for RC Bridge Columns under Cyclic Loading," *Earthquake Spectra*, Vol.17, No. 2, pp. 261-290, 2001.

Hindi, R., Turechek W., Hoven, B., and Stahl, D., "Hysteretic Behavior of R/C Columns Confined with Opposing Spirals," *ASCE Structures Congress*, 11 pages, 2006.

Hsu, T.T.C., "Torsion of Structural Concrete – Plain Concrete Rectangular Sections," *Torsion of Structural Concrete*, *(SP-18)*, American Concrete Institute, Detroit, pp. 203-238, 1968a.

Hsu, T.T.C., "Torsion of Structural Concrete – Behavior of Reinforced Concrete Rectangular Members," *Torsion of Structural Concrete*, *AIC*, SP-18, pp. 261-306, Detroit, MI, 1968b.

Hsu, T.T.C., "Ultimate Torque of Reinforced Rectangular Beams," *Journal of the Structural Division*, *ASCE*, Vol. 94, No. ST2, pp. 485-510, 1968c.

Hsu, T.T.C., Unified Theory of Reinforced Concrete, CRC Press, Boca Raton, Florida, 313 pages, 1993.

Hsu, H.L and Liang, L.L, "Performance of Hollow Composite Members Subjected to Cyclic Eccentric Loading," *Earthquake Engineering and Structural Dynamics Journal*, Vol. 32, pp. 433-461, 2003.

Hsu, T.T.C. and Mo, Y.L., "Softening of Concrete in Torsional Members," *Research Report No. ST-TH-001-83*, Department of Civil Engineering, University of Houston, Houston, TX, 107 pages, 1983.

Hsu, T.T.C. and Mo. Y.L., "Softening of Concrete in Torsional Members – Theory and Tests," *ACI Structural Journal*, Vol. 82, No. 3, pp. 290-303, 1985a.

Hsu, T.T.C. and Mo, Y.L., Unified Theory of Concrete Structures, John Wiley and Sons, Ltd, London, 516 pages, pp. 60 to 69, 2010.

Hsu, H.L. and Wang, C.L., "Flexural Torsional Behavior of Steel Reinforced Concrete Members Subjected to Repeated Loading," *Earthquake Engineering and Structural Dynamics Journal*, Vol. 29, pp. 667-682, 2000.

Hsu, T.T.C., and Zhang, L.X., "Nonlinear Analysis of Membrane Elements by Fixed-Angle Softened-Truss Model," *ACI Structural Journal*, Vol. 94, No. 5, pp. 483-492, 1997.

Hwang, C.S. and Hsu, T.T.C., "Mixed Torsion Analysis of Reinforced Concrete Channel Beams-A Fourier Series Approach," *ACI Journal*, *Proceedings*, Vol. 80, No. 5, pp. 377-386, 1983.

Hwang, T.H. and Scribner, C.F., "R/C Member Cyclic Response during Various Loading," *Journal of Structural Engineering*, *ASCE*, Vol. 110, No. 3, pp. 477-489, 1984.

Jakobsen, B., Hjorth-Hansen, E., and Holand, I., "Cyclic Torsion Tests of Concrete Box Columns," *Journal of Structural Engineering*, *ASCE*, Vol. 110, No. 4, pp 803-822, 1984.

Jeong, S.H. and Elnashai, A.S., "New Three Dimensional Damage Index for RC Buildings with Planar Irregularities," *Journal of Structural Engineering*, *ASCE*, Vol. 132, No. 9, pp. 1482-1490, 2006.

Jeong, G.D., and Ivan, W.D., "The Effect of Earthquake Duration of the Damage of Structures," *Earthquake Engineering Structural Dynamics*, Vol. 16, pp. 1201-1211, 1988.

Johnston, D.W., "Hollow Prestressed Concrete Beams Under Combined Torsion, Bending and Shear," *Ph.D. thesis*, Department of Civil Engineering, North Carolina State University, Raleigh, NC, 177 pp, 1971.

Johnston, D.W., and Zia, P., "Prestressed Box Beams Under Combined Loading," *Journal of the Structural Division*, *ASCE*, Vol. 101, No. ST7, pp. 1313-1331, 1975.

Kawano, H. and Watanabe, H., "Shear Strength of Reinforced Concrete Columns – Effect of Specimen Size and Load Reversal," *Proceedings of 2nd Italy-Japan Workshop on Seismic Design and Retrofit of Bridges*, 1997.

Kemp, E. L., Sozen, M. A., and Siess, C.P., "Torsion of Reinforced Concrete," *Structural Research Series No. 226*, University of Illinois, IL, 1961.

Kent, D.C., "Inelastic Behavior of Reinforced Concrete Members with Cyclic Loading," *Ph.D. Dissertation*, University of Canterbury, Christchurch, New Zealand, 1969.

Khashaee, P., "Damage-Based Seismic Design of Structures," *Earthquake Spectra*, Vol. 21, No. 2, pp.459-468, 2005.

Klus, J., "Ultimate Strength of Reinforced Concrete Beams in Combined Torsion and Shear," *ACI Journal*, *Proceedings*, Vol. 65, No. 3, pp. 210-216, 1968.

Koutchoukali, N. and Belarbi, A, "Effect of Concrete Strength on the Behavior of RC Beams Subjected to Pure Torsion," *Special Publication on High Strength Concrete*, American Society of Civil Engineers, pp. 38-51, 1997.

Koutchoukali, N.E. and Belarbi, A., "Torsion of High-Strength Reinforced Concrete Beams and Minimum Reinforcement Requirement," *ACI Structural Journal*, Vol. 98, No. 4, pp. 462-469, 2001.

Kowalsky, M.J. and Priestley, M.J.N., "Improved Analytical Model for Shear Strength of Circular Reinforced Concrete Columns in Seismic Regions," *ACI Structural Journal,* Vol. 97, No. S42, pp. 388-396, 2000.

Kratzig, W.B., Meyer, I.F., and Meskouris, K., "Damage Evolution in Reinforced Concrete Members under Cyclic Loading," *Proceedings of 5th International Conference on Structural Safety and Reliability*, Vol. 2, pp. 795-802, 1989.

Kunnath, S.K., Reinhorn, A.M., and Lobo, R.F., "IDARC Version 3.0: A program for the Inelastic Damage Analysis of Reinforced Concrete Structures," *Technical Report NCEER-92-0022*, National Center for Earthquake Engineering Research, State University of Illinois, Urbana, 1992.

Kunnath, S.K., El-Bahy, A., Taylor, A.W., and Stone, W.C., "Cumulative Seismic Damage of Reinforced Concrete Bridge Piers," *NISTIR*, *6075*, National Bureau of Standards and Technology, Technology Administration, U.S. Department of Commerce, 1997.

Lampert, P., and Collins, M.P., "Torsion, Bending, and Confusion – An Attempt to Establish the Facts," *ACI Journal, Proceedings*, Vol. 69, No. 8, pp. 500-504, 1972.

Lampert, P. and Thürlimann, B., "Torsionsversuch an Stahlbetonbalken," (Torsion Tests of Reinforced Concrete Beams), *Bericht Nr. 6506-2*, 101 pages, 1968.

Lampert, P. and Thürlimann, B., "Torsion-Bending Tests of Reinforced Concrete Beams," *Report No. 6506-3*, Intitut für Baustatik, ETH, Zurich, 116 pages., 1969.

Leonhardt, F. and Schelling G, 1974, "Torsionsversuche an Stahlbetonbalken," *Deutscher Ausschuß für Stahlbeton (DAfStb)*, Heft 239, W. Ernst u. Sohn, Berlin, 122 pages, 1974.

Lessig, N.N., "Determination of Load-Carrying Capacity of Rectangular Reinforced Concrete Elements Subjected to Flexure and Torsion," *Study No. 5*, Institut Betona i Zhelezobetona, Moscow, pp. 5-28, 1959.

Lessig, N.N., "Studies of Cases of Concrete Failure In Rectangular Reinforced Concrete Elements Subjected To Combined Flexure And Torsion," *Design of reinforced concrete structures*, Portland Cement Association, translator, State Publishing Offices of Literature on Structural Engineering, *Architecture and Construction Materials*, Moscow, pp. 229–271, in Russian, 1961.

Li., Q., Belarbi, A., and Prakash, S.S., "Seismic Performance of Square RC Bridge Columns under Combined Loading Including Torsion," *Proceedings of the ASCE Earth and Space Conference*, pp. 3011-3018, Honolulu, Hawaii, 2010.

Li., Q. and Belarbi, A., "Seismic Behavior of RC Columns with Interlocking Spirals under Combined Loading Including Torsion," *Proceedings of the 12th East Asia-Pacific Conference on Structural Engineering and Construction (EASEC-12)*, Procedia Engineering, Vol. 14, pp. 1281–1291, Hong Kong SAR, China, 2011.

Li., Q. and Belarbi, A., "Experimental Study on Seismic Behavior of RC Columns with Interlocking Spirals under Cyclic Combined Biaxial Bending and Torsional Moment," *Proceedings of 2012 ASCE Texas Section*, San Antonio, USA, 2012.

Lim, S.N. and Mirza, M.S., "Reinforced Concrete T-Beams without Stirrups under Combined Moment and Torsion," *ACI Journal, Proceedings*, Vol. 65, No. 7, pp. 560-563, 1968.

Lüchinger, P., "Bruchwiderstand von Kastenträgern aus Stahlbeton unter Torsion, Biegung und Querkraft (Ultimate Strength of Box-Girder Beams in Reinforced Concrete loaded in Torsion, Bending and Shear)," *Institut für Baustatik und Konstruktion*, ETH Zürich, Bericht Nr 69, Birkhäuser Verlag, Basel und Stuttgart, 107 pages, 1977.

MacGregor, J.G. and Ghoneim, M.G., "Design for Torsion," *ACI Structural Journal*, Vol. 92, No. 2, pp. 211-218, 1995.

Mander, J.B. and Cheng, C.T., "Seismic Design of Bridge Piers," *Research Report 84-2,* University of Canterbury, Christchurch, New Zealand, 1984.

Mander, J.B. and Cheng, C.T., "Renewable Hinge Detailing for Bridge Columns," *Proceedings of Pacific Conference on Earthquake Engineering*, Melbourne Australia, November, 1995.

Mander J.B., Priestley, M.J.N., and Park, R., "Observed Stress-Strain Behavior for Confined Concrete," *Journal of Structural Engineering, ASCE*, Vol. 114, No. 8, pp. 1827-1849, 1988.

McDaniel, C.C., Benzoni, G., and Priestley, M.J.N., "Scale Effects on the Shear Strength of Circular Reinforced Concrete Columns," *Report SSRP-97/02*, Structures Division, University of California, San Diego, California, 1997.

McMullen, A.E., and Warwaruk, J., "The Torsional Strength of Rectangular Reinforced Concrete Beams Subjected to Combined Loading," *Report No. 2,* Department of Civil Engineering, University of Alberta, Edmonton, Canada, 162 pages, 1967.

McMullen, A.E. and Warwaruk, J. M., "Concrete Beams in Bending, Torsion and Shear," *Journal of Structural Engineering, ASCE*, Vol. 96, No. ST5, pp. 885-903, 1970.

McMullen, A.E., and Woodhead, H.R., "Experimental Study of Prestressed Concrete under Combined Torsion, Bending, and Shear," *PCI Journal*, No. 4, pp. 85-100, 1973.

Mirza, M.S. and McCutcheon, J.O., "Torsion of Structural Concrete—Interaction Surface for Combined Torsion, Shear and Bending in Beams without Stirrups," *ACI Journal*, *Proceedings*, Vol. 65, No. 7, pp. 567-570, 1968.

Mitchell, D., "The Behavior of Structural Concrete Beams in Pure Torsion," *Ph.D. Thesis*, Department of Civil Engineering, University of Toronto, Canada, 1974.

Mitchell, D. and Collins, M.P., "Diagonal Compression Field Theory – A Rational Model for Structural Concrete in Pure Torsion," *ACI Structural Journal*, Vol. 71, pp. 396-408, 1974.

Mitchell, D., and Collins, M.P., "Influence of Pre-stressing on Torsional Response of Concrete Beams," *PCI Journal*, Vol. 23, No. 3, pp. 54-73, 1978.

Mizugami, Y., "Efficiency of Lateral Reinforcement in Interlocking Spirals Rebar," *Proceedings of the 16th US-Japan Bridge Engineering Workshop*, pp. 265-276. 2000.

Mörsch, E., Der Eisenbetonbau, seine Anwendung und Theorie, Wayss, and Freytag, A. G., Im Selbstverlag der Firma, Neustadt, a. d.; Haardt, 118 pp. 1902 (English

Translation by E. P.Goodrich, 1909, McGraw-Hill Book Company, NY, 368 pages.

Müller, P., "Failure Mechanisms for Reinforced Concrete Beams in Torsion and Bending," *Publications, International Association for Bridge and Structural Engineering (IABSE)*, Vol. 36-II, Zürich, pp. 147-163, 1976.

Müller, P., "Platische Berechnung von Stahlbetonscheiben und Balken" (Plastic Analysis of Walls and Beams of Reinforced Concrete), *Institut für Baustatik und Konstruktion*, ETH Zürich, Bericht Nr 83, Birkhauser Verlag, Basel und Stuttgart, 160 pages, 1978.

Meyer, I. F., "Ein werkstoffgerechtes Schädigungsmodell und Stababschnittselement für Stahlbeton unter zyklisher nichtlinearerBeanspruchung," *TR 88-4*, RUB, Aug. 1988.

Nylander, H., "Torsion and Torsional Restraint by Concrete Structures," *Bulletin D-19*, Statens Kommittee för Byggnadsforskning, Stockholm, 1945.

Ohtaki, T., Kuroiwa, T., Miyagi, T., and Mizugami, Y., "Seismic Performance of Bridge Columns with Interlocking Spiral/Hoop Reinforcement," *Proceedings of 10th REAAA Conference*, Tokyo, 2000.

Otsuka, H., Takeshita, E., Yabuki, W., Wang, Y., Yoshimura, T., and Tsunomoto, M., "Study on the Seismic Performance of Reinforced Concrete Columns Subjected to Torsional Moment, Bending Moment and Axial Force," *Proceedings of the 13th World Conference. on Earthquake Engineering*, Vancouver, Canada, Paper No. 393, 2004.

Onsongo, W.M., "The Diagonal Compression Field Theory for Reinforced Concrete Beams Subjected to Combined Torsion, Flexure and Axial Loads," *Ph.D. Dissertation*, Department of Civil Engineering, University of Toronto, Canada, 246 pages, 1978.

Pang, X.B. and Hsu, T.T.C., "Constitutive Laws of Reinforced Concrete in Shear," *Research Report UHCEE 92-1*, Department of Civil and Environmental Engineering, University of Houston, Houston, Texas, 1992.

Pang, X.B. and Hsu, T.T.C., "Behavior of Reinforced Concrete Membrane Elements in Shear," *ACI Structural Journal*, Vol. 92, No. 6, pp. 665-679, 1995.

Pang, X.B. and Hsu, T.T.C. "Fixed-Angle Softened-Truss Model for Reinforced Concrete," *ACI Structural Journal*, Vol. 93, No. 2, pp. 197-207, 1996.

Pandit, G.S. and Mawal, M.B., "Tests of Concrete Columns in Torsion," *Journal of Structural Division*, *ASCE*, Vol. 99, No. ST 7, pp. 1409-1421, 1973.

Park, R. and Paulay, T., Reinforced Concrete Structures, John Wiley and Sons, New York, 1975.

Park, Y.J. and Ang, A.H.S., "Mechanistic Seismic Damage Model for Reinforced Concrete," *Journal of Structural Engineering*, *ASCE*, Vol. 111, No. 4, pp. 722-739, 1985.

Park Y.J., "Seismic Damage Analysis and Damage-limiting Design of R/C Structures," *PhD Thesis*, Department of Civil Engineering, University of Illinois, Urbana, IL. 1984.

Paskova T. and Meyer C., "Damage Mechanics of Concrete Under Cyclic Load," *Mechanics of Materials and Structures*, G.Z. Voyiadjis et al, eds., Elsevier Science Publishers, 1994.

Pontangaroa, R.T., Priestley, M.J.N., and Park, R., "Ductility of Spirally Reinforced Concrete Columns Under Seismic Loading," *Report 79-8*, Department of Civil Engineering, University of Canterbury, Christchurch, New Zealand, 116 pages, 1979.

Prakash, S.S. and Belarbi, A., "Bending-Shear-Torsion Interaction Features of RC Circular Bridge Columns-An Experimental Study", *American Concrete Institute Special Publication-SP265*, Vol. 265, pp. 427-454, 2009.

Prakash, S.S. and Belarbi, A., "Towards Damage Based Design Approach for RC Bridge Columns under Combined Loading Using Damage Index Models", *Journal of Earthquake Engineering*, Vol. 14, No. 3, pp. 363-389, 2010.

Prakash, S.S., Belarbi, A., and You, Y.M., "Seismic Performance of Circular RC Columns Subjected to Axial force, Bending, and Torsion with Low and Moderate Shear", *Engineering Structures*, Vol. 32, No. 1, pp. 46-59, 2010.

Priestly, M.J.N. and Benzoni, G., "Seismic Performance of Circular Columns with Low Longitudinal Reinforcement Ratios," *ACI Structural Journal*, Vol. 93, No.4, pp. 474-485, 1996.

Priestley, M.J.N., Seible, F., and Calvi, G.M., Seismic Design and Retrofit of Bridges, John Wiley and Sons, Inc., New York, 686 pages, 1996.

Pritchard, R.G., "Torsion Shear Interaction of Reinforced Concrete Beams," *Master Thesis*, University of Calgary, Calgary, 1970.

Popovics, S., "A Numerical Approach to the Complete Stress-Strain Curve of Concrete," *Cement and Concrete Research*, Vol. 3, pp. 583-599, 1973.

Rabbat, B.G. and Collins, M.P., "Variable Angle Space Truss Model for Structural Concrete Members Subjected to Complex Loading," *Douglas McHenry Symposium on Concrete and Concrete Structures*, SP-55, American Concrete Institute, Farmington Hills, MI, pp. 547-587, 1978.

Rahal, K.N. and Collins, M.P., "Effect of the Thickness of Concrete Cover on the Shear-Torsion Interaction – an Experimental Investigation," *ACI Structural Journal*, Vol. 92, No. 3, pp. 334-342, 1995a.

Rahal, K.N. and Collins, M.P., "Analysis of Sections Subjected to Combined Shear and Torsion – A Theoretical Model," *ACI Structural Journal*, Vol. 92, No. 4, pp. 459-469, 1995b.

Rahal, K.N., "Shear strength of reinforced concrete: Part I: Membrane elements subjected to pure shear," ACI Structural Journal, Vol. 97, No. 1, pp. 86–93. 2000a.

Rahal, K.N., "Shear strength of reinforced concrete Part II: Beams subjected to shear, bending moment and axial load," *ACI Structural Journal*, Vol. 97, No. 2, pp. 219-224, 2000b.

Rahal, K.N. and Collins, M.P., "Combined Torsion and Bending in Reinforced and Prestressed Concrete Beams," *ACI Structural Journal*, Vol. 100, No. 2, pp. 157-165, 2003a.

Rahal, K.N., and Collins, M.P., "An Experimental Evaluation of the ACI and AASHTO-LRFD Design Provisions for Combined Shear and Torsion," *ACI Structural Journal*, Vol. 100, No. 3, pp. 277-282, 2003b.

Rao, P.S., Sarma, B.S., Lakshmanan, N., and Stangenberg, F., "Seismic Resistant Design and Damage Prediction of Laced Reinforced Concrete Beams," *Proceedings of Structural Engineering Convention*, Indian Institute of Technology, Madras, India, 1997.

Rao, P.S., Sarma, B.S., Lakshmanan, N., and Stangenberg, F., "Damage Model for Reinforced Concrete Elements under Cyclic Loading," *ACI Material Journal*, Vol. 95, No. 6, pp. 682 - 690, 1998.

Rasmussen, L.J. and Baker, G. "Torsion in Reinforced Normal and High-Strength Concrete Beams – Part 1: Experimental Test Series," *ACI Structural Journal*, Vol. 92, No. 1, pp. 56-62, 1995.

Rausch, E., "Design of Reinforced Concrete in Torsion," *Ph.D. Thesis*, Technische Hochschule, Berlin, 53 pages, 1929.

Ritter, W., "Die Bauweise Hennebique," *Schweizerische Bauzeitung*, Zurich, Switzerland, Vol. 33, No. 7, pp. 59-61, 1899.

Robinson, J. R., and Demorieux, J. M., " Essais de Traction-Compression sur Modèles d'Ame de Poutre en Béton Arme," IRABA Report, Institut de Recherches Appliquées du Béton de L'Ame, Part 1, 44 pages, 1968; "Resistance Ultime du Béton de L'âme de Poutres en Double Te en Béton Arme," Part 2, May, 53 pages, 1972.

Roufaiel, M.S.L. and Meyer, C., "Analytical modeling of hysteretic behavior of R/C frames," *Journal of Structural Engineering*, *ASCE*, Vol. 113, No. 3, pp. 429-444, 1987.

Saadeghvaziri, M.A. and Fouch, D.A., "Behavior of RC Columns under Non-proportionally Varying Axial load," *Journal of Structural Engineering, ASCE*, Vol.116, No 7, pp. 1835-1856, 1990.

Sadeghi, K., Lamirault, J., and Sieffert, J.G., "Damage Indicator Improvement Applied on R/C Structures Subjected to Cyclic Loading," *Proceedings of Second EURODYN*, pp. 121-128, 1993.

Sasani, M., "Shear Strength and Deformation Capacity Models for RC Columns," *Proceeding of 13th World Conference on Earthquake Engineering*, No. 1838, Vancouver, B.C., Canada, 2004.

Schickert, G. and Winkler, H., "Results of Tests Concerning Strength and Strain of Concrete Subjected to Multiaxial Compressive Stresses," *Deutscher Ausschuss fur Stahlbeton*, Heft 277, Berlin, West Germany, 1979.

Sengupta, A.K. and Belarbi, A., "Modeling Effect of Biaxial Stresses on Average Stress-Strain Relationship of Reinforcing Bar in Reinforced Concrete Panels", *ACI Structural Journal*, Vol. 98, No. 5, pp. 629-637, 2001.

Sheikh, S.A. and Uzumeri, S.M., "Analytical Model for Concrete Confinement in Tied Columns," *Journal of Structural Division,* ASCE 108 (ST12), 1982.

Sheikh, S.A. and Yeh, C.C., "Tied Concrete Columns under Axial Load and Flexure," *Journal of Structural Division, ASCE*, Vol. 116, No. 10, pp. 2780-2801, 1990.

Sheikh, S.A. and Khoury, S.S., "Confined Concrete Columns with Stubs," *ACI Structural Journal*, Vol. 90, No. 4, pp. 414–431, 1994.

Stephens, J.E. and Yao, J.T.P., "Damage Assessment Using Response Measurement," *Journal of Structural Engineering*, *ASCE*, Vol. 107, No. 3, pp. 1713-1729, 1987.

Stone, W.C. and Cheok, G.S., "Inelastic Behavior of Full Scale Bridge Columns Subjected to Cyclic Loading," *NIST Building Science Report No. 166,* U.S Department of Commerce, National Institute of Standards and Technology, Gaithersburg, MD, 252 pp., 1989.

Suda, K., Amano, R., Masikawa, J., and Ichinomiya, T., "Effect of torsional loading on seismic performance of high pier," *Proceedings of the Japan Concrete Institute*, Vol. 19, No. 2, pp. 789-94, 1997.

Tanaka, H. and Park, R., "Seismic Design and Behavior of Reinforced Concrete Columns with Interlocking Spirals," *ACI Structural Journal*, Vol. 90, No. 2, pp.192-203, 1993.

Tirasit, P., and Kawashima, K., "Seismic Torsion Response of Skewed Bridge Piers," *JSCE Journal of Earthquake Engineering*, Tokyo Institute of Technology, Tokyo, Japan, pp. 357-364, 2005.

Tirasit, P. and Kawashima, K., "Seismic Performance of Square Reinforced Concrete columns under Combined Cyclic Flexural and Torsional Loading," *Journal of Earthquake Engineering*, Vol.11, pp. 425-452, 2007.

Tirasit, P. and Kawashima, K., "Effect of Nonlinear Seismic Torsion on the Performance of Skewed Bridge Piers,*" Journal of Earthquake Engineering*, Vol. 12, No. 6, pp. 980-998, 2008.

Turechek, W., "Cyclic Behavior of R/C Circular Columns confined with Opposing Spirals," *Master Thesis*, Department of Civil Engineering and Construction, Bradley University, Peoria, IL, 2006.

Vecchio, F.J. and Collins, M.P., "Stress-Strain Characteristic of Reinforced Concrete in Pure Shear," *IABSE Colloquium, Advanced Mechanics of Reinforced Concrete*, Delft, Final Report, International Association of Bridge and Structural Engineering, Zurich, Switzerland, pp. 221-225, 1981.

Vecchio, F. and Collins, M.P., "Response of Reinforced Concrete to In-Plane Shear and Normal Stresses," *Report No.82-03*, University of Toronto, Toronto, Canada, 1982.

Vecchio, F.J. and Collins, M.P., "The Modified Compression-Field Theory for Reinforced Concrete Elements Subjected to Shear," *ACI Structural Journal*, Vol. 83, No. 2, pp. 219-231, 1986.

Vecchio, F.J., "Nonlinear Finite Element Analysis of Reinforced Concrete Membranes," *AC1 Structural Journal*, Vol. 86, No. 1, pp. 25-35, 1989.

Victor, D. J., and Ferguson, Phil. M., "Reinforced Concrete T-Beams without Stirrups 19 under Combined Moment and Torsion," *ACI Journal*, *Proceedings*, Vol. 65, No. 1, pp. 29-36, 1968.

Vu, N.D., Priestley, M.J.N., Seible, F., and Benzoni, G., "Seismic Response of Well Confined Circular Reinforced Concrete Columns with Low Aspect Ratios," *5th Caltrans Seismic Research Workshop,* 1998.

Xu SY, Zhang J. "Hysteretic Shear-Flexure Interaction Model of Reinforced Concrete Columns for Seismic Response Assessment of Bridges," *Earthquake Engineering and Structural Dynamics*, Vol. 40, pp. 731-748, 2010.

Yudin, V.K., "Determination of the Load-Carrying Capacity of Rectangular Reinforced Concrete Elements Subjected to Combined Torsion and Bending," *Beton i* Zhelezobeton, Moscow, No. 6, pp. 265-269, 1962.

Wang, M.L. and Shah, S.P., "Reinforced Concrete Hysteresis Model Based on the Damage Concept," *Earthquake Engineering and Structural Dynamics*, Vol. 16, No. 8, pp. 1201-1211, 1988.

William, K.J., and Warnke, E.P., "Constitutive model for the triaxial behavior of concrete," *Proceedings of International Association for Bridge and Structural Engineering*, Vol. 19, pp. 1-30, 1975.

Williams, M.S. and Sexsmith, R.G, "Seismic Damage Indices for Concrete Structures: A State-of-the-Art Review," *Earthquake Spectra*, Vol. 11, No. 2, pp. 319-349, 1995.

Williams, M.S., Villemure, I., and Sexsmith, R.G., "Evaluation of Seismic Damage Indices for Concrete Elements Loaded in Combined Shear and Flexure." *ACI Structural Journal*, Vol. 6, No.1, pp. 37-45, 1997.

Wong, Y.L., Paulay, T., and Priestley, M.J.N, "Squat Circular Bridge Piers under Multidirectional Seismic Attack," *Report 90*-4, Department of Civil Engineering, University of Canterbury, 264 pages, 1990.

Wong, Y.L, Paulay, T., and Priestley, M.J.N, "Response of Circular Columns to Multi-Directional Seismic Attack," *ACI Structural Journal*, Vol. 90, No. 2, pp. 180-191, 1993.

Zahn, F.A., Park, R., and Priestley, M.J.N., "Design of Reinforced Concrete Bridge Columns for Strength and Ductility," *Report 86-7,* Department of Civil

Engineering, University of Canterbury, Christchurch, New Zealand, March 380 pp., 1986.

Zahrah, T.F. and Hall, W.J., "Earthquake Energy Absorption in SDOF Structures," *Journal of Structural Engineering*, *ASCE*, Vol. 110, No. 8, pp.1757-1772, 1984.

Zhang, L.X., and Hsu, T.T.C., 1998, "Behavior and Analysis of 100 MPa Concrete Membrane Elements," *Journal of Structural Engineering*, *ASCE*, Vol. 124, No. 1, pp. 24-34, 1998.

Zhang, J. and Xu, S.Y., Seismic Response of Simulations of Bridges Considering Shear-Flexural Interaction of Columns," *Proceedings of the 4th International Conference on Advances in Structural Engineering and Mechanics*, Jeju, Korea, pp. 1167-1179, 2008.

Zia, P., "What Do We Know about Torsion in Concrete Members," *Journal of the Structural Division, ASCE*, Vol. 96, No. ST6, pp. 1185-1199, 1970.

Appendix: Additional Fabrication, Test Setup Drawings

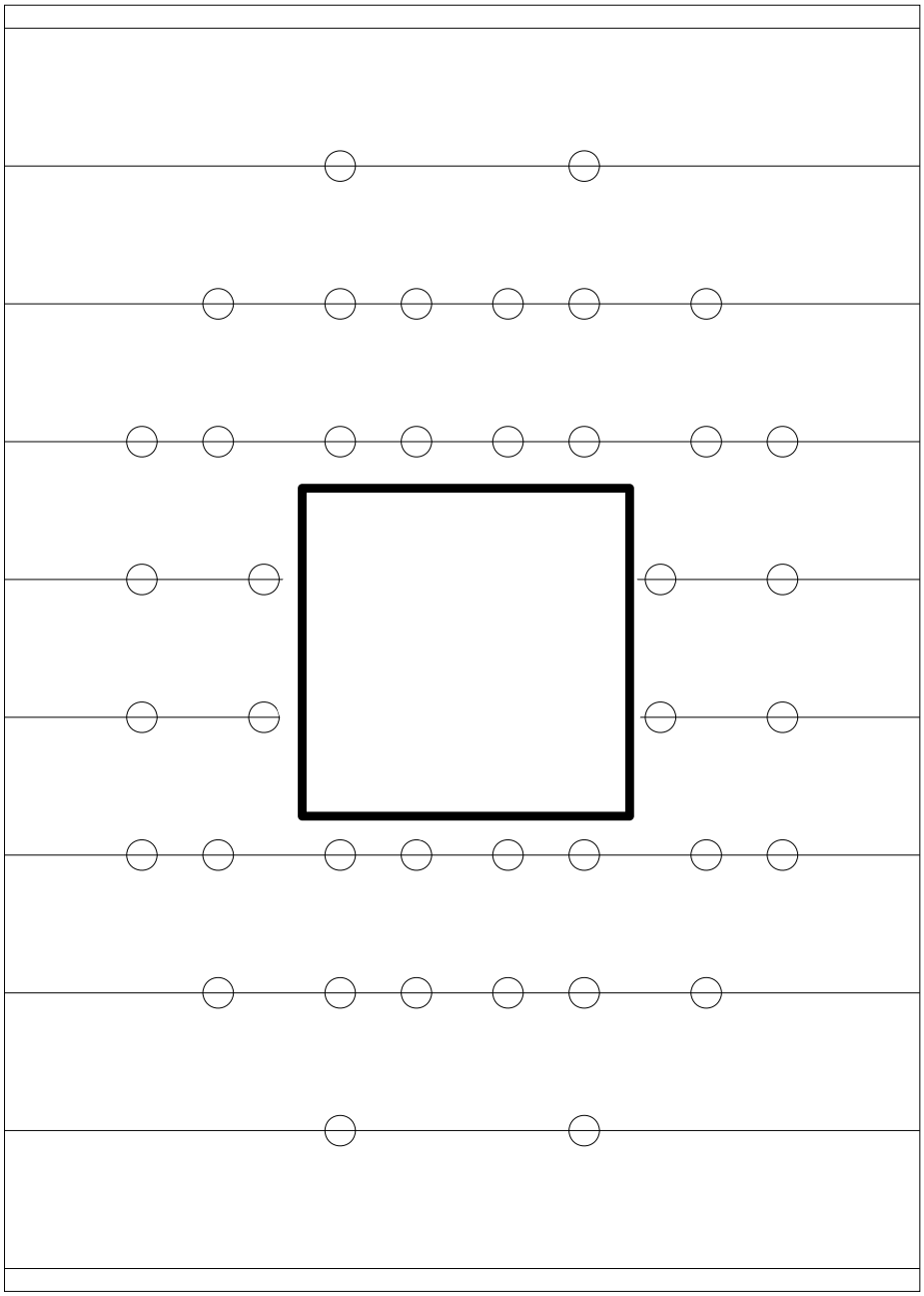

Fig. A-1 Location of Shear Legs inside the Concrete Footing (Plan View)

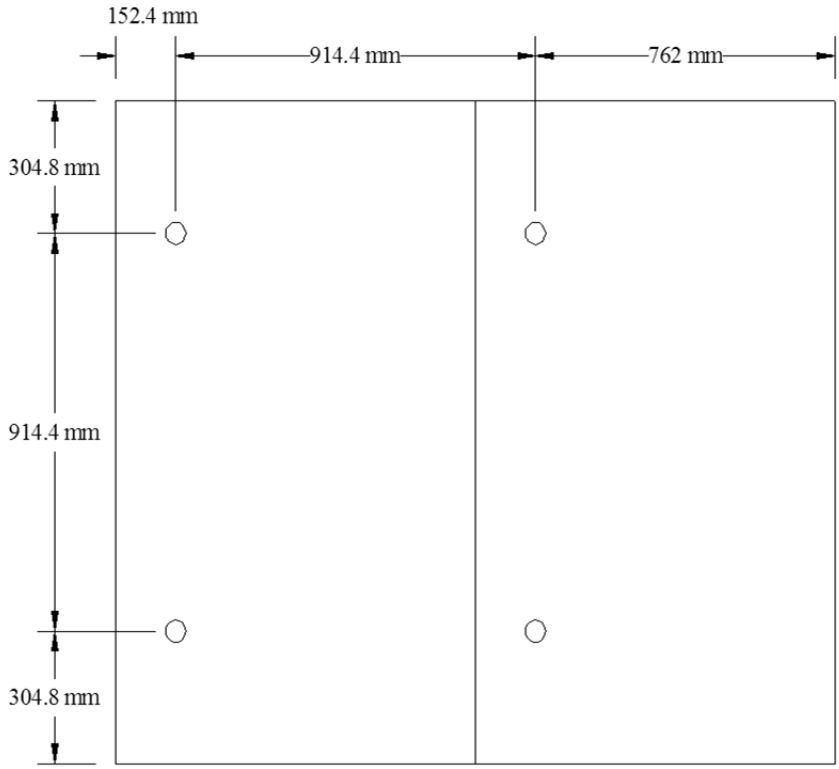

Top View

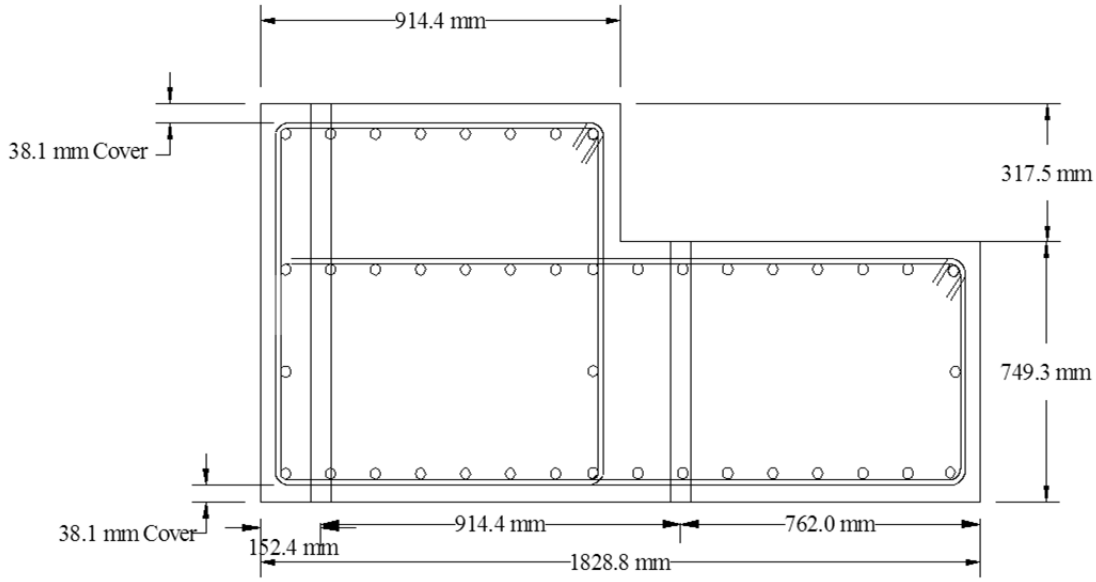

Side View

Fig. A-2 End Concrete Block Detailing

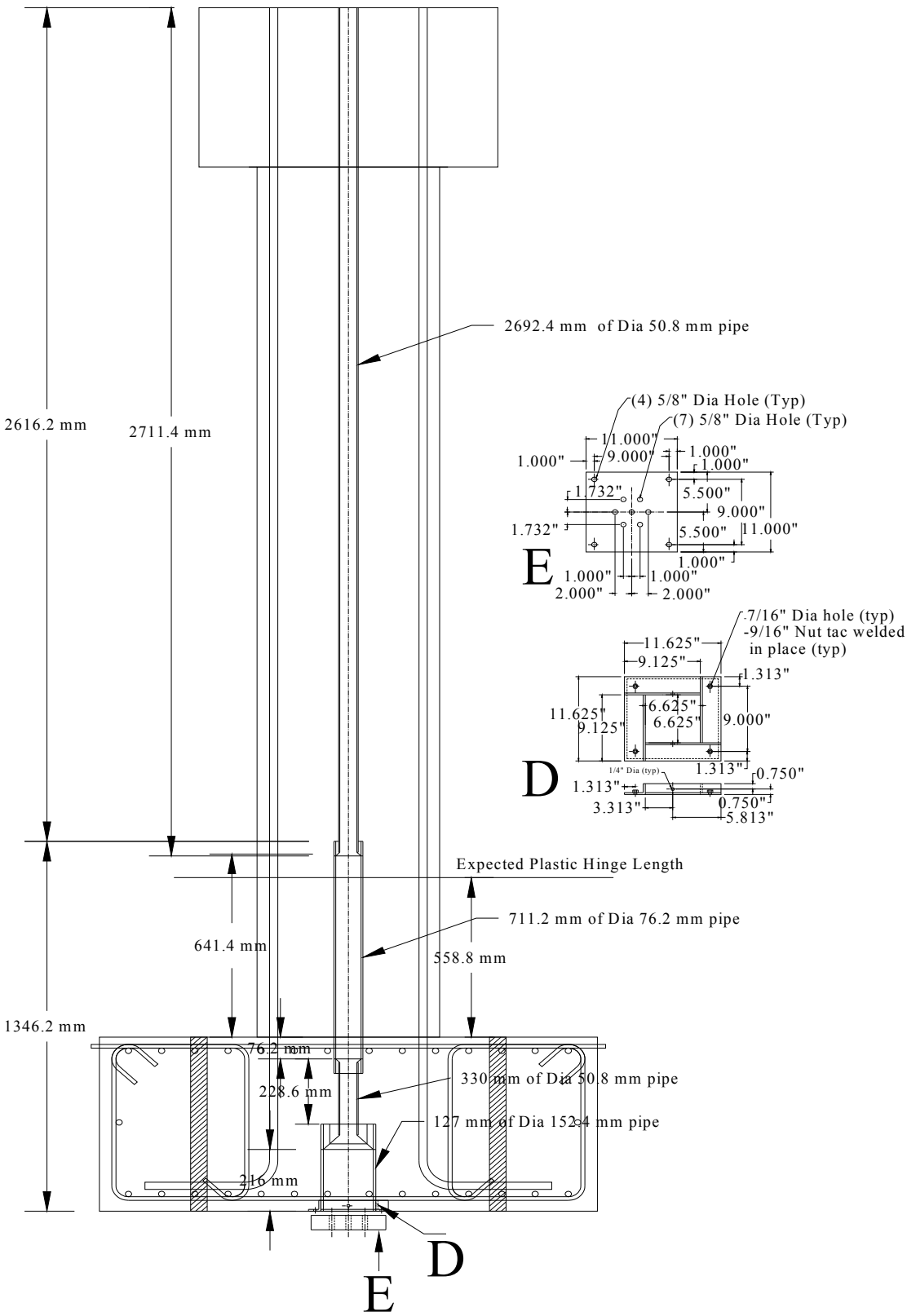

Fig. A-3 Elevation of the Column with PVC Tubing Inside
(1 inch= 25.4 mm)

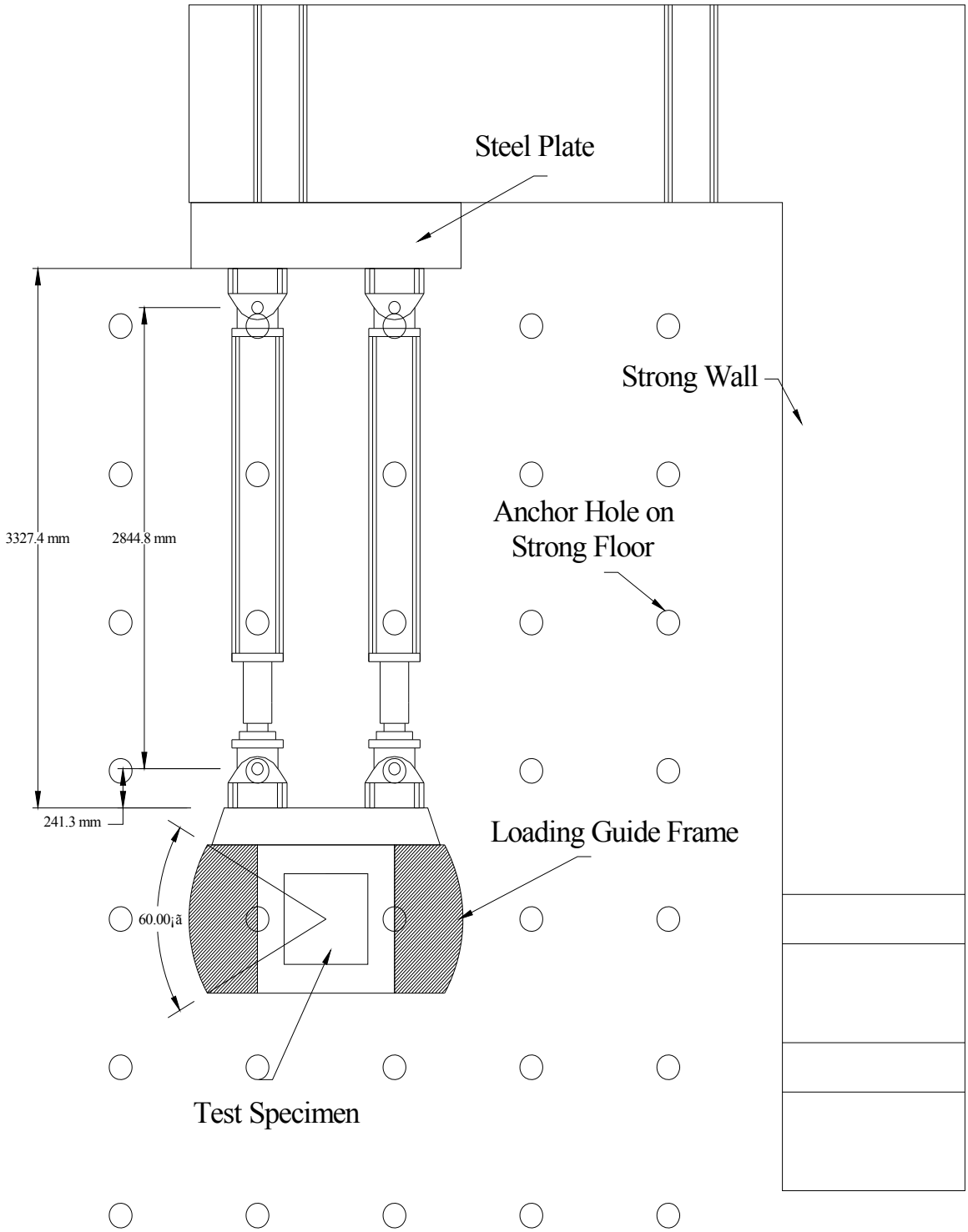

Fig. A-4 Plan View of Actuators, Specimen and Floor Holes
with Respect to Strong Wall

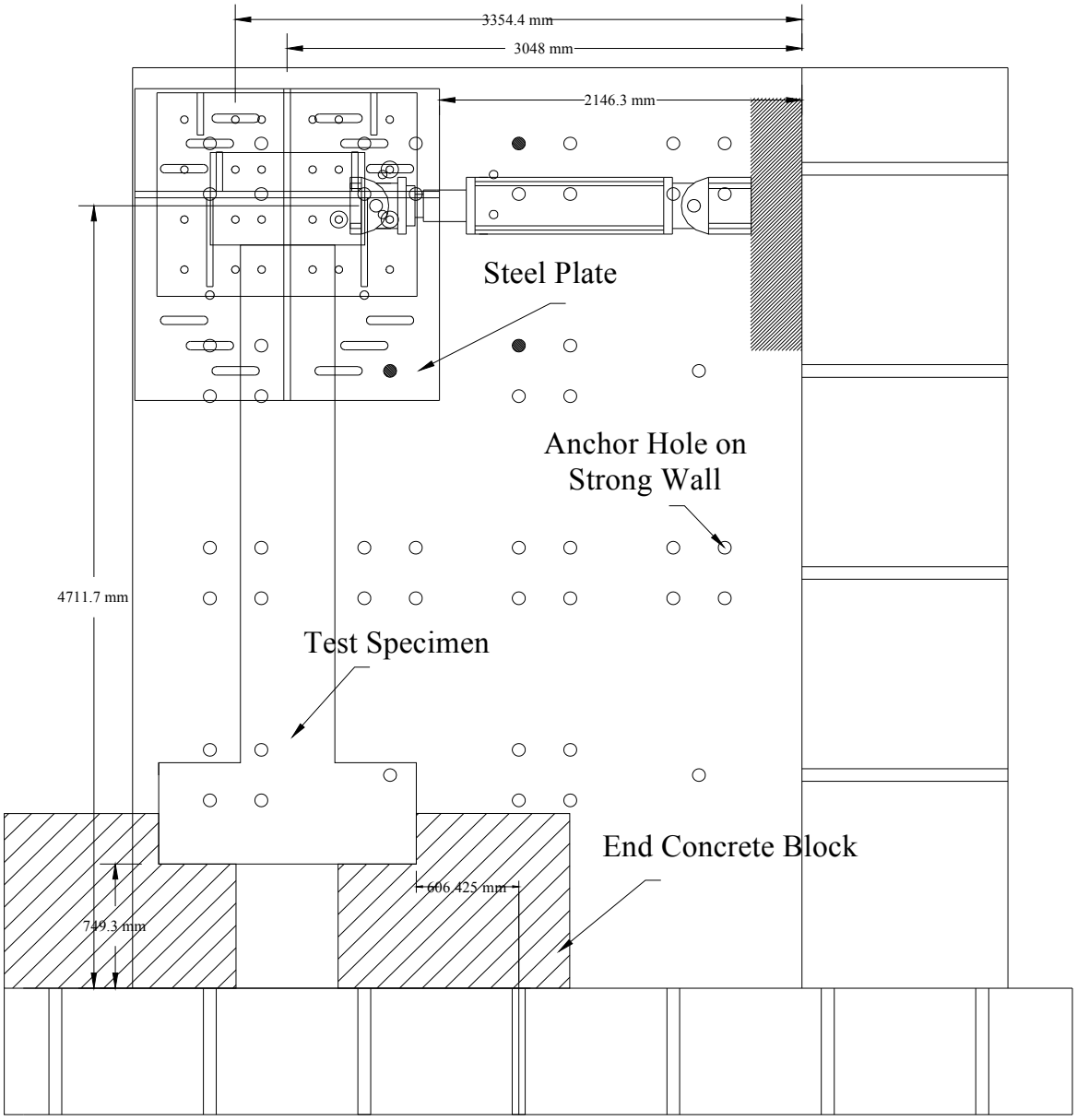

Fig. A-5 Arrangement of Steel Plate on Strong Wall

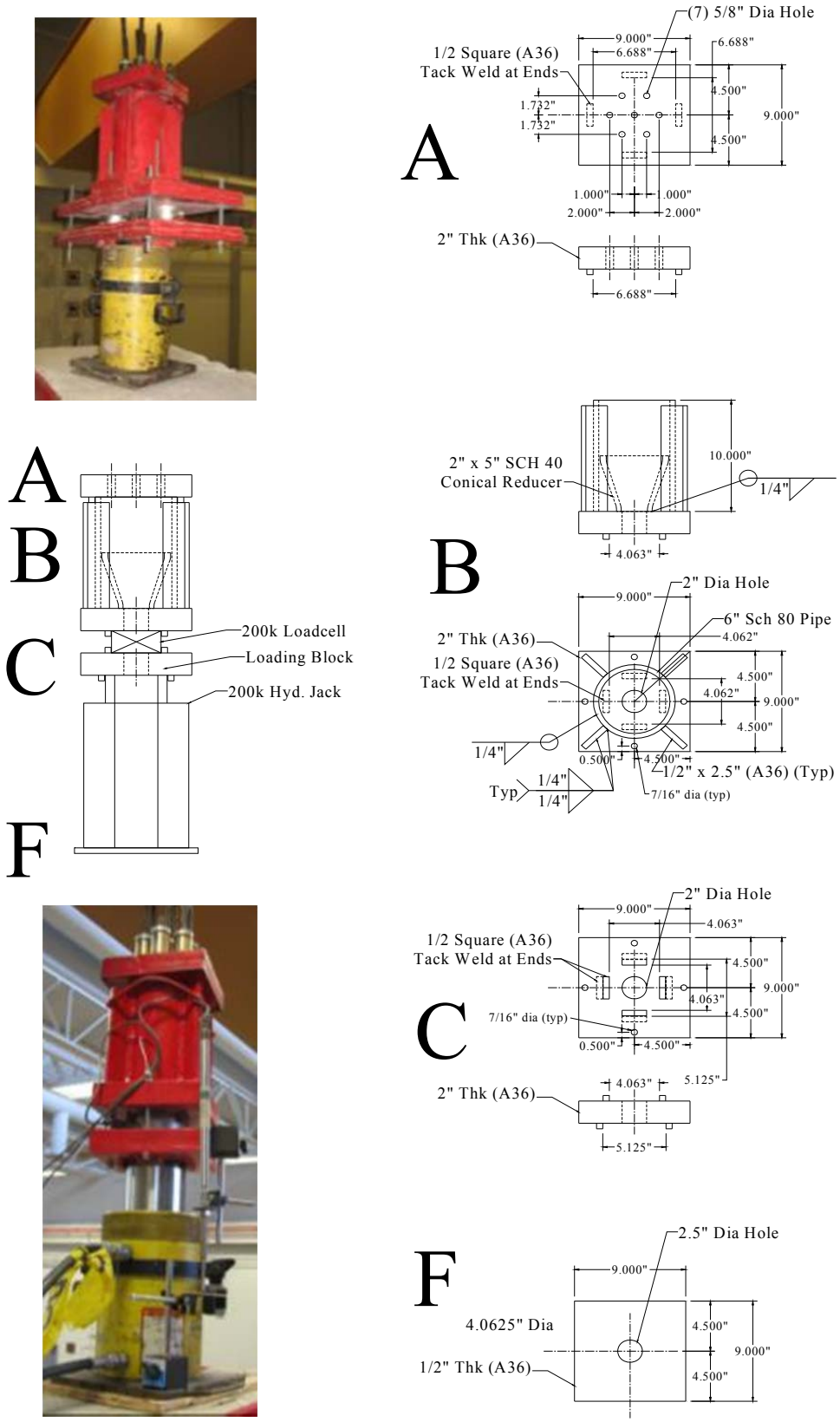

Fig. A-6 Steel Elements for Axial Load Setup at the Top of Loading Stub
(All dimensions in inches, 1 inch= 25.4 mm)

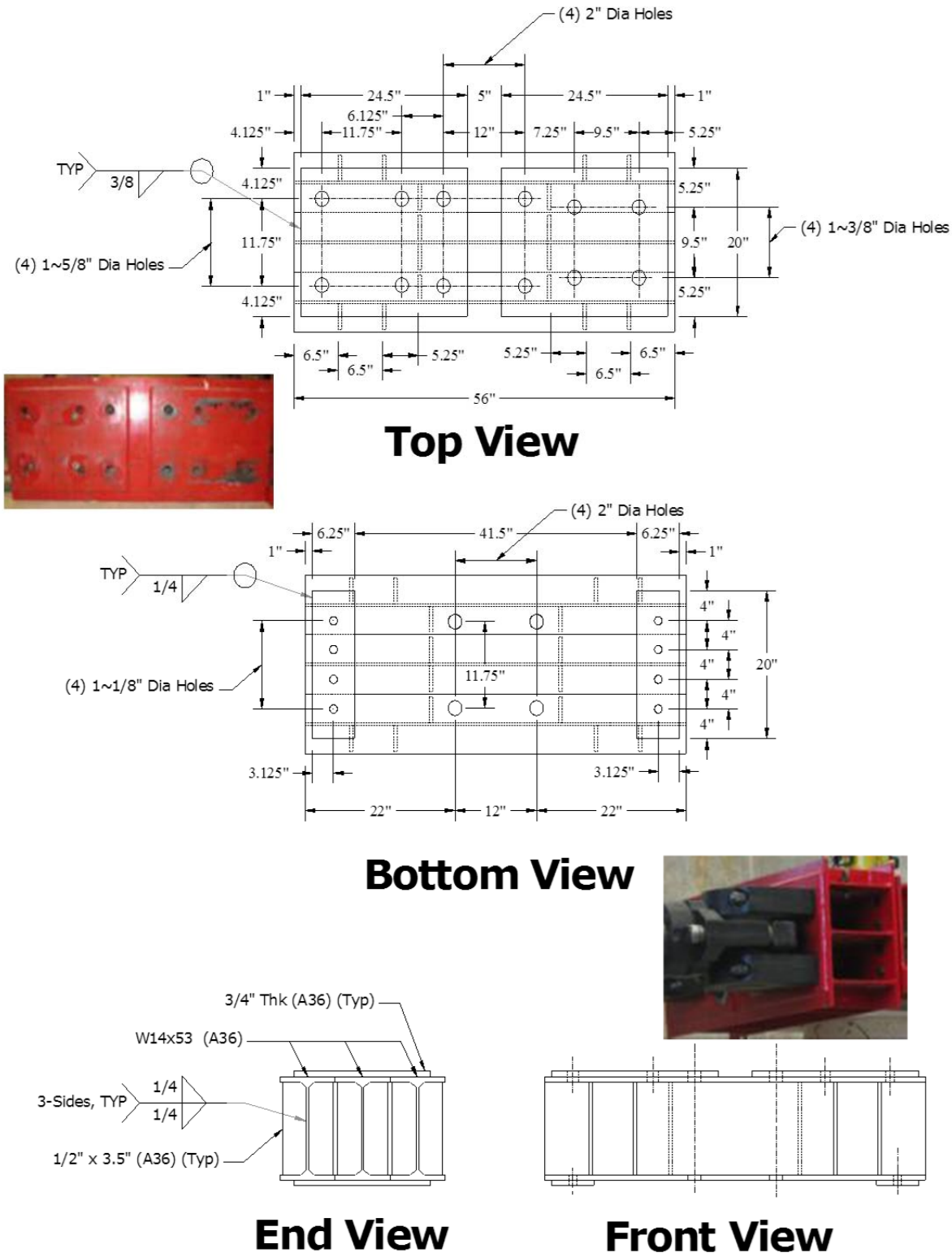

Fig. A-7 Loading Beam Details
(All dimensions in inches, 1 inch= 25.4 mm)

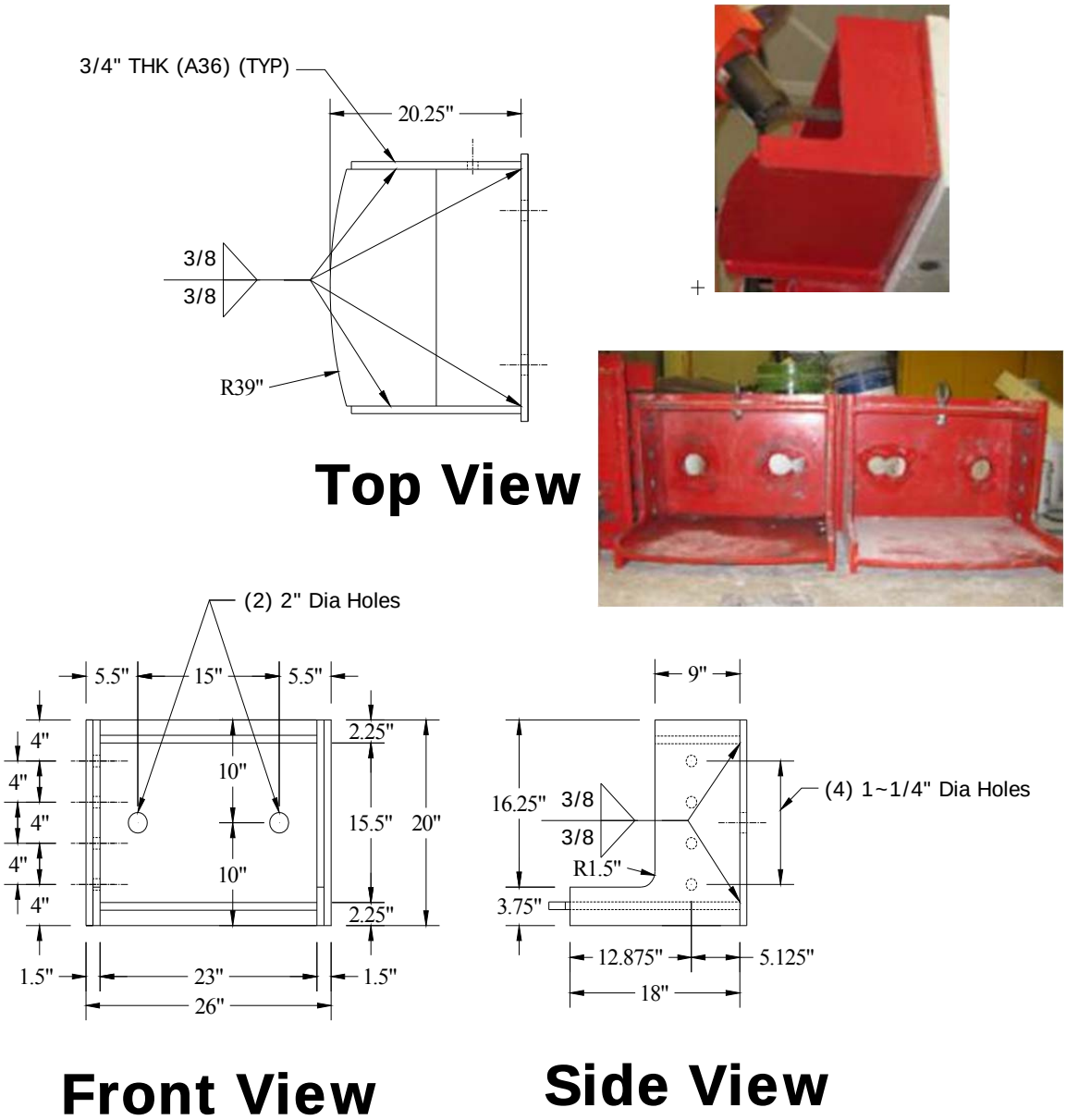

Fig. A-8 Guiding Frame Details
(All dimensions in inches, 1 inch= 25.4 mm)